



**HAL**  
open science

# Laboratory Astrophysics applied to the VUV and X-ray photo-induced desorption from molecular ices

Romain Basalgète

► **To cite this version:**

Romain Basalgète. Laboratory Astrophysics applied to the VUV and X-ray photo-induced desorption from molecular ices. Instrumentation and Methods for Astrophysic [astro-ph.IM]. Sorbonne University, 2022. English. NNT: . tel-03898082v1

**HAL Id: tel-03898082**

**<https://theses.hal.science/tel-03898082v1>**

Submitted on 14 Dec 2022 (v1), last revised 1 Feb 2023 (v2)

**HAL** is a multi-disciplinary open access archive for the deposit and dissemination of scientific research documents, whether they are published or not. The documents may come from teaching and research institutions in France or abroad, or from public or private research centers.

L'archive ouverte pluridisciplinaire **HAL**, est destinée au dépôt et à la diffusion de documents scientifiques de niveau recherche, publiés ou non, émanant des établissements d'enseignement et de recherche français ou étrangers, des laboratoires publics ou privés.



THÈSE DE DOCTORAT  
DE SORBONNE UNIVERSITÉ

Spécialité : Physique

École Doctorale n° 564: Physique Île-de-France

réalisée

au Laboratoire d'Études du Rayonnement et de la Matière  
en Astrophysique et Atmosphères

sous la direction de Mathieu BERTIN

présentée par

**Romain BASALGÈTE**

pour obtenir le grade de

DOCTEUR de SORBONNE UNIVERSITÉ

Sujet de la thèse :

Laboratory Astrophysics applied to the VUV and X-ray  
photo-induced desorption from molecular ices

soutenue le 6 Décembre 2022

Jury

Mme. Christine JOBLIN	Rapporteur
M. Guillermo MUÑOZ CARO	Rapporteur
Mme. Jennifer NOBLE	Examineur
M. Yves BENILAN	Examineur
M. Marco SAITTA	Examineur
M. Patrick ROUSSEAU	Examineur Invité
M. Jean-Hugues FILLION	Co-encadrant de thèse
M. Mathieu BERTIN	Directeur de thèse



---

## Remerciements

*Une aventure qui se termine! Rédiger cette thèse fut un réel plaisir pour moi et je tiens à remercier toutes les personnes qui m'ont soutenu pendant ces 3 années.*

*Je veux d'abord remercier tous mes proches. En premier lieu, Kaelan Donatella et Kelly Molnar pour leur amitié. Kaelan pour tous ses conseils et ces bons moments passés ensemble. Il m'a ouvert l'esprit sur beaucoup de sujets, ce qui m'a beaucoup aidé pendant ma thèse. J'espère que notre amitié durera longtemps. Kelly pour son soutien et sa sincérité, pour m'avoir toujours poussé à être une meilleure personne. Je souhaite de tout coeur que tu réussisses une carrière en recherche. Merci à toute ma famille pour m'avoir soutenu durant ma ré-orientation professionnelle qui est en quelque sorte un peu à contre-courant. Merci à Jérôme et Aurélie pour leur amitié de longue date. Merci à Gaëlle d'avoir été là avec moi pendant cette thèse et d'avoir patiemment accepté de m'écouter parler de mon sujet. Ta présence m'a réconforté dans les moments difficiles et je t'en remercie sincèrement.*

*Merci à Pascal, Patrick et Christian sans lesquels je n'aurais pas pu développer une nouvelle technique expérimentale au labo. Ils ont fortement contribué à enrichir cette thèse et je les remercie sincèrement. Merci à Tarik pour m'avoir entre autre aidé une journée entière à changer un ventilateur de PC. Merci à Géraldine pour avoir eu le courage et la patience de relire mes articles et pour avoir aussi grandement participé au développement expérimental. Merci à Laurent pour ses histoires de post-doc. Merci à Xavier pour sa bonne humeur, ses conseils et ces soirées folles passées au synchrotron de minuit à 6h du matin. J'ai vraiment adoré partager ces moments avec toi et j'espère qu'on aura l'occasion de travailler ensemble à l'avenir. Merci à Japhar pour avoir partagé mon quotidien de thésard et les galères associées. Merci à toute l'équipe de l'ISMO, Anne, Lionel et Daniella pour m'avoir accueilli brièvement dans leur équipe et m'avoir fait découvrir une nouvelle manip avec du méthanol phase gas à évacuation naturelle.*

*Enfin, merci à mes directeurs de thèse, Jean-Hugues Fillion et Mathieu Bertin. D'abord, merci à Jean-Hugues pour m'avoir formé sur les lasers, pour ces bons moments d'échange sur les développements de la manip et pour m'avoir fait confiance. J'ai vraiment adoré travailler avec toi en salle de manip et j'espère que cela se reproduira dans le futur. Merci pour cette conférence à Capri. Merci d'avoir pris le temps de relire toute cette thèse et également les articles. J'admire énormément ta sérénité et ton calme, particulièrement pendant tes présentations, et j'espère m'améliorer en ce sens un jour. Enfin le meilleur pour la fin, merci à Mathieu. En bref, on ne peut pas rêver mieux pour un directeur de thèse. Merci d'avoir été patient, présent et professionnel. Merci en premier lieu de m'avoir donné l'opportunité de réaliser cette thèse. Tu as su me redonner la motivation quand il le fallait. Merci pour ton enthousiasme et ta sympathie. Merci pour toutes ces bières bues ensemble, particulièrement lors de cette conférence à Sète qui restera mémorable. Merci également pour la relecture minutieuse de la thèse et des articles. Merci pour tout tes conseils pour m'améliorer à l'écrit et à l'oral. Merci infiniment pour m'avoir aidé à préparer l'après-thèse, pour toutes tes idées de post-docs et pour ton soutien de tout instant. Si j'ai adoré cette thèse, c'est en grande partie grâce à toi.*

*Merci encore à tout le monde!*

---

# Table of contents

<b>Table of contents</b>	<b>1</b>
<b>Introduction</b>	<b>1</b>
<b>I COMs in astrophysics</b>	<b>5</b>
I.1 The interstellar medium (ISM)	6
I.1.1 Dust and interstellar ices	6
I.1.2 The ISM described through the star cycle	10
I.1.3 Observation of COMs in the ISM	14
I.2 Non-thermal desorption processes	17
I.2.1 Cosmic Ray sputtering	17
I.2.2 VUV photodesorption and molecular clouds	19
I.2.3 X-ray photodesorption and protoplanetary disks	20
I.2.4 Electron-stimulated desorption	24
I.2.5 Other non-thermal processes	25
I.3 Objectives of the thesis	25
<b>II Experimental approach</b>	<b>29</b>
II.1 The SPICES set-up	30
II.1.1 Ultra-high vacuum chamber	31
II.1.2 Ice growth	32
II.1.2.1 Sample holder and deposition technique	32
II.1.2.2 Thickness calibration	33
II.2 Coupling to the SOLEIL synchrotron beamlines	36
II.2.1 Synchrotron beamlines	37
II.2.2 Study of photodesorption by mass spectrometry	38
II.2.2.1 Ionization by electron-impact	39
II.2.2.2 Mass filtering and SEM	40
II.2.3 Quantification of the photodesorption yields	42
II.2.3.1 Raw synchrotron data and photodesorption yields	42
II.2.3.2 Conversion factor $k_X$	45
II.2.3.3 Source of uncertainties on the photodesorption yields	48
II.2.4 Extrapolation to astrophysical yields	50
II.3 Coupling to a VUV photon source implemented at the LERMA lab	53
II.3.1 VUV generation	55
II.3.2 Detection technique : TOF + REMPI	58
II.3.3 TOF, velocity and kinetic energy distributions	59
II.3.4 Internal energy of diatomic molecules	60

II.3.5	REMPI spectra . . . . .	61
<b>III</b>	<b>Ices and their interaction with photons and electrons</b>	<b>67</b>
III.1	Molecular ices . . . . .	67
III.1.1	Physical properties . . . . .	67
III.1.2	VUV photo-absorption of molecular ices . . . . .	70
III.1.3	X-ray photo-absorption of molecular ices . . . . .	75
III.1.4	Interaction with electrons . . . . .	78
III.2	State of the art on photodesorption mechanisms . . . . .	79
III.2.1	VUV photodesorption . . . . .	79
III.2.1.1	Direct desorption mechanisms for non-dissociative states . . . . .	79
III.2.1.2	Indirect desorption mechanisms . . . . .	83
III.2.1.3	Desorption mechanisms induced by photo-dissociation . . . . .	86
III.2.2	X-ray photodesorption . . . . .	88
<b>IV</b>	<b>New insights on the desorption mechanisms in the X-ray and VUV range</b>	<b>91</b>
IV.1	Mechanisms in the X-ray range : X-ray photodesorption from mixed and layered N <sub>2</sub> -CO ices . . . . .	92
IV.1.1	X-ray absorption spectra . . . . .	93
IV.1.2	X-ray photodesorption yields from pure and mixed ices . . . . .	95
IV.1.3	Layered ice experiment . . . . .	98
IV.1.4	Estimation of $\Lambda_{des}$ and indirect desorption mechanisms . . . . .	101
IV.1.5	Modeling of the energy deposited by Auger scattering . . . . .	103
IV.1.6	Conversion of the absorbed energy to desorption . . . . .	106
IV.2	Mechanisms in the VUV range : internal and kinetic energy of photodesorbed CO from thick CO ice . . . . .	109
IV.2.1	Relative vibrational population . . . . .	112
IV.2.2	TOF, velocity and kinetic energy distributions . . . . .	112
IV.2.3	Relative rotational population . . . . .	115
IV.2.4	Discussion on the photodesorption mechanisms . . . . .	117
IV.3	Conclusion and perspectives . . . . .	118
<b>V</b>	<b>VUV photodesorption of COMs</b>	<b>121</b>
V.1	VUV photodesorption of HCOOH and HCOOCH <sub>3</sub> . . . . .	122
V.1.1	Pure ice . . . . .	122
V.1.2	Mixed and layered ices . . . . .	126
V.2	VUV photodesorption of CH <sub>3</sub> CN . . . . .	130
V.2.1	Pure ice . . . . .	130
V.2.2	Mixed and layered ices . . . . .	133
V.3	Astrophysical yields and discussion . . . . .	137
V.4	Conclusion and perspectives . . . . .	142
<b>VI</b>	<b>X-ray photodesorption of COMs</b>	<b>145</b>
VI.1	Total Electron yields and their evolution with the irradiation . . . . .	146
VI.1.1	CH <sub>3</sub> OH-containing ices . . . . .	146
VI.1.2	CH <sub>3</sub> CN-containing ices . . . . .	148
VI.1.3	HCOOH-containing ices . . . . .	151
VI.2	X-ray photodesorption from pure ices . . . . .	154

---

VI.2.1 Pure CH <sub>3</sub> OH ice . . . . .	154
VI.2.1.1 X-ray photodesorption yields . . . . .	154
VI.2.1.2 Comparison with VUV yields . . . . .	158
VI.2.1.3 Comparison with ESD yields . . . . .	160
VI.2.2 Pure CH <sub>3</sub> CN ice . . . . .	162
VI.2.3 Pure HCOOH ice . . . . .	165
VI.3 X-ray photodesorption from analogues of interstellar ices . . . . .	168
VI.3.1 CH <sub>3</sub> OH-containing ices . . . . .	168
VI.3.2 CH <sub>3</sub> CN-containing ices . . . . .	173
VI.3.3 HCOOH-containing ices . . . . .	178
VI.4 Astrophysical yields and implications . . . . .	182
VI.5 Conclusion and perspectives . . . . .	185
<b>Conclusion</b>	<b>187</b>
<b>Appendix A : Partial ionization cross sections by electron impact at 70 eV</b>	<b>193</b>
<b>Bibliographie</b>	<b>195</b>



# Introduction

In our solar system or in distant regions in space, molecules are omnipresent. They can form even in the extreme conditions of the interstellar medium (ISM), commonly described as the space between stars. Astrophysicists are constantly observing molecules thanks to ground-based and space telescopes, such as the ALMA and the NOEMA radio-telescopes or the recently launched James-Webb Space Telescope. Over  $\sim 200$  species are currently inventoried, showing the surprising and not-well understood molecular complexity and richness of the ISM. Molecules in space tend to form in the denser and colder regions of the ISM, where small dust grains are also ubiquitous. The most abundant and simple molecule is  $\text{H}_2$ , which is believed to form on the surface of dust grains. Simple molecules such as  $\text{H}_2\text{O}$ ,  $\text{CO}$ ,  $\text{CO}_2$  and  $\text{NH}_3$  and Complex Organic Molecules (COMs) such as alcohols ( $\text{CH}_3\text{OH}$ ), esters ( $\text{HCOOCH}_3$ ) or nitriles ( $\text{CH}_3\text{CN}$ ) are also present. A particularly rich variety of carbonaceous molecules is also inferred from astronomical observations. This raises several questions : how these molecules are formed? Are they forming under specific conditions, i.e. are they tracers of specific regions of space? Can COMs survive through the different evolutionary stages of star and planet formation and eventually populate young celestial bodies with enough organic material for the life to appear?

Laboratory astrophysics has emerged over the last 50 years to answer such questions. It is a large scientific field that includes theoretical and experimental techniques aiming to identify the physical and chemical processes that drive the evolution of the ISM. Among the different components of the ISM, the dust grains play a major role in the chemical evolution. They provide a third-body dissipating the excess of energy of chemical reactions, hence favoring the formation of new species at their surface. When their surface temperature is low enough, this leads to the build-up of icy mantles, referred to as interstellar ices. Furthermore, exchanges between this solid icy phase and the gas phase occur in several cold regions of the ISM. Indeed, in these regions, the surface temperature of the dust grains is low enough ( $T < 100$  K) to allow molecules to condense at their surface. On the other hand, non-thermal desorption processes can induce the desorption (i.e. the ejection) of molecules from the ices into the gas phase. These ice-to-gas exchanges explain why we observe molecules in the gas phase of these

regions where they should otherwise be condensed on the interstellar ices. They also drive the chemical evolution of both the gas and solid phases. Non-thermal desorption includes the desorption induced by the irradiation of energetic particles (cosmic rays, photons, electrons), shock-induced desorption and chemical desorption induced by the exothermicity of a chemical reaction. In view of the various processes at play, it has become crucial to provide quantitative data that inform on the relative efficiency of each process, in order to assess if there is a dominant one driving the ice-to-gas exchanges. A part of laboratory astrophysics studies has therefore focused on the characterization of these non-thermal processes.

The detection of gas phase COMs in the cold regions of the ISM has brought a peculiar attention since their way of formation in such extreme conditions was not known. This has motivated numerous experimental studies that showed in fine efficient formation routes of COMs in ice analogues by energetic or non-energetic pathways. This has led to the general belief that many COMs are formed in interstellar ices. To complete the full story of gas phase COMs, there is a need of identifying efficient non-thermal desorption processes that eject them from the ices. Among the various processes, cosmic-ray sputtering, chemical desorption and the desorption induced by photons, the so-called photodesorption, are possible candidates. These processes are currently poorly constrained for COMs, both in terms of (1) quantitative data that provide information on their relative efficiency and in terms of (2) the fundamental mechanisms at play that should be taken into account for a proper implementation of the processes in astrochemical modeling. In this context, this thesis aims to shed light on the efficiency and mechanisms associated with photodesorption, in the VUV (7 - 13.6 eV) and X-ray range (0.1 - 10 keV). An experimental approach is retained. In particular, two different sets of experiments were conducted : one at the SOLEIL synchrotron facility and the other one directly at the LERMA lab.

First, interstellar ice analogues grown in a ultra-high vacuum set-up are irradiated by synchrotron light. Such monochromatic and tunable light is used to study photodesorption as a function of the incident photon energy in the VUV and soft X-ray range (400 - 600 eV). A methodology is proposed to quantify photodesorption yields derived from mass spectrometry signals. The study of these yields as a function of the photon energy enables to highlight the fundamental mechanisms involved in the desorption process, which were especially well characterized for a simple system in the soft X-ray range. A collection of data has been obtained for the photodesorption of some COMs (methanol  $\text{CH}_3\text{OH}$ , acetonitrile  $\text{CH}_3\text{CN}$ , formic acid  $\text{HCOOH}$  and methyl formate  $\text{HCOOCH}_3$ ). Our methodology allowed us to provide the first quantitative data on the photodesorption of these COMs from interstellar ice analogues. Desorption mechanisms were also discussed, especially regarding the dependence of the yields with

the ice composition. Hopefully, these results will help to interpret observational data and open new scientific perspectives for the study of COMs. For instance, additional experiments conducted at the ISMO lab during the thesis have revealed that electron-stimulated desorption (ESD) experiments could offer a good complementary tool for the study of X-ray photodesorption.

As discussed previously, identifying the fundamental mechanisms of desorption will significantly improve our knowledge on the role of photodesorption in the ISM. Various mechanisms are already known in the literature but their full characterization is sometimes lacking. To answer such question, experiments at the LERMA lab were conducted during the thesis. I implemented a new monochromatic and tunable VUV photon source directly at the LERMA lab by using a four-wave mixing technique well-known since the 80's. The use of this photon source coupled with a Resonance Enhanced Multi-Photon Ionization (REMPI) technique and a Time-Of-Flight (TOF) delay enabled to quantify the internal and kinetic energy states of photodesorbed CO molecule from a pure CO ice. The analysis of these results surprisingly pointed towards a desorption scenario not predicted by previous theoretical studies. The interpretation of these data is still ongoing and a collaboration has been established with a theoretical team in order to provide simulation inputs. This new experimental set-up developed during the thesis opens large opportunities to progressively unravel the photodesorption mechanisms that drive the gas-to-ice exchanges in the cold ISM.

This thesis is organized as follows. The astrophysical context is described in Chapter I. A general description of the different evolutionary stages of the ISM, a brief description of the dust particles and a discussion on the observation and formation of COMs are given. Non-thermal desorption processes are also introduced. Chapter II describes the experimental approach. The growth of interstellar ice analogues under ultra-high vacuum condition and the detection of photodesorption in the SPICES set-up are described. The methodology implemented to derive photodesorption yields from synchrotron experiments is detailed. Additionally, I present the approach retained to obtain quantitative data with the new VUV photon source implemented directly at the LERMA lab. In Chapter III, I discuss the interaction of molecular ices with VUV photons, X-rays and electrons. I also review previous breakthrough from the literature, which enables to discuss the desorption mechanisms known and their implication for the desorption of COMs. In Chapter IV, I present important results obtained for ices of diatomic molecules (CO, N<sub>2</sub>). First, X-ray photodesorption studies from mixed CO:N<sub>2</sub> ices have revealed an indirect desorption mechanism that is further characterized by a layered ice experiment and associated with a simple modeling. Then, I discuss the data obtained with the new VUV photon source at the LERMA lab, that deals with the internal and kinetic energy states of photodesorbed CO molecules. Chapter V and VI focus respec-

tively on the VUV and X-ray photodesorption of COMs that are detected in the cold regions of the ISM : methanol  $\text{CH}_3\text{OH}$ , acetonitrile  $\text{CH}_3\text{CN}$ , formic acid  $\text{HCOOH}$  and methyl formate  $\text{HCOOCH}_3$ . The quantification of the photodesorption yields of the intact COM and of the photo-fragments is given and the dependence of the yields with the ice composition is detailed. This ultimately leads to suggest desorption mechanisms for COMs and to compare our experimental results with astronomical observations.

# Chapter I

## COMs in astrophysics

The starting point of this thesis originates from the recent astronomical observations of Complex Organic Molecules (COMs) in the InterStellar Medium (ISM). In astrochemistry, COMs (sometimes called iCOMs for interstellar COMs) designate molecules containing six or more atoms. They are called organic in the sense that their elemental composition is mostly a combination of H, C, O and N. COMs are considered precursors for the formation of prebiotic molecules. Therefore, they have a central part in astrochemistry and they have been extensively studied. COMs are closely related to small dust particles that are present in the ISM. These dust grains will be the topic of the first section of this chapter, along with a general description of what is the ISM and in which regions COMs are detected. The formation pathways of COMs in the ISM will be briefly discussed as well, with a focus on the COMs studied in this thesis : methanol  $\text{CH}_3\text{OH}$ , acetonitrile  $\text{CH}_3\text{CN}$ , formic acid  $\text{HCOOH}$ <sup>1</sup> and methyl formate  $\text{HCOOCH}_3$ . More importantly, the presence of COMs in the gas phase of the cold regions of the ISM, where the surface temperature of the dust grains is low ( $T < 100$  K), requires to invoke non-thermal desorption processes. These processes will be the topic of the second section of this chapter, with a peculiar attention on photodesorption, which is the central subject of this thesis. This chapter is based on several astrochemical / astrophysical reviews and books that give an excellent overview of the field of research covered by this thesis ([Herbst and van Dishoeck, 2009](#); [Tielens, 2011](#); [Draine, 2011](#); [Caselli and Ceccarelli, 2012](#); [Bennett et al., 2013](#); [van Dishoeck et al., 2013](#); [Muñoz Caro and Dartois, 2013](#); [van Dishoeck, 2014](#); [Boogert et al., 2015](#); [Öberg, K. I., 2016](#); [van Dishoeck, 2017](#); [Herbst, 2017](#); [Arumainayagam et al., 2019](#)).

---

1.  $\text{HCOOH}$  contains only 5 atoms but will anyway be considered as a COM

## I.1 The interstellar medium (ISM)

### I.1.1 Dust and interstellar ices

The ISM designates the regions in space (outside the solar system) where stars and planets are formed. It is composed of  $\sim 99\%$  gas (mainly atomic and molecular hydrogen, with traces of heavier elements such as He, O, C, N) and 1% dust grains in mass. These dust grains have a central role in the ISM and they have been extensively studied (e.g. [Draine \(2003\)](#); [Williams \(2005\)](#); [Ryden, B. and Pogge, R. \(2021\)](#)). The presence of dust grains in the ISM was first inferred from astronomical observations to account for starlight extinction : a comparison of the expected emission spectrum of a star at a known distance with the actual spectrum observed on a line of sight by telescopes displays attenuation features. This starlight extinction is systematically observed throughout the Milky Way, demonstrating that dust is omnipresent. Characterizing these dust grains has been made possible by the development of space telescopes in the last decades such as the Infrared Space Observatory (ISO), the Herschel Space Observatory and the Spitzer Space Telescope. Future observations with the James Webb Space Telescope (JWST) will also provide additional insights on dust.

The wavelength dependence of the starlight extinction, known as the interstellar extinction curve, enabled astrophysicists to discuss the composition and the structure of these dust grains, based on absorption and emission features at specific wavelengths. The strongest feature is a broad bump centered at  $2175 \text{ \AA}$ , tentatively attributed to dust particles rich in aromatic carbon (graphite, hydrogenated amorphous carbon HAC, polycyclic aromatic hydrocarbons PAHs). Mid-infrared silicate features (e.g.  $9.7 \text{ \mu m}$ ,  $18 \text{ \mu m}$ ) are also observed and associated with Si-O vibrational modes in silicates, rather amorphous than crystalline. The presence of HAC (aromatic islands connected with aliphatic chains) is proposed to account for the absorption feature at  $3.4 \text{ \mu m}$ . The Diffuse Interstellar Bands (DIBs) observed in the visible and near-infrared ranges remain to be attributed<sup>2</sup>. Features associated with the emission of light are also attributed to dust particles. For instance, PAHs are commonly admitted to be the carriers of a family of emission features at  $3.3$ ,  $6.2$ ,  $7.7$ ,  $8.6$  and  $11.3 \text{ \mu m}$ , although no precise attribution has been made yet (assumptions include free PAHs, PAH clusters or particles composed in part of PAHs; [Leger and Puget \(1984\)](#); [Allamandola et al. \(1985\)](#); [Jones, A. P. \(2012a,b,c\)](#)).

Under-abundances of gas phase elements, with respect to standard references (e.g. the Sun), observed towards stars in particular line of sights (for example towards the bright star zeta Ophiuchi, [Poteet et al. \(2015\)](#)) suggest that dust grains should also

---

2. fullerene  $C_{60}^+$  has been demonstrated to contribute to these bands ([Walker et al., 2015](#); [Campbell et al., 2015](#))

contain metallic elements such as Fe and Mg. Polarization of starlight by dust grains shows that they have an asymmetrical shape and that they must be partially aligned. The interstellar extinction curve also enables to constrain the dust grain size distribution. Typically, the size distribution of the dust grains is expected to range from 1 nm (or below for PAHs) to 1  $\mu\text{m}$  and depends on the dust composition (e.g. [Weingartner and Draine \(2001\)](#); [Compiègne et al. \(2011\)](#); [Hirashita and Nozawa \(2013\)](#)). Finally, dust grains are expected to be formed during the star end-of-life, with an important contribution of stars reaching the asymptotic giant branch AGB (e.g. [González Delgado, D. et al. \(2003\)](#); [Takigawa et al. \(2017\)](#)). Supernovae are also expected to play a role in the formation of dust. Although the exact mechanism of dust formation is still not clear, it requires high densities for material to accrete. These conditions are met, for example, in the star photosphere during its end-of-life thanks to high stellar mass-loss. Once the dust grains are formed, they can migrate to the ISM via radiation pressure for example.

More importantly for this thesis, the surface temperature of dust grains is low ( $T < 100$  K) in several regions of the ISM and the density of gas is high ( $> 10^3$   $\text{cm}^{-3}$ ). In the following, these regions will be named "cold regions" in reference to the dust surface temperature being  $< 100$  K (the gas temperature might be different) and the gas density being high. In these cold regions, most of the gas phase molecules can condense on dust grains over time. If non-thermal desorption processes (see Section I.2) are not

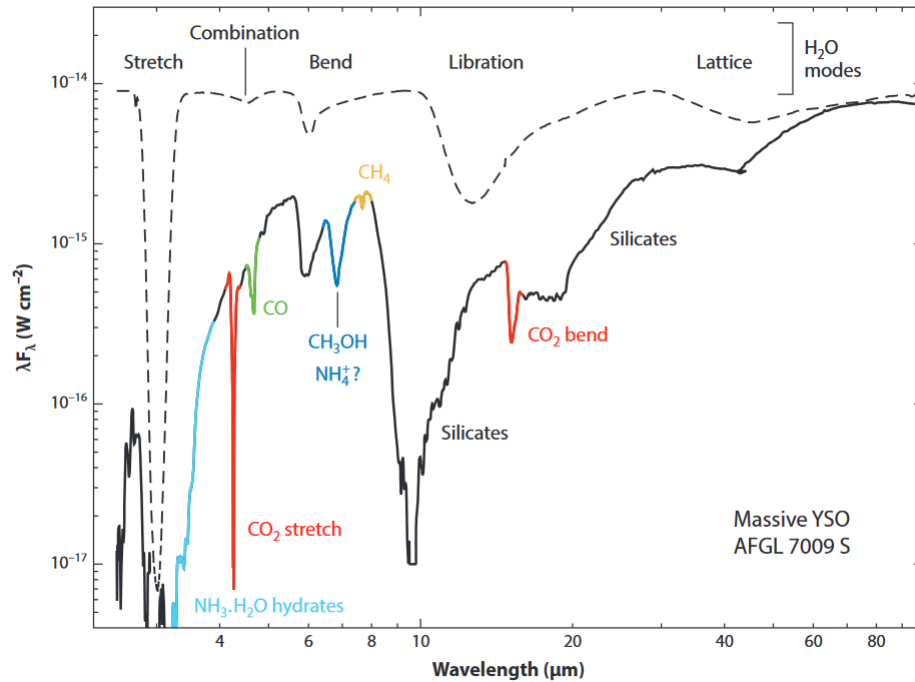


FIGURE I.1 – Ice and dust features in the massive young stellar object (YSO) AFGL 7009 S. Taken from [Boogert et al. \(2015\)](#). Ice absorption features are colored.

efficient enough to oppose the condensation, this results in the formation of what is known as interstellar ices or icy mantles. The composition of icy mantles depends, among other things, on the dust temperature and on the gas elemental budget H, O, C, N. Constraints on such composition can be derived from absorption bands attributed to ices in the  $\mu\text{m}$  wavelength range. An example is given in Figure I.1 for the region near the young stellar object AFGL 7009 (Boogert et al., 2015). The absorption features are due to the excitation of the vibrational modes of the molecules in the ice. They may strongly depend on the interaction of the molecule with its close neighbors (intermolecular interactions) and experimental spectroscopy studies of ices are crucial to identify the ice composition that best fits the absorption bands observed.

The inferred composition of the icy mantles observed through the ISM is given in Figure I.2. Ices are dominantly composed of water  $\text{H}_2\text{O}$ , whose formation by gas phase reactions is not efficient enough to explain the abundances observed, implying surface reactions on dust grains to be involved. For example, reactions of cold H atoms with condensed  $\text{O}_2$ , among other reactions involving H,  $\text{H}_2$  and O in a complex interconnected reaction network, have been experimentally proven to be an efficient formation route for forming water ice (Ioppolo et al., 2008, 2010; Miyauchi et al., 2008; Cuppen et al., 2010). Carbon dioxide  $\text{CO}_2$ , which is the second most abundant mole-

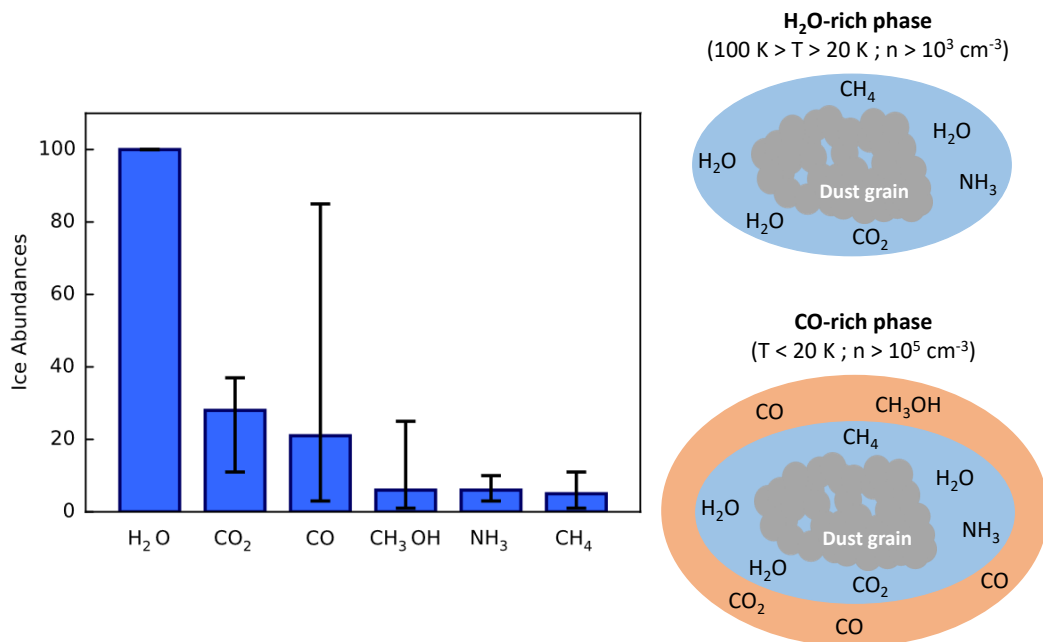


FIGURE I.2 – Left side : molecular composition of interstellar ices based on astronomical observations, relative to  $\text{H}_2\text{O}$  (taken from Öberg, K. I. (2016)). The error bars correspond to the minimum and maximum abundances detected. Right side : scheme of the different phases expected for interstellar ices (inspired from Boogert et al. (2015) and van Dishoeck (2014)). More details are given in the text.

cule in ices, is also expected to be formed mainly in the solid phase, either by energetic (UV or cosmic ray) processing of interstellar ices (Loeffler, M. J. et al., 2005; Mennella et al., 2006) or by surface reactions (Ruffle and Herbst, 2001; Ioppolo et al., 2011). On the other hand, carbon monoxide CO, which is another major constituents of interstellar ices, is formed in the gas phase and then accretes on ices. H<sub>2</sub>O and CO<sub>2</sub> stay adsorbed on dust grains when their surface temperature is less than  $\sim 100$  K whereas CO condenses when the surface temperature is very low, at  $T < 20$  K. Consequently, icy mantles are expected to be characterized by two phases that are schemed on the right side of Figure 1.2. The first phase is a H<sub>2</sub>O rich phase, corresponding to a dust surface temperature between 100 K and 20 K. This phase is also expected to be composed of CO<sub>2</sub> and of small quantities (with respect to water) of CH<sub>4</sub> and NH<sub>3</sub>. The second phase is a CO-rich phase forming an upper mantle on top of water ice in the coldest regions. This is expected to be due to a catastrophic CO freeze-out in regions where temperatures are low ( $T < 20$  K) and densities are high ( $10^5$  cm<sup>-3</sup>). The actual existence of these two phases is supported by observations in low-mass star forming clouds (Pontopidan, K. M. et al., 2003). Based on the ice column densities of H<sub>2</sub>O derived from observational data, which vary significantly depending on the object observed, Potapov et al. (2020) estimated that between 300 and 12000 layers should cover the dust grains assuming that these latter form a compact core. On the other hand, icy mantles may also be mixed with dust, especially due to the high porosity of the grains, therefore challenging the simple view depicted in the right side of Figure 1.2 where ices form upper layers above the dust. Instead, the large effective surface provided by the dust grains might imply a very different structure (Potapov et al., 2020, 2021).

In addition, COMs are expected to populate the ices, in small amounts with respect to water. To date, only CH<sub>3</sub>OH has been detected as a significant constituent but other COMs could as well contribute. Whether COMs are directly formed in icy mantles or are formed in gas phase and then accrete on ices is discussed in Section 1.1.3. Dust grains and icy mantles play a very important role in the chemistry of the ISM. They can be seen as catalysts for chemical reaction, acting as a third body that can dissipate the energy excess of reactions and increase reaction probabilities by providing a reservoir of molecules that can diffuse, meet and react. Interaction of ices with source of irradiations, through the different evolutionary stages of the ISM (see next sub-section), is also an important topic that will be discussed. Interstellar ices are also very similar, in terms of composition, to icy bodies that are found in the solar system. Namely, the composition of comets is found to strongly resemble that of interstellar ices (Mumma and Charnley, 2011b; Grady et al., 2018), which supports the idea that comets did not dramatically suffer from chemical changes since the early stages of planet formation. Icy moons, such as Triton or Europa, whose surface is covered with water ice (and sometimes other molecules such as N<sub>2</sub>, CH<sub>4</sub> or CO) are also presenting similarities with

interstellar ices (Bennett et al., 2013). The topic of this thesis may also be of interest for these icy bodies.

### I.1.2 The ISM described through the star cycle

The ISM is commonly illustrated by different stages of star and planet formation corresponding to different physical conditions. A simplified version of these different evolutionary stages is shown in Figure I.3 and detailed in the following :

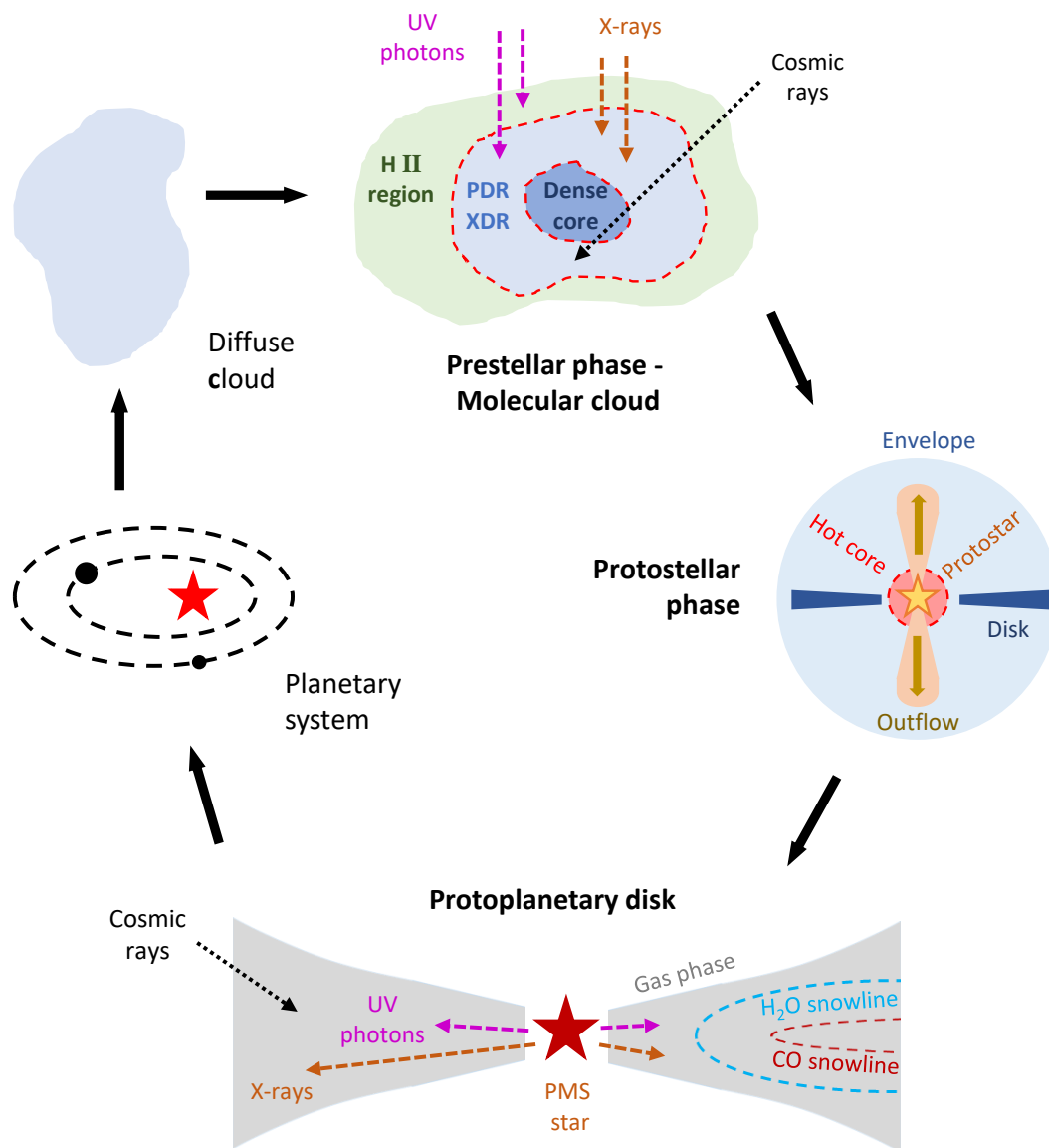


FIGURE I.3 – Simplified illustration of the regions of the ISM described through the star and planet formation cycle. Each phase is described in the text. Inspired from Caselli and Ceccarelli (2012); van Dishoeck (2014); Öberg, K. I. (2016).

- **Diffuse cloud** : diffuse clouds are regions of the ISM with the lowest density ( $10^2$  -  $10^3$  atoms and molecules per  $\text{cm}^3$ ). These clouds are irradiated with UltraViolet (UV) light originating from the InterStellar Radiation Field (ISRF) or directly from nearby stars (see Section 1.2 for more details on the source of irradiations in the ISM) that dissociates most molecules. Therefore, the molecular composition of these diffuse clouds is relatively simple. The dominant molecule in these regions is  $\text{H}_2$ , which forms primarily on dust grain surfaces. Some simple molecules (mainly CO) and radicals (such as OH, CN), whose formation is dominated by gas phase reactions, are also detected in these regions.
- **Prestellar phase (Molecular cloud)** : because of gravity, over-densities in diffuse clouds generate in time a slow accumulation of matter until a dense core is formed. In that case, the physical conditions differ between the edge and the center of the cloud. At the very edge, the cloud is exposed to UV radiations whose photons at energy  $> 13.6$  eV are absorbed via photo-ionization of H : this region is called a H II region. When going deeper into the cloud, the temperature of the gas and dust decreases while the density increases. At some point, the very interior of the cloud, referred to as a dense core, is shielded from external UV photons, the density is high ( $\sim 10^4$  -  $10^6$   $\text{cm}^{-3}$ ) and the temperature of gas and dust is very low ( $T < 20$  K). Dense cores are characterized by gas phase depletion of volatile atoms and molecules and grain surface chemistry : the temperature of the dust grains is so low such that molecules and atoms freeze-out on their surface and possibly react to form hydrogenated species. Dense cores are also irradiated by cosmic rays. These high-energy particles can penetrate deep into the clouds until reaching the dense core and they ionize the gas in their path. Consequently, ion-molecule chemistry is playing an important role in dense core. The interface between the H II region and the dense core is called a Photon-Dominated or Photo-Dissociation Region (PDR). Chemistry and physical conditions in PDRs are driven by the interaction of UV photons with gas and dust. The irradiation of molecular clouds by X-rays (if a X-ray source is nearby) can also affect its physical and chemical conditions in a different way than UV photons (see references in [van Dishoeck \(2017\)](#)). Similarly to the PDR for UV photons, X-ray dominated regions (XDR) describe the regions where X-rays dominate the physical and chemical processes. When the region of a molecular cloud is sufficiently dense to be completely opaque to visible wavelengths, it is referred to as a dark cloud.
- **Protostellar phase** : if the dense core reaches a sufficient mass, gravitational collapse occurs. The temperature of the core remains low due to radiative cooling until it becomes optically thick. Then the temperature increases and a young rotating star, also called a protostar, is formed. The temperature of the gas near the protostar can reach up to 100-300 K and the density is  $> 10^7$   $\text{cm}^{-3}$ . This region

is called a hot core or a hot corino for low-masses. Accreting material from the surrounding gas feeds the protostar that ejects part of it in supersonic jets, called outflows, hence allowing the loss of angular momentum. In the regions where the outflowing material encounters the surrounding envelope of the protostar, shocks occur. Protostars are sometimes characterized by an embedded rotating disk forming perpendicularly to its angular momentum.

- **Protoplanetary disks** : after  $\sim 10^5$  years, the protostar envelope dissipates or is incorporated into the disk. The resulting disk is called a protoplanetary disk in the sense that it will eventually hosts comets and planets after dust particles coalescing. At the center of the disk remains a pre-main sequence (PMS) star that irradiates and heats the gas and dust of the disk. The PMS star is expected to emit UV photons and X-rays depending on its evolutionary stage. Cosmic rays coming from external sources are also expected to penetrate into the disk and interact with its material. The molecular composition of the dust and gas of the protoplanetary disk depends on the local physical conditions which vary with the distance from the central star and the height from the mid-plane of the disk. These different conditions are illustrated in Figure I.4, taken from [Walsh et al.](#)

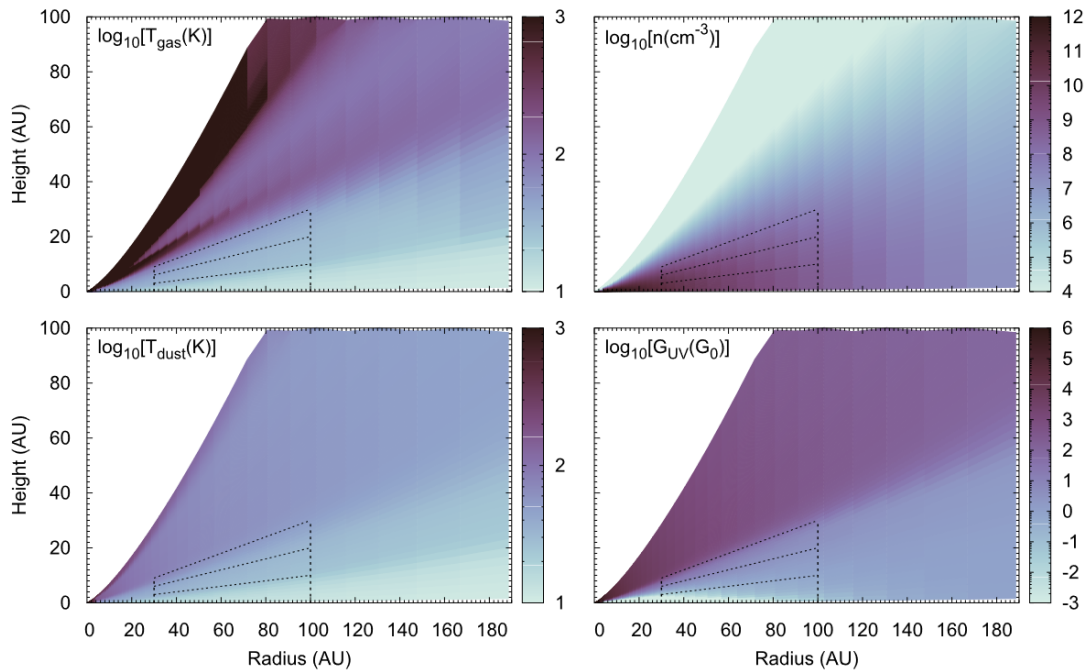


FIGURE I.4 – Example of physical conditions in a protoplanetary disk, taken from [Walsh et al. \(2016\)](#). The figures represent a vertical slice of the disk, which is symmetric with respect to the X-axis. The distance from the central star is expressed in AU (astronomical units) which is equal to  $\sim 1.5 \times 10^{11}$  m. Top left, moving clockwise : gas temperature (K), gas number density ( $\text{cm}^{-3}$ ), UV flux (in units of the ISRF), and dust temperature (K). The dashed black line delineates the layers within which gas phase  $\text{CH}_3\text{OH}$  is modeled to reside.

(2016), along with the region where an important COM, methanol  $\text{CH}_3\text{OH}$ , is expected to reside according to the observations and model. The dust temperature structure in a protoplanetary disk is often characterized by snowlines. These snowlines are associated with a dust temperature under which specific molecules are expected to condense on dust grains. In this work, we will especially be interested in  $\text{H}_2\text{O}$  and  $\text{CO}$  snowlines, associated with a dust temperature of  $\sim 100$  K and  $\sim 20$  K respectively.

- **Planetary system** : the exact mechanism of the formation of planets is not fully understood yet but the main hypothesis is that the dust grains increasingly collide with each other over time, forming rocks and planetesimals. The larger bodies migrate to the mid-plane of the disk and progressively coagulate into planet-like bodies which eventually end up forming a full planetary system. The cycle starts again when the star reaches its end-of-life, ejecting some of its material into the ISM via mass-loss driven by winds.

In this thesis, we will exclusively be interested in the physical processes happening in the cold regions of the three following phases : the prestellar and protostellar phases and protoplanetary disks. Table I.1, taken from [Caselli and Ceccarelli \(2012\)](#), gives an excellent overview of the different properties and physical conditions associated with these three phases.

TABLE I.1 – Properties and physical conditions associated with the three ISM phases of interest in this thesis, taken from [Caselli and Ceccarelli \(2012\)](#)

Phase and object	Lifetime (year)	Radius (AU)	Temp. (K)	Density ( $\text{cm}^{-3}$ )
Prestellar phase	$\sim 10^5$			
Dense core		$\sim 10^4$	7 - 15	$10^4 - 10^6$
Protostellar phase	$10^4 - 10^5$	$\sim 10^4$		
Cold envelope		$100 - 10^4$	$\leq 100$	$10^5 - 10^7$
Hot corinos		$\leq 100$	$\geq 100$	$\geq 10^7$
Protoplanetary disk	$\sim 10^6$	$\sim 200$		
Outer midplane		20 - 200	100 - 10	$10^8 - 10^6$
Inner midplane		$\leq 20$	$\geq 100$	$\geq 10^8$

### I.1.3 Observation of COMs in the ISM

COMs are regularly detected in the different regions of the ISM discussed previously. They are mainly observed in the gas phase through emitted rotational lines (roughly in the frequency domain of 5 GHz - 1 THz) detected by radiotelescopes such as the 30m-IRAM (Institut de Radioastronomie Millimétrique), the ALMA (Atacama Large Millimeter / submillimeter Array) or the NOEMA (NOrthen Extended Millimeter Array) interferometers. The only COM unambiguously detected in interstellar ices so far is CH<sub>3</sub>OH but the recent launch of the James Webb Space Telescope (JWST) is expected to bring further information on ices. Figure I.5 displays over 200 different molecules that have been identified in the ISM, including COMs. This illustrates the molecular richness of the ISM. Table I.2 sums up some observational studies made on the specific COMs studied in this thesis for the different regions of the ISM discussed previously. In some cases, the observations enable to separate the sub-regions where COMs are detected : for example, towards the Horsehead nebula (Gratier et al., 2013; Guzmán et al., 2014), a distinction can be made between the PDR and the dense core region. In other cases, observational studies are supported by an astrochemical model that aims to derive gas phase abundances and the local physical conditions (hence the

2 atoms	CS	HCO <sup>+</sup>	KCN	H <sub>3</sub> O <sup>+</sup>	HCOOH	<i>l</i> -HC <sub>4</sub> N	CH <sub>2</sub> CHCHO	CH <sub>3</sub> OCH <sub>2</sub> OH
H <sub>2</sub>	HF	HCS <sup>+</sup>	FeCN	NH <sub>3</sub>	H <sub>2</sub> CNH	<i>c</i> -H <sub>2</sub> C <sub>3</sub> O	CH <sub>2</sub> CCHCN	11 atoms
AlF	SH	HOC <sup>+</sup>	HO <sub>2</sub>	<i>c</i> -SiC <sub>3</sub>	H <sub>2</sub> C <sub>2</sub> O	C <sub>5</sub> N <sup>-</sup>	H <sub>2</sub> NCH <sub>2</sub> CN	HC <sub>9</sub> N
AlCl	SH <sup>+</sup>	H <sub>2</sub> O	TiO <sub>2</sub>	CH <sub>3</sub>	H <sub>2</sub> NCN	E-HNCHCN	CH <sub>3</sub> CHNH	CH <sub>3</sub> C <sub>6</sub> H
C <sub>2</sub>	FeO	H <sub>2</sub> S	C <sub>2</sub> N	C <sub>3</sub> N <sup>+</sup>	HNC <sub>3</sub>	SiH <sub>3</sub> CN	CH <sub>3</sub> SiH <sub>3</sub>	C <sub>2</sub> H <sub>5</sub> OCHO
CH	O <sub>2</sub>	HNC	SiCSi	PH <sub>3</sub>	SiH <sub>4</sub>	CH <sub>2</sub> CNH	C <sub>2</sub> H <sub>5</sub> N	CH <sub>3</sub> OC(O)CH <sub>3</sub>
CH <sup>+</sup>	CF <sup>+</sup>	HNO	S <sub>2</sub> H	HCNO	H <sub>2</sub> COH <sup>+</sup>	C <sub>5</sub> S	(NH <sub>2</sub> ) <sub>2</sub> CO	12 atoms
CN	PO	MgCN	HCS	HOCN	C <sub>4</sub> H <sup>+</sup>	7 atoms	9 atoms	<i>c</i> -C <sub>6</sub> H <sub>6</sub>
CO	AlO	MgNC	HSC	HSCN	HC(O)CN	C <sub>6</sub> H	CH <sub>3</sub> C <sub>4</sub> H	C <sub>3</sub> H <sub>7</sub> CN
CO <sup>+</sup>	CN <sup>-</sup>	N <sub>2</sub> H <sup>+</sup>	NCO	H <sub>2</sub> O <sub>2</sub>	HNCNH	CH <sub>2</sub> CHCN	CH <sub>3</sub> CH <sub>2</sub> CN	<i>t</i> -C <sub>2</sub> H <sub>5</sub> OCH <sub>3</sub>
CP	HCl <sup>+</sup>	N <sub>2</sub> O	OCN <sup>-</sup>	<i>l</i> -C <sub>3</sub> H <sup>+</sup>	CH <sub>3</sub> O	HC <sub>5</sub> N	(CH <sub>3</sub> ) <sub>2</sub> O	>12 atoms
CSi	TiO	NaCN	4 atoms	HMgNC	H <sub>2</sub> NCO <sup>+</sup>	CH <sub>3</sub> CHO	CH <sub>3</sub> CH <sub>2</sub> OH	C <sub>60</sub>
HCl	ArH <sup>+</sup>	OCS	C <sub>3</sub> H <sup>*</sup>	HCCO	NCCNH <sup>+</sup>	NH <sub>2</sub> CH <sub>3</sub>	HC <sub>7</sub> N	C <sub>60</sub> <sup>+</sup>
KCl	N <sub>2</sub>	SO <sub>2</sub>	<i>l</i> -C <sub>3</sub> H <sup>+</sup>	CH <sub>3</sub> Cl	NH <sub>3</sub> D <sup>+</sup>	<i>c</i> -C <sub>2</sub> H <sub>4</sub> O	C <sub>8</sub> H	C <sub>70</sub>
NH	NO <sup>+</sup>	<i>c</i> -SiC <sub>2</sub>	C <sub>3</sub> N	CNCN	6 atoms	H <sub>2</sub> CCHOH	CH <sub>3</sub> C(O)NH <sub>2</sub>	<i>c</i> -C <sub>6</sub> H <sub>5</sub> CN
NO	NS <sup>+</sup>	CO <sub>2</sub>	C <sub>3</sub> O	MgCCH	C <sub>5</sub> H	C <sub>6</sub> H <sup>-</sup>	C <sub>8</sub> H <sup>-</sup>	CO(CH <sub>2</sub> OH) <sub>2</sub> ?
NS	LiH	NH <sub>2</sub>	C <sub>3</sub> S	NCCP	<i>l</i> -C <sub>4</sub> H <sub>2</sub>	CH <sub>3</sub> NCO	C <sub>3</sub> H <sub>6</sub>	C <sub>14</sub> H <sub>10</sub> ?
NaCl	CrO	H <sub>3</sub> <sup>+</sup>	C <sub>2</sub> H <sub>2</sub>	5 atoms	C <sub>2</sub> H <sub>4</sub>	HC <sub>5</sub> O	CH <sub>3</sub> CH <sub>2</sub> SH	C <sub>14</sub> H <sub>10</sub> <sup>+</sup>
OH	3 atoms	SiCN	HC <sub>2</sub> N	C <sub>5</sub>	CH <sub>3</sub> CN	8 atoms	CH <sub>3</sub> NHCHO	C <sub>6</sub> H <sub>5</sub> OH
OH <sup>+</sup>	C <sub>3</sub>	AlNC	HCNH <sup>+</sup>	C <sub>4</sub> H	CH <sub>3</sub> NC	CH <sub>3</sub> C <sub>3</sub> N	HC <sub>7</sub> O	
PN	C <sub>2</sub> H	SiNC	HNCO	C <sub>4</sub> Si	CH <sub>3</sub> OH	HC(O)OCH <sub>3</sub>	10 atoms	
SO	C <sub>2</sub> O	HCP	HNCS	<i>c</i> -C <sub>3</sub> H <sub>2</sub>	CH <sub>3</sub> SH	CH <sub>3</sub> COOH	CH <sub>3</sub> C <sub>5</sub> N	
SO <sup>+</sup>	C <sub>2</sub> S	CCP	HOCO <sup>+</sup>	CH <sub>2</sub> CN	HC <sub>3</sub> NH <sup>+</sup>	C <sub>7</sub> H	(CH <sub>3</sub> ) <sub>2</sub> CO	
SiN	CH <sub>2</sub>	AlOH	H <sub>2</sub> CO	CH <sub>4</sub>	HC <sub>2</sub> CHO	H <sub>2</sub> C <sub>6</sub>	(CH <sub>2</sub> OH) <sub>2</sub>	
SiO	HCN	H <sub>2</sub> O <sup>+</sup>	H <sub>2</sub> CN	HC <sub>3</sub> N	NH <sub>2</sub> CHO	CH <sub>2</sub> OHCHO	CH <sub>3</sub> CH <sub>2</sub> CHO	
SiS	HCO	H <sub>2</sub> Cl <sup>+</sup>	H <sub>2</sub> CS	HC <sub>2</sub> NC	C <sub>5</sub> N	<i>l</i> -C <sub>6</sub> H <sub>2</sub>	CH <sub>3</sub> CHCH <sub>2</sub> O	

FIGURE I.5 – Example of molecules in the ISM, a large fraction being detected through molecular rotational emission, taken from Arumainayagam et al. (2019)

TABLE I.2 – Examples of observational studies of CH<sub>3</sub>OH, CH<sub>3</sub>CN, HCOOH and HCOOCH<sub>3</sub> in the different regions of the ISM. The list is not exhaustive.

	Prestellar phase	Protostellar phase	Protoplanetary disk
CH <sub>3</sub> OH	Vasyunina et al. (2013); Gratier et al. (2013); Guzmán et al. (2014); Vastel et al. (2014); Taquet et al. (2017)	Mehring and Snyder (1996); Öberg, K. I. et al. (2010); Bergner et al. (2019)	Walsh et al. (2016); van 't Hoff et al. (2018); van der Marel et al. (2021)
CH <sub>3</sub> CN	Gratier et al. (2013); Guzmán et al. (2014)	Remijan et al. (2004); Purcell et al. (2006); Calcutt et al. (2018)	Öberg, K. I. et al. (2015); Bergner et al. (2018); Loomis et al. (2018)
HCOOH	Irvine et al. (1990); Vastel et al. (2014); Taquet et al. (2017)	Liu et al. (2001); Remijan et al. (2004)	Favre et al. (2018)
HCOOCH <sub>3</sub>	Bacmann et al. (2012); Vasyunina et al. (2013); Taquet et al. (2017)	Remijan et al. (2004); Öberg, K. I. et al. (2010); Manigand et al. (2019); Bergner et al. (2019)	Tentative detection (van der Marel et al., 2021)

spatial sub-region) where COMs are detected : this is for example the case in the study of Walsh et al. (2016), reproduced in Figure I.4, for which the detected CH<sub>3</sub>OH was modeled to reside in the cold and dense regions of the protoplanetary disk ( $T_{dust}, T_{gas} \lesssim 20$  K;  $n > 10^7$  cm<sup>-3</sup>). The detection of COMs in protoplanetary disks is of primary importance since COMs are expected to be incorporated into planetesimals and comets leading to prebiotic chemistry in nascent planets at later stages. For instance, CH<sub>3</sub>CN and CH<sub>3</sub>OH are detected in several protoplanetary disks whereas the only observational study of HCOOH reported for protoplanetary disks so far is for the TW Hya disk (Favre et al., 2018). For HCOOCH<sub>3</sub>, a tentative detection has been reported recently in the IRS 48 disk (van der Marel et al., 2021).

COMs are generally assumed to be formed in interstellar ices. This is supported by a wide range of experimental studies showing that the processing (by VUV photons, X-rays, electrons or swift heavy ions) of interstellar ice analogues, whose composition mimic that of the observed ices, leads to the production of COMs and more complex molecules such as amino acids (e.g., Bernstein et al. (1995); Muñoz Caro et al. (2002); Öberg, K. I. et al. (2009a); Danger et al. (2013); Muñoz Caro and Dartois (2013); Chen et al. (2013b); Kaiser et al. (2014); Muñoz Caro et al. (2019)). In the ISM regions where

ices are shielded from external energetic sources, the formation of COMs could also be due to chemical reactions involving the diffusion of incident atoms or molecules on the surface of ices. In the next paragraph, we discuss the possible formation routes of the COMs of interest in this thesis :  $\text{CH}_3\text{OH}$ ,  $\text{CH}_3\text{CN}$ ,  $\text{HCOOH}$  and  $\text{HCOOCH}_3$ . Note that the formation pathways are numerous such that the list of studies cited in the following is not exhaustive.

$\text{CH}_3\text{OH}$  is generally assumed to be formed on the surface of dust grains by hydrogenation of CO. This is supported by (i) laboratory experiments ([Watanabe and Kouchi, 2002](#); [Fuchs et al., 2009](#); [Minissale et al., 2016b](#)) and (ii) a lack of known gas phase reactions able to efficiently produce  $\text{CH}_3\text{OH}$  compared to the abundances observed. However, as explained in [Dartois et al. \(2019\)](#), there is no clear correlation between column densities of CO ice and  $\text{CH}_3\text{OH}$  in observational data and  $\text{CH}_3\text{OH}$  may be embedded in ices dominantly composed of  $\text{H}_2\text{O}$  or  $\text{CO}_2$ . For instance, another pathway formation of  $\text{CH}_3\text{OH}$  in ices, although estimated to be 20 times less efficient than the CO hydrogenation pathway, has been evidenced experimentally (via the surface reaction  $\text{CH}_4 + \text{OH}$ ) and could occur in a  $\text{H}_2\text{O}$ -rich ice environment ([Qasim et al., 2018](#)). Experimental studies have also shown that  $\text{CH}_3\text{OH}$  could be formed in UV-irradiated  $\text{O}_2:\text{CH}_4$  and  $\text{O}_2:\text{CH}_4:\text{CO}$  mixed ices ([Bergner et al., 2017](#)) and in  $\text{H}_2\text{O}:\text{CO}$  mixed ices irradiated by fast heavy ions ([Hudson and Moore, 1999](#); [de Barros et al., 2022](#)). These last two studies also evidence the formation of  $\text{HCOOH}$  in the irradiated  $\text{H}_2\text{O}:\text{CO}$  ices. Irradiation of similar ices with 5 keV electrons also leads to  $\text{HCOOH}$  formation ([Bennett et al., 2011](#)). "Non-energetic" pathways for the formation of  $\text{HCOOH}$  could also play a role, such as the hydrogenation of  $\text{CO}:\text{O}_2$  or  $\text{H}_2\text{CO}:\text{O}_2$  mixed ices ([Ioppolo et al., 2011](#); [Qasim et al., 2019](#)). Formation of  $\text{HCOOCH}_3$  by irradiation of  $\text{CH}_3\text{OH}$ -containing ices with VUV photons, 5 keV electrons or 200 keV protons has been experimentally evidenced ([Bennett and Kaiser, 2007](#); [Öberg, K. I. et al., 2009a](#); [Modica, P. and Palumbo, M. E., 2010](#); [Ishibashi et al., 2021](#)). Studies on the formation of  $\text{CH}_3\text{CN}$  in ices are more rare : it has been evidenced by VUV photolysis of ethylamine ([Danger, G. et al., 2011](#)) and by ion irradiation of  $\text{CH}_4:\text{N}_2$  mixed ices ([Vasconcelos et al., 2020](#)). More recently, the  $\text{CH}_4\cdots\text{HCN}$  complex has been shown to be a precursor for the formation of  $\text{CH}_3\text{CN}$  by X-ray irradiation of such complex embedded in rare gas matrices ([Volosatova et al., 2021](#)). Apart from all the previous solid state formation processes, gas phase reactions are sometimes suggested to explain the abundances observed in some observational studies : for example, for  $\text{HCOOH}$  ([Irvine et al., 1990](#)) and  $\text{HCOOCH}_3$  ([Taquet et al., 2017](#)).

During the protostellar phase, the increasing temperature of the dust grains should favor the diffusion of radicals in interstellar ices and thus the formation of COMs. In cold regions, where the diffusion of radicals in ices is expected to be less efficient (this

is the case for a dust temperature  $< 30$  K), the formation of COMs is thought to be favored by the interaction of cosmic rays or UV photons with the ice, bringing sufficient energy for radicals to be created, diffuse and form COMs.

Once the COMs are formed in the ices, their presence in the gas phase of hot cores is then straightforwardly assumed to be due to their thermal desorption from the dust grains when their surface temperature increases. On the other hand, in the colder regions of the ISM (e.g. dense cores and the interior of protoplanetary disks), where the temperature of dust grains is not high enough for thermal desorption to occur ( $T_{dust} < 100$  K), the presence of COMs in the gas phase is puzzling. Indeed, whether COMs are formed on ices or directly by gas phase reactions, they should at some point condense on the icy mantles as these mantles exhibit a surface temperature low enough to allow this phenomenon. The time scale for condensation is generally sufficiently short compared to the lifetime of the typical ISM regions considered such that the gas should be depleted from COMs (and also other simple molecules such as CO, H<sub>2</sub>O, CO<sub>2</sub>) except if the formation routes in gas phase are efficient enough to maintain the gas budget, which is generally not assumed to be the case for COMs. Therefore, the fact that these COMs are actually observed in the gas phase of these cold regions means that there is necessarily a process that is responsible for their desorption (ejection) from the ices into the gas phase. This process should be non-thermal and more efficient than the condensation process to maintain a sufficient amount of COMs in the gas phase. The possible non-thermal processes at play are discussed in the next section.

## I.2 Non-thermal desorption processes

Non-thermal desorption of molecules from ices, including COMs, in the colder regions of the ISM, implies that energy should be supplied to the ices. In the ISM, this energy is available in the form of photons (only Vacuum UV (VUV) photons and X-rays will be considered in this thesis), electrons or cosmic rays (CR) and can also originate from the excess of energy of a chemical reaction occurring at the ice surface. The non-thermal processes at play are schemed in Figure I.6. Their definition is introduced in the next sub-sections and I will also discuss in which regions of the ISM these processes are expected to play a role.

### I.2.1 Cosmic Ray sputtering

CRs are high energy charged particles ( $\sim 85\%$  H<sup>+</sup>,  $\sim 13\%$  He<sup>2+</sup>,  $\sim 2\%$  heavier atoms and electrons) that span the  $1 - 10^{14}$  MeV range. CRs are expected to originate, for example, from supernovae or active galactic nuclei (although this is still debated) and create an isotropic field. Their high energy enables them to penetrate in dense and

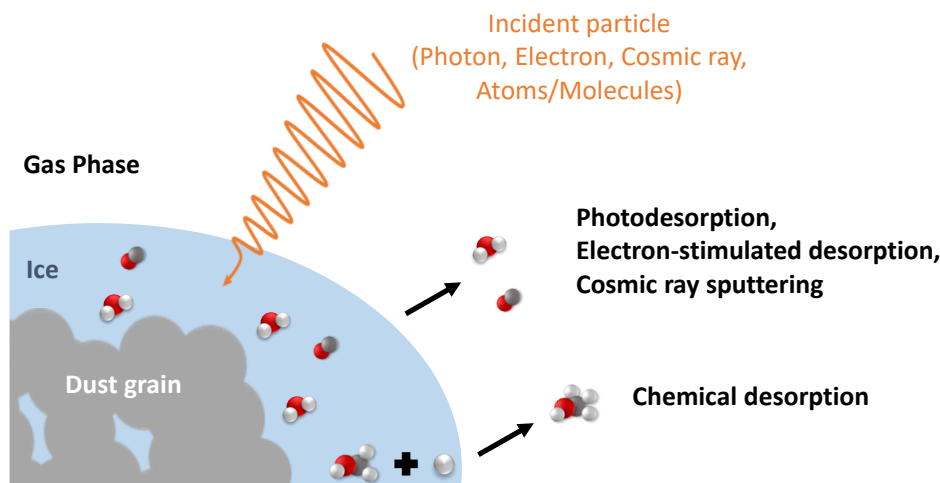


FIGURE I.6 – Scheme of the different non-thermal processes occurring at the surface of an icy mantle

photo-shielded regions of the ISM such as the interior of dense cores and of protoplanetary disks where other radiations, namely photons, cannot. The flux of CRs decreases with energy going from  $\sim 1$  particle/m<sup>2</sup>/s near 10 GeV to  $\sim 1$  particle/km<sup>2</sup>/year near  $10^{10}$  GeV such that only the part of energy below  $\sim 100$  MeV is expected to contribute the most to the irradiation of interstellar ices (Cronin et al., 1997; Arumainayagam et al., 2019). In dense cores, ices are expected to be irradiated by CRs with a flux of 1 particle/cm<sup>2</sup>/s at 1 MeV (Moore et al., 2001). CRs ionize gas phase H<sub>2</sub> thus creating secondary electrons (Gredel et al., 1989). These secondary electrons excite the molecular hydrogen Lyman and Werner band systems leading to *in situ* emission of UV light.

CR sputtering occurs when a cosmic ray impacts an interstellar ice and ejects some of its material in the gas phase. Due to their very high energy, the mechanisms involved in CR sputtering are specific. Namely, when interacting with ices, CRs are expected to remove molecules, through transient heating, from a sputtered volume whose shape is similar to a crater (see for example Dartois et al. (2018, 2020b)), resulting to a number of molecules ejected equivalent to several layers. CRs can ionize molecules in the ice, creating a cascade of secondary electrons that scatter through the ice and induce its radiolysis (i.e. chemical reactions) and also possibly desorption. For more details on CR sputtering from molecular ices, the reader is referred to the many studies available on this topic (for example Dartois et al. (2020a); Dartois, E. et al. (2021); Garg et al. (2020); Sipilä et al. (2021)). A comparison of the results of some of these studies with respect to the other non-thermal processes will be conducted in this thesis.

## I.2.2 VUV photodesorption and molecular clouds

VUV photodesorption is a process through which the photo-absorption of an incoming VUV photon (the energy range considered is 7 - 13.6 eV) by a molecule in the ice is inducing the desorption of molecule(s) from the ice to the gas phase. VUV absorption induces valence electronic excitation or ionization of the molecules in the ice. The decay of the excited or ionized molecular state may lead in fine to the desorption of the photo-absorbing molecule and/or the desorption of neighboring molecules. The physical mechanisms at play in VUV photodesorption from molecular ices have been extensively studied over the recent years. These mechanisms will be discussed in more details in Chapter III.

In the ISM, VUV photons originate from starlight emission whose spectrum is close to a black body radiation at temperatures of 10 000 - 30 000 K. UV photons at energies > 13.6 eV are absorbed via photo-ionization of H leading to the formation of H II re-

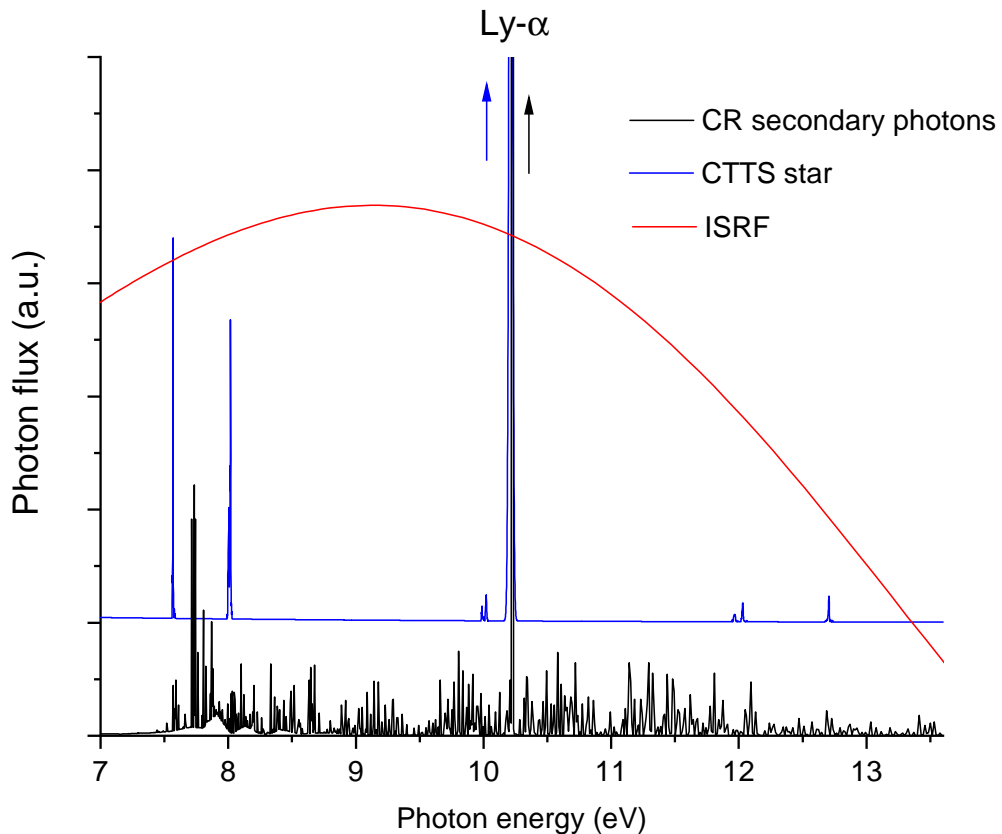


FIGURE I.7 – VUV spectra associated with the different sources discussed in the text. In black is the VUV spectrum of the secondary photons created by Cosmic Rays from [Gredel et al. \(1987\)](#). In blue is the VUV spectrum emitted from a Classical T-Tauri Star (CTTS) from [France et al. \(2014\)](#). In red is the InterStellar Radiation Field spectrum from [Gredel et al. \(1989\)](#). The Lyman- $\alpha$  line largely dominates the blue and black spectra. The spectra are vertically shifted for more clarity.

gions near to massive stars. The spectrum of UV photons therefore cuts-off at 13.6 eV. We then commonly referred to the 6 - 13.6 eV range as Vacuum UV (VUV) photons. The UV field averaged over all background stars in the ISM is known as the InterStellar Radiation Field (ISRF), which is an isotropic background field. VUV photons emitted from stars are absorbed before being able to penetrate dense regions such as dense cores in molecular clouds or the interior of protoplanetary disks. However, CRs are able to reach such regions and, as explained before, induce a local secondary UV field due to their interactions with the gas. Figure I.7 displays the VUV spectra of the different VUV sources discussed previously : VUV photons emitted by a classical T Tauri Star (CTTS), representative of a solar-type low-mass young star at the center of a protoplanetary disk, the ISRF and VUV photons induced by CRs.

In terms of flux, the secondary VUV photons are expected to dominate over the CRs in dense cores : from [Moore et al. \(2001\)](#), the photon flux at 10 eV is estimated to be  $\sim 1.4 \times 10^3$  photon/cm<sup>2</sup>/s whereas the CR flux at 1 MeV is 1 particle/cm<sup>2</sup>/s. However, the contribution of VUV photons and CRs is similar in terms of energy absorbed by interstellar ices, i.e.  $1.7 \times 10^3$  eV/cm<sup>2</sup>/s for VUV photons at 10 eV and  $1.2 \times 10^3$  eV/cm<sup>2</sup>/s for CRs at 1 MeV (note that these values may vary with the ice composition, see [Moore et al. \(2001\)](#) for more details). Finally, by computing the dose (expressed in eV per molecule) received by ices over the lifetime of dense cores, which is more relevant to qualitatively compare the role of different irradiation sources, this also gives similar contributions. Other modeling studies of dense cores however reported a higher contribution of VUV photons to the energetic processing of the icy dust ([Cecchi-Pestellini and Aiello, 1992](#); [Shen, C. J. et al., 2004](#)). In the less dense regions of molecular clouds where the physical conditions resemble that of diffuse clouds, [Moore et al. \(2001\)](#) estimated that VUV photons (in that case primary photons, coming from the ISRF) are expected to be dominant over CRs in terms of energy absorbed and dose received by ices, by orders of magnitude. In PDR and XDR, by definition, the dominant source of energy are respectively VUV photons and X-rays. However, the fluxes may significantly vary from one PDR (or XDR) to another. For example, the Orion Bar presents an intense radiation field ( $10^4 - 10^5$  orders of magnitude larger than the ISRF in terms of flux) while the Horsehead is illuminated by a weaker radiation field, approximately 60 times greater than the ISRF ([Guzmán et al., 2014](#)).

### I.2.3 X-ray photodesorption and protoplanetary disks

X-ray photodesorption is a process through which the photo-absorption of an incoming X-ray (0.1 - 10 keV) causes the desorption of molecules from the absorbing ice. X-ray photo-absorption induces a core electronic excitation or ionization. For low Z elements ( $1 \leq Z \leq 18$ ), the decay of the core hole state occurs, with a probability close

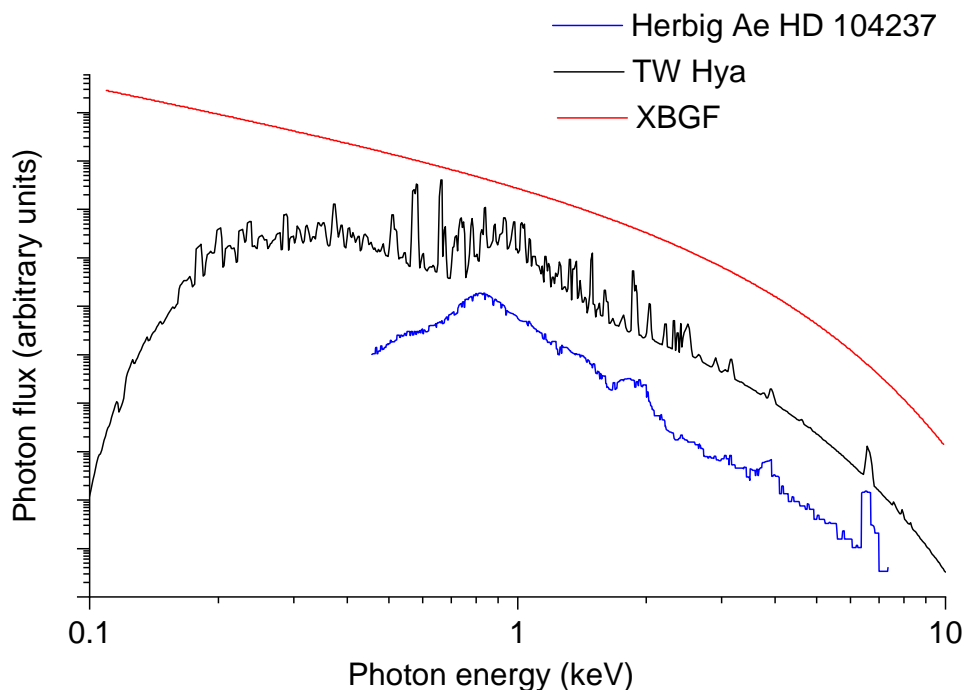


FIGURE I.8 – X-ray spectra of different sources discussed in the text. In black and blue are the X-ray emission spectra of respectively HD 104237 (Skinner et al., 2004) and TW Hya (Nomura et al., 2007) young stars. In red is the X-ray BackGround Field (XBGF) from Rab et al. (2018). The spectra have been shifted vertically for more clarity and the Y-scale is in arbitrary units.

to 1 (Walters and Bhalla, 1971; Krause, 1979), by emission of an electron referred to as the Auger electron. The Auger electron (and the ionized core electron in the case of photo-ionization) scatters inelastically in the ice, creating secondary events (e.g. ionizations and excitations) and a cascade of low energy ( $< 20$  eV) secondary electrons that may also cause desorption. The mechanisms involved in the X-ray photodesorption process will be discussed in more details in Chapter III. X-rays are emitted by pre-main sequence (PMS) stars. Observations with the CHANDRA and the XMM-Newton telescopes over the last decades have provided new understanding on the processes at work and the properties of X-ray emission from PMS stars (Testa, 2010; Feigelson, 2010). These X-rays are expected to originate from the enhanced stellar and magnetic activity of the young stars, possibly inducing long-lasting X-ray flare events similar to that emitted from the Sun but more intense by several orders of magnitude (Güdel and Nazé, 2009). In addition, Adams et al. (2012) argued that most stars are born in embedded clusters where each young star contributes to a background stellar field. These clusters of young star X-ray sources therefore generate a X-ray background field (XBGF) irradiating the nearby regions of the ISM. Figure I.8 displays different X-ray spectra from different X-ray sources in the 0.1 - 10 keV range.

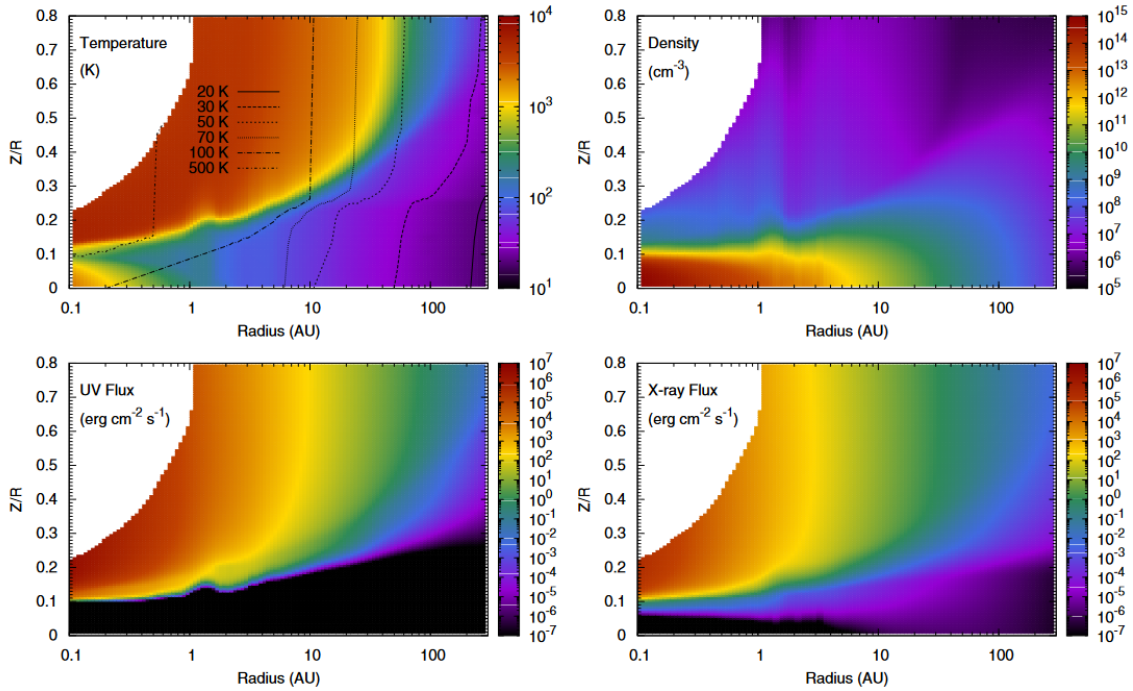


FIGURE I.9 – Modeling of a typical T Tauri protoplanetary disk from [Walsh et al. \(2012\)](#). Top left : temperature of dust (black contours) and gas (color map) in K. Top right : gas number density in  $\text{cm}^{-3}$ . Bottom left and right : stellar UV and X-ray flux (wavelength-integrated) respectively in  $\text{erg}/\text{cm}^2/\text{s}$ . Quantities are plotted as a function of the disk radius  $R$  (in AU) and height scaled by the radius i.e.  $Z/R$ .

X-rays are therefore especially relevant in the case of protoplanetary disks. Within disks, the flux of the different sources of irradiation strongly depends on the disk density structure. In that case, protoplanetary disk modeling studies are mandatory to quantify the relative importance of the irradiation sources in the different regions of the disk. In Figure I.9 is presented an example of such a modeling study for a typical T Tauri protoplanetary disk. We can see that both UV photons and X-rays emitted from the central young star (named stellar UV and X-rays in the following) are able to reach the regions of the disk, with similar fluxes, where the dust temperature is cold ( $T_{dust} < 100 \text{ K}$ ). Compared to stellar VUV photons, stellar X-rays can penetrate deeper into the disk, near the mid-plane. Soft X-rays (0.1 - 5 keV) tend to be absorbed by the gas and dust whereas hard X-rays (5 - 10 keV) have a higher probability of being scattered via Compton scattering, losing part of their energy while going in deeper regions. The energy spectrum of the stellar X-rays reaching the disk near-mid-plane is therefore expected to be dominated by the high energy part (5 - 10 keV).

VUV and X-ray background fields are also expected to irradiate protoplanetary disks. The key difference compared to the stellar fields resides in the fact that these background fields are irradiating the disk in an isotropic way, therefore playing a role in cold

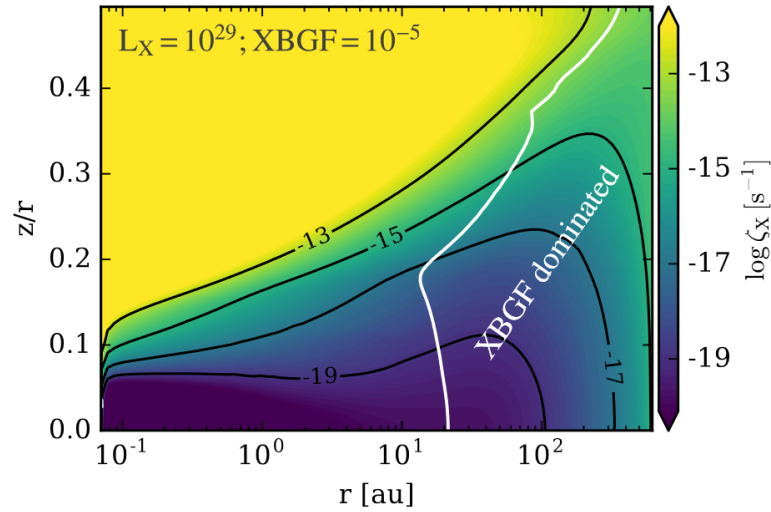


FIGURE I.10 – X-ray ionization rate in a protoplanetary disk including both the stellar X-ray field (luminosity of  $10^{29}$  erg/s) and the XBGF (flux of  $2 \times 10^5$  erg/cm<sup>2</sup>/s), taken from Rab et al. (2018), based on the work of Adams et al. (2012). The white solid contour line encloses the region where the XBGF contribute the most to the ionization rate compared to the stellar X-ray field.

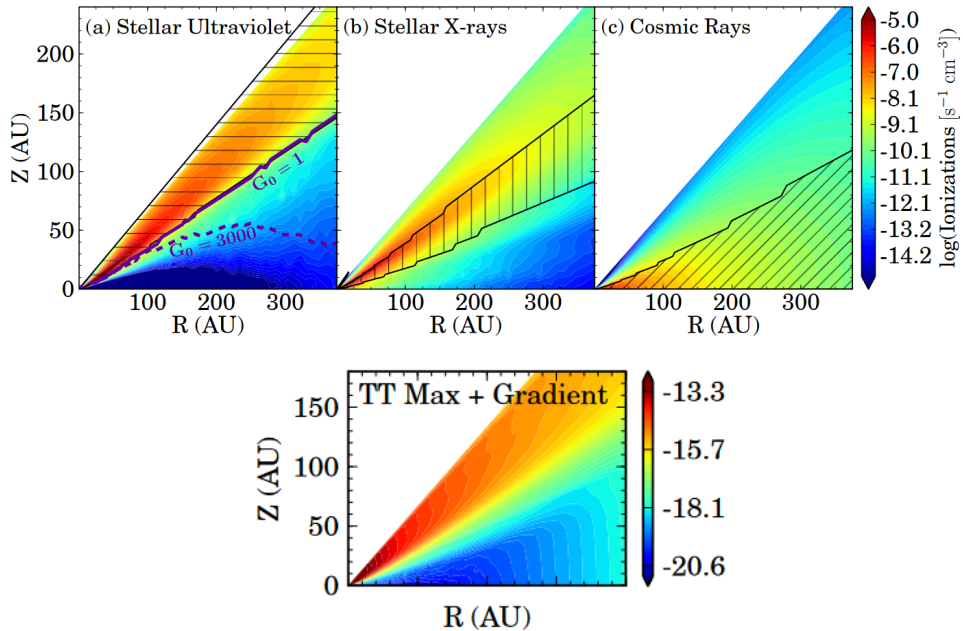


FIGURE I.11 – Taken from Cleeves et al. (2013). Top panels : modeling of the total gas ionization rate by UV (ionization of C), X-rays and CRs (ionization of H<sub>2</sub>) in a protoplanetary disk. The hatched region delineates the region of the disk where each respective source of ionization provides > 30% of the total ionizations per unit time per unit volume. Bottom panel : modeling of H<sub>2</sub> ionization rate by CRs and X-rays by taking into account the exclusion of CRs by stellar winds and magnetic fields (Cleeves et al., 2013).

regions far from the central star, where the stellar fields are negligible. For instance, the XBGF generated by clusters of young stars (Rab et al., 2018) have been modeled to dominate the ionization rate of gas (sum of ionization rates of H and H<sub>2</sub>) compared to the contribution of the X-ray stellar field in the cold outer regions of protoplanetary disks, as displayed in Figure I.10. This XBGF is therefore expected to irradiate the interstellar ices populating these outer cold regions. The ISRF and the background VUV field generated by clusters of young star (analogue to the XBGF) are also expected to contribute to the irradiation of interstellar ices in regions whose shape is similar to the one depicted by the XBGF in Figure I.10. Finally, CRs, with their ability to penetrate in dense regions, are also expected to irradiate deep regions of protoplanetary disks. The top panel of figure I.11 gives an example of the relative contribution of the stellar UV, the stellar X-ray and the CR field to the ionization rate of gas. In the very deep regions, near the mid-plane of the disk, only CRs significantly contribute to the ionization rate. However, as explained in Cleeves et al. (2013), interaction of CRs with stellar winds and magnetic fields generated by the central young star can strongly reduce the incident CR flux on the disk. For instance, the bottom panel of Figure I.11 displays the resulting ionization rate due to X-rays and CRs when taking into account the effect of stellar winds and magnetic fields (see Cleeves et al. (2013) for more details). This shows that the irradiation of interstellar ices by CRs in protoplanetary disks might not be as significant as expected.

## I.2.4 Electron-stimulated desorption

Electron-Stimulated Desorption (ESD) is the desorption induced by the irradiation of ices with electrons of low (< 20 eV) or high (0.1 keV to a few keV) energies (electrons of higher energy will not be considered in this thesis). The interaction of electrons with molecular ices depends on their energy : in the energy ranges considered here, electrons inelastically scatter in the ice and either excite, ionize or attach to molecules. As explained previously, electrons can also be generated inside the ice after X-ray absorption or by CR impact. These secondary electrons can also induce the desorption of molecules from interstellar ices. The exact processes involved in the interaction of electrons with molecular ices will be discussed in more details in Chapter III. A particular process that will be of interest in this thesis is X-ray induced electron-stimulated desorption (XESD) which designates the desorption induced by the cascade of secondary electrons generated by the Auger electron scattering after X-ray absorption. A comparison between ESD experiments, with electrons of energy similar to the expected energy for Auger electrons, and X-ray photodesorption experiments sometimes provides insights on the photodesorption mechanisms. Such comparisons will be made in this thesis.

### I.2.5 Other non-thermal processes

In addition to the non-thermal processes discussed above, the following processes might also play a role but will not be addressed in this thesis :

- Chemical desorption takes place when the exothermicity of a chemical reaction occurring on the ice surface induces the desorption of the reaction product(s). The chemical reaction at play can be induced by incoming atoms (for example incoming H atoms that diffuse on the ice surface and react with its species) but also by incoming photons, electrons or CRs that dissociate the ice molecules, forming radicals that further react near the ice surface with the surrounding species. Chemical desorption is experimentally and theoretically constrained for a few reactions involving the desorption of simple molecules such as H<sub>2</sub>O, N<sub>2</sub>, CO (Dulieu et al., 2013; Minissale et al., 2016a; Oba et al., 2018; Nguyen et al., 2020; Fredon et al., 2021). For the COMs studied in this thesis, only the chemical desorption of CH<sub>3</sub>OH was studied experimentally via especially the hydrogenation reactions of CO (Minissale et al., 2016a,b). For the other COMs, chemical desorption is poorly constrained such that it is not possible to discuss its efficiency compared to the other non-thermal processes cited above. However, some theoretical studies enable to quantitatively estimate the role of chemical desorption in the ISM with regards to astronomical observations, which is especially relevant in dense cores (Vasyunin and Herbst, 2013; Vasyunin et al., 2017). Chemical desorption induced by irradiation of ices with VUV photons was demonstrated experimentally for some species like C<sub>2</sub>H<sub>6</sub> and C<sub>3</sub>H<sub>8</sub> from pure CH<sub>4</sub> ice (Carrascosa et al., 2020) or H<sub>2</sub>CO from pure ethanol ice (Martín-Doménech, R. et al., 2016).
- shock-induced desorption may also play a role. This process is expected to mainly occur in outflow regions during the protostellar phase where the outflowing jets encounter the quiescent gas, creating shocks responsible of sputtering molecules from dust grains.

## I.3 Objectives of the thesis

Understanding the gas phase abundances of COMs in the cold and dense regions of the ISM necessitate having access to the efficiency of the non-thermal desorption processes mentioned previously. It is therefore crucial to experimentally constrain these non-thermal processes by especially providing quantitative data that can be implemented in astrochemical models. For such implementation to be relevant, it is also mandatory to understand the physical mechanisms of non-thermal desorption at a

microscopic scale, especially their dependence on the ice characteristics, such as the ice composition, temperature or phase, as they can significantly change from one ISM region to another. For COMs, the desorption of the intact molecule as well as that of its fragments is of particular importance for astrochemistry as it may play a role in the evolution of the molecular composition of the gas phase. In this context, the thesis focuses on the study of VUV and X-ray photodesorption from molecular ices, with a comparison with ESD experiments in some cases.

VUV photodesorption has been extensively studied, first regarding the desorption of the simple molecules constituting the ices such as H<sub>2</sub>O (Öberg, K. I. et al., 2009b; Cruz-Diaz et al., 2017; Fillion et al., 2022), CO (Öberg, K. I. et al., 2009c; Muñoz Caro, G. M. et al., 2010; Fayolle et al., 2011; Chen et al., 2013a; Muñoz Caro, G. M. et al., 2016), CO<sub>2</sub> (Öberg, K. I. et al., 2009c; Fillion et al., 2014; Martín-Doménech, R. et al., 2015b), CH<sub>4</sub> (Cruz-Diaz, 2015; Dupuy, R. et al., 2017; Carrascosa et al., 2020) and NH<sub>3</sub> (Loeffler and Baragiola, 2010; Martín-Doménech et al., 2018). The VUV photodesorption of CH<sub>3</sub>OH received a peculiar attention (Öberg, K. I. et al., 2009a; Cruz-Diaz et al., 2016; Bertin et al., 2016; Bulak et al., 2020) since this molecule has been detected in several regions of the ISM where VUV photodesorption could play a role. More recently, X-rays have been proven to induce desorption from ices of simple molecules such as H<sub>2</sub>O (Dupuy et al., 2018) and CO (Dupuy et al., 2021b) and also from ices containing CH<sub>3</sub>OH (Ciaravella et al., 2012).

One major finding of the previous studies is that VUV and X-ray photodesorption are characterized by indirect desorption processes in the sense that the photo-absorption by a specific molecule of the ice is inducing the desorption of other molecules from its surface. This implies that the ice composition influences the photodesorption of molecules. In particular, indirect desorption of simple molecules, induced by the photo-absorption of H<sub>2</sub>O and CO has been proven efficient (Bertin et al., 2012, 2013; Dupuy et al., 2021a) for some binary ices. This process is of particular importance since the presence of specific molecules in ices can promote the desorption of other ones. One question that I will try to answer in this thesis is knowing if this indirect process also occurs for the photodesorption of COMs.

The approach retained is experimental and it is described in Chapter II. In Chapter III, I sum up the advancements made over the past years regarding the study of VUV and X-ray photodesorption from molecular ices, based on the studies cited above. Finally, I have presented the thesis results in two distinct parts :

- in Chapter IV, I explore in more details the VUV and X-ray photodesorption of diatomic molecules by presenting new results I obtained, with the objective of

going further on our understanding of the physical mechanisms involved in the desorption process. Constraining such mechanisms is crucial to know how photodesorption should be implemented in astrochemical modeling and how these mechanisms could play a role in the evolution of the ISM

- the second objective of the thesis is addressed in Chapter V and VI, where I quantify the VUV and X-ray photodesorption of COMs from interstellar ice analogues by providing, among other things, photodesorption yields derived from experimental results. As explained previously, these yields will be studied as a function of the ice composition, especially in order to study the possible indirect desorption of COMs induced by photo-absorption of H<sub>2</sub>O and CO in mixed or layered ices. The COMs studied in this thesis are methanol CH<sub>3</sub>OH, acetonitrile CH<sub>3</sub>CN, formic acid HCOOH and methyl formate HCOOCH<sub>3</sub>. In order to give an overview of the thesis contribution to the study of non-thermal desorption of COMs, Table I.3 sums up the experimental studies and the thesis chapters related to such topic (excluding chemical desorption, which has only been studied for CH<sub>3</sub>OH as explained before)

TABLE I.3 – List of experimental studies and chapter of the thesis that deal with the non-thermal desorption of the intact neutral COMs studied in this thesis, from pure or mixed ices.

	CR sputtering	ESD	X-ray photodesorption	VUV photodesorption
CH <sub>3</sub> OH	<a href="#">Dartois et al. (2019, 2020a)</a>	Chapter VI	<a href="#">Ciaravella et al. (2012, 2020)</a> , Chapter VI	<a href="#">Öberg, K. I. et al. (2009a)</a> ; <a href="#">Cruz-Diaz et al. (2016)</a> ; <a href="#">Bertin et al. (2016)</a> ; <a href="#">Bulak et al. (2020)</a>
CH <sub>3</sub> CN			Chapter VI	<a href="#">Bulak et al. (2020)</a> , Chapter V
HCOOH			Chapter VI	Chapter V
HCOOCH <sub>3</sub>				Chapter V



# Chapter II

## Experimental approach

The experimental approach retained is presented in this chapter. A general description of the Surface Processes and ICES (SPICES, see Figure II.1) set-up is given in the first section. Coupling of the SPICES set-up with synchrotron light from the SOLEIL synchrotron facility, which enables to derive photodesorption yields, is described in the second section. Coupling with a VUV source that was implemented directly at the LERMA lab during the thesis is described in the third section.

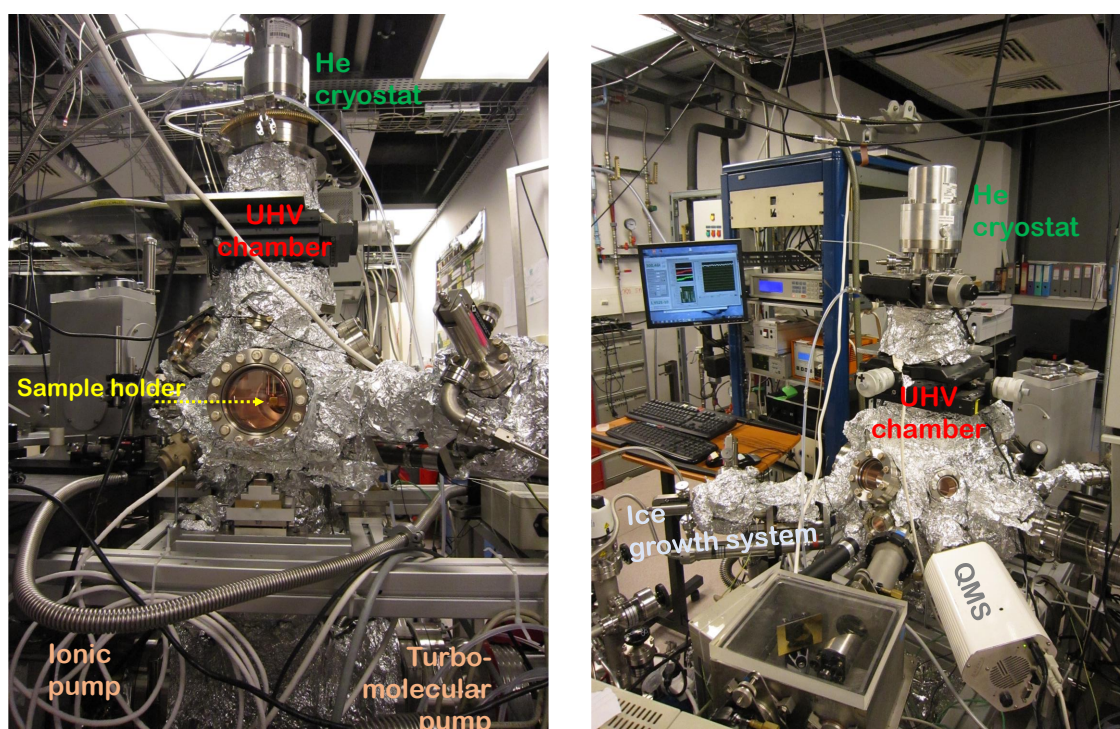


FIGURE II.1 – Pictures of the SPICES set-up at the LERMA lab. Details on the different elements are given in Section II.1

## II.1 The SPICES set-up

The SPICES set-up is schemed in Figure II.2. It consists of an ultra-high vacuum (UHV) chamber at the center of which a sample holder is mounted on the tip of a rotatable 2 stages closed-cycle Helium (He) compression cryostat. An ice growth system enables to form the ices on the cold sample holder and the set-up is coupled to a photon source in order to irradiate the so-called ices. The photodesorption is directly probed in the gas phase during the irradiation of the molecular ices by the use of a quadrupole mass spectrometer (QMS), associated with different ionization techniques depending on the photon source used (synchrotron light or lab VUV source).

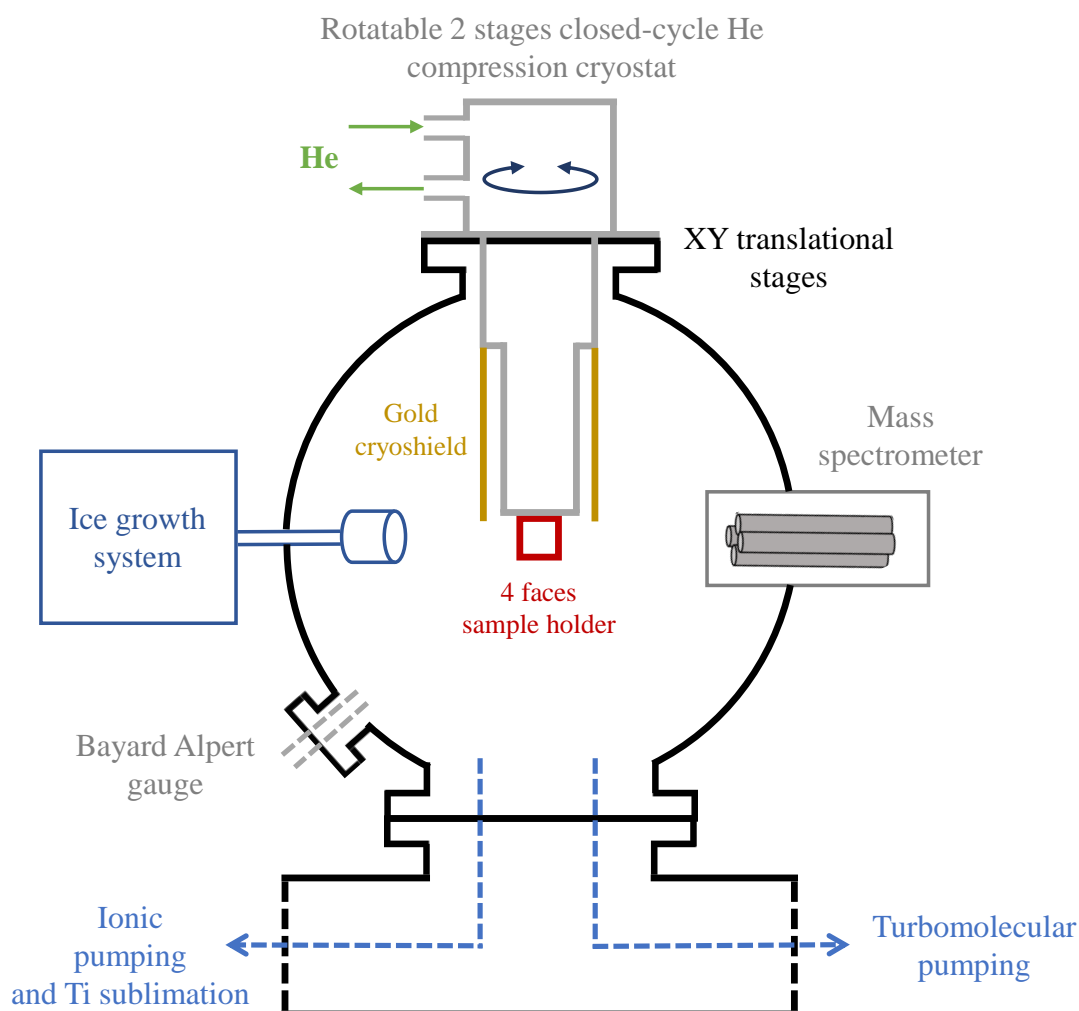


FIGURE II.2 – Scheme of the SPICES set-up implemented at the LERMA lab.

### II.1.1 Ultra-high vacuum chamber

An ultra-high vacuum chamber (UHV) designates a chamber in which a base pressure less than  $10^{-9}$  Torr is reached. It is the central part of the SPICES set-up and specific pumping techniques are required to achieve such low pressure. Starting from a chamber at ambient pressure, low to medium vacuum, which designates pressure from 1 to  $10^{-3}$  Torr (1 Torr = 1.33 mbar), can be achieved by the use of a primary pump. The ones used on the SPICES set-up are dry scroll pumps. They consist of two identical spirals with one rotating inside the other one, the latter being fixed. This rotational movement causes compression of the gas, which increases its pressure until it is expelled at the outlet of the pump located at the center of the fixed spiral. After medium vacuum is reached, high vacuum ( $\sim 10^{-9}$  Torr) can be achieved by the use of a turbomolecular pump and an ion pump. A turbomolecular pump uses high speed rotating blades (similar to a plane motor) to transfer momentum to the incoming gas phase molecules towards the outlet of the pump, propelling them. An ion pump ionizes the incoming gas phase molecules by electron impact in an anode region where the electrons are produced by an electric discharge and trapped in a magnetic field. Once the gas phase molecules are ionized, they are accelerated to strike a chemically active cathode where they become entrapped. The ionic pump is also equipped with a Titanium sublimation pump. It consists of a filament of Titanium that can be heated in order to sublimate titanium particles that will cover the surrounding walls with a thin film. As titanium is very reactive, the gas molecules hitting the walls react and form a stable, solid product hence reducing the gas pressure. Since the number of molecules that can be trapped by the titanium film is limited, the filament needs to be regularly heated to deposit a fresh coating on the walls.

UHV pressure of the order of  $10^{-10}$  Torr are not directly reachable with these techniques within a reasonable amount of time. In fact, the interior walls of a vacuum chamber are usually "polluted" by adsorbed molecules or molecules trapped in pores. These molecules, mainly  $H_2O$  adsorbed at the surface and  $H_2$  that forms at the surface by recombination of H atoms diffusing from the bulk of the metal, are constantly desorbing from the walls over time, thus preventing the base pressure of the chamber to significantly decrease within at least a month when considering the pumping speed of the previously mentioned pumps. This phenomenon, called outgassing, can however be accelerated by baking out the vacuum chamber. The bake-out consists of heating the exterior walls of the vacuum chamber up to 100-200° C to accelerate the desorption of the pollutants from the interior walls. This technique enables to decrease the base pressure by one order of magnitude every 100°C within a few days and it requires wrapping the chamber with aluminum foils as one can see in Figure II.1, to ensure homogeneous heating.

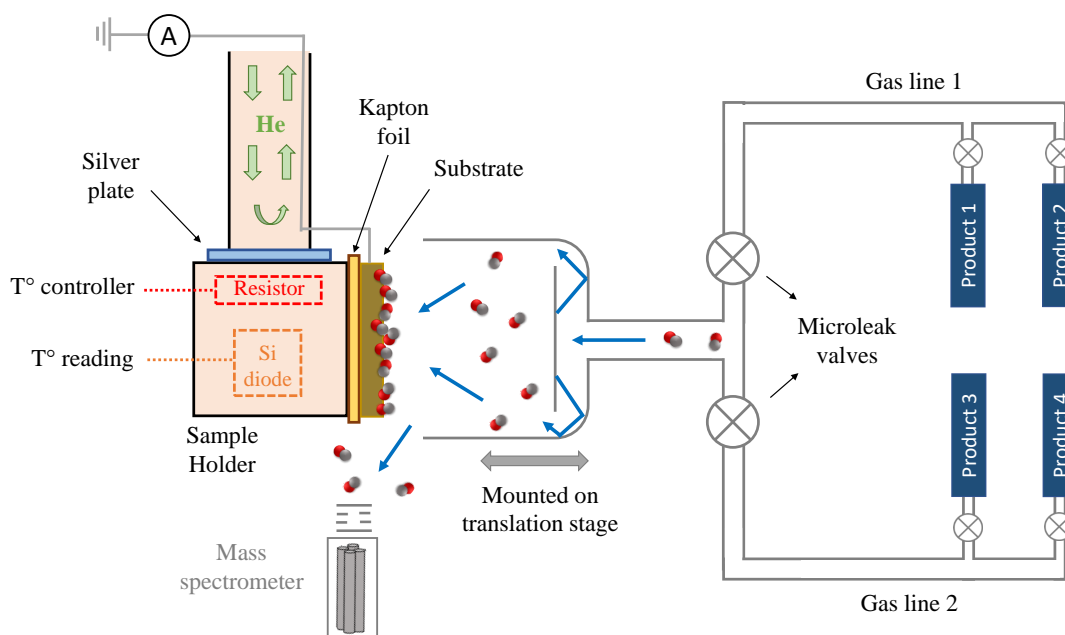


FIGURE II.3 – Dosing system in the SPICES set-up.

## II.1.2 Ice growth

### II.1.2.1 Sample holder and deposition technique

The ices studied in this work are grown as sketched in Figure II.3. The sample holder is a home-made OFHC copper piece screwed into the head of the closed-cycle Helium cryostat and with which the thermal contact is optimized by a silver plate. The substrate is pasted on the sample holder with a UHV-compatible cryogenic silver epoxy glue which ensures thermal conductivity. The usual substrate used in this work is a copper (Cu) substrate but graphite (HOPG) and gold (Au) substrates can also be used. The Cu substrate is electrically insulated from the sample holder by a Kapton foil (which is also a good thermal conductor) such that the current induced on the surface by the photo-electric effect can be measured, especially in the case of the X-ray experiments. The temperature of the sample holder is monitored thanks to a calibrated silicon (Si) diode with a precision of  $\sim 0.5$  K. A feedback loop between a current applied to a heating resistor mounted into the sample holder and the temperature measured by the Si diode enables to control the temperature of the substrate. A tube that can be translated a few millimeters from the substrate is connected to gas lines by microleak valves. This enables to inject gas phase molecules through the tube with very low partial pressure in order to grow the ice on the substrate : this is called the dosing procedure in the following. Several products can be connected to different gas lines in order to grow mixed ices containing two or more species. The mixture ratios can be controlled by adjusting the partial pressure of the species either in a single gas line or within the vacuum chamber by using the two gas lines and microleak valves. During

the dosing procedure the molecules are colliding with the substrate and are sticking to it if the latter is sufficiently cold, with a probability close to unity. A plate at the exit of the tube randomizes the direction of the molecules hitting the substrate in order to homogenize the ice growth. During the dosing procedure, some molecules are escaping the tube without hitting the substrate and go into the vacuum chamber such that the base pressure is increasing (between a few  $10^{-10}$  to a few  $10^{-8}$  Torr depending on the aimed thickness). This increase of pressure is monitored by the mass spectrometer by selecting the mass channel corresponding to the molecules injected while the ice is growing. The time integrated mass signal of the escaping molecules is followed and further related to the ice thickness thanks to pre-calibration experiments (see next section).

### II.1.2.2 Thickness calibration

The ice thickness is expressed in monolayers (ML) which is the surface molecular density corresponding to a full and compact layer, equivalent to  $\sim 10^{15}$  molecules/cm<sup>2</sup> although this could slightly vary with the species studied. The relation between the number of monolayers deposited on the substrate during the dosing procedure and the integrated mass signal of the escaping molecules can be calibrated by a technique called Temperature-Programmed-Desorption (TPD). It consists of growing an ice of unknown thickness and, afterwards, heating the substrate to temperatures high enough for the molecules to thermally desorb. The corresponding mass signal of the thermally desorbing molecules can be monitored by the QMS as a function of the substrate temperature. The resulting QMS data are called TPD curves. They have been recorded during the thesis (see Figure II.4) for the molecules studied in this work. The TPD curves are characteristic of the species desorbing : COMs are usually thermally desorbing at a temperature higher than 100 K whereas simpler molecules such as CO, N<sub>2</sub>, O<sub>2</sub> are usually thermally desorbing at a temperature lower than 100 K. The thermal desorption of molecules from a given substrate can be described as a desorption flux  $\phi_{des}$  which is a function of the substrate temperature  $T$  and which represents the amount of ejected molecules into the gas phase per time unit.  $\phi_{des}$  can be expressed using the Polanyi-Wigner equation (Redhead, 1962) :

$$\phi_{des}(T) = -\frac{d\theta}{dT} = \nu \theta^N(T) e^{-E_{ads}/(kT)} \quad (\text{II.1})$$

where  $k$  is the Boltzmann constant,  $\nu$  is a pre-exponential entropic factor,  $\theta$  is the surface molecule coverage ( $\theta = 1$  for a saturated monolayer),  $N$  is the kinetic order of the desorption and  $E_{ads}$  is the adsorption energy of the molecule on the surface which is usually referred to as the binding energy. In practice,  $E_{ads}$  is described as an energy distribution as it is varying around an average value depending on parameters such as

the molecule orientation or surface defects. What is of interest for us here is the change of thermal desorption kinetic between the multilayer and submonolayer regime. In the multilayer regime, for which more than a single layer of molecules is adsorbed on the surface, the total amount of molecules at the surface is constant over time : if one molecule desorbs from the surface, another one from the lower layer will take its place. In that case, the desorption flux is independent of the coverage ( $N = 0$ ) and the desorption kinetic is said to be a  $0^{th}$  order kinetic. In the submonolayer regime, for which  $\theta < 1$ , the desorption flux depends on the coverage ( $N \geq 1$ ) and the desorption kinetic is of order  $\geq 1$ .

In practice, this change of kinetic can be detected by successive TPD experiments for which a decreasing amount of molecules is deposited on the substrate before heating. Simulated TPD curves of  $\text{CH}_3\text{OH}$  displayed in Figure II.4 ((f) panel) enables to discuss how this kinetic change occurs. In the multilayer regime, the maximum of the TPD curves shifts to lower temperature for decreasing coverage and the start of the desorption kinetic is similar : the TPD curves share a common leading edge in the low temperature regime (135 - 140 K). When going from the multilayer to the (sub)-monolayer regime, the maximum stops shifting and the start of the kinetic changes : the drop of the leading edge increases for decreasing coverage. The attribution of the experimental TPD curves in Figure II.4 to the number of monolayers deposited on the substrate is done by considering this change of desorption kinetic. This attribution was counter-checked with experimental studies for : CO (Collings et al., 2004; Noble et al., 2012),  $\text{CH}_3\text{CN}$  (Bertin et al., 2017; Corazzi et al., 2021),  $\text{CH}_3\text{OH}$  (Martín-Doménech, R. et al., 2014; Doronin et al., 2015),  $\text{HCOOCH}_3$  (Bertin et al., 2011) and  $\text{HCOOH}$  (Baber et al., 2013; Shiozawa et al., 2015). The case of  $\text{HCOOH}$  is particular : the TPD curves in Figure II.4.(e) exhibit two separated features with decreasing coverage : one bump whose maximum is at  $143 \text{ K} \leq T \leq 150 \text{ K}$  and another bump whose maximum is at  $155 \text{ K} \leq T \leq 160 \text{ K}$ . This is attributed to the fact that  $\text{HCOOH}$  tends to form clusters when adsorbed at submonolayer coverage (Baber et al., 2013; Shiozawa et al., 2015). As the single  $\text{HCOOH}$  adsorbed molecule and the adsorbed clusters are expected to have different adsorption energy distributions, this results in two distinct features in the TPD curves, with the one at higher temperature being attributed to the thermal desorption of the  $\text{HCOOH}$  clusters.

Once the correct TPD curve is associated with a monolayer coverage, the corresponding integral signal of the escaping molecules during the dosing procedure is used as a reference to control the ice thickness during other dosing procedures, as there is a linear relationship between the amount of monolayers deposited during the dosing procedure and the integrated signal of the escaping molecules. The precision of the technique is estimated to be  $\sim 10 \%$  (this corresponds to the error made on the aimed

thickness with respect to the actual one). In this work, I will also study ices containing  $N_2$  and  $H_2O$ . The monolayer calibration of  $N_2$  is assumed to match the one for CO, which is a reasonable assumption considering that their TPD curves are similar and their adsorption energies almost equal (Collings et al., 2004; Bisschop et al., 2006). The thermal desorption of  $H_2O$  involves more complicated processes such as phase changes (e.g. from amorphous to crystalline ice) or clusterization when heating (Smith et al., 1996, 1997; Fraser et al., 2001). This makes the attribution of TPD curves to multilayer or submonolayer regime difficult. Therefore, another methodology is used to estimate the monolayer calibration of  $H_2O$  in our set-up : this is mentioned in Section II.2.3.

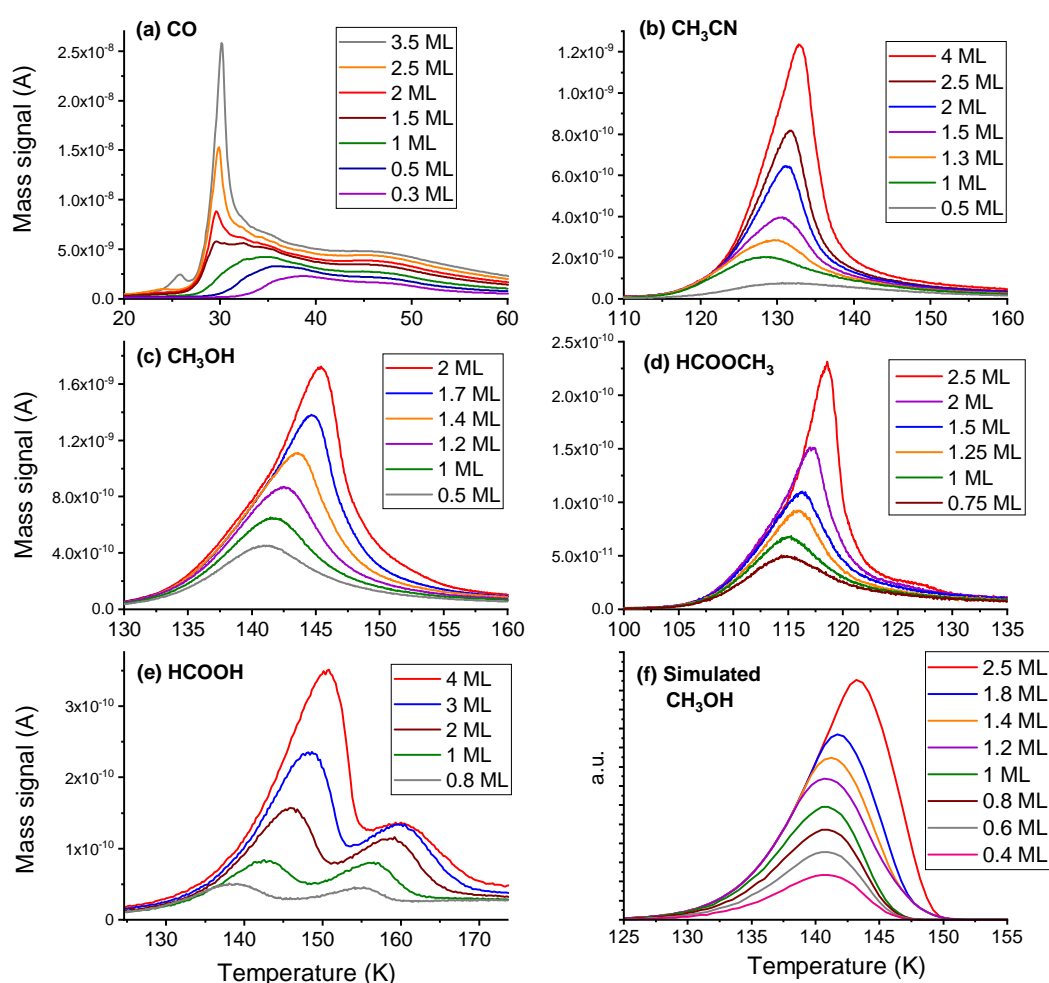


FIGURE II.4 – Temperature Programmed Desorption (TPD) curves recorded with the SPICES set-up during the thesis, from Cu substrate, of (a) carbon monoxide CO, (b) acetonitrile  $CH_3CN$ , (c) methanol  $CH_3OH$ , (d) methyl formate  $HCOOCH_3$  and (e) formic acid  $HCOOH$ . The estimation of the corresponding number of monolayers is explained in the text. The heating ramp used was 12 K/min. (f) Simulated TPD curves of  $CH_3OH$  by the Polanyi-Wigner equation, using the parameters estimated in Doronin et al. (2015).

## II.2 Coupling to the SOLEIL synchrotron beamlines

Coupling of the SPICES set-up to the synchrotron beamlines of the SOLEIL synchrotron facility at Paris-Saclay is achieved via a windowless connection tube which is pumped to preserve the ultra-high vacuum as sketched in Figure II.5. The photons are then routed to the SPICES set-up to irradiate the ices grown on the cold substrate. Before running the experiments, the photodesorption mass signal of CO<sup>1</sup> from a previously grown CO ice (at 15 K) is optimized by adjusting the angle between the QMS axis and the normal of the sample holder surface and the parameters of the beamline. This results in a geometry for which the incidence angle of the photons is  $\sim 45 - 47^\circ$ . This procedure is expected to ensure that the potential photodesorption signals for other molecules will also be optimized. This is a reasonable assertion if we assume that the angular photodesorption distribution does not significantly differ between different desorbing molecules. The synchrotron run then consists of growing molecular ices and irradiate them while monitoring the potential photodesorption signals of molecules in the gas phase by the use of a mass spectrometer. Before the irradiation procedure, a Fourier Transform infrared spectrometer is also used in Reflection

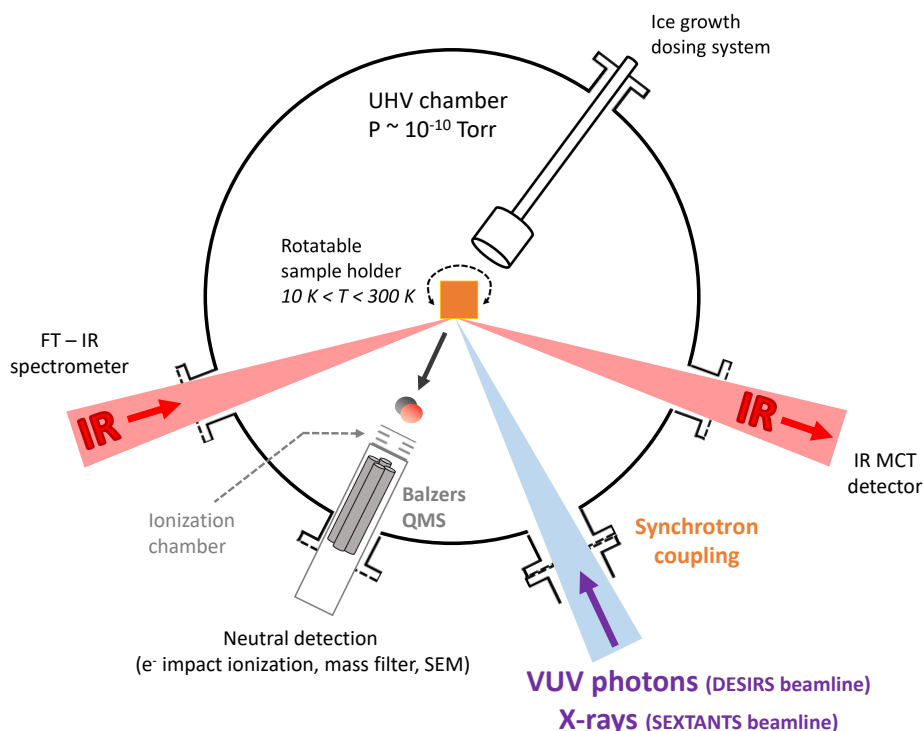


FIGURE II.5 – Photodesorption studies at the synchrotron SOLEIL : coupling of the SPICES experiment to the synchrotron beamlines (DESIRS or SEXTANTS).

1. This procedure can also be done by optimizing the photodesorption signal of H<sub>2</sub>O from a pure H<sub>2</sub>O ice although the photodesorption yield of CO from a pure CO ice is higher by more than one order of magnitude.

Absorption Infrared Spectroscopy (RAIRS) to probe the composition of the ice in order to check for any impurities. The results presented in this thesis were obtained during several campaigns at the SOLEIL synchrotron. X-ray photodesorption yields from CH<sub>3</sub>OH-containing ices were derived from the 2019 synchrotron run. VUV photodesorption yields from CH<sub>3</sub>CN, HCOOH and HCOOCH<sub>3</sub>-containing ices were derived from the 2020 synchrotron run. X-ray photodesorption yields from N<sub>2</sub>, CH<sub>3</sub>CN and HCOOH-containing ices were derived from the 2021 synchrotron run.

## II.2.1 Synchrotron beamlines

Synchrotron experiments were done on two beamlines : the DESIRS beamline (VUV range; Nahon et al. (2012)) and the SEXTANTS beamline (X-ray range; Sacchi et al. (2013)). A synchrotron facility consists of an electron accelerator that aims to take advantage of the synchrotron radiation to produce a wide spectral range of tunable monochromatic and coherent light (from the far-infrared domain up to hard X-rays). Electrons are first produced and accelerated by a linear accelerator (LINAC) before entering into a booster ring and being injected in a storage ring in which they have a high kinetic energy of a few GeV (2.75 GeV for the SOLEIL synchrotron). Undulators that consist of a periodic structure of dipole magnets are implemented in the storage ring close to the beamline entrance in order to bend the electrons trajectories : they produce a spatially alternating static magnetic field perpendicular to the electrons trajectory such as the electrons are oscillating and emitting coherent synchrotron radiation. The resulting emitted light is coherent, bright (high flux) and contains harmonics, with the fundamental frequency being related to the spatial frequency of the alternating magnetic field of the undulator, the latter being set by the user. The emission of such light is considered as continuous with respect to the integration time of our QMS ( $\sim 1$ s) as the frequency of the photon wave packets is of the order of 1 MHz.

TABLE II.1 – Characteristics of the output light of the DESIRS and the SEXTANTS synchrotron beamlines as used for the data presented in this thesis.

	DESIRS (VUV)		SEXTANTS (soft X-ray)
	1 <sup>st</sup> order	0 <sup>th</sup> order	1 <sup>st</sup> order
Beamsize (cm <sup>2</sup> )	~1		~0.1
Energy range (eV)	7-14		380-460 (N edge) 525 - 600 (O edge) 950-1450 (high energy)
Flux (photon/s)	$\sim 10^{12}$	$\sim 10^{14} - 10^{15}$	$\sim 10^{13}$
Spectral width (eV)	$\sim 0.04$	$\sim 1$	$\sim 0.1 - 0.35$

In Table II.1 are displayed some of the characteristics of the output light of the DESIRS and SEXTANTS beamlines in the configuration used for this thesis. The polarization of the beam was set to a linear, horizontal polarization for the experiments in this thesis. On the DESIRS beamline, the harmonics of the undulator output light are cut-off by ionization of a rare gas that acts as a filter. In this work, Krypton was used in order to suppress energies higher than 14 eV. On the SEXTANTS beamline, the harmonics are cut-off by the optics of the beamline. A monochromator implemented on the beamlines enables to control the spectral resolution of the output light. It can also be used as a mirror ( $0^{th}$  order) : the spectral resolution of the output light is then deteriorated compared to the normal use of the monochromator ( $1^{st}$  order) but the photon flux is higher, which enables having a better signal-to-noise ratio for the photodesorption signals. The photon flux can also be modified by adjusting the aperture slits inserted on the beamlines and this also changes the spectral resolution. On the DESIRS beamline, in the VUV range, the photodesorption signals of the COMs studied in this work were always very close to the background noise such that only the  $0^{th}$  order of the monochromator was used. This was not the case for the SEXTANTS beamline, in the soft X-ray range, for which the monochromator was used at the  $1^{st}$  order while opening the aperture slits was sufficient to get a good signal-to-noise ratio.

## II.2.2 Study of photodesorption by mass spectrometry

In this thesis, photodesorption is studied with a direct method : the molecules photodesorbing from the grown ice are detected in the gas phase by the means of a quadrupole mass spectrometer (QMS) which is mounted in front of the sample holder (on the same horizontal plane). The detection efficiency depends on several parameters and it is required to understand and quantify the sensitivity of our detection instrument to the different molecules studied in this work. The QMS can be described as a three

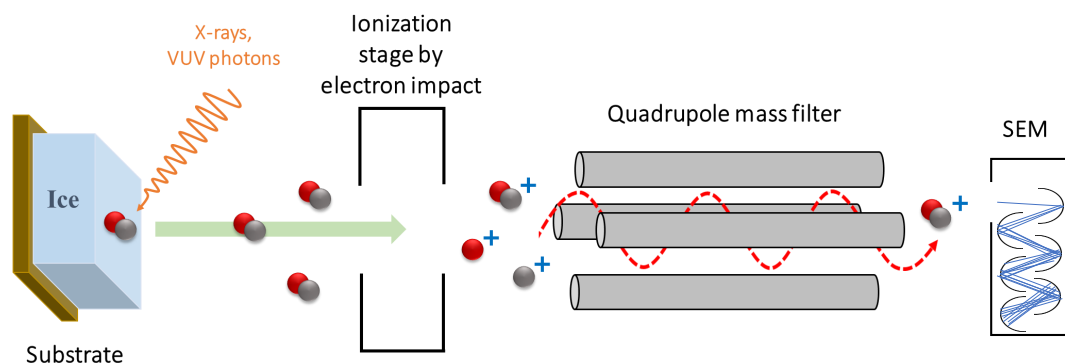
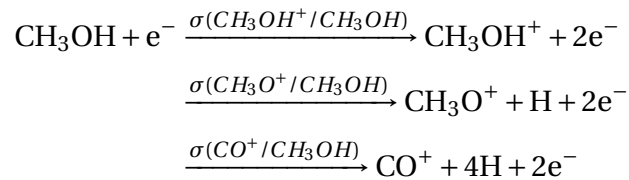


FIGURE II.6 – Quadrupole mass spectrometry technique.

steps instrument (see Figure II.6) that will be detailed in the next subsections. In this work, we are only interested in the photodesorption of neutral molecules<sup>2</sup>. The first step to detect them after their desorption is to ionize them. The resulting cations are then routed through a quadrupole depending on their  $m/z$  ratio, where  $m$  is the mass of the cation and  $z$  its charge (we will mainly be in the case of  $z = 1$  in this work). At the quadrupole output, the cations are hitting a secondary electron multiplier (SEM) to generate the detection signal (a current in A).

### II.2.2.1 Ionization by electron-impact

In the synchrotron configuration, the ionization stage is an ionization chamber mounted at the entrance of the quadrupole. It is composed of a Tungsten-Iridium filament emitting electrons (emission current  $\sim 1$  mA) that are accelerated by a voltage between the filament and an anode. This results in the electrons having a kinetic energy of  $\sim 70$  eV, which corresponds to the energy at which the electron-impact ionization cross section is maximum for most of the molecules of interest. The molecules entering the ionization chamber collide with the electrons. In this regime, an incident electron is interacting with a molecule by inelastic scattering : part of the kinetic energy of the incident electron is given to a bounded electron, resulting in the ionization of the molecule. The final electronic state of the ion created can be either non-dissociative or dissociative. This results in a specific fragmentation pattern, known as the mass spectrum of the molecule studied. This mass spectrum can be described by branching ratios that are equals to the ratios of the partial electron-impact ionization cross sections  $\sigma(A_i^+/X)$  over the total electron-impact ionization cross section  $\sigma_{tot} = \sum_i \sigma(A_i^+/X)$  where  $A_i^+$  is the final ion species and  $X$  is the initial molecule interacting with the incoming electron. Mass spectra are tabulated in the National Institute of Standards and Technology (NIST) chemistry Webbook (Wallace) (or other databases) for the molecules studied in this work. For example, the electron-impact ionization process of methanol  $\text{CH}_3\text{OH}$  can be described by the following equations and the corresponding mass spectrum is plotted in Figure II.7 (red squares and blue dots) :



2. The photodesorption of ions from molecular ices is negligible compared to the photodesorption of neutral molecules for the molecules studied (see for example, experiments on water ice (Dupuy et al., 2020) and on methanol ice (Andrade et al., 2010; Basalgète et al., 2021a))

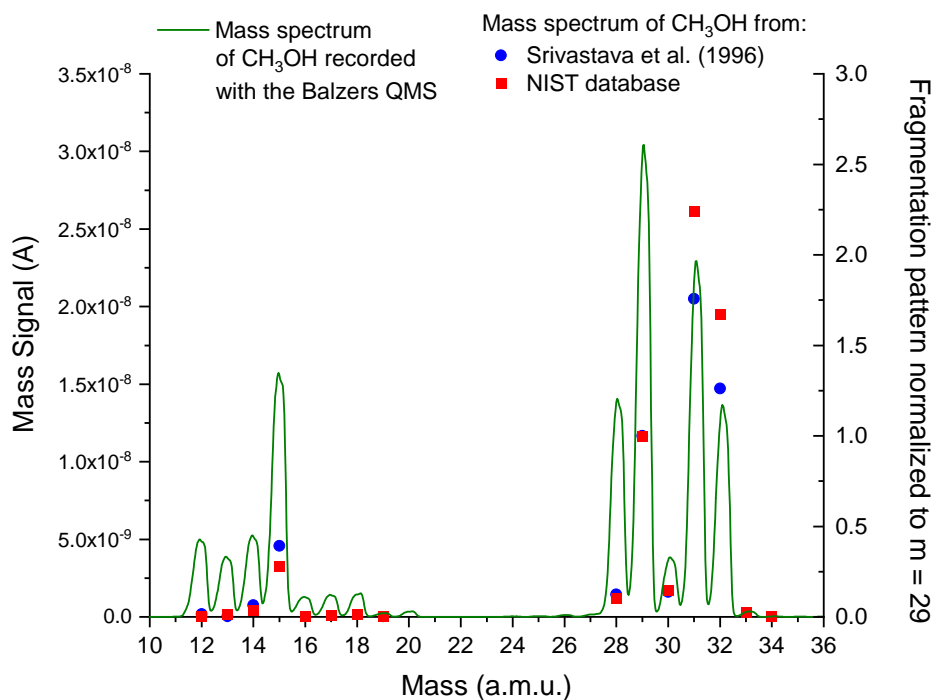


FIGURE II.7 – Comparison of the mass spectrum of  $\text{CH}_3\text{OH}$  measured experimentally (using the SPICES set-up with a  $\text{CH}_3\text{OH}$  pressure of  $1.10^{-8}$  Torr) with mass spectra of reference from the NIST Chemistry Webbook and from [Srivastava et al. \(1996\)](#). The latter values are computed relatively to the mass 29.

### II.2.2.2 Mass filtering and SEM

After ionization, the ions are guided through a quadrupole to the SEM. The quadrupole consists of four rods (see Figure II.6) that are positioned symmetrically with respect to the quadrupole axis. On each rod pair is applied a different alternative voltage in the radio-frequency domain such as the incoming cation interacting with the generated electric field will be routed towards the outlet of the quadrupole depending on its  $m/z$  ratio. Here we will be mainly in the case of  $z = 1$  such that I will rather be referring to the mass of the molecules instead of their  $m/z$  ratio in the following. The quadrupole is therefore used as a mass filter by setting the right voltages and frequencies to select a given mass for the cations. The cations that have a different mass than the one selected will be neutralized by hitting the walls or the rods. The cations exiting the quadrupole are then entering the SEM which consists of a first dynode struck by the incoming cations, releasing secondary electrons that are accelerated to hit successive dynodes, creating an electron cascade that generates, in fine, a current signal (amplification factors are typically in the  $10^5 - 10^9$  range). The transmission efficiency of the quadrupole and the detection efficiency of the SEM depend on the  $m/z$  ratio. The relative dependence of this efficiency with respect to the  $m/z$  ratio can be estimated by calibrating the apparatus function  $AF$ . In other words, the apparatus function

represents the sensitivity of our mass spectrometer to the  $m/z$  ratio. For more simplicity, I will consider  $AF$  to be a function only of the mass  $m$  of the incoming cation ( $z = 1$ ). The apparatus function is generally fitted as a power law and, for this thesis, it is computed relatively to the mass 28 (for which its value is set to  $AF(28) = 1$ ) :

$$AF(m) = (m/28)^\alpha \quad (\text{II.2})$$

To fit this function for the mass spectrometer used in the SPICES set-up, mass spectra of several well-chosen molecules are recorded by the QMS by injecting them in the vacuum chamber with a partial pressure of  $P \sim 10^{-8}$  Torr. These mass spectra are then compared to the tabulated ones on the NIST Webbook (Wallace) : an example is given in Figure II.7 for  $\text{CH}_3\text{OH}$ . The apparatus function is fitted by considering that the mass spectra recorded and corrected from  $AF$  should be similar to the reference mass spectra from the NIST database such as :

$$\frac{I_{NIST}(m)}{I_{NIST}(28)} = \frac{I_{QMS}(m)}{I_{QMS}(28)} * AF(m) \quad (\text{II.3})$$

where  $I_{NIST}(m)$  is the intensity at the mass  $m$  from the NIST database and  $I_{QMS}(m)$  is that recorded by the QMS. The resulting fit is displayed in Figure II.8 for two different calibration procedures in 2016 and 2022. The data are quite comparable, showing the stability of the mass spectrometer over time. The fitting however displays non-negligible dispersion from the data, which is partly due to the fact that, for the points that exhibit the higher dispersion, the branching ratios measured are associated with minor dissociation channels, hence for which the uncertainty is non-negligible. Other source of uncertainties on this calibration will be discussed in section II.2.3.3.

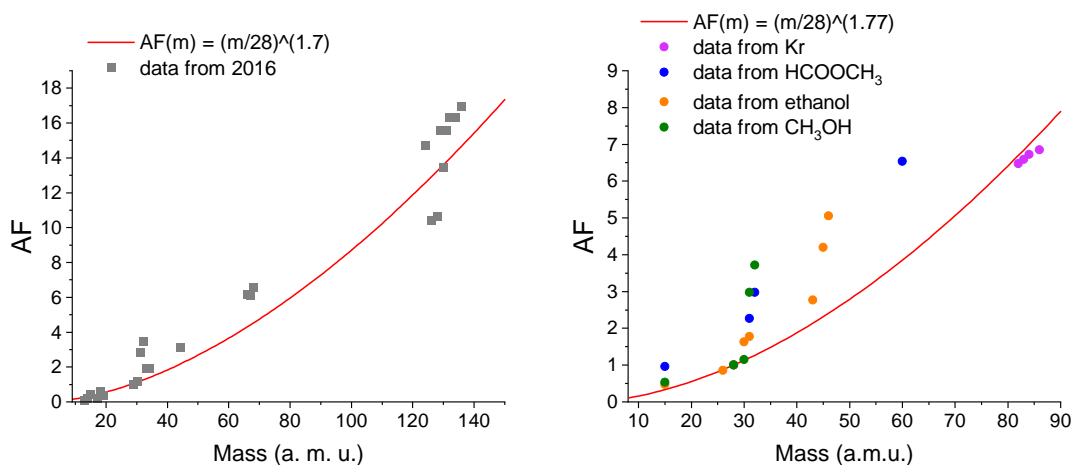


FIGURE II.8 – Calibration of the apparatus function  $AF(m/z)$  from 2021 data (right panel) and 2016 data (left panel). Note that the panels do not have the same Y and X-scale.

## II.2.3 Quantification of the photodesorption yields

### II.2.3.1 Raw synchrotron data and photodesorption yields

The photodesorption experiments at the SOLEIL synchrotron facility can be carried out in two different ways :

1. the studied ice is irradiated continuously while scanning the incident photon energy over time and while the desorbing masses are monitored by the QMS. An example of data obtained from this methodology is given in Figure II.9.(c) where the photodesorption intensity is displayed on the y-axis and the time is displayed on the x-axis. Starting from these data, the time scale is converted to an energy scale matching the incident photon energy at a given time and a photodesorption intensity  $I_X(E)$  is computed for the species  $X$  as a function of the photon energy  $E$  by correcting the signal from the background level.
2. the studied ice is sequentially irradiated during a few seconds at several fixed energies, step by step, while the masses are continuously recorded by the QMS. Examples of data obtained from this methodology are shown in Figure II.9.(a), (b) and (d) where the sudden increase and decrease of the mass signals are respectively associated with the opening (irradiation) and closing (background) of the beamline shutter. This methodology is useful to avoid the photo-ageing of the ice, that is a significant chemical and structural transformation of the ice due to a high photon fluence (the fluence is defined as the number of photons that have irradiated the ice, usually expressed in photon/cm<sup>2</sup>). This ageing is particularly problematic when studying ices containing COMs for which the dissociation induced by photo-absorption is efficient and can modify the ice composition significantly. This can result in a fast decrease of the photodesorption signals with the fluence, which is not representative of what we aim to measure, i.e. a photodesorption yield associated with an "intact" ice having received a low photon fluence. In the VUV domain, the photon flux at the first order of the beamline monochromator is not sufficient to observe the photodesorption of COMs such that only the zeroth order of the monochromator is used. Considering the spectral width of the resulting light ( $\sim 1$  eV), the photodesorption spectra are then reconstructed manually by sequentially irradiating the ice from 7 to 14 eV by step of 0.5 eV.

For each photon energy  $E$  and each species  $X$ , a photodesorption intensity  $I_X(E)$  is derived by computing the height of the mass signal with respect to the background level for the irradiation step considered. This computation is done only

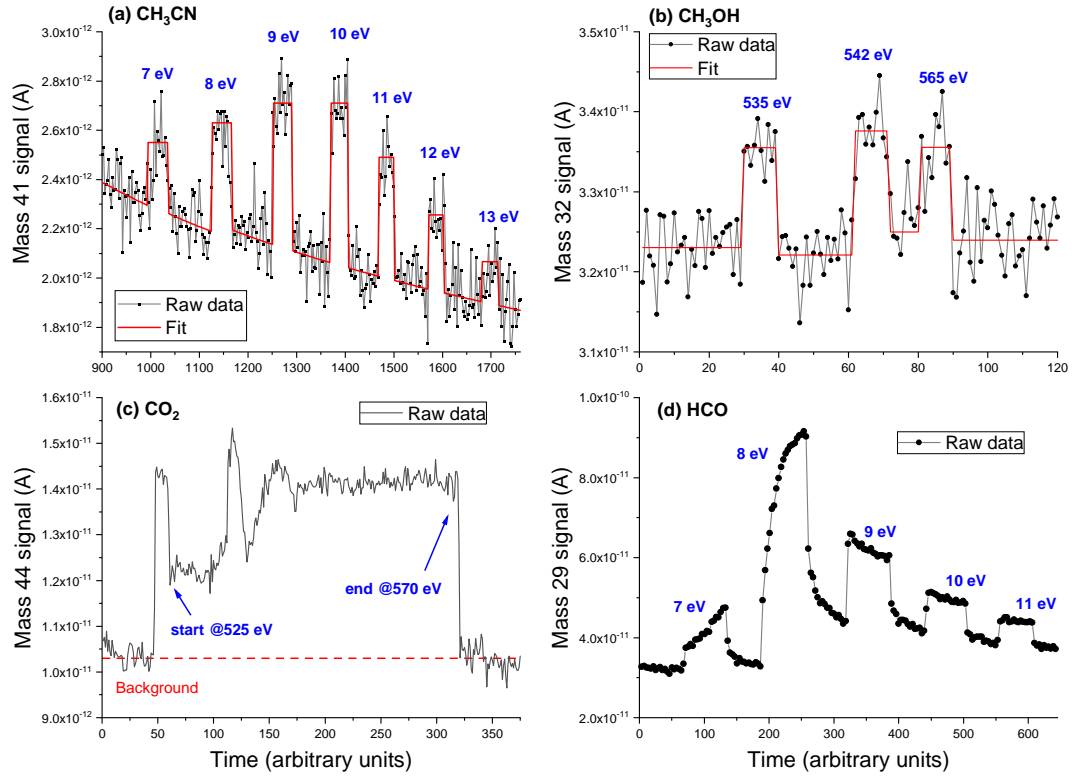


FIGURE II.9 – Synchrotron raw photodesorption data from mass spectrometry measurements. (a) VUV photodesorption of CH<sub>3</sub>CN (mass 41) from pure CH<sub>3</sub>CN ice at 15 K. (b) X-ray photodesorption of CH<sub>3</sub>OH from pure CH<sub>3</sub>OH ice at 15 K. (c) X-ray photodesorption of CO<sub>2</sub> from pure CH<sub>3</sub>OH ice at 15 K. (d) VUV photodesorption of HCO from pure HCOOH ice at 90 K. The energies of the incident photons are given in blue.

when the mass signal recorded during the irradiation does not display strong variations such that the photodesorption can be considered a steady state process over the irradiation time. This is the case for the data in Figure II.9. (a) and (b). For a raw signal such as the one displayed in Figure II.9.(d), the photodesorption intensity is varying with the photon fluence during the irradiation time, which is a kinetic signature of chemistry processes happening at the ice surface. In that case, a "steady state" photodesorption intensity cannot be derived.

The photodesorption intensities  $I_X(E)$  (in A) obtained from the previous methodologies are then divided by the photon flux  $\Phi(E)$  (in photon/s) and multiplied by a conversion factor  $k_X$  (in molecule/(A × s)) to obtain the so-called photodesorption yield  $\Gamma_X(E)$  expressed in molecules desorbed by incident photon, displayed as molecule/photon through this manuscript :

$$\Gamma_X(E) = k_X \frac{I_X(E)}{\Phi(E)} \quad (\text{II.4})$$

The photon flux is measured by a calibrated photodiode mounted on the beamline. The conversion factor  $k_X$  depends on the species considered and can be calibrated using different methods described in Section II.2.3.2. For molecules that could originate from the fragmentation of their photodesorbing parent molecule in the ionization chamber of the QMS (see Section II.2.2.1),  $I_X(E)$  should be corrected according to the fragmentation patterns available on the NIST chemistry Webbook (Wallace). The correction is done as follows : we consider a desorbing species  $Y$  associated to a raw signal  $I_Y^{raw}$  and dissociating into a species  $X$  in the ionization chamber according to the NIST ratio  $I_{NIST}(X)/I_{NIST}(Y)$ , which generates a raw signal on the mass channel of  $X$ . In order to assess if the observed signal on the mass channel of  $X$ ,  $I_X^{raw}$ , is only due to the fragmentation of  $Y$  or if it could also be due to a species  $X$  photodesorbing from the ice, one has to correct  $I_X^{raw}$  by the fragmentation of  $Y$ . This correction is quantified by considering that  $I_Y^{raw}$ , before being transmitted through the QMS ( $I_Y^{raw} \times AF(m_Y)$ ), is generating a signal on the mass channel of  $X$  after transmission through the QMS and according to the fragmentation pattern ( $I_Y^{raw} \times \frac{AF(m_Y)}{AF(m_X)} \times \frac{I_{NIST}(X)}{I_{NIST}(Y)}$ ). This results in the following formula :

$$I_X^{corrected} = I_X^{raw} - I_Y^{raw} \times \frac{AF(m_Y)}{AF(m_X)} \times \frac{I_{NIST}(X)}{I_{NIST}(Y)} \quad (\text{II.5})$$

If  $I_X^{corrected} > I_X^{background}$ , where  $I_X^{background}$  is the background level for the mass channel of  $X$ , then it means that  $X$  is photodesorbing from the ice with a yield equal to  $k_X \times (I_X^{corrected}(E)/\Phi(E))$  whereas if  $I_X^{corrected} \sim I_X^{background}$  then it means that the raw signal observed on the mass channel of  $X$  is only due to the fragmentation of  $Y$  in the ionization chamber of the QMS.

Finally, it is sometimes useful to derive the photodesorption yield  $\Gamma_X$  in molecules desorbed per eV deposited in the ice, especially when one wants to compare the VUV and the X-ray photodesorption yields (comparison with electron-stimulated-desorption (ESD) yields will also be done). This can be done by correcting the experimental yields by the absorption cross section as follows :

$$\Gamma_X^{eV}(E) = \frac{1}{E} \times \frac{\Gamma_X(E)}{a_{dil}(1 - e^{-N\sigma(E)})} \quad (\text{II.6})$$

where  $E$  is the photon energy,  $\Gamma_X^{eV}(E)$  is the photodesorption yield expressed in molecule/eV deposited,  $\sigma$  is the photoabsorption cross section,  $a_{dil}$  is taking into account the dilution factor of the photodesorbing molecule for the case of mixed ices and  $N$  is the column density of molecules involved in the photodesorption process. Equation II.6 requires to know the absorption cross section  $\sigma$  for COMs in the VUV and the X-ray domain. It also requires an estimation of the number of monolayers  $\Lambda_{des}$  involved

in the photodesorption process (named the desorption-relevant depth in this thesis) to compute  $N$  such as  $N = \Lambda_{des} \times b_{dil} \times 10^{15}$ , where we consider a surface molecular density of  $10^{15} \text{ cm}^{-2}$  and where  $b_{dil}$  is a factor taking into account the dilution of the photo-absorbing molecule in the case of mixed ices. It is not always possible to know these quantities for COMs and assumptions have to be made in some cases. More details on the meaning and the estimation of the desorption-relevant depth  $\Lambda_{des}$  with regards to experimental data are given in Chapter IV. The resulting yields  $\Gamma_X^{eV}(E)$  are quantifying the efficiency of the photon energy conversion to the desorption channel. Comparisons of  $\Gamma_X^{eV}(E)$  between the VUV and the X-ray domain (and also with ESD experiments) can provide insights on the mechanism involved in the photodesorption process. Such comparisons will be discussed in Chapters V and VI.

### II.2.3.2 Conversion factor $k_X$

The conversion factor  $k_X$  is first calibrated for a specific molecule of reference, that I will refer to as  $X_{ref}$ . The aim of the calibration is to relate the QMS desorption signal (in A or in  $A \times s$ /photon when corrected from the photon flux) on the mass channel of  $X_{ref}$  to the actual number of incoming molecules at the QMS entrance. Before the thesis, Öberg, K. I. et al. (2007); Muñoz Caro, G. M. et al. (2010); Fayolle et al. (2011) implemented a methodology based on the decrease of infrared bands, monitored by Reflection Absorption InfraRed Spectroscopy (RAIRS) or in transmittance, of CO molecules in the solid phase during VUV irradiation of pure CO ice. In the VUV range between 7 and 10 eV, the corresponding excited electronic state of CO ( $A^1 \Pi$ ) is non-dissociative and no significant chemistry is observed such that the decrease of infrared CO-related vibrational features with the photon fluence is essentially associated with CO photodesorption (see Figure II.10). The calibration procedure consists of fitting this decrease by a linear function to deduce the photodesorption yield of CO expressed in  $\text{cm}^{-1}/(\text{photon}/\text{cm}^2)$  at a given energy. Knowing the absorbance associated with 1 ML of CO, this yield can be converted in molecule/photon. Finally, a photodesorption spectrum of CO from a pure CO ice is recorded by the QMS and corrected by the photon flux (then expressed in  $(A \times s)/\text{photon}$ ). Conversion of this mass signal to obtain the previously derived photodesorption yield in molecule/photon gives access to the conversion factor  $k_{CO}$  expressed in molecule/ $(A \times s)$ .

The VUV photodesorption spectrum of CO derived in Fayolle et al. (2011), where the yield is expressed in molecule/photon, is used as a reference spectrum for other synchrotron runs (in the VUV range). Consequently, an easy way to derive  $k_{CO}$  for other synchrotron runs is to record the QMS signal associated with the photodesorption of CO from a pure CO ice at 15 K, expressed in  $A \times s/\text{photon}$  after correction from the photon flux, and match it with the reference spectrum from Fayolle et al. (2011), expressed

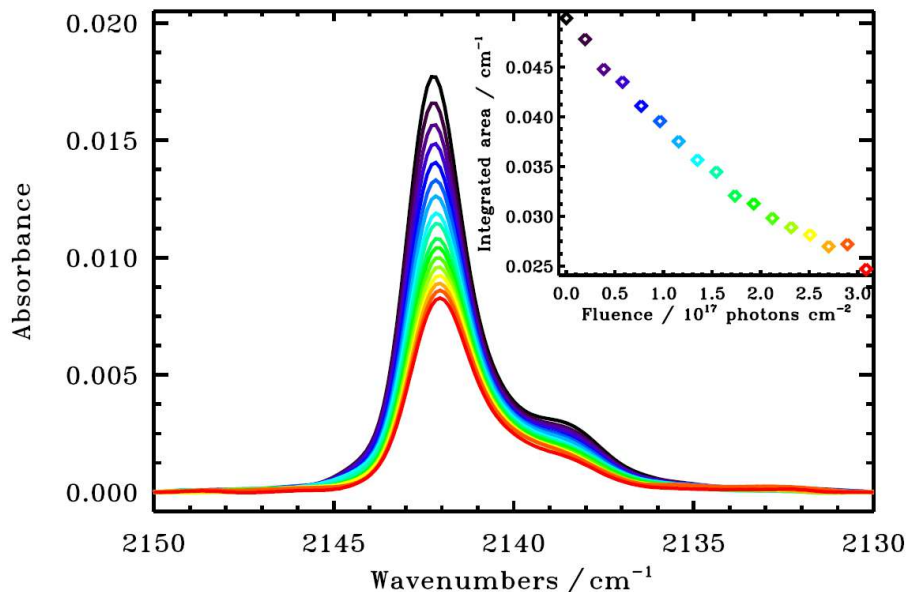


FIGURE II.10 – Evolution of the infrared spectrum of 20 ML of CO at 15 K on gold surface during irradiation by 8.5 eV photons; the upper inset shows the integrated area versus the photon fluence. Taken from [Fayolle et al. \(2011\)](#).

in molecule/photon. The objective of this procedure is to take into account the slight differences in the experimental conditions that might occur between two synchrotron runs and that result in a change of detection efficiency hence in a different  $k_{CO}$  factor. This mainly aims to correct (i) the dependence of the photodesorption signal to the desorption angle as the latter might be different between the runs due to the alignment procedure and (ii) the possible ageing of the SEM detector. This methodology was conducted during the 2020 synchrotron run (VUV photodesorption of  $\text{CH}_3\text{CN}$ ,  $\text{HCOOH}$  and  $\text{HCOOCH}_3$ ) and it is presented in Figure II.11. The reference photodesorption spectrum of CO, which was obtained using the 1<sup>st</sup> order of the synchrotron beamline monochromator (see Section II.2.1), had to be "deteriorated" to match the beam resolution of the 2020 synchrotron run, which was  $\sim 1$  eV (0<sup>th</sup> order of monochromator). The factor  $k_{CO}$  is deduced by converting the signal in As/photon (right Y scale of Figure II.11) to a photodesorption yield in molecule/photon (left Y scale of Figure II.11).

In the X-ray range, the previous methodology, based on the decrease of the infrared bands of solid CO with the photon fluence, cannot be apply because non-negligible photo-dissociation and photo-chemistry occur in the ice bulk. Therefore, the decrease of the IR bands cannot be exclusively attributed to CO photodesorbing from the ice surface as it is also due to its destruction in the ice bulk and the two processes cannot be distinguished in the IR data. For the X-ray synchrotron runs, namely the 2019 and 2021

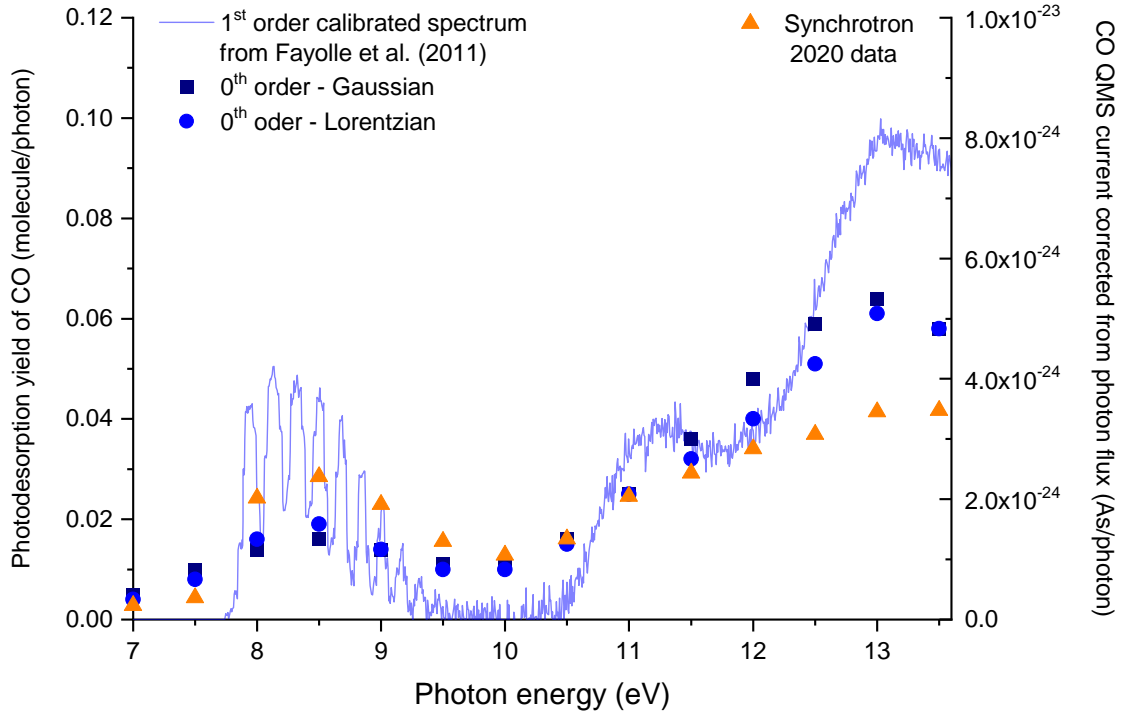


FIGURE II.11 – Left Y-scale : in blue solid line is the photodesorption spectrum of CO from a pure CO ice at 15 K (using the 1<sup>st</sup> order of the synchrotron beamline monochromator), from [Fayolle et al. \(2011\)](#) and expressed in molecule/photon. The squares and circles represent the spectrum "deteriorated" by taking into account a  $\sim 1$  eV full width at half-maximum (FWHM) for the photon source (0<sup>th</sup> order of monochromator), with a Gaussian or Lorentzian profile, respectively. Right Y-scale (triangles) : photodesorption spectrum of CO from a pure CO ice at 15 K, from the 2020 synchrotron run where the 0<sup>th</sup> order of the monochromator was used, expressed in As/photon (QMS signal corrected by the photon flux).

runs (X-ray photodesorption of CH<sub>3</sub>OH, CH<sub>3</sub>CN and HCOOH), another methodology was used via TPD experiments (see Section II.1.2.2). The method is rather simple : once the TPD curve corresponding to one ML of the molecule  $X_{ref}$  is identified, we can easily relate the integrated signal of the TPD curve to the number of incoming molecules by considering that 1 ML is equivalent to a surface density of  $10^{15}$  molecules/cm<sup>2</sup> on the surface of the substrate, the latter being equal to  $1.5 \times 1.5$  cm<sup>2</sup>. This results in the following formula :

$$1_{ML}(X_{ref}) = 10^{15} \times 1.5 \times 1.5 = k_{X_{ref}} \times \int_{1_{ML}} I_{X_{ref}} dt \quad (\text{II.7})$$

with  $1_{ML}(X_{ref})$  corresponds to the number of molecules in 1 ML of the species  $X_{ref}$ . The time integral is computed on the TPD curve corresponding to 1 ML of  $X_{ref}$  as shown in Figure II.4 (the integral over the temperature can be converted to the time integral by dividing it by the heating ramp in K/s) and the conversion factor  $k_{X_{ref}}$  is de-

duced and expressed in molecule/(A×s). Compared to the methodology based on the IR bands, the TPD methodology is expected to be less relevant when trying to quantify a number of photodesorbed molecules. In fact, the state of thermally desorbed and photodesorbed molecules, such as their velocity or their desorption angle, might be very different such that they might not be detected by our QMS with the same efficiency. It would result that one ML of photodesorbed molecules would not give the same level of QMS signal than one ML of thermally desorbed molecules, which would make the calibration by the TPD methodology inaccurate. This is discussed in more details in Section II.2.3.3.

The conversion factor  $k_{X_{ref}}$  can be extrapolated to other molecules  $X$  by considering the relative sensitivity of our QMS to the  $m/z$  ratios associated with  $X_{ref}$  and  $X$ . This implies correcting  $k_{X_{ref}}$  by (i) the differences in the apparatus functions  $AF(m_X)$  and  $AF(m_{X_{ref}})$  (considering that  $k_X > k_{X_{ref}}$  if  $X$  is less efficiently transmitted through the QMS than  $X_{ref}$ , i.e. if  $m_X > m_{X_{ref}}$ , and  $k_X < k_{X_{ref}}$  if  $m_X < m_{X_{ref}}$ , consistent with our definition of  $AF(m)$  in section II.2.2.2) and by (ii) the differences in the ionization cross sections by electron impact at 70 eV,  $\sigma(X^+/X)$  and  $\sigma(X_{ref}^+/X_{ref})$  (considering that  $k_X > k_{X_{ref}}$  if  $X$  is less efficiently ionized than  $X_{ref}$ , i.e. if  $\sigma(X^+/X) < \sigma(X_{ref}^+/X_{ref})$ , and  $k_X < k_{X_{ref}}$  if  $\sigma(X^+/X) > \sigma(X_{ref}^+/X_{ref})$ ). This results in the following formula :

$$k_X = k_{X_{ref}} \times \frac{AF(m_X)}{AF(m_{X_{ref}})} \times \frac{\sigma(X_{ref}^+/X_{ref})}{\sigma(X^+/X)} \quad (\text{II.8})$$

Equation II.8 can also be used to deduce the integrated mass signal corresponding to a monolayer deposition during a dosing procedure for molecules for which the calibration of the monolayer by TPD is not possible (see Section II.1.2.2). This was done for H<sub>2</sub>O by replacing, in equation II.8, the conversion factor  $k_{CO}$  by the integrated mass signal of the escaping molecules during a monolayer deposition of CO in order to deduce that of H<sub>2</sub>O. The cross sections  $\sigma$  are often available in the literature for the molecules studied in this work. However, the photodesorption of radicals is often detected in our experiments. Ionization cross sections of these radicals are not available such that assumptions need to be made in order to estimate them. The values of the cross sections used in this work, and the assumptions made are presented in appendix A.

### II.2.3.3 Source of uncertainties on the photodesorption yields

The first source of uncertainty associated with the photodesorption yields  $\Gamma_X$  is a measurement uncertainty related to the signal-to-noise ratio of the QMS mass channel of  $X$ . This is the only source of uncertainty that is taken into account in the error bars associated with the photodesorption yields displayed in the result chapters. Other source of uncertainties associated with the experimental methodology apply to

the photodesorption yields but are not explicitly displayed in the results. These uncertainties are systematic in the sense that they are related to the calibration methodologies previously mentioned. They include :

- uncertainties on the calibration of the apparatus function  $AF(m)$  : as displayed in Figure II.8, there are non-negligible deviations from the experimental data in the fitting of  $AF(m)$ . This is expected to be mainly due to uncertainties on the reference data used to compute  $AF(m)$  from equation II.3. The reference data retained for the derivation of  $AF(m)$  are taken from the NIST Chemistry Webbook database (Wallace). As one can see in Figure II.7 for the example of  $\text{CH}_3\text{OH}$ , the branching ratios deduced from these data can differ between different reference sources. A quantification of the uncertainties associated with the NIST data is not available and the experimental conditions under which these data are obtained might differ from the ones under which we measured the branching ratios associated with our QMS. This is expected to result in a non-negligible uncertainty on the points  $AF(m)$  derived and displayed in Figure II.8, which cannot be estimated quantitatively. This in turns result in an uncertainty on the  $k_X$  factors and on the photodesorption yields via equations II.8 and II.4 respectively.
- uncertainties on the ionization cross sections by electron impact  $\sigma(X^+/X)$  used in equation II.8 : the cross sections retained are presented in appendix A with the associated references. The uncertainty on the values of the cross sections is generally estimated from the references to be  $\sim 20\%$ . This uncertainty propagates to the  $k_X$  factors and the photodesorption yields through equation II.8 and II.4 respectively.
- uncertainties on the monolayer calibration : this concerns only the calibration procedure of  $k_{X_{ref}}$  by the TPD methodology. The uncertainty on the identification of the TPD curve associated with one ML of the molecule considered (see Figure II.4) results in an uncertainty on the absolute coverage of  $\sim 0.2$  ML (Doronin et al., 2015). When considering the integrals of the TPD curves, this implies, via equation II.7, an uncertainty on  $k_{X_{ref}}$  of  $\sim 10\%$ . Note that this methodology was only used to derive the X-ray photodesorption yields from methanol-containing ices.
- dependence of the apparatus function  $AF$  on the velocity of photodesorbed molecules : in the ionization chamber of the QMS, for a given ionization cross section, molecules with high velocity are less efficiently ionized than molecules with lower velocity (because their residence time in the ionization chamber is lower).

Therefore, the QMS response decreases inversely with the molecules velocity. This affects the relative detection efficiency of our QMS between photodesorbed molecules of different velocity distributions. Quantifying this change in the detection efficiency requires having access to the velocity distribution of the photodesorbed molecules (which may vary with the incident photon energy). For example, the mean velocity of H<sub>2</sub>O ( $v = 0$  in the electronic ground state) photodesorbing from pure H<sub>2</sub>O ice at 157 nm and at 108 K is  $\sim 1100$  m/s according to [DeSimone et al. \(2013\)](#). For comparison, the mean velocity of CO ( $v = 0$  in the electronic ground state) photodesorbing from pure CO ice at 157 nm is  $\sim 800$  m/s (based on this thesis result, see Chapter IV). This would mean that the QMS has a better efficiency detection for CO than for H<sub>2</sub>O, by a factor roughly equal to 1.375 (by taking the ratio of the velocities and knowing that the ionization cross sections are similar for CO and H<sub>2</sub>O). The velocity distribution of photodesorbed COMs are not known so far such that the corresponding relative detection efficiency cannot be taken into account in the calibration of  $AF$ , which was calibrated on gas phase molecules at ambient temperature.

The resulting systematic uncertainty on the photodesorption yields, due to the previous sources and associated with the calibration procedure, is estimated to be in the order of magnitude of 50 %. In consequence to this non-negligible uncertainty, variations observed on the photodesorption yields will be considered as "actual" variations only when they are at least greater than half an order of magnitude. Photodesorption yields that differ by less than half an order of magnitude cannot be considered to be significantly different.

## II.2.4 Extrapolation to astrophysical yields

One of the main objective of the synchrotron experiments is to quantify the VUV and X-ray photodesorption of specific COMs that have been detected in several regions of the ISM, namely, methanol CH<sub>3</sub>OH, acetonitrile CH<sub>3</sub>CN, formic acid HCOOH and methyl formate HCOOCH<sub>3</sub>. The photodesorption was systematically studied as a function of the ice composition, from pure ices made of the studied COM and from binary mixed ices in which the studied COM is embedded in either a CO or a H<sub>2</sub>O ice. These mixed ices serve as models of the realistic icy mantles that could be found in the ISM, mainly composed of water but which can also present a CO-rich phase in denser regions beyond the CO snowlines ([Pontoppidan, K. M. et al., 2003](#); [Boogert et al., 2015](#)), as explained in Chapter I. The photodesorption yields computed from the synchrotron experiments are given as a function of the photon energy. In order to be more easily implemented in astrochemical models, we can provide photodesorption yields averaged in energy on a VUV or X-ray field representative of the local field irradiating the inter-

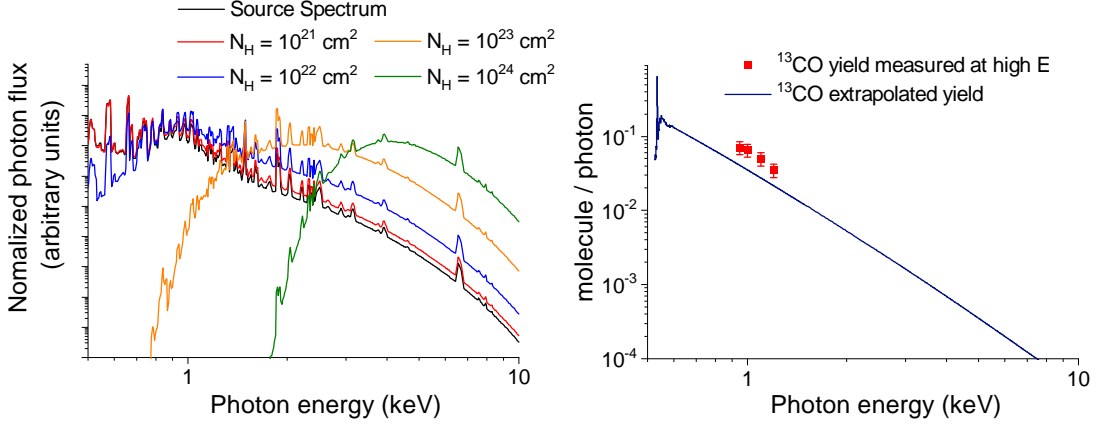


FIGURE II.12 – Left panel : normalized source and attenuated X-ray spectrum of TW Hya (Nomura et al., 2007). Right panel : extrapolated X-ray photodesorption yield spectrum of  $^{13}\text{CO}$  from a pure  $^{13}\text{CO}$  ice at 15 K, from the 2019 synchrotron experiments and using the photoabsorption cross section of gas-phase methanol from Berkowitz (2002). In the right panel, the red squares correspond to the derivation of the yields measured at energies near 1 keV during the 2021 synchrotron run.

stellar ices in different regions of the ISM. This results in the following formula :

$$\Gamma_X^{astro} = \frac{\int \Gamma_X(E) \Phi_{local}(E) dE}{\int \Phi_{local}(E) dE} \quad (\text{II.9})$$

where  $\Gamma_X(E)$  is the experimental photodesorption yield at  $E$  and  $\Gamma_X^{astro}$  is the averaged photodesorption yield associated with the spectrum  $\Phi_{local}(E)$ . The spectra used in equation II.9 are the ones presented in Chapter I (Figures I.7 and I.8) which are representative of different regions of the ISM such as dense cores or the interior of protoplanetary disks. For the case of X-rays, the spectrum of the emitting young star can be attenuated to take into account the absorption by gas and dust when going deeper into the disk. This results in the following formula :

$$\Phi_{local}(E) = \Phi_{em}(E) \times e^{-\sigma_{pe}(E) \times N_H} \quad (\text{II.10})$$

where  $\Phi_{em}(E)$  is the non-attenuated X-ray emission spectrum of the young star,  $\sigma_{pe}(E)$  is the photoelectric (photo-absorption, without the near-edge absorption fine structure) cross section of gas and dust in a typical T-Tauri protoplanetary disk taken from Bethell and Bergin (2011) and  $N_H$  is the H column density traversed by the X-rays. An example of an attenuated X-ray spectrum from a T-Tauri star is given in the left panel of Figure II.12, where we see that only hard X-rays ( $> 3$  keV) remain in the local spectrum at high  $N_H$ . In the X-ray energy range, the experimental photodesorption yields  $\Gamma_X(E)$  are derived only for a limited energy range, generally in the 525 - 560 eV or 400 - 450 eV range, whereas the local X-ray spectrum considered in equation II.9 spans the 0.1

- 10 keV range. Before using equation II.9 for the X-ray range, it is therefore required to extrapolate the experimental X-ray photodesorption yields  $\Gamma_X(E)$  to higher energies. This is done by assuming that the photodesorption yield at higher energies are following the same variations as the gas-phase X-ray photoabsorption cross section of the molecule constituting the studied ice. This assumption is supported by (i) the fact that the X-ray photodesorption spectra are following the same variations as the X-ray photoabsorption spectra of the studied ices (see results in Chapter IV and Chapter VI) and by (ii) the fact that the X-ray photoabsorption of molecules in solid phase at high energy (>0.6 keV) is dominated by the ionization of their core 1s electron, whose cross section is not expected to be significantly modified compared to the gas phase as core electrons are atomic in nature hence they should not be strongly affected by the solid phase.

An example of such extrapolated X-ray photodesorption spectrum is given in the right panel of Figure II.12 for the desorption of  $^{13}\text{CO}$  from a pure  $^{13}\text{CO}$  ice at 15 K. Additionally, in order to test the validity of such extrapolation, X-ray photodesorption yields of  $^{13}\text{CO}$  from a pure  $^{13}\text{CO}$  ice at 15 K were measured at energies near 1 keV. The measured yields are displayed in the right panel of Figure II.12 in red squares. We can see that the measured yields are quite consistent with the extrapolation. The difference, of approximately a factor 2, can be due to (i) an uncertainty on the absorption cross section taken from Berkowitz (2002), (ii) a difference in the experimental conditions for which the yields have been derived (the yields in blue are extrapolated from data of the 2019 synchrotron run whereas the yields at high energy are taken from the 2021 synchrotron run).

The main issue of extrapolating astrophysical yields from experimental ones is that the photon flux is significantly different between experimental conditions and the expected interstellar conditions. In astrophysics, fluxes are generally expressed in  $\text{erg}/\text{cm}^2/\text{s}$  (energy flux) whereas in laboratory experiments, fluxes are expressed in  $\text{particles}/\text{cm}^2/\text{s}$  (particle flux). The conversion factor is  $1 \text{ erg}/\text{cm}^2/\text{s} \sim 10^{12} \text{ eV}/\text{cm}^2/\text{s}$  and then one must divide by the particle energy to get the number of  $\text{particles}/\text{cm}^2/\text{s}$ . I will use the same term "flux" for the two different units for more simplicity in this thesis. The term "dose" is sometimes used to refer to the energy deposited in ices for a given period of time, namely the lifetime of the region considered. It is generally expressed in  $\text{eV}/\text{cm}^2$  or  $\text{eV}/\text{molecule}$ . The equivalent in terms of  $\text{particles}/\text{cm}^2$  is referred to as the "fluence". In molecular clouds, typical VUV fluxes are  $\sim 10^8$  and  $\sim 10^3 \text{ photon}/\text{cm}^2/\text{s}$  at the edges and in dense cores respectively (Moore et al., 2001). In the cold regions of protoplanetary disks ( $T_{\text{dust}} < 100 \text{ K}$ ), according to Figure I.9 from Walsh et al. (2012), it ranges from  $\sim 10^{12}$  to  $10^4 \text{ photon}/\text{cm}^2/\text{s}$ . In comparison, experimental VUV fluxes at the synchrotron are between  $\sim 10^{14}$  and  $\sim 10^{15} \text{ photon}/\text{cm}^2/\text{s}$ . In the case of X-rays,

the fluxes in the cold regions of protoplanetary disks range between  $\sim 10^{10}$  and  $10^2$  photon/cm<sup>2</sup>/s (by taking a photon energy of 1 keV) whereas experimental fluxes are  $\sim 10^{14}$  photon/cm<sup>2</sup>/s. Experimental fluxes are therefore systematically higher, by several orders of magnitude, than the fluxes expected in the cold regions of the ISM, where photodesorption could play a role. This raises a question on the relevance of the extrapolation of our experimental photodesorption yields to astrophysical environments as the dependence of the photodesorption yields to photon fluxes is not known so far.

### II.3 Coupling to a VUV photon source implemented at the LERMA lab

During this thesis, an important part of my work was to implement a VUV photon source directly at the LERMA lab. The aim of such implementation was to quantify the internal and kinetic energy of photodesorbed molecules thanks to a Time-Of-Flight (TOF) + Resonance Enhanced Multi-Photon Ionization (REMPI) technique which will be described in the next sections. Accessing such data provides key information to discuss the photodesorption mechanisms involved in the VUV photodesorption process. In this thesis, these experiments focused on the VUV photodesorption of CO from pure CO ice at 15 K, whose results will be presented in Chapter IV.

The general principle of the experimental set-up is presented in Figure II.13 and briefly described in the following. VUV photons are generated by focusing two nanosecond pulsed laser beams (one in the UV range and the other one in the visible or near-infrared range) into a rare gas chamber. A frequency conversion occurs via a third order non-linear optical effect in the gas medium, resulting in the emission of VUV light from the gas chamber (see Section II.3.1). Wavelengths are then separated by a Lithium Fluoride (LiF) prism and the VUV beam goes through a tube coupled with the SPICES set-up and irradiates previously grown ices. A home-made detector is implemented into this tube in order to measure the VUV flux and to ensure the alignment of the beam with the SPICES set-up. The set-up from the separation stage to the SPICES chamber is under vacuum ( $\sim 10^{-6}$  Torr) to reduce the absorption of the VUV light by residual gas. To detect the photodesorbing molecules via mass spectrometry, a REMPI technique, associated with a TOF delay, is used thanks to a third nanosecond pulsed laser tunable in the UV/Visible range (see Section II.3.2). The temporal synchronization between the different instruments (lasers and mass spectrometer) is ensured by a GINI (Générateur d'Impulsions Numériques Informatisé) which is a nanosecond-precision generator of numerical pulses, made at the ISMO lab (Institut des Sciences Moléculaires d'Orsay - Univ. Paris-Saclay).

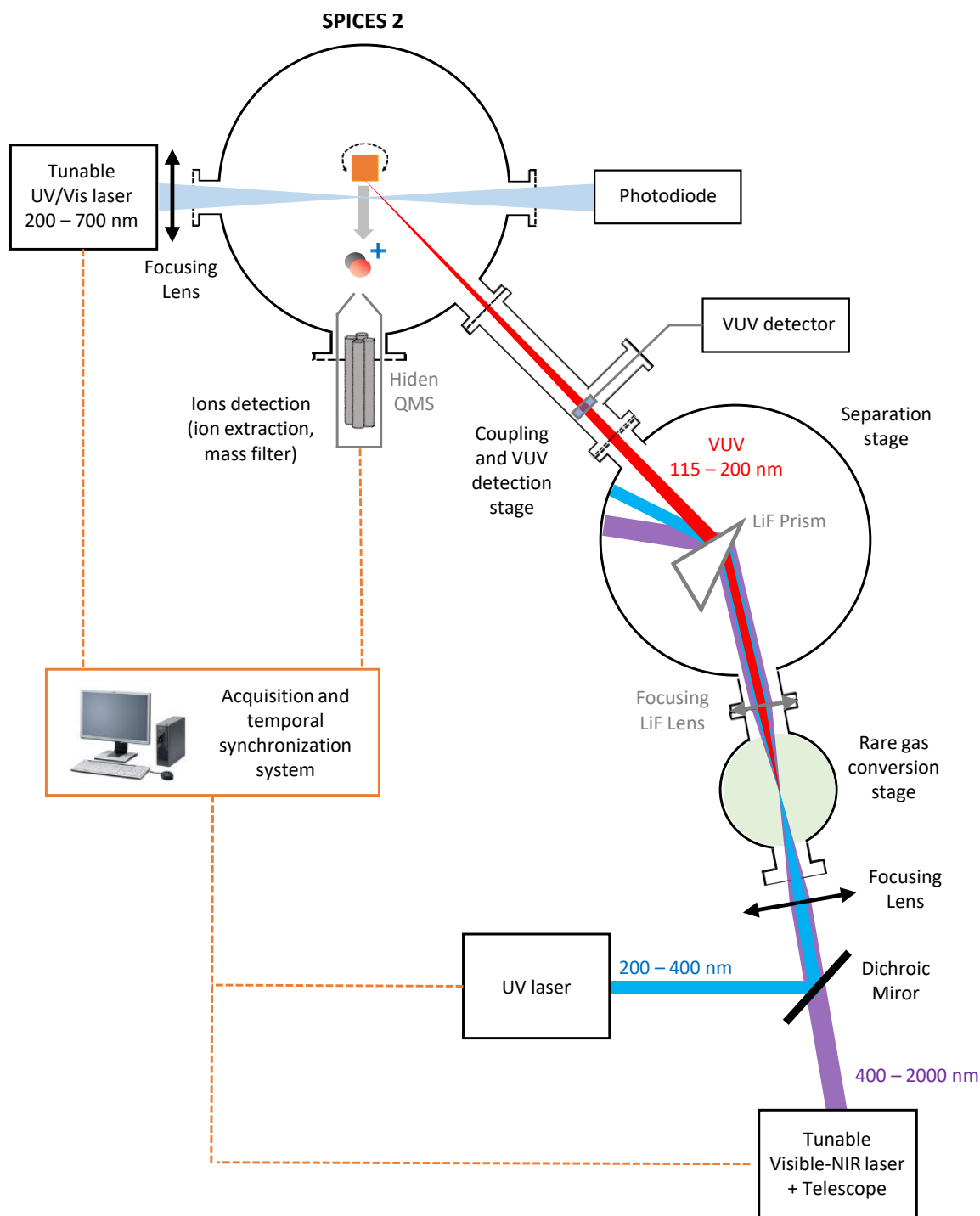


FIGURE II.13 – Laboratory configuration of the SPICES set-up coupled to a VUV photon source that was implemented at the LERMA lab during this thesis for the study of VUV photodesorption from molecular ices. A detailed description of this set-up is given in the text. The wavelengths displayed are the possible wavelengths provided by the lasers, which are pulsed at 10 Hz. Actual wavelengths used during the experiments are detailed in the text. The possible VUV wavelengths provided by the conversion frequency occurring in the rare gas cell are also discussed in the text.

### II.3.1 VUV generation

The technique I implemented during the thesis to generate light in the VUV range is known since the 80's (Hilbig and Wallenstein, 1982, 1983; Marangos et al., 1990; Faris et al., 2000). It is based on a resonant four-wave frequency mixing in noble gas, which is the result of a third order non-linear optical effect ( $\chi^{(3)}$ ) in such medium. A UV beam and a visible (or near infrared) beam of frequency  $\omega_{UV}$  and  $\omega_{Vis/IR}$  respectively are focused by a spherical lens into a chamber containing gas phase Xenon (Xe). The UV beam is provided at the output of a Dye laser pumped by Nd :YAG Quantel laser, and after frequency doubling and mixing. For the visible (or near infrared) beam, an Optical Parametric Oscillator (OPO; EKSPLA) pumped by a YAG laser was used. The beams are pulsed at 10 Hz, with a  $\sim 10$  ns pulse duration. After correction of the achromaticity of the focusing lens (difference in the focal length at  $\omega_{UV}$  and  $\omega_{Vis/IR}$ ) by a telescope (combination of convergent and divergent lenses) and after a good spatial and temporal recovering of the two beams, the non-linear coupling between the input fields result in a frequency conversion associated with two schemes :

— Sum frequency mixing :  $\omega_{sum}^{VUV} = 2 \times \omega_{UV} + \omega_{Vis/IR}$

— Difference frequency mixing :  $\omega_{diff}^{VUV} = 2 \times \omega_{UV} - \omega_{Vis/IR}$

where both  $\omega_{sum}^{VUV}$  and  $\omega_{diff}^{VUV}$  are generated by the non-linear effect. The effect is called resonant because the frequency  $\omega_{UV}$  is set onto a two-photon transition of Xe. The tuning of  $\omega_{Vis/IR}$  enables to indirectly tune the frequency of the VUV light output. For this thesis, the UV wavelength was set to 249.6 nm, which corresponds to the two-photon transition  $5p^6 \rightarrow 5p^5 6p$  ( $^2P_{3/2}$ ) of Xe. The visible wavelengths used were between 400 and 650 nm, which results in  $\lambda_{sum}^{VUV} \in [96; 105]$  nm and  $\lambda_{diff}^{VUV} \in [154; 177]$  nm. The optics used to guide the VUV beam through the SPICES set-up are composed of LiF, whose transmission cuts-off below 115 nm (above  $\sim 10.8$  eV). Consequently, wavelengths corresponding to  $\lambda_{sum}^{VUV}$  are not transmitted through the experiment and only wavelengths corresponding to  $\lambda_{diff}^{VUV}$  remain. The energy range of  $\lambda_{diff}^{VUV}$  covers the whole A - X ( $\nu' \geq 0$ ,  $\nu'' = 0$ ) band transition of  $^{13}\text{CO}$  in condensed phase, which is the transition studied in this thesis. In Figure II.14 is displayed the VUV energy and wavelength range that could theoretically be covered by this technique, depending on (i) the rare gas and its electronic transition chosen, (ii) the wavelength of the OPO,  $\lambda_{Vis/IR}$  (signal or idler)<sup>3</sup> and (iii) the optics used to guide the VUV beam. The major limitation of the energy range is currently due to the cut-off of the LiF optics (see the gray zone in Figure II.14),

3. an OPO converts a pumping frequency  $\omega_p$  into two lower frequencies  $\omega_i$  and  $\omega_s$  such that  $\omega_p = \omega_i + \omega_s$ . The output corresponding to the higher frequency  $\omega_s$  is called the "signal" and the other one,  $\omega_i$ , is called the "idler". In our case,  $\lambda_p = 355$  nm.

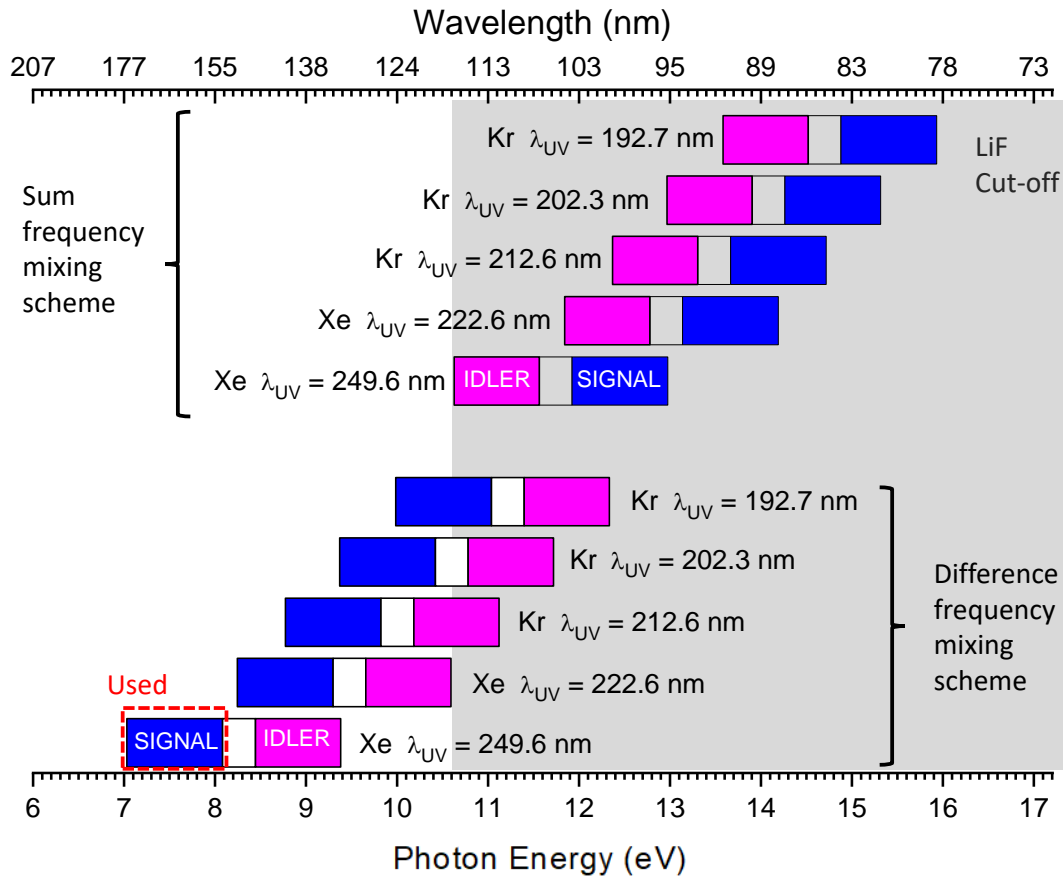


FIGURE II.14 – VUV wavelength and energy range (blue and pink zone) theoretically covered by sum and difference frequency mixing in rare gas. The rare gas and their corresponding electronic transition, associated with the wavelength  $\lambda_{UV}$ , are indicated. The tuning of  $\lambda_{VIS/IR}$  in the signal or idler range enables to tune the VUV frequency. The gray zone corresponds to the wavelength that are not transmitted through the experiment due to the LiF optics currently used.

which can be solved by using optics similar to the ones generally used in VUV synchrotron beamlines (Howells, 1980; Nahon et al., 2012). Another possible improvement of the set-up would be to replace the rare gas cell by a pulsed jet and to pump the whole experiment in UHV.

In order to detect the VUV beam, a home-made detector is implemented on a translational stage mounted into the coupling tube (see Figure II.13). It consists of two plates: one made of copper or gold and another one which is holed and put to high voltage (500 - 800 V). As VUV photons hit the copper or gold plate, electrons are stripped from the material (photoelectric effect) and collected by the other plate. The resulting current enters a RC circuit and the voltage of the capacitor, after amplification with a 50 dB gain, is measured by an oscilloscope. The VUV photon flux (per pulse) can be derived from the peak voltage by taking into account the amplification factor and the photo-

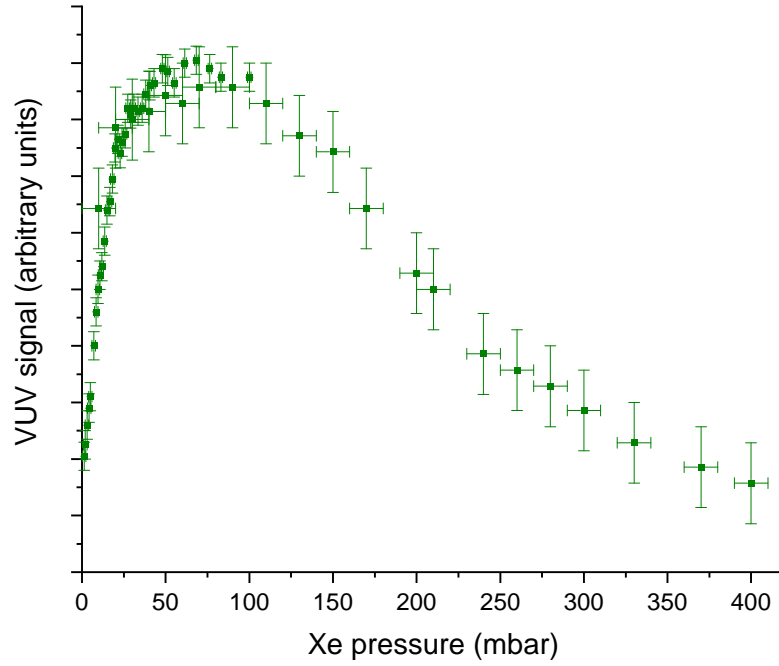


FIGURE II.15 – VUV signal ( $\lambda_{VUV} \sim 157$  nm) measured as a function of the Xe pressure.

emission quantum yield of the material used (copper or gold). The power of the VUV output is given by (see also [Marangos et al. \(1990\)](#)) :

$$P_{VUV} = P_{Vis} P_{UV}^2 (\chi^{(3)})^2 N^2 F$$

$$F \propto \exp(-\alpha b_{UV} \Delta k)$$

$$\Delta k = k_{VUV} - (2k_{UV} - k_{Vis})$$

where  $N$  is the number density of Xe atoms,  $\alpha$  is a constant of the order of unity,  $b_{UV}$  is the confocal parameter<sup>4</sup> of the UV beam and  $\Delta k$  is the wave-vector mismatch. By defining a phase-mismatch per atom  $C = \Delta k/N$ , then  $P_{VUV} \propto N^2 \exp(-b_{UV} C N)$ . Maximizing  $P_{VUV}$  is then possible by achieving the optimal  $N$  corresponding to the optimal Xe pressure, for a given  $b_{UV}$ . An example of such optimization is displayed in Figure II.15 where  $P_{VUV}$  (peak voltage read on the oscilloscope) is plotted against the Xe pressure and for which the optimum is reached around 100 mbar. The curve shape is consistent with the previous equation but might deviate from it at high pressure due to self-absorption (multi-photon ionization in that case because the ionization threshold of Xe is 12.13 eV) or due to the decay of the excited state of Xe by collisional processes that prevents the frequency conversion. Examples of such curves are also available in the references cited above ([Hilbig and Wallenstein, 1982, 1983](#); [Marangos et al., 1990](#); [Faris et al., 2000](#)). The usual experimental conditions are such that  $E_{UV} = 0.5 - 1$  mJ per pulse,  $E_{Vis} = 10 - 50$  mJ per pulse, for pulses of  $\sim 10$  ns duration. The

4.  $b = 2z_R$  where  $z_R$  is the Rayleigh range

confocal parameter is especially fixed by the focal length of the focusing lens which is 100 mm. The resulting VUV photon flux is estimated to be between  $\sim 10^5$  and  $10^7$  photons per pulse depending on the experimental conditions. The spectral width of this VUV photon source is equal to that of the Vis/IR source, which is  $< 5 \text{ cm}^{-1}$ .

### II.3.2 Detection technique : TOF + REMPI

The VUV photon source implemented is used to trigger photodesorption from previously grown ices in the SPICES set-up. The detection of photodesorbed neutral molecules using this VUV photon source relies on a QMS optimized for ion detection associated with a Resonance-Enhanced Multi-Photon Ionization (REMPI) technique, which is sketched in Figure II.16. The VUV pulse induces desorption of neutral molecules that are further photo-ionized by a UV/Vis pulse. This latter UV/Vis pulse is generated by an OPO laser pumped by a Nd :Yag, with output energy of  $\sim 0.5 - 5 \text{ mJ}$  per pulse in the  $\sim 200 - 450 \text{ nm}$  range and  $6 - 30 \text{ mJ}$  per pulse in the  $450 - 700 \text{ nm}$  range. The delay between the VUV and the UV/Vis pulse is associated with the time-of-flight of the neutral photodesorbed species from their desorption to the ionization region. In the following, this will be referred to as the TOF<sup>5</sup> of the photodesorbed molecules. The wavelength of the UV/Vis pulse  $\lambda_{ion}$  is set to a multi-photon transition of

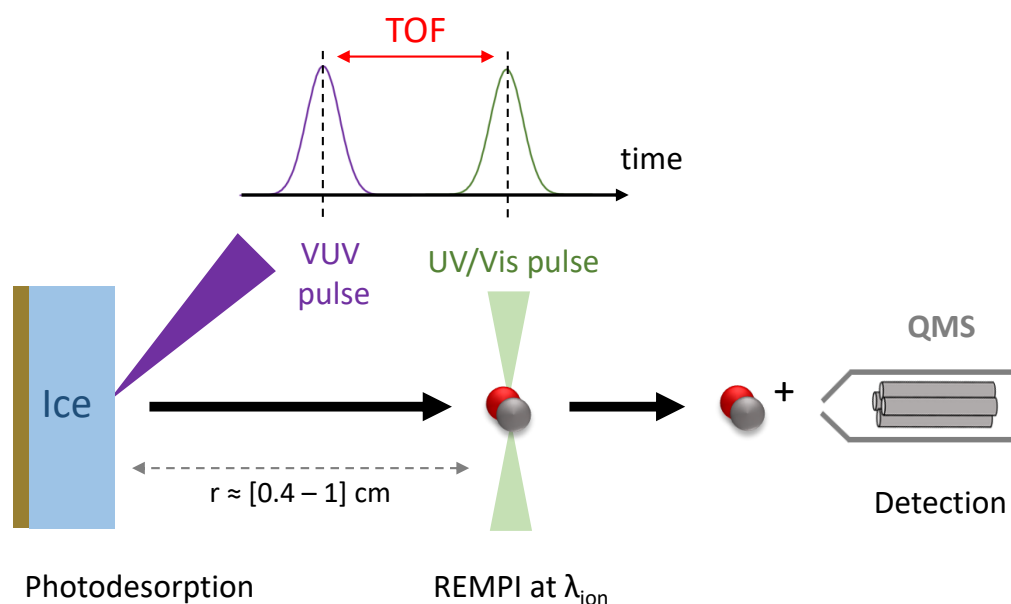


FIGURE II.16 – Scheme of the TOF + REMPI detection technique associated with the pulsed VUV photon source implemented at the LERMA lab. Details are provided in the text.

5. the TOF is generally referred to as the time for a molecule to go through a detector after ionization. Here this is different : we refer to the TOF as the time interval between the photodesorption and the ionization of a neutral molecule, as sketched in Figure II.16.

the molecule considered. The scheme of such transition is referred to as a REMPI( $n + m$ ) where  $n$  is the number of photons used to transition to an excited electronic state of the molecule and  $m$  is the number of photons used to ionize the molecule from the excited electronic state (see section II.3.5). After ionization, the ions are collected at the QMS entrance, go through a mass filter (quadrupole) and generate a current signal in the SEM (same principle as in Figure II.6, after the ionization stage). This detection technique enables to probe the internal and kinetic energy state of the photodesorbed molecule by varying  $\lambda_{ion}$  and the TOF, the latter being, once again, the delay between the desorbing VUV pulse and the probing REMPI-UV/Vis pulse.

### II.3.3 TOF, velocity and kinetic energy distributions

TOF spectra  $S(t)$  are obtained by recording the ion signal as a function of the TOF  $t$  at a fixed  $\lambda_{ion}$ . As explained in Zimmermann and Ho (1995),  $S(t)$  is proportional to the number density of the neutral molecules  $\rho(r, t)$  in the ionization region, where  $r$  is the distance between the ice surface and the ionization region, which is known and fixed.  $\rho(r, t)$  is a distribution in space, not in time, as we are probing the molecules density in the ionization region as a function of flight time such as fast molecules will be less efficiently detected than slow molecules because they spend less time in the ionization region. To obtain the distribution in time (TOF distribution  $I(t)$ ), one must consider the flux of molecules passing through the ionization region per unit time (flux versus time). This results in computing  $I(t) = v \rho(t) \propto S(t)/t$  where  $v$  is the molecule velocity such as  $v = r/t$ . The velocity distribution  $P_v(v)$  can be converted from the time distribution via  $I(t) dt = P_v(v) dv$ . Similarly, the translational energy distribution  $P_{E_t}(E_t)$  is obtained by  $I(t) dt = P_{E_t}(E_t) dE_t$  where  $E_t$  is the molecule translational energy such as  $E_t = (1/2)mv^2$ . Using the Jacobian  $|dv/dt| = r/t^2$ , this results in :

$$P_v(v) \propto \frac{1}{v} S(t)$$

$$P_{E_t}(E_t) \propto \frac{1}{E_t} S(t)$$

A mean translational energy  $\langle E_t \rangle$  is often deduced from the translational energy distribution by  $\langle E_t \rangle = \int E_t P_{E_t} dE_t$ .

Trying to fit the actual translational energy distribution of photodesorbing molecules with a Maxwell-Boltzmann (MB) distribution is not necessarily relevant because the desorbing molecules are not expected to be in thermal equilibrium. However, the derivation of  $\langle E_t \rangle$  enables to compute the temperature  $T_{trans}$  associated with a "Flux-

weighted<sup>6</sup> MB distribution  $P_{MB}(E_t)$  with :

$$\langle E_t \rangle = 2k_B T_{trans}$$

$$P_{MB}(E_t) \propto E_t \exp\left(-\frac{E_t}{k_B T_{trans}}\right) \propto \frac{1}{t^2} \exp\left(-\frac{E_t}{k_B T_{trans}}\right)$$

Deriving  $T_{trans}$  is useful to discuss the photodesorption mechanisms and to compare the data between experimental studies. During this thesis, TOF, velocity and translational energy distributions were derived for CO photodesorbing from a pure CO ice at 15 K near  $\lambda_{UV} = 157$  nm. These distributions can depend on  $\lambda_{ion}$ , namely : the kinetic energy of photodesorbed molecules can depend on their internal energy state, the latter being probed by varying  $\lambda_{ion}$ . This is discussed in the next sections.

### II.3.4 Internal energy of diatomic molecules

The REMPI technique used in this thesis requires some basic knowledge on the modeling of the internal energy levels of diatomic molecules (in the case of free molecules) and on their interaction with photons. In the following, I will give general results from molecular physics relevant to the present study with the aim of illustrating the experimental approach retained. For more details on molecular physics theory, see for example [Demtröder \(2002\)](#). Electronic states of diatomic molecules are labeled by a letter X for the fundamental state and A, B, C ... for the excited states, followed by  $(2S+1)\Lambda$  where S is the total spin and  $\Lambda$  is the quantum number associated with the projection of the electronic angular momentum on the inter-nuclear axis<sup>7</sup> (labeled  $\Sigma$  if  $\Lambda = 0$ ,  $\Pi$  if  $\Lambda = 1$ ,  $\Delta$  if  $\Lambda = 2$ , etc.). For a  $\Sigma$  state, the symmetry of the state is labeled "+" or "-" depending on the symmetry of the electronic wave function with respect to a plane containing the inter-nuclear axis, which corresponds to different parity of the total molecular wavefunction. The energy levels of a free diatomic molecule are derived by finding the eigenvalues of its hamiltonian. In the Born-Oppenheimer approximation<sup>8</sup>, the motion of the electrons and the nuclei are decoupled such that the total wave function can be written as the product of the electronic wave function with the molecular wave function, associated with the vibration and rotation motions of the nuclei in the potential of the electronic state. The total energy of the diatomic molecule is given by :

$$E_e(v, J) = T_e + G(v) + F(J) \quad (\text{II.11})$$

6. we measure a desorbing flux, not a volume of gas phase molecules

7. for an electronic state  $\Phi_e$ ,  $L_z \Phi_e = \pm \Lambda \hbar \Phi_e$  with (Oz) the inter-nuclear axis

8. the physical meaning of this approximation is that the vibration of the nuclei does not change the electronic state. It is no longer valid when the vibration of the nuclei can induce a coupling between two electronic states such as the electronic state changes with the vibration of the molecule.

where  $\nu$  and  $J$  are respectively the vibrational and rotational quantum numbers.  $T_e$  is equal to the minimum value of the potential at  $R = R_e$  where  $R$  is the inter-nuclear distance.  $G(\nu)$  corresponds to the energy of an anharmonic oscillator :

$$G(\nu) = \omega_e (\nu + 1/2) - \omega_e x_e (\nu + 1/2)^2 + \omega_e y_e (\nu + 1/2)^3 \quad , \omega_e \gg \omega_e x_e \gg \omega_e y_e$$

where  $\omega_e = \hbar\omega_0$  is the constant associated with the pulsation  $\omega_0$  of the harmonic oscillator and  $x_e$  and  $y_e$  are molecular constants associated with the anharmonic corrections.  $F(J)$  is equal to :

$$F(J) = B_\nu J(J+1) - D_\nu J^2(J+1)^2 + \dots$$

where  $B_\nu$  is the rotational constant and  $D_\nu$  is the centrifugal distortion constant for the vibrational state defined by  $\nu$ . Their dependence with  $\nu$  can be described as followed :

$$\begin{aligned} B_\nu &= B_e - \alpha_e(\nu + 1/2) \quad , B_e \gg \alpha_e \\ D_\nu &= D_e + \beta_e(\nu + 1/2) \quad , D_e \gg \beta_e \end{aligned}$$

where  $B_e = \hbar^2/2\mu R_e^2$  is the constant of a rigid rotor,  $D_e = \hbar^4/2\omega_0^2\mu^3 R_e^6$  is the centrifugal distortion constant and  $\mu$  is the reduced mass. The different molecular constants are tabulated for most of the diatomic molecules.

### II.3.5 REMPI spectra

The REMPI ( $n + m$ ) technique is based on a multi-photon transition :  $n$  photons induce an electronic transition while  $m$  photons induce the ionization of the molecule from its electronic excited state. Examples of such transitions are given in Figure II.17 for the REMPI (2+1)  $B^1\Sigma^+ (\nu' = 0, J') \leftarrow X^1\Sigma^+ (\nu'' = 0, J'')$  and the REMPI (2+1)  $B^1\Sigma^+ (\nu' = 1, J') \leftarrow X^1\Sigma^+ (\nu'' = 1, J'')$  transitions with the associated wavelengths. Note that the transition cited corresponds to the electronic transition induced by the  $n$  photons. The transition is called a rovibronic transition in the sense that the rotational and vibrational quantum numbers  $J$  and  $\nu$  can change between the initial and final electronic states  $e_i$  and  $e_f$ .  $J'$  and  $\nu'$  denote the upper state quantum numbers while  $J''$  and  $\nu''$  denote that of the lower state. The transition energy can be directly deduced from equation II.11 by  $\Delta E = E_{e_f}(\nu', J') - E_{e_i}(\nu'', J'')$  if the molecular constants of the upper and lower electronic states are known. This energy should be divided by  $n$  for a  $n$ -photon transition to obtain the photon energy associated with  $\lambda_{ion}$ . Experimentally,  $\lambda_{ion}$  can be tuned by the OPO laser to a given rovibronic transition. The QMS signal intensity associated with a  $n$ -photon rovibronic transition  $I_{if}^{(n)}$  is proportional to the transition probability  $P_{i \rightarrow f}^{(n)}$  and the population of molecules  $N(e_i, \nu'', J'')$  in the initial

rovibronic state ( $e_i, v'', J''$ ):

$$I_{if}^{(n)} \propto N(e_i, v'', J'') P_{i \rightarrow f}^{(n)} \quad (\text{II.12})$$

These intensities can be obtained experimentally by using the set-up described previously. In this thesis, I will focus on the REMPI of CO in the initial state corresponding to its fundamental state  $X^1\Sigma^+$  and the REMPI transitions will be such that  $n = 2$ . General expressions of  $P_{i \rightarrow f}^{(1)}$  and  $P_{i \rightarrow f}^{(2)}$  are detailed in several references such as [Bonin and McIlrath \(1984\)](#) and [Demtröder \(2002\)](#). In the framework of the Born-Oppenheimer approximation, in  $P_{i \rightarrow f}^{(n)}$ , the wavefunctions of the initial and final state of the tran-

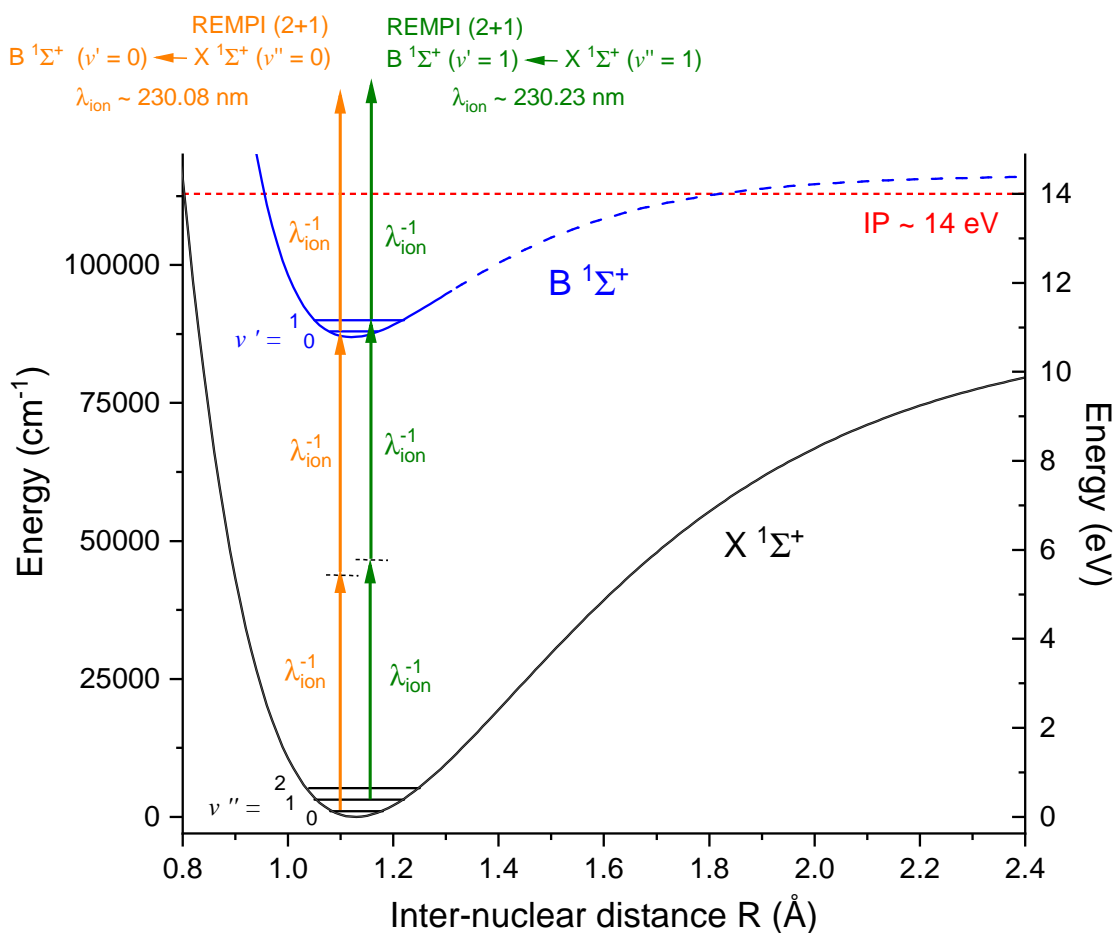


FIGURE II.17 – Morse potential curves of the  $X^1\Sigma^+$  (in black line) and  $B^1\Sigma^+$  (in blue line) electronic states of  $^{13}\text{CO}$  with molecular constants taken from [Guelachvili et al. \(1983\)](#) and [Eidelsberg et al. \(1987\)](#). In red dashed horizontal line is the ionization potential (IP) of  $^{13}\text{CO}$  which is near 14 eV. The REMPI (2+1) transitions are showed in orange and green for the  $B^1\Sigma^+ (v' = 0) \leftarrow X^1\Sigma^+ (v'' = 0)$  and  $B^1\Sigma^+ (v' = 1) \leftarrow X^1\Sigma^+ (v'' = 1)$  transitions respectively. The wavelengths  $\lambda_{ion}$  corresponding to these transitions are also given approximately.

sition can be separated as a product of an electronic, vibrational, rotational and spin wavefunctions. This results in the derivation of dipole electric selection rules such that  $P_{i \rightarrow f}^{(n)} \neq 0$  (in practice, forbidden transitions can still be observed but they are significantly weaker than allowed ones), which are summed up in the following :

- conservation of the spin :  $\Delta S = 0$
- $\Delta \Lambda = 0, \pm 1, \dots \pm n$
- $\Delta J = 0, \pm 1, \dots \pm n$  for  $\Delta \Lambda > 0$   
 $\Delta J = \pm 1, \pm 3, \dots \pm n$ ,  $n = \text{odd number}$ , for  $\Delta \Lambda = 0$   
 $\Delta J = 0, \pm 2, \dots \pm n$ ,  $n = \text{even number}$ , for  $\Delta \Lambda = 0$
- for  $n = 1$ ,  $\Sigma^+ \rightarrow \Sigma^+$  (and  $\Sigma^- \rightarrow \Sigma^-$ ) are forbidden transitions and  $\Sigma^+ \leftrightarrow \Sigma^-$  are allowed transitions

Transitions  $J' \leftrightarrow J''$  between the rotational levels  $J''$  of a given vibrational state  $v''$  in the initial electronic state and the rotational levels  $J'$  of a given vibrational state  $v'$  in the final electronic state form a "band". Within this band, transitions such as  $\Delta J = J' - J'' = -2, -1, 0, +1, +2$  are respectively called the O, P, Q, R and S-branch of the band. The total system of all vibrational bands of a given electronic transition is called a "band system". Knowing the relative intensity  $I_{if}^{(n)}$  in any given band enables to derive the rotational population distribution of the molecule in its initial electronic state by inverting equation II.12 (to find  $N$ ). Similarly, knowing the relative intensity  $I_{if}^{(n)}$  of the bands in a given band system enables to derive the initial vibrational population distribution. Note however that, in order to derive the exact population distributions, one has to remember that the transition probabilities depend on the Franck-Condon (FC) and Hönl-London (HL) factors :

$$P_{i \rightarrow f}^{(n)} \propto FC(v', v'') HL(J', J'')$$

such that the intensities of the transitions should be corrected from these factors in order to obtain the vibrational and rotational population distributions  $N(v'')$  and  $N(J'')$  :

$$N(v'') \propto \frac{I_{if}^{(n)}(v', v'')}{FC(v', v'')} \quad , \quad N(J'') \propto \frac{I_{if}^{(n)}(J', J'')}{HL(J', J'')}$$

Similarly to the case of the translational energy distribution, even if we do not necessarily expect the vibrational and rotational populations of photodesorbing molecules to follow a MB distribution, deriving from experimental data a vibrational and a rotational temperature ( $T_{vib}$  and  $T_{rot}$  respectively) associated with these MB distributions could be useful to discuss the photodesorption mechanisms and to compare the data between experimental studies. Experimentally, the Q branch of the band used to esti-

mate the rotational population is the most intense but we do not resolve the transitions associated with low  $J''$  numbers (for  $J'' < 7$ ) in this branch. Consequently, in order to estimate the rotational population, we chose to compare our experimental REMPI spectra to simulated ones from the PGOPHER software (Western, 2017). This software enables to simulate, from the molecular constants of the initial and final electronic states, the intensity  $I_{if}^{(n)}$  associated with a  $n$ -photon transition and for a rotational temperature  $T_{rot}$  associated with a rotational population following a MB distribution. Matching our experimental REMPI spectra with the simulated ones enables to derive a temperature  $T_{rot}$  that serves as an estimation of the "cold" or "hot" nature of the rotational population of photodesorbed CO molecules. Note that the Hönl-London factors are included in the simulated spectrum.

In order to illustrate the previous methodology, a REMPI spectrum of gas phase  $^{13}\text{CO}$  is obtained by injecting a partial pressure of  $^{13}\text{CO}$  ( $P \sim 10^{-8}$  Torr) in the SPICES set-up and by setting  $\lambda_{ion}$  to the B - X ( $v' = 0, v'' = 0$ ) band near 230.08 nm. Tuning  $\lambda_{ion}$  in

REMPI (2+1) B ( $v' = 0$ )  $\leftarrow$  X ( $v'' = 0$ ) band

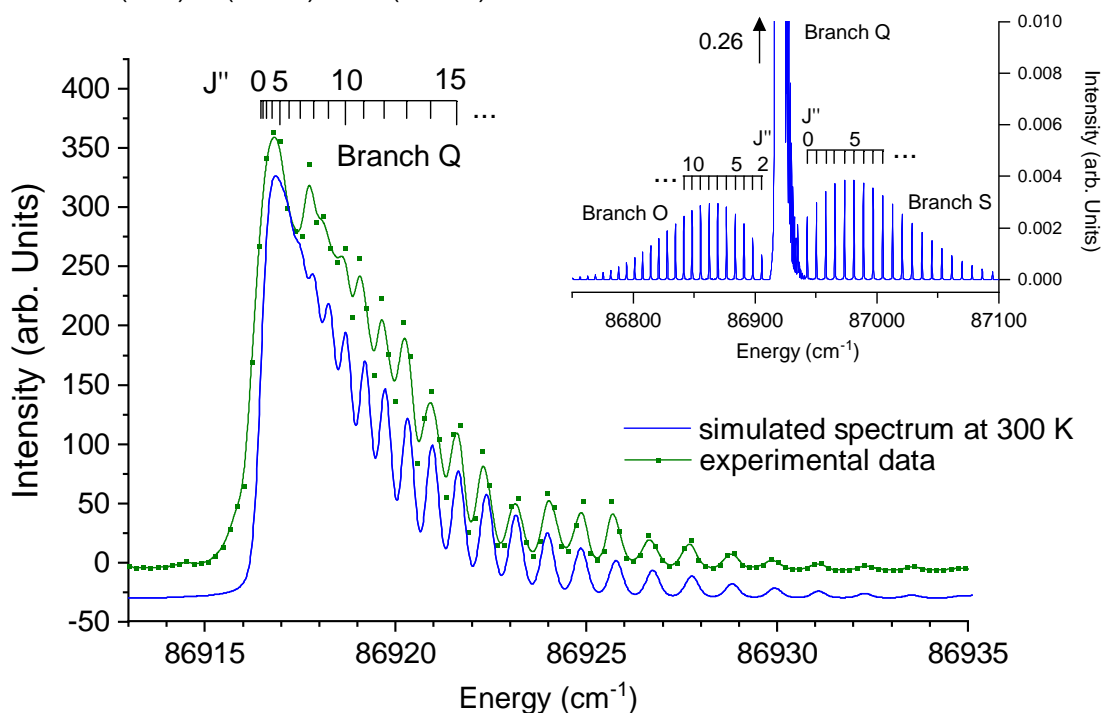


FIGURE II.18 – REMPI (2+1) B - X ( $v' = 0, v'' = 0$ ) band spectrum of gas phase  $^{13}\text{CO}$  from experimental data (green line and dots) using the SPICES set-up (with  $P \sim 10^{-8}$  Torr) and from PGOPHER (blue lines) with a rotational temperature of 300 K. The inset shows the O and S branches. The lowest graph shows a zoom on the Q branch. The features of each branch are associated with the quantum number  $J''$  of the initial electronic state. The experimental data (green dots) are interpolated using a B-spline method to obtain the green line. More details are given in the text.

this band results in the ionization of  $^{13}\text{CO}$  molecules from the  $X^1\Sigma^+ (v'' = 0, J'')$  states for different  $J''$  and therefore it gives access to the rotational population distribution of gas phase  $^{13}\text{CO}$  (at ambient temperature). The QMS signal intensity as a function of  $\lambda_{ion}$  is displayed in Figure II.18 in green line and dots. For this REMPI (2+1)  $B^1\Sigma^+ (v' = 0, J') \leftarrow X^1\Sigma^+ (v'' = 0, J'')$  transition, and according to the previous selection rules, the allowed transitions are the ones such that  $\Delta J = 0, \pm 2$ . Therefore, only the O, Q and S branches are observed. For linear polarization, the Q branch is largely dominating the spectrum. The experimental data can be compared to a spectrum obtained from the PGOPHER software. The resulting simulated REMPI spectrum is displayed in blue lines in Figure II.18. A broadening of  $0.35 \text{ cm}^{-1}$  was taken into account to include the intrinsic (or natural) width of the transition, the Doppler broadening effect and the spectral width of the photon source. A good agreement between the experimental data and the simulated spectrum is reached for a simulated MB rotational temperature  $T_{rot}$  of 300 K, which is consistent with gas phase molecules being at thermal equilibrium at ambient temperature within the SPICES set-up.



# Chapter III

## Ices and their interaction with photons and electrons

In this chapter, we aim at characterizing the physical properties of molecular ices and their interaction with photons and electrons in the first section. In the second section, these interactions will be discussed regarding photodesorption (and Electron-Stimulated Desorption; ESD) for which the main mechanisms known and most studied in the literature will be highlighted by the case of "simple" molecular ices such as H<sub>2</sub>O, CO and N<sub>2</sub>-containing ices. Previous experimental studies, including that conducted at the LERMA lab before this thesis, will enable to illustrate these mechanisms in the VUV and X-ray range.

### III.1 Molecular ices

#### III.1.1 Physical properties

The systems experimentally studied in this thesis are referred to as molecular ices. This describes molecules mainly containing H, C, N and O atoms, in condensed phase, at low temperature ( $T < 100$  K). The molecular volumic density of these solids is of the order of  $1 \text{ g/cm}^3$ , with a surface density between  $5 \times 10^{14}$  and  $1 \times 10^{15}$  molecules/cm<sup>2</sup>. This corresponds roughly to a monolayer (ML) thickness of 3 to 4.5 Å. The ices studied in this thesis are typically between 50 and 100 ML, corresponding to a total thickness between 15 and 40 nm.

Inter-molecular interactions for weakly bound species in molecular ices, such as CO, N<sub>2</sub> and/or O<sub>2</sub>, in pure or mixed ices, are governed by Van der Waals forces. These ices are often referred to as Van der Waals solids. In such ices, the binding energies are of the order of 100-200 meV. In contrast, molecules such as H<sub>2</sub>O or HCOOH tend to form hydrogen bonds in the solid phase hence the corresponding binding energies are hi-

TABLE III.1 – Properties of some molecules of interest in the solid phase

Molecule	Surface density (molecule/cm <sup>2</sup> )	Equivalent ML (Å)	Binding energy (meV)	
			Pure ice	on H <sub>2</sub> O
CO	8.10 <sup>14</sup>	3.6	74 <sup>a</sup>	113 <sup>b</sup>
N <sub>2</sub>	7.10 <sup>14</sup>	3.7	68 <sup>a</sup>	100 <sup>b</sup>
CO <sub>2</sub>	8.10 <sup>14</sup>	3.5	232 <sup>c</sup>	195 <sup>d</sup>
H <sub>2</sub> O	1.10 <sup>15</sup>	3.2	500 <sup>e</sup>	
CH <sub>3</sub> OH	5.10 <sup>14</sup>	4.4	430 <sup>f</sup>	529 <sup>g</sup>
CH <sub>3</sub> CN	5.10 <sup>14</sup>	4.4	390 <sup>h</sup>	530 <sup>i</sup>
HCOOH	6.10 <sup>14</sup>	3.8	798 <sup>j</sup>	637 <sup>k</sup>
HCOOCH <sub>3</sub>	5.10 <sup>14</sup>	4.7	352 <sup>l</sup>	383 <sup>m</sup>

<sup>a</sup> From [Öberg, K. I. et al. \(2005\)](#)    <sup>b</sup> Average value from the energy distribution given in [Nguyen et al. \(2018\)](#), on compact amorphous (c-ASW) water ice

<sup>c</sup> From [Sandford and Allamandola \(1990\)](#)    <sup>d</sup> From [Noble et al. \(2012\)](#)

<sup>e</sup> From [Fraser et al. \(2001\)](#)    <sup>f</sup> From [Doronin et al. \(2015\)](#)

<sup>g</sup> From [Winkler et al. \(2002\)](#), on polycrystalline water ice    <sup>h</sup> From [Bertin et al. \(2017\)](#)

<sup>i</sup> From [Bertin et al. \(2017\)](#), on compact amorphous (c-ASW) water ice    <sup>j</sup> From [Jedlovszky et al. \(2008\)](#)    <sup>k</sup> From [Jedlovszky et al. \(2008\)](#), on polycrystalline water ice    <sup>l</sup> From [Schwaner et al. \(1997\)](#)    <sup>m</sup> From [Bertin et al. \(2011\)](#), on compact amorphous (c-ASW) water ice

gher than for Van der Waals solids ( $\gtrsim 500$  meV). Molecular ices are electrical insulators : from a solid-state physics point of view, the band-gap between the valence and the conduction bands is large. The ionization potential of molecules in the solid phase, which can be viewed as the equivalent of the work function in solid-state physics (threshold energy for photo-emission from the solid), is  $\gtrsim 10$  eV for the molecules of interest in this thesis.

The binding energy of molecules in molecular ices is a quantitative estimate of how much energy should be given to a molecule at the ice surface to induce its desorption. It can be seen as the dissociation limit of the adsorption well of the surface-molecule bond. These binding energies are often derived from TPD experiments (see Chapter II.1.2.2) via the Polanyi-Wigner equation or theoretically e.g. by Density Functional Theory (DFT) calculations. Examples of average binding energies for the molecules of interest in this thesis are given in Table III.1. These binding energies depend on the surface considered. That corresponding to a multilayer regime, for which the molecule at the surface is bound to its similar neighbors, are displayed in the column "Pure ice" of Table III.1.

In the astrophysical context discussed in Chapter I, interstellar molecules, including COMs, may be adsorbed on the surface of water ice depending on the region considered. Therefore, several experimental studies have been conducted in order to derive

binding energies corresponding to the case where the considered molecule is adsorbed on a water ice. The results of such studies are displayed in the column "on H<sub>2</sub>O" of Table III.1. Note that the single values displayed for the binding energies in Table III.1 do not give an accurate physical description of the binding energy between a molecule and the ice surface. In practice, the binding energy depends on several parameters such as the orientation of the molecule or the presence of defects and/or pores at the ice surface such that it is more accurately described by an energy distribution. These energies are negligible, by more than one order of magnitude, compared to the energy brought by X-rays or VUV photons and therefore desorption is energetically favorable but will depend on the conversion efficiency of the desorption mechanism at play, i.e. the efficiency with which a specific mechanism achieves to transfer the energy towards the desorption event (see Section III.2).

Whether molecules within molecular ices form a disordered material, referred to as an amorphous solid, or are organized in a crystal-like behavior is not necessarily always known and modification of the molecular "order" is sometimes observed when varying the temperature of the ice or when irradiating it with photons or energetic particles. The most famous and most studied case is water ice (see for example [Speedy et al. \(1996\)](#); [Kimmel et al. \(2001\)](#)). In our experimental context, the deposition technique of water vapor onto a cold substrate influences the phase of water ice. Depositing water at 100 K or ~ 15 K will result in compact amorphous ice (c-ASW) or a porous amorphous ice (p-ASW) respectively while polycrystalline water ice is obtained by condensation at 150 K. The amorphous phase, as opposed to the polycrystalline phase where molecules are regularly arranged in an hexagonal lattice, displays a lack of long-range order.

More importantly for this thesis, the deposition technique (mainly the deposition temperature), and thus the phase of the ice, can have a significant influence on the photodesorption yields : see for example, the decrease of the photodesorption yields of CO from a pure CO ice with increasing deposition temperature ([Muñoz Caro, G. M. et al., 2016](#)) or the desorption of CO from amorphous or crystalline water ice ([Bertin et al., 2012](#)). Some COMs also tend to form clusters, islands or polymers under specific experimental conditions. This is for example the case of HCOOH that tends to form dimers ([Bisschop et al., 2007](#)) or the case of H<sub>2</sub>O:CH<sub>3</sub>CN mixed ices for which a phase segregation can occur at high temperature ([Bhuin et al., 2015](#)). Such exotic ice structures are not necessarily well-constrained and well-controlled under experimental conditions and they may influence the photodesorption yields derived from one experiment to another.

### III.1.2 VUV photo-absorption of molecular ices

Interaction of VUV photons with molecular ices in the 7 - 14 eV range can induce valence electronic transitions. In the following, I will briefly remind some basic notions regarding electronic transition for gas phase molecules (i.e. free molecules) and I will discuss such transitions when molecules are condensed into a molecular ice. Electronic states of diatomic molecules and the associated electronic transitions were already discussed in Chapter II.3.4 and II.3.5. Molecular orbitals and electronic states of polyatomic molecules are labeled according to their symmetry group, with the spin multiplicity ( $2S+1$ ) being the same as for diatomic molecules (examples will be given in the following). We will only consider dipole allowed electronic transitions. In the VUV range, electrons belonging to valence molecular orbitals are excited or ionized, most generally from the Highest Occupied Molecular Orbital (HOMO). The excited electronic state, below the ionization threshold, can be either a valence state or a Rydberg state, although interaction of low-lying Rydberg states with valence states can occur in some cases. The distinction between valence and Rydberg excited states can be qualitatively discussed regarding the spatial extent of the excited electron orbital. Rydberg states are characterized by delocalized and diffuse orbitals, with large spatial extent, such that the excited molecule can be viewed as an ionised core with a weakly bound electron, similarly to Rydberg states for atoms. On the contrary, valence states are such that the excited electron is more localized and tightly bound to the molecule. For increasing energy, Rydberg states form series converging to the ground (or excited) electronic state of the ion. Above the ionization threshold of the molecule, excited states of the neutral molecule can still exist. These states are associated with the promotion of an electron from below the HOMO to an empty orbital, with the transition energy being higher than the ionization threshold of the electron in the HOMO. Such excited states can decay to an ionic state via a process called autoionization.

The question now is what happens to the excited states of a free molecule when it is embedded into a molecular ice and does it make sense to compare these states to the absorption features observed in molecular ice spectroscopy? Regarding the spatial extent of valence and Rydberg orbitals as discussed previously, we would expect valence states to not significantly be modified in weakly bound molecular ices because of their localized character. On the other hand, the large spatial extent of Rydberg orbitals, that could be higher than several inter-molecular distance in the ice, implies that they will overlap with that of the neighboring molecules such that Rydberg states are expected to be heavily modified. Collective excitations can also arise in molecular ices when there is an equivalence by translation of the molecules in the ice. That said, as discussed in (Lu et al., 2005) or Kuo et al. (2007), the attribution of an absorption feature of a molecular ice to an electronic transition of a single molecule, with direct

comparison of an electronic transition associated with the free molecule, is questionable. Additionally, the motion of molecules (e.g. rotation) inside a molecular ice is expected to be "frustrated" in the sense that it is not comparable to the motion of a free molecule (the term "libration" is often used to describe such frustrated motion in the solid phase).

Electronic excitations in molecular ices are often referred to as excitons (this term can also be used to describe collective excitations), which were initially theorized by Frenkel and Wannier for insulating crystals (Frenkel, 1931; Wannier, 1937). Excitons are organized in energy bands and can be described as a bound electron-hole pair, whose excitation energy lies below the ionization threshold. In the Frenkel theory, an electronic excitation in a crystal is not located on a particular atom but is described as a linear combination, that runs over the lattice sites, of localized states of excitation, forming "excitation waves" that emerge due to the interaction of neighboring atoms, similarly to sound waves that describe the heat motion in the crystal. An excitation packet can be constructed by superimposing such excitation waves and describes the traveling of the excitation from one atom to another. The excitation is also coupled to the vibrational states of the crystal (phonons). Wannier excitons are described as a linear combination of excited states that correspond to states where an electron is removed from a lattice site and placed into another site. Wannier excitons are also not stationary and can migrate through the solid. Excitons can therefore be regarded as an electron-hole pair that can propagate in a wave-like manner in the crystal, with Frenkel exciton being more localized and having a smaller radii (distance between the electron and the hole) than Wannier excitons that are more diffuse and whose radii can enclose numerous lattice sites. With such definition, it is tempting to view Frenkel and Wannier excitons as the equivalent of, respectively, excited valence and Rydberg states of the free molecule in the solid state. An extension of the Frenkel and Wannier model to amorphous solids is proposed in Fiermans and Phariseau (1966); Christiaens and Phariseau (1968) where they showed that exciton bands can still be observed when a short-range order is maintained. In that case, the radii of the electron-hole pair is somewhere between that of a Frenkel and a Wannier exciton, and the exciton migration behaves like a damped oscillation.

In order to illustrate the previous notions, the VUV photo-absorption spectra, in the 7 - 12 eV range, of gas phase CO (in red) and of pure CO ice at 8 K (in blue) are displayed in Figure III.1. The ground electronic state of CO is the  $X^1\Sigma^+$  state and its first electronic state is the  $A^1\Pi$  state, which is a valence state. The B, C and E states are Rydberg states. The vibrational structure of the  $A^1\Pi$  state is visible in the spectrum where the relative intensity of the peaks is governed by the Franck-Condon principle (via the  $A^1\Pi - X^1\Sigma^+$  transition). In the pure CO ice spectrum, we can see that the first fea-

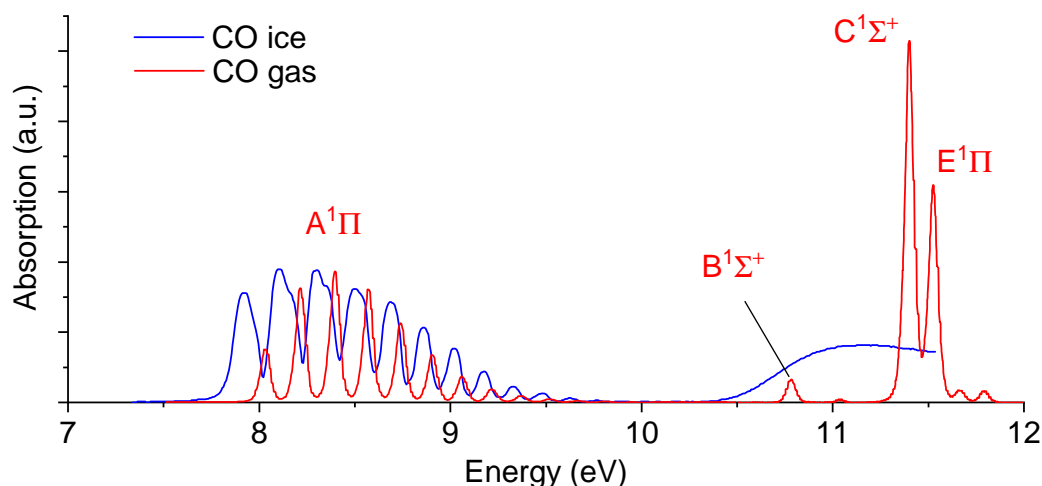


FIGURE III.1 – VUV absorption spectra of gas phase CO (red line, from [Chan et al. \(1993\)](#)) and of pure CO ice at 8 K (blue line, from [Cruz-Diaz et al. \(2014a\)](#)). The two spectra are not displayed in the same Y-scale. Labeling of the electronic states of gas phase CO are also displayed in red.

tures between 7.5 and 10 eV are very similar to the one associated with the gas phase  $A^1\Pi$  state. In that case, the  $A^1\Pi$  state of the gas phase does not seem to be significantly modified in the solid phase except that it is shifted in energy and that the width of the vibronic bands are larger in the solid phase, with a splitting appearing for some bands (this could be explained by the Davydov effect, see [Chen et al. \(2017\)](#)). This is consistent with the excited electronic state of the solid phase being a Frenkel exciton, retaining its molecular character from the valence gas phase state, with the electron-hole pair being localized on the excited CO molecule. However, [Chen et al. \(2017\)](#) also showed, by a temperature dependence study of the VUV absorption spectrum of CO ice, that Wannier excitons might also be present in the A state of solid CO. The Rydberg states B, C and E of the gas phase are not visible in the ice spectrum. Instead, a broad bump centered at 11 eV is observed for pure CO ice and a comparison with gas phase states is not possible. The ionization threshold (of the electron in the HOMO) for gas phase CO is approximately at 14 eV and red-shifted for solid CO, near 12.5 eV. This is a general trend for molecules embedded into an ice : the ion is stabilized by the reorganization of the surrounding molecules via dipole interactions (similarly to the solvation in liquids), inducing a lower ionization threshold in the solid phase.

The example of  $\text{H}_2\text{O}$  also gives a clear view on how electronic states are organized in molecular ices. In Figure III.2 are displayed the absorption spectra of gas phase  $\text{H}_2\text{O}$  (red line) and of pure  $\text{H}_2\text{O}$  ice at 80 K (blue line) in the 6.5 - 15 eV range. The first electronic state of gas phase  $\text{H}_2\text{O}$  is a  $\tilde{A}^1B_1$  state, which is dissociative and corresponds to the promotion of an electron from the  $1b_1$  orbital to the  $4a_1$  orbital. The second state is

the  $\tilde{B}^1A_1$  state which corresponds to the promotion of an electron from the  $3a_1$  orbital to the  $4a_1$  orbital. Higher in energy are Rydberg states and the ionization threshold is near 12.6 eV. The ionization threshold in the solid phase is lower, near 11 eV (similar behavior than for CO). More importantly, the electronic band structure of water ice has been estimated by [Orlando and Kimmel \(1997\)](#) and is displayed in the right side of Figure III.2, with some associated electronic transition. The orbitals of the solid phase are labeled similarly to that of the gas phase because they conserve their gas phase valence character. Just below the vacuum level lies the conduction band of the ice. In the solid state, excitations of an electron from the  $1b_2$ ,  $3a_1$  and  $1b_1$  to the  $4a_1$  orbital are referred to as Frenkel excitons in [Orlando and Kimmel \(1997\)](#). The energies of such transitions are displayed in the right of the Figure III.2 and their position are marked on the graph by a blue star, square and circle. Although the first exciton could be attributed to the broad bump seen near 8.6 eV in the ice absorption spectrum (blue star), there are no similar features observed near the energy of the two other excitons (blue square and blue circle) such that their attribution is difficult and they might overlap with other electronic transitions in the conduction band. Concerning the Rydberg states of gas phase  $H_2O$ , they are not visible in the solid phase, similarly to what is observed for CO.

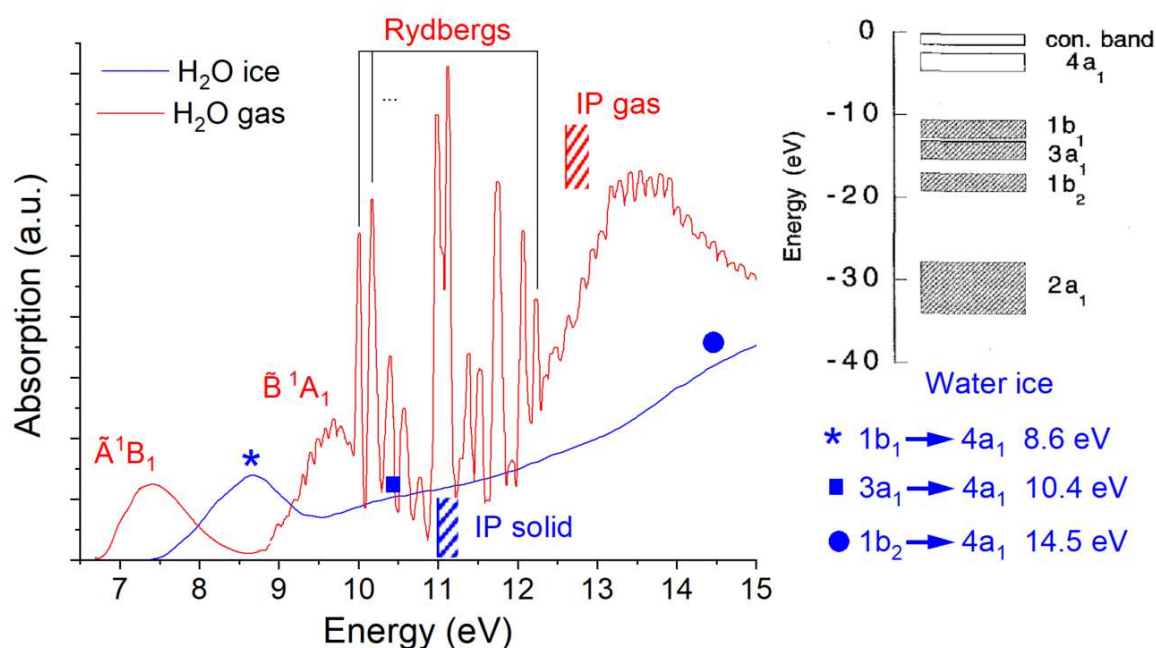


FIGURE III.2 – VUV absorption spectra of gas phase  $H_2O$  (red line, from [Lee and Suto \(1986\)](#)) and of pure  $H_2O$  ice at 80 K (blue line, from [Kobayashi \(1983\)](#)). The two spectra are not displayed in the same Y-scale. Labeling of the electronic states of gas phase  $H_2O$  are also displayed in red. In the right part of the figure is displayed the electronic band structure of water ice taken from [Orlando and Kimmel \(1997\)](#), with some associated electronic transition in the solid phase, marked on the graph.

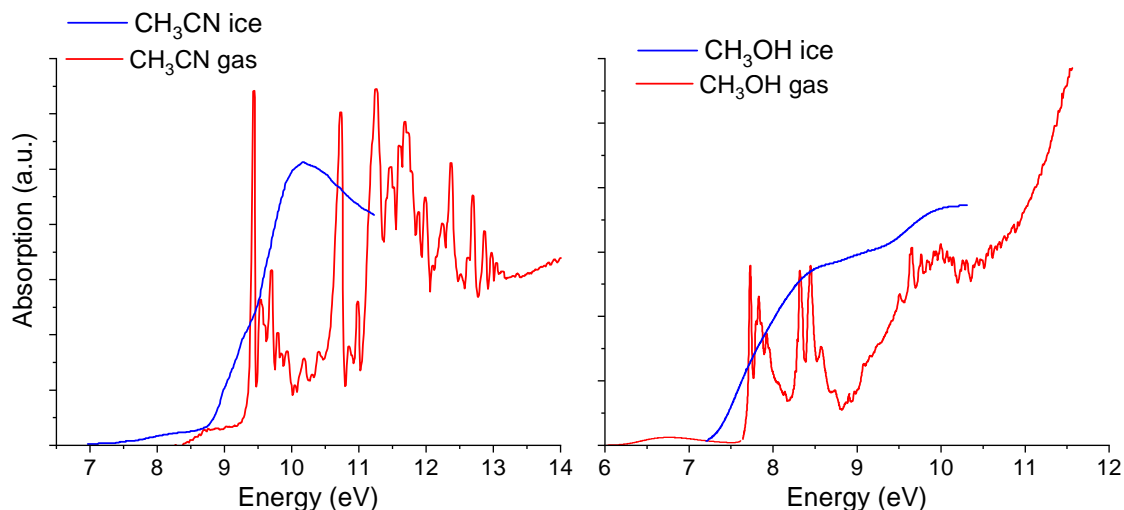


FIGURE III.3 – VUV absorption spectra of gas phase  $\text{CH}_3\text{OH}$  and  $\text{CH}_3\text{CN}$  (red line, from Cheng et al. (2002) and Leach et al. (2008)) and of pure  $\text{CH}_3\text{OH}$  and  $\text{CH}_3\text{CN}$  ices at 80 K (blue line, from Kuo et al. (2007) and Sivaraman et al. (2016)). The gas and ice spectra are not displayed in the same Y-scale.

A last example of VUV absorption spectra for two COMs studied in this thesis,  $\text{CH}_3\text{OH}$  and  $\text{CH}_3\text{CN}$ , is given in Figure III.3. The attribution of the gas phase states are detailed in Kuo et al. (2007) and Sivaraman et al. (2016). The absorption spectra of the ices once again significantly differ from that of the gas phase and no information about the nature of the features observed are given. This illustrates the difficulty of studying the interaction of VUV photons with such molecular ices. A particular issue concerning these interactions, especially relevant for COMs, is to know whether or not the excited states of the solid phase are dissociative and what are the dissociation routes. For such molecular ices, the possible fragments of a photo-dissociated molecule can either be stabilized in the form of radicals in the ice, can recombine to reform the parent molecule or can react with neighboring ones (or with other molecules after diffusion) to form new species. Photolysis experimental studies, for which the formation of products are monitored (generally by infrared spectroscopy) during the VUV irradiation of COMs-containing ices, are often providing a chemical network where the initial dissociation pathways are inferred from the experimental data. These studies are however focusing on the formation of the final photo-products and do not necessarily aim to provide branching ratios associated with specific VUV wavelength. On the other hand, experimental studies where the COM studied is isolated into a rare gas matrix can provide information on the major photo-dissociation routes although the branching ratios might depend on the matrix used : see for example the photo-dissociation of  $\text{HCOOH}$  studied by Raman spectroscopy in solid argon (Olbert-Majkut et al., 2010)

or the photo-dissociation of CH<sub>3</sub>OH studied by laser-induced fluorescence spectroscopy in solid neon and argon (Cheng et al., 2001). More generally, the dissociation pathways of COMs in ices are often assumed to be similar to that of the free molecule from gas phase experiments, but their respective cross sections are probably different.

### III.1.3 X-ray photo-absorption of molecular ices

Interaction of molecular ices with X-rays, especially in the soft X-ray range (0.2 - 5 keV), results in the electronic excitation or ionization of a K shell (1s) core electron bound to an atom of the photo-absorbing molecule. For the molecules of interest in this thesis, the K shell electrons are bound to the C, N or O atoms of the molecules and the energies at which the core transitions are observed are often referred to as the C, N and O K-edge respectively (which are near the 300, 400 and 500 eV range respectively). The basic process of a X-ray absorption is sketched in the top side of Figure III.4 where the excited or ionized electron leaves a core hole in the electronic structure of the photo-absorbing molecule. The lifetime of this core hole state is of the order of the femtosecond ( $10^{-15}$  s) and the decay results in fine in the emission of a valence electron with a probability of  $\sim 99\%$  for low Z elements ( $1 \leq Z \leq 18$ ; Walters and Bhalla (1971); Krause (1979)), the remaining 1% being radiative decay. The detail of the decay is schemed in the top side of Figure III.4 : one valence electron is filling the core hole while another valence electron is promoted to the vacuum. Such decay is called Auger decay and the ionized electron is referred to as the Auger electron. Below the ionization threshold, the decay is called "Participant" Auger decay if the electron filling the core is the initially excited one whereas it is called "Spectator" decay if it is another valence one. In any case, after Auger decay, the molecule is singly or doubly ionized if the initial absorption event is a core excitation or ionization respectively. The resulting ion found itself in an electronically excited state but the majority of the initial photon energy is carried away by the Auger electron<sup>1</sup> in the form of kinetic energy.

The emitted Auger electron thermalizes in the molecular ice by inelastic scattering, exciting and/or ionizing the molecules in its path (see bottom side of Figure III.4). These secondary events generate a cloud of low energy (< 20 eV) secondary electrons that are expected to drive the physical and chemical processes in the ice. Additionally, some of these electrons (both the Auger and the secondary electrons) are escaping the ice surface, generating a drain current in the ice. Experimentally, the escaping electrons can be collected or the drain current can be measured, equivalently resulting in the Total Electron Yield (TEY). If a kinetic energy filter is applied to the escaping electrons, the resulting measurement is referred to as the Partial Electron Yield (PEY) and the signal

---

1. for photon energies above the ionization threshold, the primary ionized electron also plays a similar role than the Auger electron

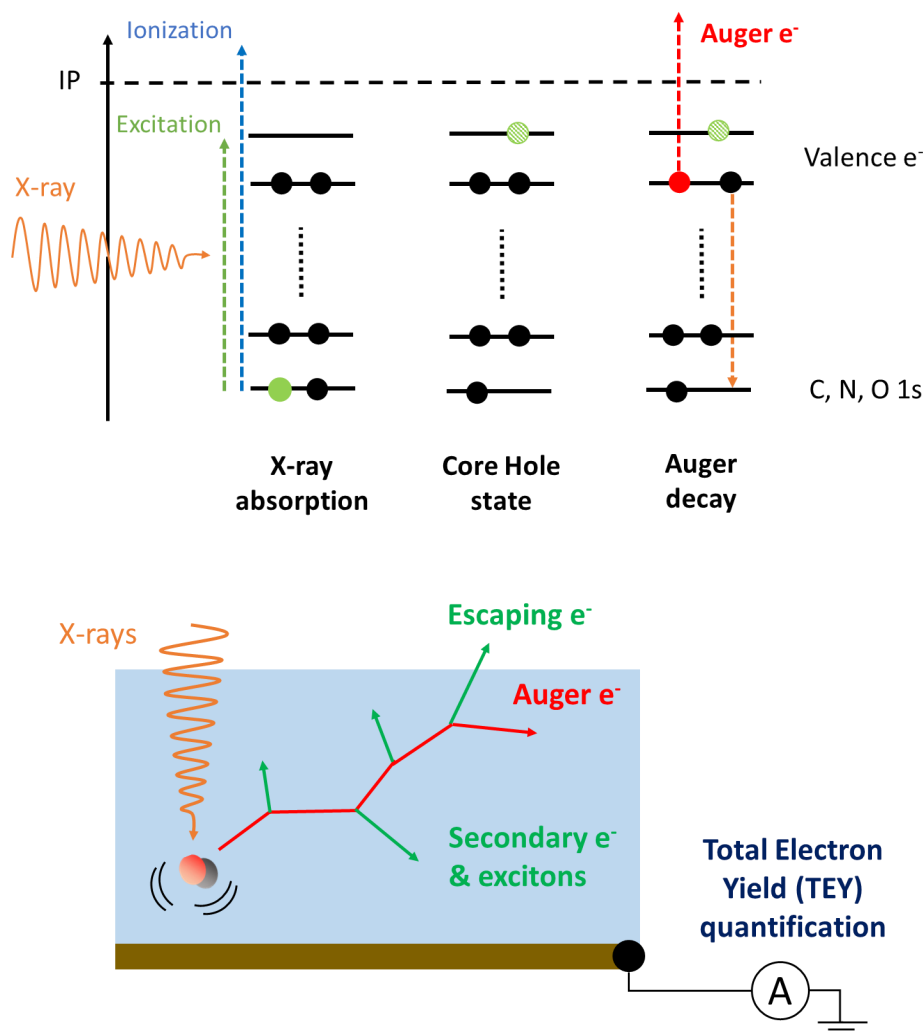


FIGURE III.4 – Top side : general scheme of X-ray photo-absorption and Auger decay processes. Bottom side : thermalization of the Auger electron after Auger decay in molecular ices and drain current measurement (Total Electron Yield - TEY).

intensity as a function of the kinetic energy of the escaping electrons is called the Auger spectrum. Measuring the TEY as a function of the energy of the incident photon represent the Extended X-Ray Absorption Fine Structure (EXAFS) of the molecules in the ice. When the energy of the incident photon is near the edge, it is especially referred to as the Near EXAFS (NEXAFS) or X-ray Absorption Near Edge Structure (XANES)<sup>2</sup>. These measurements give access to the X-ray photo-absorption spectrum of the ice studied. The TEY signal is somehow surface sensitive because the escaping electrons are the ones scattering near the ice surface. The exact probing depth depend on the mean free path of the Auger and secondary electrons. For example, in water ice, the radii of the electron cascade is estimated to be  $\sim 30$  ML (Tîmneanu et al., 2004).

2. Note that these acronyms (EXAFS, NEXAFS, XANES) describe the spectroscopy technique not only applied for solids but also for liquids and gas.

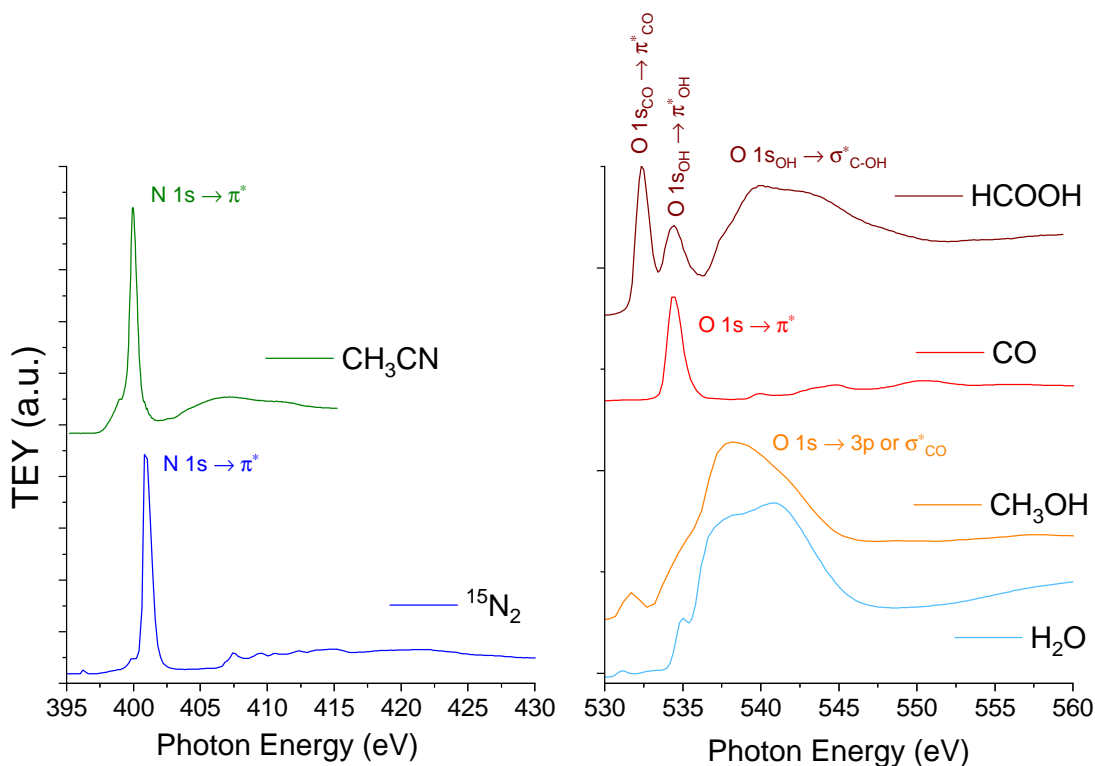


FIGURE III.5 – Left panel : Total Electron Yield (TEY) of pure  $^{15}\text{N}_2$  and pure  $\text{CH}_3\text{CN}$  ices at 15 K from this thesis, near the N K-edge (395 - 430 eV). Right side : TEY, near the O K-edge (530 - 560 eV) of pure CO ice at 15 K from Dupuy et al. (2021b), of pure  $\text{H}_2\text{O}$  ice at 15 K from Dupuy et al. (2020) and of pure  $\text{CH}_3\text{OH}$  and pure  $\text{HCOOH}$  at 15 and 90 K respectively, from this thesis. The TEYs are shifted vertically for more clarity. Attribution of the main features are also displayed.

In Figure III.5 are displayed the Total Electron Yield (TEY) of some molecular ices studied in this thesis ( $^{15}\text{N}_2$ , CO,  $\text{H}_2\text{O}$ ,  $\text{CH}_3\text{CN}$ ,  $\text{CH}_3\text{OH}$  and  $\text{HCOOH}$ ) near the N and O K-edges. The attribution of the main features to core transitions are based on previous work for  $^{15}\text{N}_2$  (Feulner et al., 1992), CO (Jugnet et al., 1984),  $\text{CH}_3\text{CN}$  (Parent et al., 2000),  $\text{CH}_3\text{OH}$  (Wilson et al., 2005) and  $\text{HCOOH}$  (based on gas phase; Prince et al. (2003)). More details on the other features will be discussed in the results chapters. The attribution of the features for  $\text{H}_2\text{O}$  is not straightforward and is discussed in Dupuy et al. (2020). The TEYs are representing the X-ray absorption spectra of the molecules studied in condensed phase. Similarly to what is observed in the VUV range, X-ray absorption spectra of gas phase and solid phase molecules do not necessarily display similar features depending on the orbitals involved in the core transition. Above the ionization threshold of the 1s electron, double excitation (simultaneous excitation of a core and a valence electron), shake-up (simultaneous excitation and ionization of

a valence and a core electron respectively) and shake-off (simultaneous ionization of a core and a valence electron) transitions can also occur and give rise to specific features. Additionally, still above the ionization threshold, broad resonances associated with shape resonances often appear : these states can be viewed as quasi-bound states in which the electron stays trapped during a sufficiently long time before tunneling in the vacuum.

### III.1.4 Interaction with electrons

Interaction of electrons with molecular ices will be discussed in the low ( $< 20$  eV) to medium (a few keV) energy range. The collision of an electron with a molecule occurs either via an elastic or inelastic process. The probability of an elastic or inelastic collision depends on the electron energy and on the molecule considered. The collision is driven by the electrostatic interaction between the incident electron and the electrons bound to the molecule. For elastic collisions, there is a transfer of kinetic energy between the electron and the molecule and the total kinetic energy of the system is conserved such that the internal energy of the molecule is unchanged. For inelastic collisions, on the other hand, the kinetic energy of the incident electron is partly given to the molecule in the form of internal energy and the molecule internal state changes. Inelastic collisions can induce an electronic transition or an ionization of the molecule if the energy of the incident electron exceeds the electronic excitation or the ionization thresholds respectively. The excess of energy above these thresholds remains to the scattered electron in the form of kinetic energy. In molecular ices, inelastic collisions will therefore occur for keV electrons until the electron becomes a sub-excitation electron, with energy below the first electronic excitation threshold. Excitation by inelastic collision can also induce forbidden optical transitions with changes in spin (e.g., from fundamental singlet to triplet states).

For low energy ( $< 20$  eV) electrons, electron attachment can also take place. It is a resonant effect for which the electron fills an unoccupied low-lying orbital of the molecule to form a transient anion, occurring when the electron energy corresponds exactly to the transition energy needed to form the anion. The decay of the transient anion state occurs either via dissociation to form a stable anion and one or more neutral species (in that case the process is called Dissociative Electron Attachment or DEA) or via autodetachment of the electron, potentially leaving the neutral molecule in a high vibrational state in its fundamental electronic state.

What will be of particular importance for desorption is the energy deposition profile of electrons in molecular ices. It quantifies the amount of eV deposited by an electron as a function of depth. [Valkealahti et al. \(1989\)](#) showed that this profile can be approxi-

mated by a Gaussian distribution in one dimension for keV electrons incident on light materials ( $Z \leq 18$ ). The parameters of the Gaussian depend on the electron energy and on the stopping power of the material and they have been calibrated for a  $N_2$  ice for example. Interaction of electrons with molecular ices is relevant for X-ray photodesorption and Electron-Stimulated Desorption (ESD) experiments. For the first one, as explained in the previous section, Auger electrons are expected to be emitted after X-ray absorption in the bulk as well as near the surface of the ice. In our case, these Auger electrons will have a few hundreds of eV of energy and will create a cascade of secondary low energy electrons. The energy deposition profile of electrons in the case of the X-ray experiments is very different than for ESD. For ESD, the electrons are all incident on the molecular ice and deposit their energy from the surface towards the bulk whereas for X-ray experiment, the Auger electrons can be generated in the ice bulk or near its surface and they are, a priori, emitted from the photo-absorbing molecule in all possible directions. This should be kept in mind when comparing X-ray photodesorption and ESD experiments.

## III.2 State of the art on photodesorption mechanisms

The aim of this section is to introduce the main findings on VUV and X-ray photodesorption from ices of molecules containing few atoms (diatomic or triatomic molecules), which serve as model ices to illustrate the desorption mechanisms. I will especially focus on the case of CO and  $H_2O$  which were extensively studied in the literature and which are good examples to highlight the different physical-chemical mechanisms involved in the photodesorption process. Note that several studies have been conducted in the literature for other simple molecules such as  $N_2$  (Öberg, K. I. et al., 2007, 2009c; Bertin et al., 2013),  $CH_4$  (Cruz-Diaz, 2015; Martín-Doménech, R. et al., 2016; Dupuy, R. et al., 2017; Carrascosa et al., 2020),  $NH_3$  (Nishi et al., 1984; Loeffler and Baragiola, 2010; Martín-Doménech et al., 2018; Dupuy, 2019),  $CO_2$  (Öberg, K. I. et al., 2009c; Bahr and Baragiola, 2012; Yuan and Yates, 2013; Fillion et al., 2014; Martín-Doménech, R. et al., 2015a), NO (Dupuy et al., 2017), especially in the VUV range. Only photodesorption of neutral molecules will be studied in this thesis.

### III.2.1 VUV photodesorption

#### III.2.1.1 Direct desorption mechanisms for non-dissociative states

Pure CO ice is a simple case to illustrate VUV photodesorption : photo-chemistry is negligible in such ice (except for high fluences; Gerakines et al. (1996)) and the dissociation threshold of CO is high (11.1 eV). VUV photodesorption from pure CO ice has been first studied by Öberg, K. I. et al. (2007, 2009c) with a broadband hydrogen di-

charge lamp. It was later studied by [Muñoz Caro, G. M. et al. \(2010\)](#) who found higher photodesorption yields of CO. This was partly explained by a difference in the spectral composition of the photon source used, supported by a wavelength-dependence study of the photodesorption yield of CO by [Fayolle et al. \(2011\)](#) (using a monochromatic VUV photon source from synchrotron radiation) and by a study of the emission spectrum of hydrogen lamps in different configurations, with an application to photodesorption from CO ice ([Chen et al., 2013a](#)). The photodesorption yields were also found to depend on the ice deposition temperature ([Muñoz Caro, G. M. et al., 2016](#)). More importantly for this section, the study by [Fayolle et al. \(2011\)](#) enables to discuss the possible mechanisms at play. In figure III.6 is displayed the photodesorption spectrum of CO from a pure CO ice at 18 K (top panel), compared with the photo-absorption

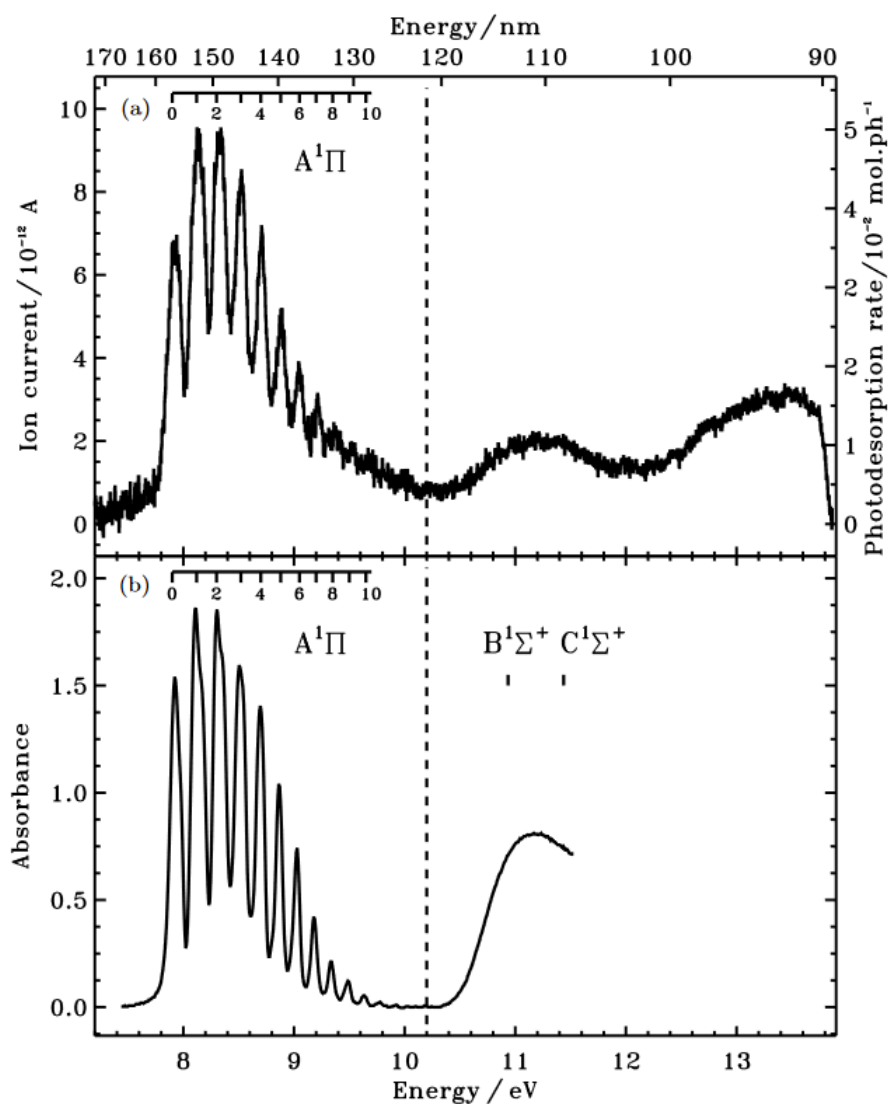


FIGURE III.6 – Top panel : photodesorption spectrum of CO from a 10 ML CO ice at 18 K, with a resolution of 40 meV. Bottom panel : photo-absorption spectrum of CO ice at 10 K. The figure is taken from [Fayolle et al. \(2011\)](#).

spectrum of CO ice (bottom panel), taken from [Fayolle et al. \(2011\)](#). We will first focus on transition to non-dissociative state, which is the case in [Figure III.6](#) in the  $\sim 8 - 10$  eV range where CO is excited to its non-dissociative  $A^1II$  state. In this energy range, both spectra are very well matching, meaning that the photodesorption of CO is a desorption induced by an electronic transition (DIET). This is also a proof that the desorption is not initiated by the interaction of photons with the metallic substrate.

To discuss the desorption mechanism, we consider the case of an electronically excited molecule at the ice surface (i.e. at the interface between the ice bulk and the vacuum), in that case  $CO^*$ , and we want to explain how it could desorb. To such end, an interesting framework is provided by the Menzel-Gomer-Redhead model, introduced by Menzel, Gomer ([Menzel and Gomer, 1964a,b](#)) and, independently, Redhead ([Redhead, 1964a,b](#)), and later reviewed by [Antoniewicz \(1980\)](#). The model is discussed with respect to the potential energy surface of the Substrate-Adsorbate (S-A) bond, simplified in [Figure III.7](#), where the X-scale is the S-A distance. In our example, the substrate S is the CO ice and the adsorbate A is the excited  $CO^*$ . The adsorbate is initially bound to the substrate in the ground state of the S-A bond. After VUV absorption, the CO molecule that has absorbed the photon found itself in an electronically excited state and the new charge distribution associated with this excited state changes the interaction with the neighboring molecules i.e. with the ice substrate. This results in a change of the S-A bond state, which could be left in a repulsive (dissociative) state similar to that denoted  $S-A^*$  on [Figure III.7](#). From there, the main idea is that part of the potential electronic energy of the repulsive  $S-A^*$  state is given (converted) to the adsorbate in the form of kinetic energy and several processes can occur :

- case 1 : after a short time passed on the dissociative  $S-A^*$  potential, the excited molecule  $A^*$  relaxes to its ground state and lands onto the ground S-A potential such that the kinetic energy gained by A is not sufficient to overcome the dissociation limit of the S-A bond and no desorption occurs. In [Menzel and Gomer \(1964a\)](#); [Redhead \(1964b\)](#); [Antoniewicz \(1980\)](#), where the substrate is a metal, it was assumed that such relaxation are due to a reformation of the S-A bond or to a reneutralization (if the adsorbate is ionized) and that the lifetime of the  $S-A^*$  state must be sufficiently short to produce a high rate of de-excitation hence explaining the small desorption cross sections observed. Such decay processes were assumed to involve electron tunneling from or to the substrate and are specific to the case of molecules adsorbed on metals. They might not occur in the case of molecular ices but other relaxation mechanisms could exist, such as an internal conversion from the excited state to the ground state for the case of CO ([van Hemert et al., 2015](#)).

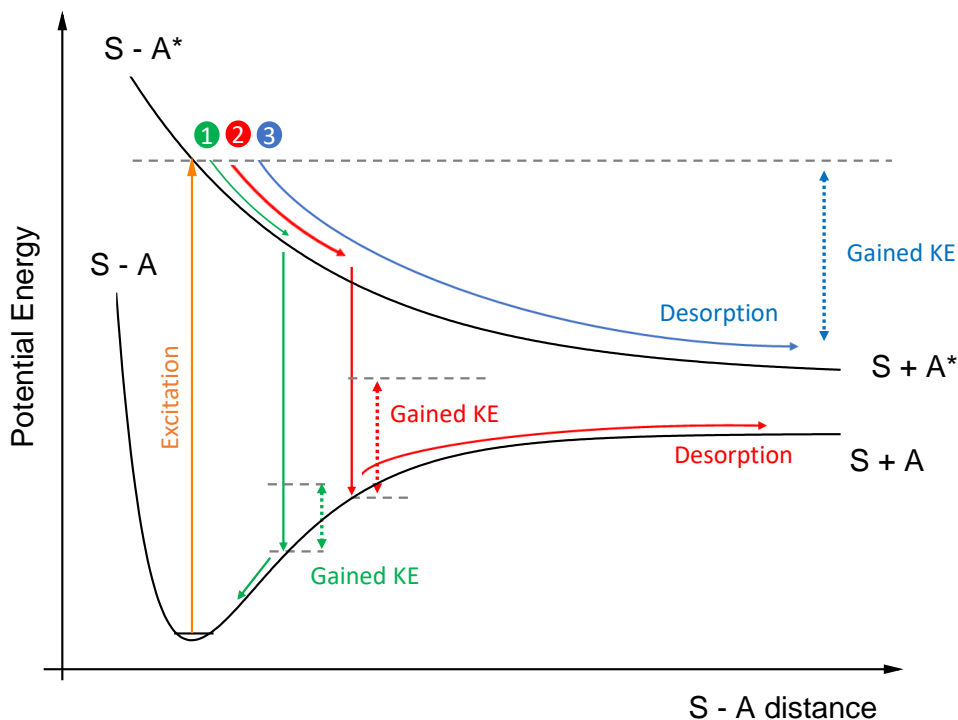


FIGURE III.7 – Simplified version of the MGR model, adapted from [Menzel and Gomer \(1964a\)](#). The ground and dissociative energy potential curves of the substrate-adsorbate (S-A) bond are represented. The fate of the adsorbate is dictated by the decay processes and their characteristic timescales, eventually leading to desorption from the substrate. More details are given in the text.

- case 2 : if the transition to the ground S-A state occurs after a sufficiently long time, the adsorbate would have gained enough kinetic energy to overcome the dissociation limit of the S-A bond and would desorb.
- case 3 : if the S-A\* state does not relax into the ground state after some time, the adsorbate desorbs (if the adsorbate is initially ionized then it desorbs as an ion). As one can see in Figure III.7, the energy state (kinetic and internal) of the adsorbate after desorption is expected to depend on the desorption mechanism (case 2 or case 3 for instance) such that probing the energy state of the photodesorbed adsorbate might provide important information on the desorption dynamics.

The previous model gives the general idea of one possible photodesorption mechanism : as long as the electronically excited molecule found itself on a repulsive part of the potential energy curve associated with the S-A bond (during the lifetime of the excited state or after decay), it can gain sufficient kinetic energy to desorb. More recently, [van Hemert et al. \(2015\)](#) simulated the photodesorption of CO from a CO cluster (amorphous or crystalline) by molecular dynamics and derived the potential energy surface

associated with the ground and excited state of the CO dimer (CO-CO). The simulation starts with a CO molecule in the electronically excited state  $A^1\Pi$ . After a finite time spent on this excited state, the decay occurs via internal conversion from the  $A^1\Pi$  state to the ground state  $X^1\Sigma^+$  with a high vibrational level ( $\nu''=48$ ). This decay results in the landing of the CO molecule onto the ground state potential energy surface of the CO dimer with an orientation and position favorable for desorption. This mechanism is similar to the case 2 of the MGR process described previously : the excited molecule needs to evolve on the excited state potential energy surface of the CO dimer during a sufficiently long time before relaxing, via internal conversion, onto the ground state of the CO dimer with a configuration favorable to desorption. The photodesorbed CO molecule is expected to be left in a highly vibrational state (in its fundamental electronic state) in that case. I will come back to this study in more details in Chapter IV.2.

### III.2.1.2 Indirect desorption mechanisms

The previous mechanisms describe the photodesorption of a photo-excited molecule located on the surface of the ice. A natural way of thinking would be to consider that the desorbing molecule is the one that has absorbed the photon. However, experimental studies conducted on CO ices by [Bertin et al. \(2012, 2013\)](#) show that this is not always the case, i.e. the desorbing molecule is not necessarily the photo-excited one. These experiments consist of irradiating, still in the VUV range, mixed  $^{13}\text{CO}:^{15}\text{N}_2$  or layered (a few layers of  $^{13}\text{CO}$  on top of a  $^{15}\text{N}_2$  ice or inversely) ices<sup>3</sup> while probing the desorbing molecules. The main findings are presented in Figure III.8. On the top panel are the photodesorption spectra from the pure ices : the photodesorption spectrum of  $^{13}\text{CO}$  and  $^{15}\text{N}_2$  follows the photo-absorption spectrum of  $^{13}\text{CO}$  and  $^{15}\text{N}_2$  respectively. On the other hand, when looking at the photodesorption spectra from the mixed  $^{13}\text{CO}:^{15}\text{N}_2$  ice (bottom panel), one can see that the photodesorption of  $^{15}\text{N}_2$  in the 7.9 - 9.5 eV region, where  $^{15}\text{N}_2$  does not absorb<sup>4</sup>, follows the photo-absorption spectrum of  $^{13}\text{CO}$ . This means that the desorption of  $^{15}\text{N}_2$  is induced by an electronic transition of  $^{13}\text{CO}$  ( $A^1\Pi - X^1\Sigma^+$ ). The same behavior is observed, although less visible, for the desorption of  $^{13}\text{CO}$  above 12.3 eV induced by an electronic transition of  $^{15}\text{N}_2$  ( $b^1\Pi_u - X^1\Sigma_g^+$ ) for which the vibrational progression of the  $b^1\Pi_u$  state of  $^{15}\text{N}_2$  is seen on the photodesorption spectrum of  $^{13}\text{CO}$ . This illustrates an indirect desorption process (sometimes referred to as an indirect DIET) for which the photo-excitation of one molecule induces the desorption of another one. This process was further confirmed and characterized by experiments on layered ices : the photo-excitation of the sub-surface

3. the isotopes are chosen in order to distinguish the molecules by mass spectrometry

4. actually there are some dipole forbidden transitions in this energy range for  $^{15}\text{N}_2$  in the condensed phase but the absorption cross section is negligible ( $\sim 2 \times 10^{-20} \text{ cm}^2$ ) compared to that of the transitions of  $^{13}\text{CO}$  ( $\sim 1 \times 10^{-17} \text{ cm}^2$ ) and the absorption features do not match the photodesorption spectrum ([Cruz-Diaz et al., 2014a,b](#))

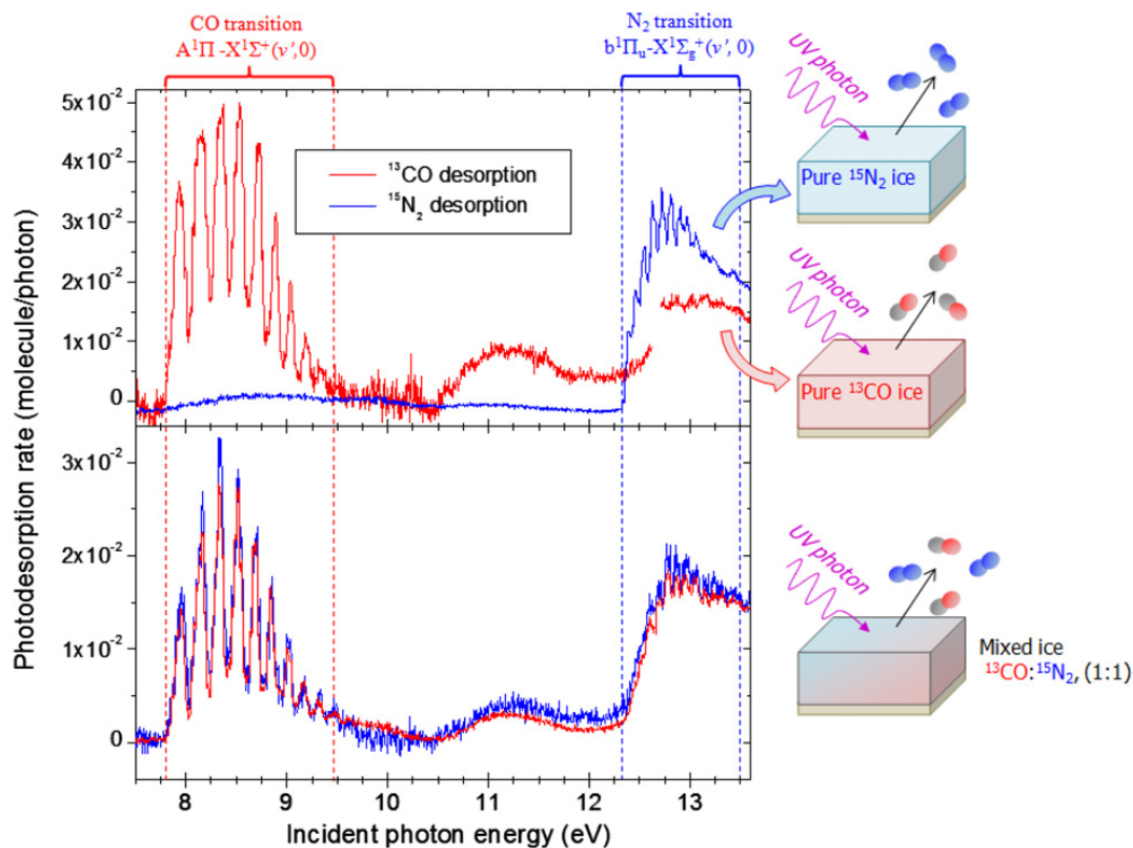


FIGURE III.8 – Photodesorption spectra of  $^{13}\text{CO}$  (red) and  $^{15}\text{N}_2$  (blue) from their pure respective ice (top panel) and from a mixed  $^{13}\text{CO}:^{15}\text{N}_2$  ice in a 1 :1 proportion (bottom panel). The ices are 30 ML thick and were grown and irradiated at 15 K. The electronic transitions associated with  $^{13}\text{CO}$  and  $^{15}\text{N}_2$  are also displayed. These data illustrate the indirect desorption mechanism discussed in the text. Taken from Bertin et al. (2013).

$^{13}\text{CO}$  and  $^{15}\text{N}_2$  molecules trigger the desorption of, respectively, the  $^{15}\text{N}_2$  and  $^{13}\text{CO}$  molecules deposited on top. The indirect mechanism cannot be described by the MGR model previously mentioned, at least not entirely, and additional processes should be invoked. First, the change in the charge distribution around a photo-excited molecule near the ice surface might induce a local reorganization of the surrounding molecules during the lifetime of the excited state. This could in turn results in the desorption of the photo-excited molecule as well as the surrounding ones (indirect process) if the latter found themselves in a favorable orientation for desorption. On the other hand, the indirect desorption mechanism might involve an energy transfer from the photo-excited molecule to the desorbing one, in the form of internal (electronic excitation as well as librational excitation) or translational energy. Among the possible mechanisms, the following list depict the most studied ones in the literature (to simplify the discussion, we will still consider that the initial electronic state of the photo-absorbing molecule is non-dissociative) :

- indirect desorption due to the migration of the electronic excitation at the ice surface. This mechanism stems from the theory of excitons in crystals described previously in Section III.1.2, which stipulates that exciton can propagate through a crystal in a wave-like manner with Frenkel excitons having a lower radii than Wannier excitons. These migration of excitons can also occur in amorphous solids (Fiermans and Phariseau, 1966; Christiaens and Phariseau, 1968). Experimentally, the migration of excitons in molecular ices has been highlighted in the case of Electron-Stimulated Desorption (ESD) from water ice (Orlando and Kimmel, 1997; Petrik and Kimmel, 2003). In these experiments, the diffusion of excitons from the bulk to the ice surface (at the water/vacuum interface) is shown to be responsible for the desorption of molecular hydrogen and of water fragments. Additionally, it was assumed in ESD experiments (Marchione et al., 2016) that benzene  $C_6H_6$  adsorbed at the surface of water ice can also desorb due to the migration of such exciton from the water ice bulk to the  $H_2O/C_6H_6$  interface. Exciton migration in more weakly bound Van der Waals amorphous solids such as CO ice has not been experimentally found yet. Moreover, exciton migration in the case of mixed ices, for which the excitonic states associated with the different molecules might not be coupled, is questionable.
- indirect desorption due to the coupling of the electronic excitation to phonon modes of the ice. This process originates from the Frenkel theory of excitons in which it is mentioned that the electronic excitation in a crystal can couple to its vibrational states (phonons) in a radiationless way. If the energy relaxed into these phonon modes is sufficiently high and if the phonon modes are efficiently coupled to desorption, then this indirect process should play a role. Considering the binding energies of Table III.1, only high energy phonon modes, of a few hundreds of meV, have enough energy to desorb molecules, with a higher efficiency expected for weakly bound ices such as CO or  $N_2$  ice.
- indirect desorption by collision processes, involving an energy transfer between the libration motion of a sub-surface molecule to the translational motion of a surface one. This process is briefly referred to as a "kick-out" mechanism in the simulations of van Hemert et al. (2015) although it is not detailed. In that case, a photo-excited CO sub-surface molecule relaxes by internal conversion from its excited electronic state A to its ground state X in a high vibrational mode. The large extension of the CO bond in such high vibrational mode is probably inducing the kick-out desorption of a surface molecule, as suggested in van Hemert et al. (2015).

The mechanism responsible for the indirect desorption presented in Figure III.8 from Bertin et al. (2013) is still not understood and additional experiments have to be conducted. For instance, the REMPI + TOF technique developed during the thesis should help elucidating such process. Knowing the dominant mechanism could also have important implications for astrophysics.

### III.2.1.3 Desorption mechanisms induced by photo-dissociation

The previous processes have been illustrated for the case where the excited state is non-dissociative. Additional mechanisms can occur when the photo-absorption induces the dissociation of the molecules in the ice bulk or at its surface. This is especially relevant for COMs that are easily photo-dissociated. In the following, I will briefly introduce, through some examples, the additional mechanisms expected.

The photo-dissociation of molecules in the VUV range provides additional pathways (compared to the previous ones) for desorption. If the fragments originating from the photo-absorbing molecule do not desorb or diffuse away from each other, they might recombine and lead to desorption of the initial parent molecule if the reaction is sufficiently exothermic. This process is called chemical or reactive desorption by geminate recombination. It is expected to depend on the ice composition, namely, reactive neighboring species surrounding the photo-absorbing molecule might react with the fragments, preventing the recombination reaction. Non-geminate recombination leading to desorption, for which the reacting species originate from different molecules can also take place. In the latter case, the reaction might occur between a photo-fragment and a neighboring intact molecule or it might depend on the accumulation of the species involved in the reaction at the ice surface. The ice temperature and phase should play a role for chemical desorption (geminate and non-geminate) as higher temperature and pores should favor the diffusion of radicals. This is for example what has been suggested to participate in the VUV photodesorption of H<sub>2</sub>O from water ice at temperatures above 70 K (Fillion et al., 2022). High reaction exothermicity can also result in the desorption of molecules with high energy. For instance, this was suggested in Yabushita et al. (2008) to explain the photodesorption of translationally and internally hot H<sub>2</sub> at 157 nm from water ice due to the exothermic recombination  $\text{H} + \text{H} \rightarrow \text{H}_2$ . On the other hand, the desorption of vibrationally cold H<sub>2</sub> was assumed to occur via the endothermic abstraction reaction  $\text{H} + \text{HOH} \rightarrow \text{H}_2 + \text{OH}$ .

Additionally, the kick-out mechanism, which is a collision-like process similar to the one described in section III.2.1.2 but due here to the release of energetic fragments in the ice after photo-dissociation, can also play a role. For instance, this process has been shown to be responsible of the desorption of atoms and diatomic molecules, such as

$\text{N}_2$  and CO, adsorbed on the surface of water ice (Dupuy et al., 2021a). In that case, the photodesorption yields show a dependence on the photon energy and on the mass of the adsorbates consistent with a collision process with H/D fragments. This kick-out mechanism strongly depends on the capability of the fragments to diffuse through the ice. Light fragments such as H/D are expected to diffuse more efficiently than heavier ones, possibly thanks to tunneling effects. The diffusion of ions from the ice bulk is expected to be quenched due to the solvation of the ion by the surrounding molecules. Therefore, this process should be more efficient when the dissociation of the photo-excited molecule result in the formation of light neutral fragments, especially H atoms. Moreover, this mechanism is generally expected to produce desorbed molecules with little internal energy compared to their translational energy and the desorption should not depend on the photon fluence. For instance, these arguments were used to conclude that the kick-out mechanism plays a role in the photodesorption of  $\text{H}_2\text{O}(\nu = 0)$  from water ice at 157 nm in experimental studies (Hama et al., 2010; Andersson et al., 2011).

The desorption of the fragments can also occur promptly after photo-dissociation of the molecule at the ice surface if the fragments have sufficient kinetic energy. This could lead to the desorption of radicals in the gas phase, often observed in this thesis from COMs-containing ices. In astrophysical environments, the desorption of radicals from interstellar ices provide reactive species for the gas phase, eventually inducing additional chemical reactions and influencing the molecular composition of the region considered.

Finally, the photo-dissociation of the initial parent (intact) molecules implies that the photodesorption yields should somehow depend on the photon fluence i.e. on the change of the molecular composition of the ice with irradiation time, previously referred to as the ice photo-aging. Namely, the destruction of the parent molecules with the photon fluence, at the ice surface and in its bulk, might defavor their desorption while inducing the accumulation and subsequent desorption of new species. Studying the dependence of the desorption yields with the photon fluence could therefore provide information on the mechanisms at play. This is especially true for the previous chemical desorption processes, which are expected to exhibit a different behavior with the photon fluence because they depend on the presence of the parent molecule at the ice surface and/or on the accumulation of new species involved in the exothermic reaction. For example, in the study of Martín-Doménech, R. et al. (2016), the UV photodesorption of CO and  $\text{H}_2\text{CO}$  from a pure ethanol ice and a mixed  $\text{H}_2\text{O}:\text{CH}_4$  ice at 8 K was discussed regarding the dependence of the yields with the photon fluence. It was concluded that the increase of the desorption yield of CO with the photon fluence was due to its accumulation in the ice bulk, thereby implying that more CO molecules are

available for desorption with irradiation time. In that case, mechanisms similar to the one discussed in the previous sections III.2.1.1 and III.2.1.2 were suggested to occur for CO desorption. On the other hand, the desorption yield of H<sub>2</sub>CO was found constant with the photon fluence, suggesting that, even though H<sub>2</sub>CO accumulates in the ice bulk, its desorption yield does not increase with the photon fluence because it is not able to desorb via the processes described in sections III.2.1.1 and III.2.1.2 over time. Consequently, the desorption observed should be due to a chemical desorption process. Another example illustrating the effect of the photo-dissociation of molecules on the desorption behavior is the study of [Fillion et al. \(2014\)](#). In such study, it was shown that the photodesorption of CO<sub>2</sub> from a pre-irradiated pure CO<sub>2</sub> ice at 10 K can occur in the 7.5 - 9.5 eV range whereas it is not observed in this energy range for a "fresh" (low fluence) ice. This was explained to be due to an indirect process induced by the photo-absorption of CO accumulating with the photon fluence after photo-dissociation of the parent CO<sub>2</sub> molecules in the case of the pre-irradiated ice.

The previous studies demonstrate the interconnection between photolysis and photodesorption from molecular ices, the latter being dependent on the ice composition. In this thesis, for the study of the photodesorption of COMs from interstellar ice analogues presented in Chapter V and VI, we tried to limit as much as possible the effect of the ice photo-aging in our experiments, in order to derived photodesorption yields representative of a "fresh" sample.

### III.2.2 X-ray photodesorption

X-ray's ability to trigger the desorption of neutral molecules from interstellar ices has been recently highlighted by experimental studies ([Ciaravella et al., 2016](#); [Dupuy et al., 2018](#); [Jiménez-Escobar et al., 2018](#); [Ciaravella et al., 2020](#)). At the LERMA lab, detailed studies on the X-ray photodesorption from pure CO and pure H<sub>2</sub>O ices have been conducted near the O K-edge ([Dupuy et al., 2018, 2021b](#)). During these experiments, the photodesorption signal of the desorbing molecules and the Total Electron Yield (TEY) are monitored simultaneously as a function of the photon energy. For instance, the photodesorption spectrum of CO from a pure CO ice at 15 K is displayed in [Figure III.9](#) along with the Total Electron Yield (TEY) taken from [Dupuy et al. \(2021b\)](#). As one can see on this figure, the photodesorption of neutral CO is very well-correlated to the TEY, which represent the X-ray photo-absorption spectrum of the ice. The same correlation is found for the X-ray photodesorption of H<sub>2</sub>O from a pure amorphous H<sub>2</sub>O ice at 15 K ([Dupuy et al., 2018](#)). In the case of X-ray photodesorption, there are often two different mechanisms discussed in the literature. The first one is X-ray Electron-Stimulated Desorption (XESD). XESD is the consequence of the relaxation of the core hole state by Auger decay. The Auger electron scatters inelastically in the ice, crea-

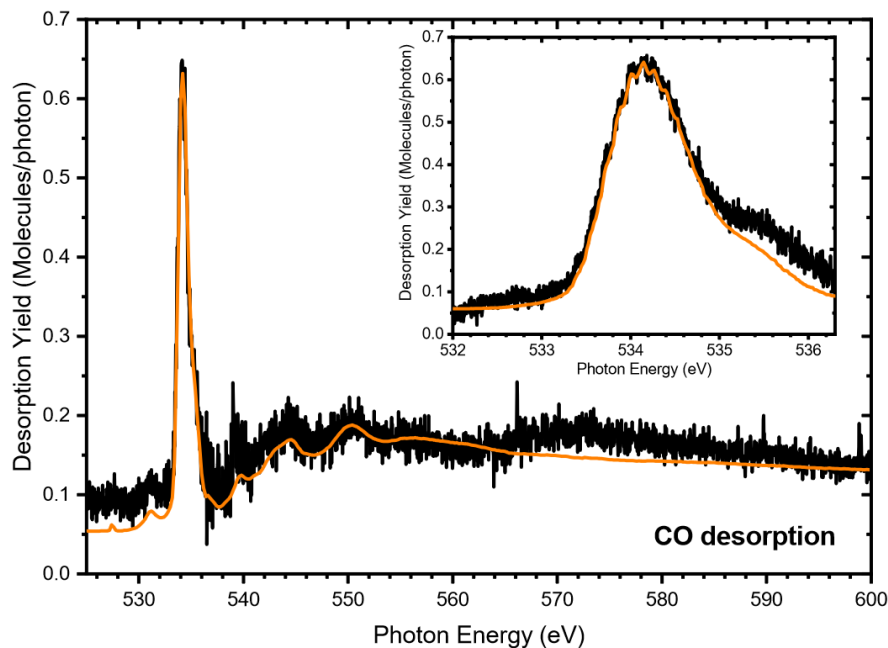


FIGURE III.9 – Solid black line : X-ray photodesorption spectrum of CO from a pure CO ice at 15 K, near the O 1s edge. Solid orange line : Total Electron Yield (TEY) measured simultaneously during the irradiation. The inset shows the O  $1s^{-1} \pi^*$  resonance near 534.2 eV. Taken from Dupuy et al. (2021b).

ting secondary events (e.g, ionizations and excitations) and especially a cascade of low energy ( $< 20$  eV) secondary electrons, that may lead in fine to desorption. The second mechanism discussed includes all processes related to the energy left to the photo-absorbing molecule after Auger decay, referred to as non-XESD mechanisms in the following. Non-XESD processes are therefore decorrelated from the Auger scattering and originate from the photo-absorbing molecule which is left in an electronic excited state after Auger decay and singly or doubly ionized. From there, all the processes discussed previously for VUV photodesorption and that dealt with the desorption induced by an electronically excited molecule could occur. However, in the case of X-rays, the excited state is always an ionized state (dissociative or non-dissociative) such that it is not likely for the photo-absorbing molecule to desorb as a neutral (therefore no direct processes are expected). In terms of energy, most of the internal energy of the core hole state is carried away by the Auger electron in the form of kinetic energy such that only a few tens of eV is left to the photo-absorbing molecule after Auger decay.

XESD is necessarily an indirect process for which the photodesorption should be proportional to the number of electrons scattering near the ice surface. Therefore, in the case of a XESD process, the photodesorption spectra should necessarily follow the TEY but the fact that it does is not a sufficient argument to assess that XESD is the dominant mechanism because non-XESD processes might also exhibit such behavior. On

the other hand, we do not necessarily expect the X-ray photodesorption spectra to follow the TEY for non-XESD processes because, in that case, the desorption efficiency is decorrelated from the Auger scattering. Therefore, the fact that the X-ray photodesorption spectrum is not following the TEY is a strong and sufficient argument in favor of non-XESD processes but the fact that it does is not a sufficient argument neither for XESD nor for non-XESD processes.

In [Dupuy et al. \(2018\)](#) and [Dupuy et al. \(2021b\)](#), it is strongly suggested that the X-ray photodesorption of CO and H<sub>2</sub>O from their pure respective ices occurs via a XESD process. The authors propose two arguments. The first one is the fact that X-ray photodesorption yields (in molecules desorbed per absorbed photon) and electron-stimulated desorption (ESD) yields (for incident electrons with energy similar to the Auger electron i.e.  $\sim 500$  eV) are found similar. The second one is the fact that the energy threshold for ESD of CO and H<sub>2</sub>O from their respective pure ices is lower than the mean energy of the secondary electrons created by the Auger scattering, which is  $\sim 10$  eV. Therefore, it is energetically possible for the secondary electrons to induce the desorption of CO and H<sub>2</sub>O at the ice surface. In that case, the exact process responsible for desorption is expected to be due to the valence electronic excitations induced by the low energy secondary electrons, which are processes similar to the ones discussed previously for the case of VUV photodesorption. Additionally, electron attachment can also arise from the interaction of the molecules with the secondary low energy electrons and possibly induce desorption.

Non-XESD mechanisms have been highlighted by [Menzel and Feulner \(2001\)](#) (see also [Feulner et al. \(2000\)](#)) in the case of X-ray photodesorption of neutrals from N<sub>2</sub> or CO adsorbed on noble transition metals. Without getting into too much details, it was found that the desorption of N and N<sub>2</sub> and that of O and CO from the metals is due to specific decay processes of the core hole state into different final states, strongly influenced by the coupling with the metal. This resulted in the desorption spectra not necessarily following the PEY and with the selective excitation of the N 1s, C 1s or O 1s electron, for different photon energies, leading to different desorption efficiencies.

In addition to the previous processes, the X-ray induced chemistry, expected to be dominated by the low energy secondary electrons, should also play a role in desorption, especially when studying COMs-containing ices. In fact, numerous radicals are expected to be formed in the scattering path of electrons and to react with surrounding molecules, which can lead to desorption induced by exothermic reaction.

## Chapter IV

# New insights on the desorption mechanisms in the X-ray and VUV range

The results presented in the following section were obtained during this thesis with the objective of better characterizing the photodesorption processes involved in the VUV and X-ray range. The first section deals with a study that was conducted at the synchrotron SOLEIL (2021) on the SEXTANTS beamline, in the soft X-ray range. It follows recent X-ray photodesorption studies on pure CO and pure H<sub>2</sub>O ices ([Dupuy et al., 2018, 2021b](#)) that led to the general conclusion that XESD was the dominant process explaining the desorption of neutrals. However, a detailed characterization of this mechanism at a microscopic scale, with its implications for astrophysics, was lacking. The study presented in the first section aims to fill this gap, by studying mixed CO and N<sub>2</sub>-containing ices.

The second section presents the very first experimental data on the internal and kinetic energy of photodesorbed CO from a pure CO ice in the VUV range. These data were obtained directly at the lab by using the VUV photon source implemented as described in Section II.3. We present the quantification of the data and we discuss the possible photodesorption mechanisms, especially by comparing them to the study of [van Hemert et al. \(2015\)](#).

## IV.1 Mechanisms in the X-ray range : X-ray photodesorption from mixed and layered N<sub>2</sub>-CO ices

Diatomic molecules such as CO and N<sub>2</sub> have been extensively studied in laboratory at very low temperature ( $T < 20$  K), in their solid phase. This is supported by the fact that these molecules are expected to be found in the (ISM) and the solar system in a diversity of icy solids such as interstellar ices, comets and icy moons and planets. For instance, observations of CO at the surface of these cold bodies have been reported in several studies (Mumma and Charnley, 2011a; Bennett et al., 2013; Boogert et al., 2015). This is in contrast with N<sub>2</sub> that possesses no permanent dipole moment hence for which direct detection is rare. In the ISM, only one direct detection of N<sub>2</sub> at far-ultraviolet wavelengths has been proposed towards the HD 124314 star (Knauth et al., 2004). In the solar system, ices containing N<sub>2</sub> have been observed at the surface of Pluto (Owen et al., 1993) and Triton (Cruikshank et al., 1993) and N<sub>2</sub> was detected on a comet for the first time a few years ago by the Rosetta spacecraft (comet 67P/Churyumov-Gerasimenko, Rubin et al. (2015)).

The X-ray photodesorption from condensed N<sub>2</sub> and CO has been previously studied for thin layers deposited on top of transition and noble metals (Frigo et al., 1998; Feulner et al., 2000; Romberg et al., 2000; Feulner et al., 2002). In that case, the desorption of neutral and ionic molecules (N<sub>2</sub>, CO, CO<sup>+</sup>) as well as fragments (N, N<sup>+</sup>, N<sup>2+</sup>, C, O, O<sup>+</sup>, C<sup>+</sup>) was found to be due to non-XESD processes that strongly depend on singly or multiply valence-excited states, after decay of the core hole state. These states were associated with specific desorption mechanisms. In some cases, ultra-fast processes happening during the core hole state lifetime were also suggested to play a role for the desorption of ionic fragments (Frigo et al., 1998).

In the following work, we experimentally study the X-ray photodesorption process for neutral desorption from pure <sup>15</sup>N<sub>2</sub> ice and from mixed and layered <sup>13</sup>CO:<sup>15</sup>N<sub>2</sub> ices (isotopes are chosen to differentiate the molecules by mass spectrometry). Resonant 1s core excitation (or ionization) near the N (~ 400 eV) or O (~ 500 eV) K-edge, accessible thanks to tunable and high spectral resolution X-rays from the synchrotron SOLEIL, enables to selectively photo-excite <sup>15</sup>N<sub>2</sub> or <sup>13</sup>CO to trigger desorption from ices containing these molecules. We first provide a quantitative study of the X-ray photodesorption of neutral molecules from pure <sup>15</sup>N<sub>2</sub> ice. Then, we quantify this process for mixed <sup>13</sup>CO:<sup>15</sup>N<sub>2</sub> and layered <sup>13</sup>CO/<sup>15</sup>N<sub>2</sub> (<sup>13</sup>CO on top of <sup>15</sup>N<sub>2</sub>) ices. This latter set of experiments enables to discuss the desorption mechanisms. The results presented in this section are published in Basalgète et al. (2022).

### IV.1.1 X-ray absorption spectra

Before discussing the photodesorption of neutrals from the ices studied, we present the data obtained for TEYs, which are representative of the X-ray absorption profile of the ices. The calibration of the energy scale near the N and O K-edge was performed thanks to these TEYs, using the following method :

- near the N K-edge, the TEY was measured on a pure  $^{15}\text{N}_2$  ice as a function of the energy of the incident photons and it was compared to gas phase X-ray absorption spectroscopy experiments (e.g. [Chen et al. \(1989\)](#); [Feifel et al. \(2004\)](#)). The TEY peak corresponding to the  $\text{N } 1s \rightarrow \pi^*$  ( $\nu' = 0$ ) transition of  $^{15}\text{N}_2$  was set to 400.868 eV according to [Chen et al. \(1989\)](#) (see Figure IV.1). We therefore assumed that this energy position was not significantly shifted when going from gas phase to solid phase, as observed for a similar molecule : CO ([Jugnet et al., 1984](#)). Note that the energy of the transition is slightly varying ( $\pm 20$  meV) from one gas phase experiment to another ([King et al., 1977](#); [Hitchcock and Brion, 1980](#); [Sodhi and Brion, 1984](#); [Kempgens et al., 1996](#); [Feifel et al., 2004](#); [Kato et al., 2007](#)).

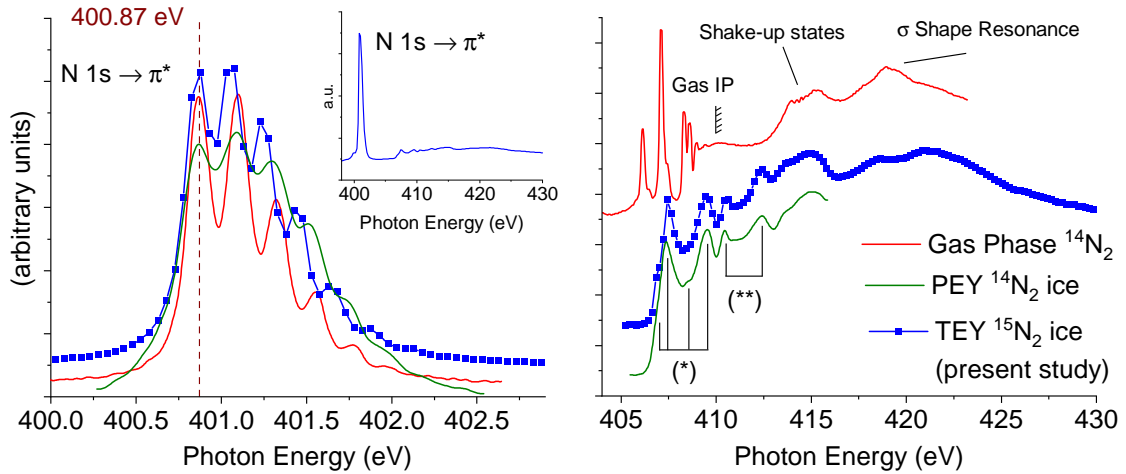


FIGURE IV.1 – Left panel : X-ray absorption spectrum of  $\text{N}_2$  in the  $\text{N } 1s \rightarrow \pi^*$  excitation region. The inset shows the whole TEY between 398 and 430 eV from our experiment. Right panel : X-ray absorption spectrum in the region near the ionization threshold between 405 and 430 eV. In solid red lines are the X-ray photoabsorption spectra of gas phase  $^{14}\text{N}_2$  from [Chen et al. \(1989\)](#) with a spectral resolution of 40 meV. In solid green lines are the partial electron yields (PEYs) of 50 ML of  $^{14}\text{N}_2$  ice at 15 K from [Feulner et al. \(1992\)](#) with a spectral resolution of 100 meV. In blue lines are the TEYs of 50 ML of  $^{15}\text{N}_2$  ice at 15 K from our experiments with a spectral resolution of 100 meV for the left panel and 350 meV for the inset of the left panel and for the right panel. The baselines of the different curves have been shifted for more clarity.

- near the O K-edge, the O  $1s \rightarrow \pi^*$  transition of  $^{13}\text{CO}$  observed on the TEY of a mixed  $^{13}\text{CO}:^{15}\text{N}_2$  ice was centered at 534.4 eV (see Figure IV.2) according to pure CO ice spectroscopy experiments (Jugnet et al., 1984), assuming that the inter-molecular interactions between  $^{13}\text{CO}$  and  $^{15}\text{N}_2$  are not significantly shifting the energy position of the electronic transition, which is reasonable considering such weakly interacting solids.

The TEY of pure  $^{15}\text{N}_2$  ice at 15 K near the N K-edge is displayed in Figure IV.1 (blue lines) for different energy ranges and spectral resolutions. The absorption is dominated by the N  $1s \rightarrow \pi^*$  transition of  $^{15}\text{N}_2$  near 401 eV, whose vibrational structure has been resolved with a spectral resolution of 100 meV. Our TEY in the N  $1s \rightarrow \pi^*$  region compares well with other absorption spectra of gas phase  $^{14}\text{N}_2$  (Chen et al., 1989) and  $^{14}\text{N}_2$  ice at 15 K (Feulner et al., 1992). The N  $1s^{-1}\pi^*$  core electronic state of the free molecule is not significantly modified in the solid phase, as expected for weak Van der Waals interactions between  $\text{N}_2$  molecules in the solid. There are however some slight discrepancies in the position of the vibrational levels between the three curves in the left panel of Figure IV.1. When going from gas phase (red line) to solid phase (green line), the small differences in the position of the vibrational levels of the N  $1s^{-1}\pi^*$  state of  $^{14}\text{N}_2$  could be attributed to either experimental uncertainties on the relative position of the peaks or to inter-molecular interactions in the solid phase. The comparison of our TEY of  $^{15}\text{N}_2$  ice (blue line) with the PEY of  $^{14}\text{N}_2$  ice (green line) shows a smaller vibrational level spacing for  $^{15}\text{N}_2$ . This is expected to come from an isotopic effect. A similar behaviour is for example observed in the vibrational level spacing of the  $A^1\Pi$  state of  $^{13}\text{CO}$  versus  $^{12}\text{CO}$  ice and of the  $b^1\Pi_u$  state of  $^{15}\text{N}_2$  versus  $^{14}\text{N}_2$  ice probed by VUV photodesorption experiments (Bertin et al., 2012; Fayolle et al., 2013).

In the right panel of Figure IV.1, the Rydberg states of gas phase  $^{14}\text{N}_2$  seen below the ionization potential (IP) are significantly modified in the solid phase, as expected from the overlapping of the Rydberg orbitals with that of the neighboring molecules in the solid. Instead, series of broad peaks (labelled (\*) and (\*\*)) in Figure IV.1, whose positions go above the gas phase IP, populate this region. There is no significant difference in this region between  $^{14}\text{N}_2$  and  $^{15}\text{N}_2$  in solid phase. The first series of the four peaks labelled (\*) has been attributed to the equivalent of the gas phase Rydberg states  $3s\sigma$ ,  $3p\pi$ ,  $4s\sigma$  and  $5s\sigma$  in solid phase by Feulner et al. (1992), based on polarization dependent X-ray photodesorption of  $\text{N}^+$  and based on the data from Chen et al. (1989). The attribution of the peaks labelled (\*\*) above the gas phase IP in Figure IV.1 has not been studied in the literature to my knowledge. The gas phase broad feature observed near 415 eV has been attributed by Chen et al. (1989) to shake-up states, tentatively associated with the state configurations  $(1s)^{-1}(5\sigma)^{-1}(1\pi_g^*)^1(3s\sigma)^1$  and  $(1s)^{-1}(1\pi)^{-1}(1\pi_g^*)^1(3p\pi)^1$ .

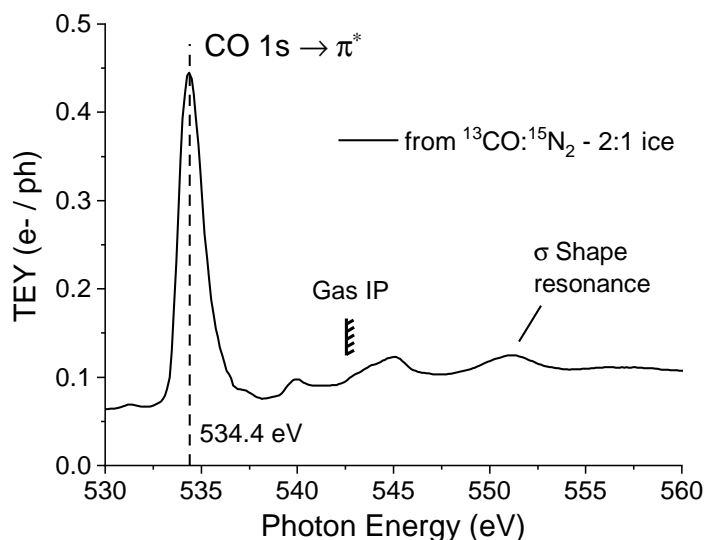


FIGURE IV.2 – TEY of a mixed  $^{13}\text{CO}:^{15}\text{N}_2$  - 2 :1 ice at 15 K (total of 100 ML) in the O K-edge region between 530 and 560 eV from our experiments, with a spectral resolution of 350 meV.

As one can see in Figure IV.1, a similar feature is observed in this region for  $^{15}\text{N}_2$  and  $^{14}\text{N}_2$  ice. The feature observed near 419 eV in the gas phase has been attributed to a  $\sigma$  shape resonance (Chen et al., 1989). A similar feature is observed for  $^{15}\text{N}_2$  ice.

The TEY of a mixed  $^{13}\text{CO}:^{15}\text{N}_2$  ice (2:1) ice at 15 K near the O K-edge is displayed in Figure IV.2. The absorption is dominated by the O  $1s \rightarrow \pi^*$  transition of  $^{13}\text{CO}$  centered at 534.4 eV. The spectrum is similar to that of a pure CO ice studied in similar experiments and for which more details are available regarding the attribution of the spectral features (Dupuy et al., 2021b). The inter-molecular interactions between  $^{13}\text{CO}$  and  $^{15}\text{N}_2$  in the mixed ice are not modifying the transitions observed in this energy range compared to a pure CO ice. The N  $1s$  core electron photo-ionization of  $^{15}\text{N}_2$  is expected to contribute to the absorption spectrum in this energy range but it is reasonably assumed to be negligible compared to  $^{13}\text{CO}$  photo-absorption, and it should in any case account for a monotonically decreasing signal over the whole energy range.

#### IV.1.2 X-ray photodesorption yields from pure and mixed ices

The photodesorption spectra of  $^{15}\text{N}_2$  from a pure  $^{15}\text{N}_2$  ice at 15 K are shown in Figure IV.3 (green lines) with the left panel corresponding to the N  $1s \rightarrow \pi^*$  transition and the right panel corresponding to the near-IP region. The TEYs measured simultaneously during the irradiation procedure are also displayed in blue lines for comparison. The photodesorption yields are higher by more than one order of magnitude in the N  $1s \rightarrow \pi^*$  region than in the near-IP region, with a maximum of  $\sim 5$  molecule photon $^{-1}$  at the N  $1s \rightarrow \pi^*$  ( $\nu' = 0, 1$ ) transitions. The photodesorption spectra are fol-

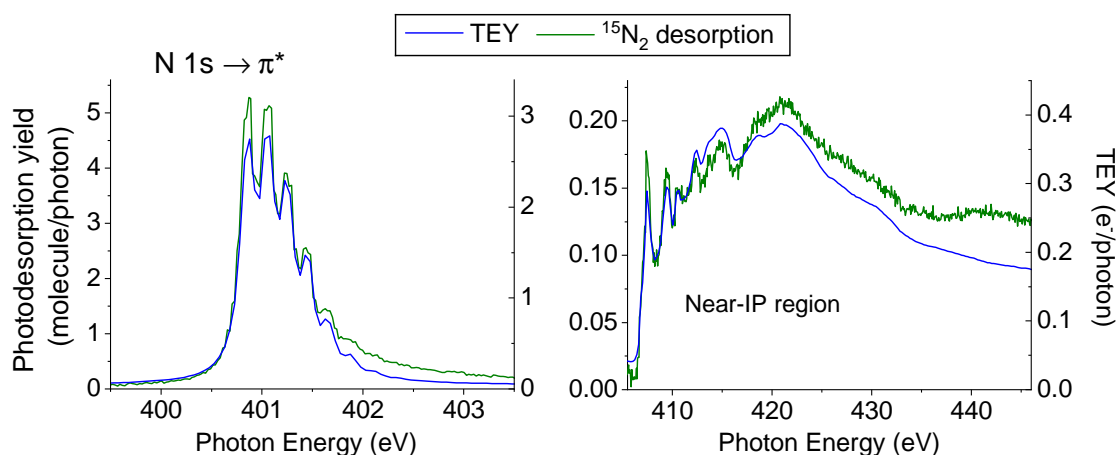


FIGURE IV.3 – X-ray photodesorption yields of  $^{15}\text{N}_2$  (green lines, left Y scale) from pure  $^{15}\text{N}_2$  ice at 15 K (50 ML) in the  $\text{N } 1s \rightarrow \pi^*$  excitation region (left panel, spectral resolution of 100 meV) and in the near-IP region (right panel, spectral resolution of 350 meV). The TEYs measured during the irradiations are also displayed for comparison (in blue lines, right Y scale).

lowing the same variations as the TEYs except for small discrepancies on the relative intensities of the features, that are likely due to background correction issues and for which we do not attribute any physical meaning. The photodesorption yields of  $^{15}\text{N}_2$  and the TEYs are obtained from an ice having received a fluence  $< 3.10^{16}$  ph  $\text{cm}^{-2}$ . They both decrease with increasing fluence due to the ice photo-aging but the shape of the spectra remains the same and no significant new absorption features are observed in the energy range probed (400 - 450 eV). Photodesorption of atomic  $^{15}\text{N}$  was only detectable (with a detection limit of  $10^{-3}$  molecule  $\text{photon}^{-1}$ ) at the  $\text{N } 1s \rightarrow \pi^*$  transition, with a yield of  $\sim 0.01$  molecule  $\text{photon}^{-1}$ , which is two orders of magnitude less than the desorption yield of  $^{15}\text{N}_2$ .

The photodesorption yields of  $^{13}\text{CO}$  and  $^{15}\text{N}_2$  from mixed  $^{13}\text{CO}:^{15}\text{N}_2$  (2:1 and 20:1) ices are displayed in Figure IV.4 in the N K-edge and O K-edge energy range. The TEYs measured simultaneously during the irradiation procedures are also displayed in dashed lines and vertically shifted for more clarity. The shape of the photodesorption spectra are well-correlated to the TEYs both at the N and O K-edge, similarly to what is observed for a pure  $^{15}\text{N}_2$  ice. There is however a small discrepancy : in the lower panels of Figure IV.4, the photodesorption yield of  $^{15}\text{N}_2$  from a mixed  $^{13}\text{CO}:^{15}\text{N}_2$  (2:1) ice is decreasing after 403 eV for the N K-edge and after 555 eV for the O K-edge whereas the corresponding TEY is constant. This is due to background correction issues. The photodesorption of  $^{15}\text{N}_2$  from mixed  $^{13}\text{CO}:^{15}\text{N}_2$  ices is significantly decreasing between the 2:1 and 20:1 ratio both at the N and O K-edge (lower panels of Figure IV.4) due to the high dilution of  $^{15}\text{N}_2$  whereas  $^{13}\text{CO}$  desorption yield is in any case found in the same

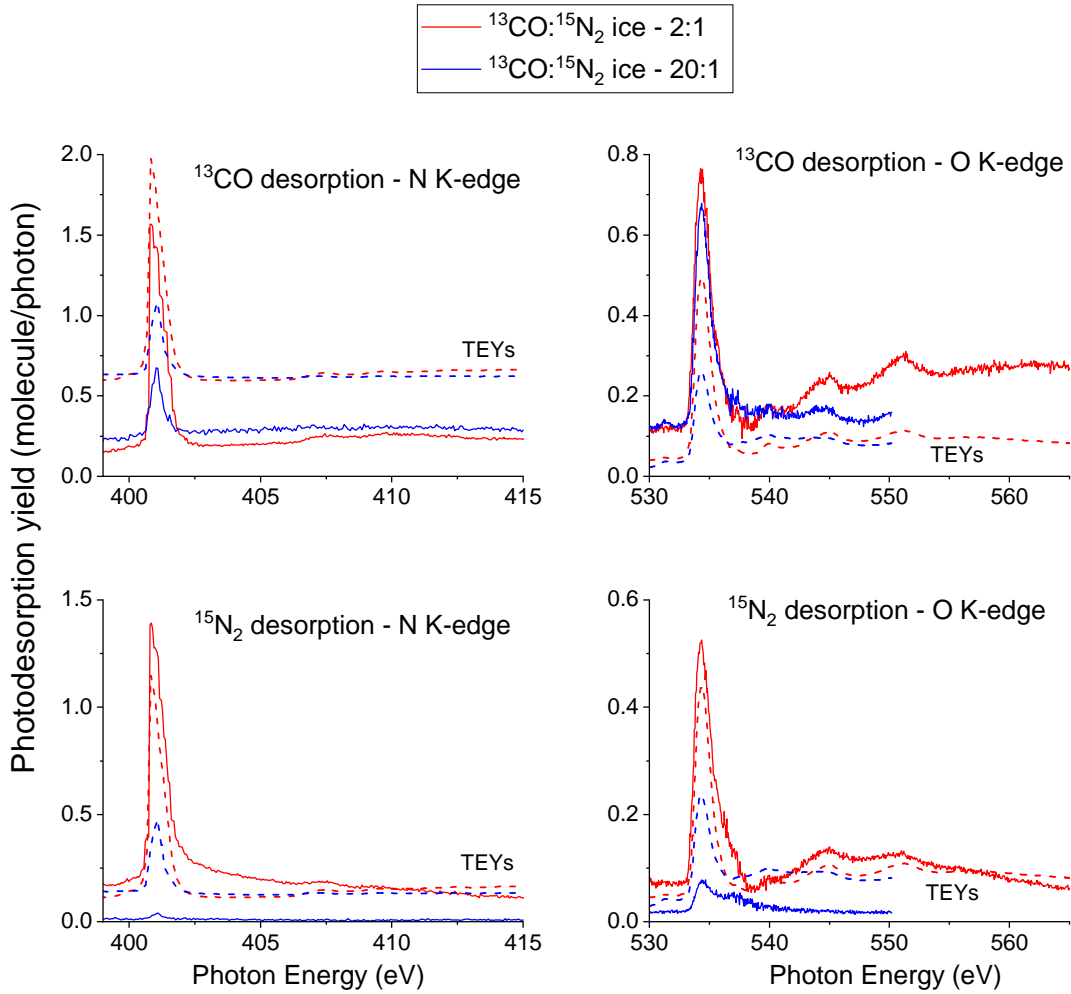


FIGURE IV.4 – X-ray photodesorption yields of  $^{13}\text{CO}$  and  $^{15}\text{N}_2$  (solid lines) in the N K-edge (left panels) and O K-edge (right panels) regions from mixed  $^{13}\text{CO}:^{15}\text{N}_2$  ices at 15 K (total of 100 ML) with mixing ratio of 2:1 (red lines) and 20:1 (blue lines). The TEYs measured simultaneously during the corresponding irradiation procedure are also displayed in dashed lines in arbitrary units.

order of magnitude (upper panels). In the case of a mixed  $^{13}\text{CO}:^{15}\text{N}_2$  (2:1) ice, the photodesorption yields of  $^{13}\text{CO}$  and  $^{15}\text{N}_2$  are found in the same order of magnitude at the  $\text{N } 1s \rightarrow \pi^*$  ( $\sim 1.4 - 1.5$  molecule photon $^{-1}$ ) and the  $\text{O } 1s \rightarrow \pi^*$  ( $\sim 0.5 - 0.7$  molecule photon $^{-1}$ ) transitions of  $^{15}\text{N}_2$  and  $^{13}\text{CO}$  respectively. This is consistent with the fact that CO and  $\text{N}_2$  have similar binding energies in mixed CO: $\text{N}_2$  ices (Öberg, K. I. et al., 2005; Bisschop et al., 2006). The fact that the photodesorption yields are lower at the  $\text{O } 1s \rightarrow \pi^*$  transition as compared to the  $\text{N } 1s \rightarrow \pi^*$  transition in the case of the 2:1 ratio is probably due to a higher absorption cross section (based on gas phase experiments) of  $^{15}\text{N}_2$  at 401 eV ( $\sim 26$  Mbarn from Kato et al. (2007)) and when considering the spectral resolution of our photon source) compared to that of  $^{13}\text{CO}$  at 534.4 eV ( $\sim 2.8 - 3.2$  Mbarn from Barrus et al. (1979)).

Photodesorption signals were observed on the mass channels 28 u. and 44 u. for the mixed ices. They could correspond to the desorption of  $^{13}\text{C}^{15}\text{N}$  and  $^{13}\text{C}^{15}\text{NO}$  respectively. However, the signals were too weak ( $S/N \gtrsim 1$ , with a yield of  $\sim 0.02$  molecule photon $^{-1}$  at the N  $1s \rightarrow \pi^*$  and the O  $1s \rightarrow \pi^*$  for both mass channels) and more easily detected in the case of a 20 :1 ratio such that we cannot totally exclude the contribution of  $^{12}\text{CO}$ ,  $^{14}\text{N}_2$  (mass 28 u.) and  $^{12}\text{CO}_2$  (mass 44 u.) photodesorption to these mass channels due to natural isotopes in our gas samples ( $\sim 1\%$ ). Finally, a desorption signal was found on the mass channel 31 u., which is associated with the X-ray photodesorption of  $^{15}\text{NO}$ . The photodesorption spectra of  $^{15}\text{NO}$  are also following the same variations as the TEYs and the corresponding yields are  $5.3 \times 10^{-2}$  molecule photon $^{-1}$  at the N  $1s \rightarrow \pi^*$  transition of  $^{15}\text{N}_2$  and  $2.7 \times 10^{-2}$  molecule photon $^{-1}$  at the O  $1s \rightarrow \pi^*$  transition of  $^{13}\text{CO}$  for a  $^{13}\text{CO} : ^{15}\text{N}_2$  (2:1) ice. Photodesorption of atomic  $^{15}\text{N}$ ,  $^{13}\text{C}$  and O was not detected from the mixed ices (with a detection limit of  $10^{-3}$  molecule photon $^{-1}$ ).

### IV.1.3 Layered ice experiment

Our experiments on mixed  $^{13}\text{CO} : ^{15}\text{N}_2$  ices highlight an indirect desorption mechanism. This is clearly seen in the mixed  $^{13}\text{CO} : ^{15}\text{N}_2$  (2:1) ice for which the photodesorption of  $^{13}\text{CO}$  at the  $^{15}\text{N}_2$  N  $1s \rightarrow \pi^*$  transition (upper left panel of Figure IV.4) and that of  $^{15}\text{N}_2$  at the  $^{13}\text{CO}$  O  $1s \rightarrow \pi^*$  transition (lower right panel of Figure IV.4) dominates the photodesorption spectrum of respectively  $^{13}\text{CO}$  and  $^{15}\text{N}_2$ . More globally, the fact that the photodesorption spectrum of  $^{15}\text{N}_2$  and  $^{13}\text{CO}$  follows the X-ray absorption spectrum of, respectively,  $^{13}\text{CO}$  near the O K-edge and  $^{15}\text{N}_2$  near the N K-edge confirms this indirect mechanism. Such mechanism should involve an energy transport from the molecule that absorbs the incident photon to the molecule that desorbs from the ice surface. The length scale of such energy transport can be defined as the maximum distance from the ice surface (or the depth) at which an absorbed photon can induce desorption or in other words, the maximum distance between the photo-absorbing molecule and the ice surface for which indirect desorption is occurring. This depth will be defined as  $\lambda_{des}$  in the following and it will be expressed in ML.  $\lambda_{des}$  depends on the indirect desorption mechanism and may vary with the photon energy and the ice composition.

Experiments with a layered ice, similar to that conducted in the VUV range by [Bertin et al. \(2013\)](#), nicely enable to estimate  $\lambda_{des}$ . The principle of the experiment is sketched in the left side of Figure IV.5. A pure  $^{15}\text{N}_2$  ice (50 ML) is first deposited on the substrate. Then, on top of it, a given number of ML of  $^{13}\text{CO}$  is deposited and the ice is irradiated to measure the photodesorption yields. This operation (deposition of  $^{13}\text{CO}$  on top and irradiation) is sequentially repeated on the same ice until reaching  $\sim 90$  ML of  $^{13}\text{CO}$  on top of the  $^{15}\text{N}_2$  ice. The idea of this experiment is therefore to trigger the

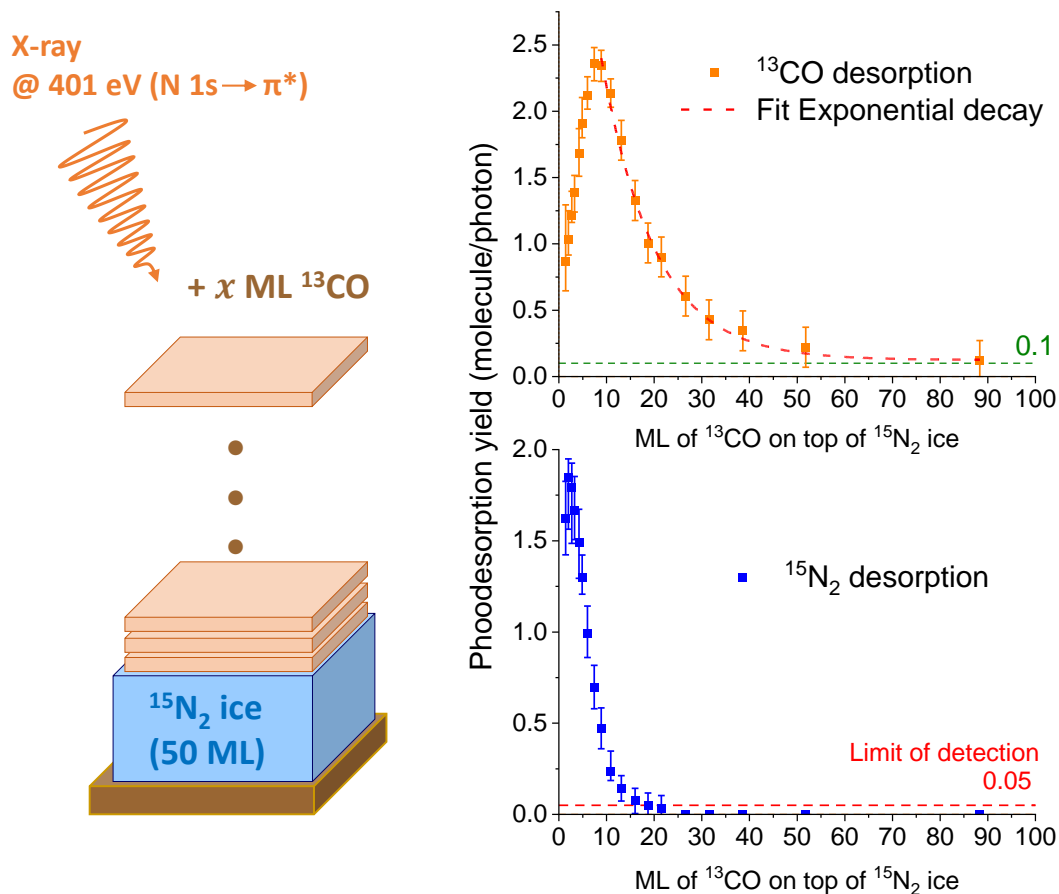


FIGURE IV.5 – Left side : scheme of the layered ice experiment, explained in more details in the text. Right side : X-ray photodesorption yields at 401 eV of  $^{13}\text{CO}$  (upper panel) and  $^{15}\text{N}_2$  (lower panel) from a layered  $^{13}\text{CO}$  /  $^{15}\text{N}_2$  ice at 15 K, as a function of the number of ML of  $^{13}\text{CO}$  deposited on top of a 50 ML  $^{15}\text{N}_2$  ice.

desorption of the above lying  $^{13}\text{CO}$  molecules by photo-excitation of the supporting  $^{15}\text{N}_2$  molecules. Monitoring the desorption signal of  $^{13}\text{CO}$  as a function of the number of ML of  $^{13}\text{CO}$  deposited on top of the  $^{15}\text{N}_2$  ice enables to estimate  $\Lambda_{des}$ . For this experiment, the photon flux was low ( $\sim 10^{11}$  photon  $\text{s}^{-1}$ ) and the irradiation time was short (a few seconds) to ensure that the number of  $^{13}\text{CO}$  molecules photodesorbed during one irradiation step are negligible compared to the number of ML of  $^{13}\text{CO}$  deposited on top of the  $^{15}\text{N}_2$  ice. Considering a X-ray photodesorption yield of  $^{13}\text{CO}$  between 1.0 and 2.4 molecule photon $^{-1}$ , an equivalent of 0.01 - 0.03 ML of  $^{13}\text{CO}$  is desorbed during one irradiation step. In comparison, the first point measured in Figure IV.5 is at 1.4 ML of  $^{13}\text{CO}$  on top of the  $^{15}\text{N}_2$  ice. We do not expect significant structural changes of the ice during each irradiation step at such low fluence. Chemical changes are also limited based on the fact that no signs of significant chemistry are observed on both the TEYs and in desorption for the previous pure and mixed irradiated ices.

The photodesorption yields at 401 eV of  $^{13}\text{CO}$  and  $^{15}\text{N}_2$  from the layered  $^{13}\text{CO}/^{15}\text{N}_2$  ice are displayed in the right side of Figure IV.5 as a function of the number of ML of  $^{13}\text{CO}$  on top of a  $^{15}\text{N}_2$  ice. At 401 eV, photo-absorption of  $^{15}\text{N}_2$  is due to the  $\text{N } 1s \rightarrow \pi^*$  transition and photo-absorption of  $^{13}\text{CO}$  is due to the ionization of its C 1s electron (IP  $\sim 296$  eV). Quantitatively speaking, and based on gas phase data, the absorption cross section of  $^{15}\text{N}_2$  and  $^{13}\text{CO}$  at 401 eV are  $\sim 20 - 40$  Mbarn and  $\sim 0.3$  Mbarn respectively (Barrus et al., 1979; Kato et al., 2007). Hence, photo-absorption at 401 eV in our layered  $^{13}\text{CO}/^{15}\text{N}_2$  ice is dominated by  $^{15}\text{N}_2$  photo-absorption. The contribution of  $^{13}\text{CO}$  photo-absorption to the desorption of  $^{13}\text{CO}$  at 401 eV can be estimated by considering that it is quantitatively similar to the photodesorption of CO from a pure CO ice at 530 eV, which exhibits a photodesorption yield of  $\sim 0.1$  molecule photon $^{-1}$  (Dupuy et al., 2021b). This stems from the fact that the photo-absorption of  $^{13}\text{CO}$  at 530 eV is also due to the ionization of its C 1s electron and that we do not expect the ionization cross section to significantly differs between 401 to 530 eV. Consequently, the photodesorption yield of 0.1 molecule photon $^{-1}$  is used as a reference to estimate the contribution of  $^{13}\text{CO}$  photo-absorption to the desorption of  $^{13}\text{CO}$  at 401 eV in our layered ice experiment (it is displayed as a horizontal dashed green line in the upper panel of Figure IV.5). From the upper panel of Figure IV.5, we observe two different regimes for the photodesorption yield of  $^{13}\text{CO}$  :

- a low to medium coverage regime, for a number of ML of  $^{13}\text{CO}$  from 1 to roughly 30 - 40 ML. In this regime, the photodesorption yield of  $^{13}\text{CO}$  is  $> 0.1 - 0.2$  molecule photon $^{-1}$  such that the desorption of  $^{13}\text{CO}$  is dominantly triggered by photo-excitation of  $^{15}\text{N}_2$ . In that case, the photodesorption yield of  $^{13}\text{CO}$  is increasing until  $\sim 10$  ML and then starts to decrease
- a high coverage regime, for a number of ML of  $^{13}\text{CO}$   $> 40$  ML. In this regime, the photodesorption yield of  $^{13}\text{CO}$  is close to 0.1 molecule photon $^{-1}$  such that the desorption of  $^{13}\text{CO}$  is dominantly triggered by photo-ionization of  $^{13}\text{CO}$ . In that case, the possible photodesorption of  $^{13}\text{CO}$  triggered by photo-excitation of  $^{15}\text{N}_2$  can be neglected

The photodesorption yield of  $^{15}\text{N}_2$  from our layered ice is displayed in the lower panel of Figure IV.5. It is decreasing as the number of ML of  $^{13}\text{CO}$  increases until it goes below our detection limit of  $\sim 0.05$  molecule photon $^{-1}$  (considering the low photon flux for this experiment) for a number of ML of  $^{13}\text{CO}$   $> 15$  ML. The fact that we still observe  $^{15}\text{N}_2$  desorption even when the  $^{15}\text{N}_2$  ice is covered by a few ML of  $^{13}\text{CO}$  may be due to diffusion of  $^{15}\text{N}_2$  from below the ML of  $^{13}\text{CO}$  or to a few  $^{15}\text{N}_2$  molecules still present at the surface due to inhomogeneous deposition of  $^{13}\text{CO}$ . This is further discussed in the next section.

#### IV.1.4 Estimation of $\Lambda_{des}$ and indirect desorption mechanisms

Our previous experiment on the layered  $^{13}\text{CO}/^{15}\text{N}_2$  ice nicely enables to estimate  $\Lambda_{des}$  for the indirect desorption process of  $^{13}\text{CO}$  induced by the photo-absorption of  $^{15}\text{N}_2$  at 401 eV. In Figure IV.5, we can see that  $^{15}\text{N}_2$  photo-absorption can induce  $^{13}\text{CO}$  desorption when the  $^{15}\text{N}_2$  ice is covered by a number of ML of  $^{13}\text{CO}$  from 1 to roughly 30 - 40 ML, with a maximum efficiency around 10 ML. After fitting, the exponential decay of the  $^{13}\text{CO}$  photodesorption yield starting at  $\sim 10$  ML is associated with a characteristic length of  $\Lambda_c \sim 11$  ML. The exponential reaches 95% extinction at  $3 \times \Lambda_c = 33$  ML, which corresponds to a good estimate of  $\Lambda_{des}$  and for which the indirect desorption of  $^{13}\text{CO}$  becomes negligible. In order to take into account the uncertainty associated with the number of ML of  $^{13}\text{CO}$ , which is approximately 10%, we finally estimate that  $\Lambda_{des}$  is between 30 - 40 ML in the case of our layered  $^{13}\text{CO}/^{15}\text{N}_2$  ice and at 401 eV. This shows that desorption can be triggered from the bulk of the ice, beyond the first few ML.

This conclusion can also be drawn for the case of mixed  $^{13}\text{CO}:^{15}\text{N}_2$  ices. In that case, the photodesorption yield of  $^{13}\text{CO}$  at the  $\text{N } 1s \rightarrow \pi^*$  transition of  $^{15}\text{N}_2$  is exactly following the variations of the TEY from a 2:1 to a 20:1 ratio (see upper left panel of Figure IV.4). This is not the case for the desorption of  $^{15}\text{N}_2$  which is barely visible in the case of a 20:1 ratio (see lower left panel of Figure IV.4). This could be explained as followed. In the case of the 2:1 ratio,  $^{15}\text{N}_2$  molecules are sufficiently present near the ice surface and within its bulk to observe desorption of both  $^{15}\text{N}_2$  and  $^{13}\text{CO}$  at the  $\text{N } 1s \rightarrow \pi^*$  transition of  $^{15}\text{N}_2$ . Whereas, in the case of the 20:1 ratio,  $^{15}\text{N}_2$  molecules are not sufficiently present near the ice surface to significantly desorb but they are sufficiently photo-absorbing from the surface to the bulk of the ice to produce a non-negligible TEY value and to induce the desorption of  $^{13}\text{CO}$ . In the case of mixed  $^{13}\text{CO}:^{15}\text{N}_2$  ices, X-ray photodesorption can therefore also be triggered from the bulk of the ice.

The value derived for  $\Lambda_{des}$  enables to discuss the possible photodesorption mechanism at play. As described in Section III.2.2, we will differentiate between XESD and non-XESD processes. We will mainly consider the following non-XESD processes associated with the energy left to the photo-absorbing molecule after Auger decay, in that case  $^{15}\text{N}_2^{+*}$ : exciton migration (process 1(a)), excitation of collective vibrational modes (process 1(b)) and kick-out by fragment diffusion (process (2)). The mechanisms are sketched in Figure IV.6 and they will be discussed with regards to the value derived for  $\Lambda_{des}$  in the following.

For a XESD process, the energy absorbed in the bulk of the ice by  $^{15}\text{N}_2$  can be transported towards the ice surface by the scattering of the Auger electron. Considering the energy deposition profile of keV electrons in light materials ( $1 \leq Z \leq 18$ ) from the work

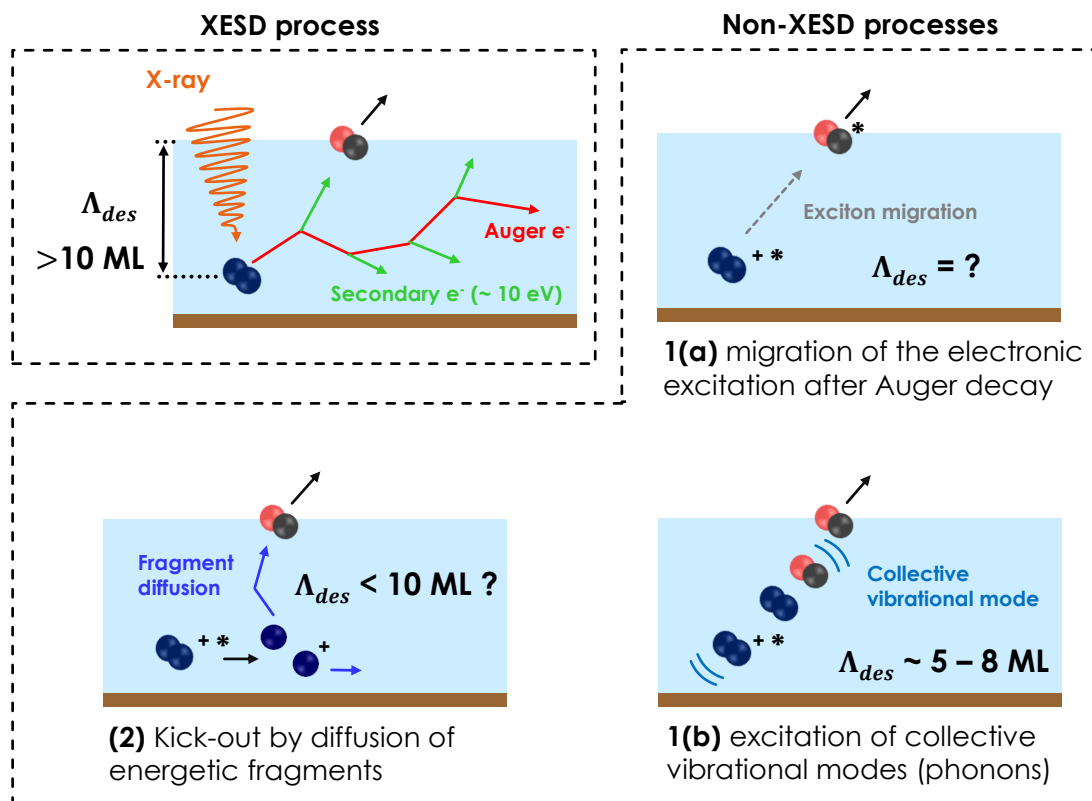


FIGURE IV.6 – Scheme of the different possible mechanisms to explain the indirect desorption of  $^{13}\text{CO}$  induced by the photo-absorption of  $^{15}\text{N}_2$  from our layered ice experiment presented in Figure IV.5. A differentiation is made between XESD and non-XESD processes, which are described in more details in Section III.2.2. For each process, the values displayed for the corresponding  $\Lambda_{des}$  (only for the XESD process and for desorption due to excitation of collective vibrational modes) are based on the literature (Valkealahti et al., 1989; Bertin et al., 2013).

of Valkealahti et al. (1989), we can reasonably expect that the Auger electron and the secondary electrons can deposit their energy through a few tens of ML. In that sense, the value of  $\Lambda_{des}$  previously estimated (30 - 40 ML) is consistent with a XESD process. The migration distance of excitons in water ice is potentially tens of ML (Petrik and Kimmel, 2003). Migration of excitons in the case of weakly interacting Van der Waals solids such as in  $^{15}\text{N}_2$  ice and migration between  $^{15}\text{N}_2$  and  $^{13}\text{CO}$  layers has not been studied yet such that the process (1)(a) cannot be discussed regarding the value derived for  $\Lambda_{des}$ . However, we expect this process to depend on the exciton state hence on the incident photon energy. This will be discussed in more details in the last section.

Process (1)(b) has been assumed to occur in Bertin et al. (2013) for the indirect desorption of  $^{13}\text{CO}$  and  $^{15}\text{N}_2$  by valence excitation of respectively  $^{15}\text{N}_2$  and  $^{13}\text{CO}$  in layered ice experiments. In that case, it has been shown that the energy can be efficiently transferred over  $\sim 5 \text{ ML}$  to the desorbing molecules at the surface (this value was similar

for excitation of  $^{13}\text{CO}$  to the  $A^1\Pi$  state and for excitation of  $^{15}\text{N}_2$  to the  $b^1\Pi_u$  state). Following the assumption made by Bertin et al. (2013), we expect process (1)(b) to be a near-surface process. Process (2) involves the diffusion of ionic or neutral fragments (in that case N or  $\text{N}^+$ ) towards the ice surface and collision with  $^{13}\text{CO}$  molecules followed by desorption. After possible dissociation of  $(^{15}\text{N}_2^+)^*$ , we expect the fragments to have less than 10 eV of kinetic energy. Although no studies are available on the typical diffusion length of such fragments in the bulk of molecular ices, we do not expect it to be comparable with the value of  $\lambda_{des}$  derived. Instead, we expect process (2) to be a near-surface process involving just the first few ML of the ice. This is also supported by the very low level of desorbing  $^{15}\text{N}$  fragments from pure  $^{15}\text{N}_2$  ice.

Processes (1)(b) and (2) are then expected to possibly occur in the low coverage regime of our layered ice experiment, for a few ML of  $^{13}\text{CO}$  on top of the  $^{15}\text{N}_2$  ice. Regarding the photodesorption yields of  $^{13}\text{CO}$  in Figure IV.5, these near-surface processes seem to be negligible compared to the processes involving deeper layers of the  $^{15}\text{N}_2$  ice, such as XESD. In fact, the yields for low coverage of  $^{13}\text{CO}$  (between 1 and 10 ML) are of the same order of magnitude than for higher coverage. In the low coverage regime, both near-surface processes and bulk processes can participate to indirect desorption whereas for higher coverage, only bulk processes participate. The fact that the yields are similar in both regimes excludes a significant contribution of the near-surface processes compared to the bulk ones. Therefore, processes (1)(b) and (2) can be neglected. In the next section, we focus on characterizing the Auger scattering for our layered ice experiment.

### IV.1.5 Modeling of the energy deposited by Auger scattering

XESD is mediated by the scattering of Auger electrons. These electrons deposit their energy through the ice via ionization and excitation of the molecules in their path. For a XESD process, the photodesorption yields are expected to be correlated to the amount of energy deposited near the ice surface by the scattering of Auger electrons. This amount of energy can be estimated based on the work of Valkealahti et al. (1989) where the author showed, by Monte Carlo simulations, that the energy deposition profile of a keV electron in a light material ( $1 \leq Z \leq 18$ ) as a function of depth can be approximated by a Gaussian distribution (in 1D). The parameters of the distribution depend on the energy of the electron and on the stopping power of the material at this energy. These parameters have been fitted for a  $\text{N}_2$  ice. We can therefore estimate the amount of energy deposited near the ice surface by the scattering of Auger electrons in the case of our layered  $^{13}\text{CO}/^{15}\text{N}_2$  ice experiment using the following methodology and assumptions (this is also sketched in the left side of Figure IV.7) :

- we consider a layered  $^{13}\text{CO}/^{15}\text{N}_2$  ice : 50 ML of  $^{15}\text{N}_2$  on top of which an increasing number of ML of  $^{13}\text{CO}$  is deposited. We neglect the photo-absorption of the  $^{13}\text{CO}$  layers at 401 eV
- we assume that the initial kinetic energy of the Auger electron emitted by relaxation of the  $\text{N } (1s)^{-1}\pi^*$  state of  $^{15}\text{N}_2$  is  $\sim 380$  eV, based on Auger spectra of gas phase  $\text{N}_2$  ([Moddeman et al., 1971](#))
- we only consider the emitted Auger electrons that statistically contribute the most to the energy deposited near the ice surface, i.e. the Auger electrons that are emitted from the bulk towards the surface of the ice
- the energy deposition profile of the Auger electrons is approximated by a Gaussian distribution with parameters taken from [Valkealahti et al. \(1989\)](#), in 1D. This also takes into account the energy loss of secondary electrons and it is computed as the sum of the average kinetic energy of all electrons in a depth element. According to the Born-Bethe approximation and Bragg's rule, the stopping power of  $^{13}\text{CO}$  and  $^{15}\text{N}_2$  at 380 eV are similar such that we reasonably assume that the energy deposition profile does not significantly differs in  $^{15}\text{N}_2$  or  $^{13}\text{CO}$  layers. The shape of the energy deposition profiles are plotted in arbitrary units in the left panel of Figure [IV.7](#) for Auger electrons emitted from three different depths within the  $^{15}\text{N}_2$  ice
- we consider that each ML of  $^{15}\text{N}_2$  is emitting a number of Auger electrons that are equal to the number of photons absorbed in that ML. It results that the relative intensity of the energy deposition distributions from two different ML is driven by a Beer-Lambert law, with an absorption cross section at 401 eV taken between 20 and 40 Mbarn ([Kato et al., 2007](#))

The energy deposited in the top layer of the  $^{13}\text{CO}$  ice is then computed by summing the contributions from each ML of  $^{15}\text{N}_2$ . This operation is repeated for an increasing number of ML of  $^{13}\text{CO}$  deposited on top of the  $^{15}\text{N}_2$  ice. The results are presented in the right panel of Figure [IV.7](#) : the energy deposited on the top layer of the  $^{13}\text{CO}$  ice is compared to the experimental photodesorption yields of  $^{13}\text{CO}$  from our layered  $^{13}\text{CO}/^{15}\text{N}_2$  ice (taken from Figure [IV.5](#)). A comparison with the sum of the photodesorption yields of  $^{13}\text{CO}$  plus  $^{15}\text{N}_2$ , which have similar photodesorption yields at 401 eV when mixed in similar stoichiometries (according to our results from mixed ices), is also done for the following discussion. At low coverage (number of ML of  $^{13}\text{CO} \lesssim 10$  ML), the ice surface is not homogeneously covered by  $^{13}\text{CO}$  molecules and the photodesorption yield

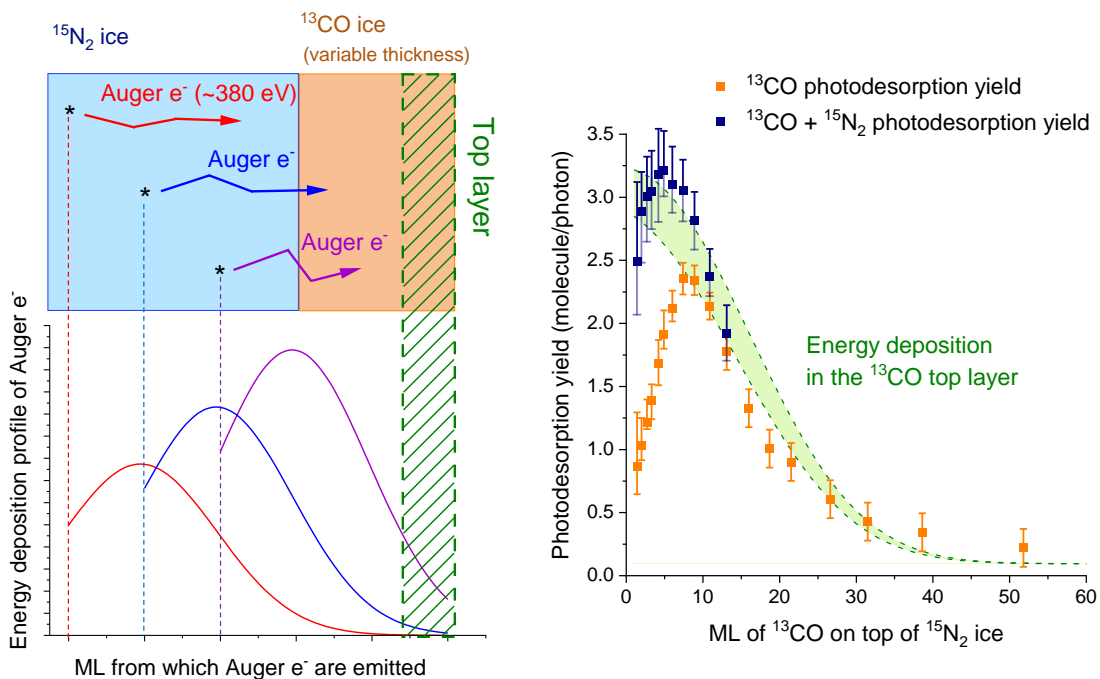


FIGURE IV.7 – Left side : scheme of our simple model to estimate the energy deposited to the top  $^{13}\text{CO}$  layer of a layered  $^{13}\text{CO}/^{15}\text{N}_2$  ice by scattering of Auger electrons. Right side : in green is displayed the estimation of this energy (in arbitrary units and where the zero of the right side distribution has been scaled with a photodesorption yield of 0.1 molecule/photon), compared with the X-ray photodesorption yields of  $^{13}\text{CO}$  (orange squares) from our layered  $^{13}\text{CO}/^{15}\text{N}_2$  ice. The blue squares show the sum of the yields of  $^{13}\text{CO}$  plus  $^{15}\text{N}_2$ . The upper and lower green curves were computed by taking a photoabsorption cross section at 401 eV of 40 and 20 Mbarn respectively.

of  $^{13}\text{CO}$  increases linearly with the number of  $^{13}\text{CO}$  molecules available for desorption. Therefore, in this regime, the photodesorption yield of  $^{13}\text{CO}$  is not correlated to the energy deposition of Auger electrons since it actually depends on the ice surface homogeneity. This lack of homogeneity is supported by the fact that  $^{15}\text{N}_2$  still desorbs in this regime. Furthermore, in this low coverage regime, we observe a good agreement between the energy deposition profile and the sum of the photodesorption yields of  $^{13}\text{CO}$  plus  $^{15}\text{N}_2$  (see blue squares in Figure IV.7). This is consistent with the ice surface being composed of a mix of  $^{13}\text{CO}$  and  $^{15}\text{N}_2$  molecules in the low coverage regime and for which photodesorption of neutral molecules is correlated to the energy deposited at the top layer and dominated by  $^{13}\text{CO}$  plus  $^{15}\text{N}_2$  desorption (no significant desorption is found for other possible neutral molecules). For medium coverage (number of ML of  $^{13}\text{CO}$  between 10 and 40 ML), the exponential decay of the  $^{13}\text{CO}$  desorption yield is in good agreement with the modeled deposited energy. For high coverage (number of ML of  $^{13}\text{CO}$  > 40 ML), the photodesorption is triggered by the photo-ionization of  $^{13}\text{CO}$  as explained previously.

These results strongly suggest that XESD is the dominant mechanism responsible for the indirect desorption of  $^{13}\text{CO}$  at 401 eV from our layered  $^{13}\text{CO}/^{15}\text{N}_2$  ice. It also confirms our estimated value for  $\Lambda_{des}$ . In that case, excitation of  $^{13}\text{CO}$  to non-dissociative states by low energy secondary electrons (produced by the Auger scattering) may be the exact mechanism explaining  $^{13}\text{CO}$  desorption. For comparison, ESD of CO from pure CO ice has an energy threshold around 6 eV (Rakhovskaia et al., 1995), which is accessible to the secondary electrons, as suggested in Dupuy et al. (2021b). This energy threshold is around 7 eV for the ESD of  $\text{N}_2$  from pure  $\text{N}_2$  ice.

Auger emission occurs with a probability close to one for each core hole state of  $^{15}\text{N}_2$  or  $^{13}\text{CO}$  above and below their respective core N 1s and O 1s ionization thresholds. The energy deposition profile due to the Auger scattering is also reasonably expected to be similar in the different ices tested in this work (pure  $^{15}\text{N}_2$  ice, mixed  $^{13}\text{CO}:^{15}\text{N}_2$  ices and layered  $^{13}\text{CO}/^{15}\text{N}_2$  ice), based on the fact that  $^{13}\text{CO}$  and  $^{15}\text{N}_2$  have similar stopping power in the energy range considered. It is therefore straightforward to consider that XESD should also play a role for the desorption of  $^{15}\text{N}_2$  from pure  $^{15}\text{N}_2$  ice and for the desorption of  $^{13}\text{CO}$  and  $^{15}\text{N}_2$  from mixed  $^{13}\text{CO}:^{15}\text{N}_2$  ices, at each photon energy. The simple model previously implemented nicely enables to estimate  $\Lambda_{des}$  for a XESD process at different photon energy as long as the photo-absorption cross section and the initial kinetic energy of the Auger electron emitted after core hole decay are known. This is used in the next section.

#### IV.1.6 Conversion of the absorbed energy to desorption

In this section, we correct our X-ray photodesorption yields by taking into account only the part of the absorbed energy that can participate to the desorption process. This results in expressing the yields in molecule  $(\text{eV deposited})^{-1}$  using equation (II.6)<sup>1</sup>. We consider that the number of the top monolayers involved in the desorption process ( $\Lambda_{des}$ ) should be at least equal to the one corresponding to a XESD process. The energy absorbed in the layers beyond  $\Lambda_{des}$  is "lost" in the sense that it cannot be converted to desorption. This results in taking  $\Lambda_{des} = 30 - 40$  ML near the N K-edge, where the photo-absorption is dominated by  $^{15}\text{N}_2$  absorption. Near the O K-edge, the photo-absorption is dominated by  $^{13}\text{CO}$  absorption and the Auger electron is expected to have an initial kinetic energy between 500 and 520 eV (Moddeman et al., 1971). Based on our simple modeling in the previous section, this results in a slightly higher  $\Lambda_{des}$  (40 - 50 ML). The results are presented in Table IV.1 (first four rows) for the desorption of  $^{13}\text{CO}$  and  $^{15}\text{N}_2$  from their respective pure ice and from mixed  $^{13}\text{CO}:^{15}\text{N}_2$  (2:1) ices at different values of the photon energy.

---

1. I remind the equation here :  $\Gamma_X^{eV}(E) = \frac{\Gamma_X(E)}{E a_{dil} (1 - e^{-\sigma(E) \Lambda_{des} b_{dil} \times 10^{15}})}$

The yields displayed in Table IV.1 represent a quantitative estimate of how efficiently the absorbed energy (only the part that can participate to the desorption process) is converted to the desorption channel. This takes into account all the desorption processes that may occur due to photo-absorption in the first  $\Lambda_{des}$  ML of the ice. The estimated yields are very similar for the desorption of  $^{13}\text{CO}$  and  $^{15}\text{N}_2$  from pure or mixed ices and at each energy considered. They range between  $\sim 0.02$  and  $\sim 0.04$  molecule (eV deposited) $^{-1}$ . There is however a small discrepancy with the photodesorption yield of  $^{15}\text{N}_2$  from pure  $^{15}\text{N}_2$  ice at 425 eV, which is lower than the previous values. This is assumed to be due to a higher fluence received by the ice before this specific measurement compared to the other ones.

TABLE IV.1 – Photodesorption yields expressed in molecule desorbed by eV deposited, of  $^{13}\text{CO}$  and  $^{15}\text{N}_2$  from different ices and at different energies, computed via equation (II.6) and by using the experimental yields derived previously. The lower and higher values of the yields are derived by taking the higher and lower value of  $\Lambda_{des}$  respectively.

Photon Energy	$\sigma$ (Mbarn) <sup>(a)</sup>	$\Lambda_{des}$ (ML)	Photodesorption yield ( $\times 10^{-2}$ molecule/eV deposited)			
			$^{15}\text{N}_2$ from		$^{13}\text{CO}$ from	
			Pure $^{15}\text{N}_2$	$^{13}\text{CO}:^{15}\text{N}_2$ (2:1)	Pure $^{13}\text{CO}$	$^{13}\text{CO}:^{15}\text{N}_2$ (2:1)
401 eV ( $^{15}\text{N}_2$ ; N 1s $\rightarrow \pi^*$ )	26	30 - 40	1.9 - 2.3	3.2 - 4.1		1.9 - 2.5
425 eV ( $^{15}\text{N}_2$ ; N 1s $^{-1}$ )	1.8	30 - 40	0.6 - 0.8	(*)		2.1 - 2.8
534.2 eV ( $^{13}\text{CO}$ ; O 1s $\rightarrow \pi^*$ )	3.0	40 - 50		2.8 - 3.5		2.1 - 2.6
570 eV ( $^{13}\text{CO}$ ; O 1s $^{-1}$ )	0.8	40 - 50		(*)	1.5 <sup>(b)</sup>	2.4 - 3.0
8.3 eV <sup>(c)</sup> ( $^{13}\text{CO}$ ; A $^1\Pi$ - X $^1\Sigma^+$ )	15	5		18	8.3	21

(\*) Background issues on the mass channel 30 around 425 eV and 570 eV during the X-ray irradiation of the  $^{13}\text{CO}:^{15}\text{N}_2$  -2:1 ice prevent us from using the experimental yields of  $^{15}\text{N}_2$  at these energies

(a) The photo-absorption cross section are taken from gas phase measurements (Barrus et al., 1979; Kato et al., 2007) and we took into account the spectral resolution of our photon source.

(b) Taken from Dupuy et al. (2021b) where it was assumed  $\Lambda_{des} = 30$  ML

(c) From Bertin et al. (2013)

These results indicate that there is presumably a unique dominant process explaining the desorption of  $^{13}\text{CO}$  and  $^{15}\text{N}_2$  from the ices tested and whose efficiency does not strongly depend on the photon energy hence neither on the photo-absorbing molecule nor on its state after Auger decay (singly or doubly ionized excited state). This is fully consistent with a XESD process for which desorption depends only on the Auger scattering, the latter being expected to not significantly differ between pure and mixed ices of  $^{13}\text{CO}$  and  $^{15}\text{N}_2$ . The similarity of the yields between  $^{13}\text{CO}$  and  $^{15}\text{N}_2$  is also consistent with their similar binding energies in pure or mixed ice (Öberg, K. I. et al., 2005; Bisschop et al., 2006). A possible significant desorption due to exciton migration from the photo-absorbing molecule (process (1)(a)) can be excluded by the fact that the efficiency of this process is expected to depend on the exciton state after Auger decay and therefore on the photon energy, which is not what we observe in Table IV.1.

Finally, in Table IV.1, we also computed the VUV photodesorption yields in molecule  $(\text{eV deposited})^{-1}$  at 8.3 eV, which corresponds to the  $A^1\Pi - X^1\Sigma^+ (2, 0)$  electronic transition of  $^{13}\text{CO}$ , from the data published in Bertin et al. (2013). In this study,  $\Lambda_{des}$  was estimated to be  $\sim 5$  ML for the indirect desorption mechanism from layered  $^{15}\text{N}_2/^{13}\text{CO}$  experiments. The yields in molecule  $(\text{eV deposited})^{-1}$  are found higher in the VUV range (at 8.3 eV) than in the X-ray range. This means that the energy absorbed by a valence excitation of  $^{13}\text{CO}$  (to the  $A^1\Pi$  state), is more efficiently converted to desorption, by non-XESD processes, than the energy absorbed by a core hole excitation or ionization (of  $^{13}\text{CO}$  or  $^{15}\text{N}_2$ ) and for which a XESD process is expected to be dominant according to our results. This is true for both the VUV photodesorption of  $^{13}\text{CO}$  (direct and/or indirect process) and  $^{15}\text{N}_2$  (indirect process) from pure  $^{13}\text{CO}$  ice and mixed  $^{13}\text{CO} : ^{15}\text{N}_2$  ice. These quantitative differences highlight the various mechanisms involved in VUV and X-ray photodesorption.

## IV.2 Mechanisms in the VUV range : internal and kinetic energy of photodesorbed CO from thick CO ice

VUV photodesorption of CO from pure CO ice has been extensively studied with various photon sources, namely broadband hydrogen microwave discharge lamps (Öberg, K. I. et al., 2007; Muñoz Caro, G. M. et al., 2010, 2016) and synchrotron radiation (Fayolle et al., 2011; Bertin et al., 2013). We focus here on the photodesorption induced by the A-X electronic transition of CO, as shown in Figure III.1 in Chapter III. The advantage of studying such system in the 8-10 eV range is that (i) CO only dissociates at energies higher than 10 eV and (ii) the induced photo-chemistry is very limited (restricted to the reaction of excited CO\* with ground state CO) such that photodesorption from a CO ice is dominated by the desorption of the intact CO. Consequently, the number of possible photodesorption mechanisms involved is reduced compared to other systems such as water ice for which multiple competing processes occur (Hama et al., 2010; DeSimone et al., 2013; Cruz-Diaz et al., 2017; Fillion et al., 2022). Finally, VUV photodesorption yield of CO from pure CO ice is relatively high ( $\sim 4 \times 10^{-2}$  molecule/photon) as compared to other systems such that we can experimentally expect to more easily catch a desorption signal, with a good signal-to-noise ratio.

The results presented in this section were obtained thanks to the VUV photon source implemented at the LERMA lab, coupled with the REMPI + TOF technique described in Chapter II.3. Before presenting them, I quickly remind the experimental technique in the following. We want to probe the internal and kinetic energy states of photodesorbed CO molecules from a pure CO ice at 15 K, by mass spectrometry and by the use of two pulsed lasers : one laser that triggers the desorption from the ice in the 8-10 eV range, referred to as the VUV pulse, and one laser that probes the photodesorbing molecules by a Resonant Enhanced Multi-Photon Ionization (REMPI) technique, referred to as the UV pulse. By varying (i) the time delay between the desorption event (VUV pulse focused on the ice) and the REMPI probing event in the ionization region (UV pulse focused in front of the ice), referred to as the Time-Of-Flight (TOF) of the desorbing molecules and (ii) the ionization wavelength  $\lambda_{ion}$  of the UV pulsed laser, we have access to the internal and kinetic energy states of photodesorbed CO molecules. This technique is selective in the sense that we can only probe photodesorbed molecules in a given state. In other words, we cannot directly detect, in one measurement, all the photodesorbing molecules in any state. This is in contrast with the synchrotron experiments described in Chapter II.2 for which the mass spectrometry technique involves an ionization by electron impact at 70 eV hence for which the photodesorbing molecules are ionized whatever their state.

In the set of experiments ran at the LERMA lab, we studied either the natural isotope of CO,  $^{12}\text{CO}$ , or the isotope  $^{13}\text{CO}$ . We did not observe any significant difference in the quantitative or qualitative results we are going to show in the following (for example, the quantification of the mean kinetic energy or the couplings between kinetic and internal states are similar). I will still indicate which isotope is associated with the graphs displayed but the reader should keep in mind that the behavior is similar between the two isotopes studied (only the ionization wavelength  $\lambda_{ion}$  slightly differs). Preliminary studies were conducted to check that the desorption signal observed during the experiments with the pulsed VUV photon source can fully and only be attributed to the one-photon A-X electronic transition of CO. In fact, a possible issue when using such pulsed VUV photon source is that the short duration of the pulse ( $\sim 10$  ns) results in non-negligible peak power (0.1 - 10 mW in our case, near 8 eV) such that processes other than the one-photon electronic transition of CO might induce desorption. These

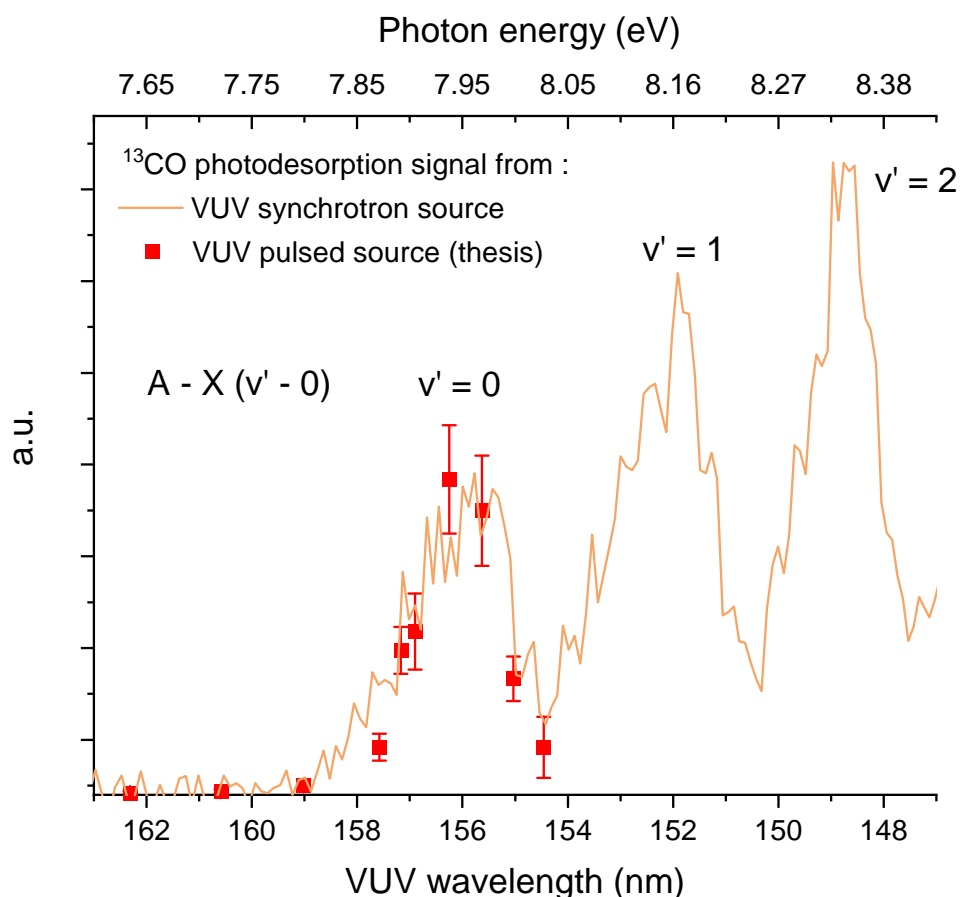


FIGURE IV.8 – VUV photodesorption signal of  $^{13}\text{CO}$  ( $v'' = 0$ ,  $J'' < 7$ ) from a pure  $^{13}\text{CO}$  ice at 15 K as a function of the incident photon wavelength for two different photon sources : synchrotron radiation (orange line, from Bertin et al. (2012)) and the VUV photon source implemented at the lab during my thesis (red squares, obtained with fixed  $\lambda_{ion}$  and TOF and after correction of the raw intensities by the VUV and REMPI fluxes).

processes mainly include the photo-thermal heating of the substrate or multi-photon processes. A sufficient way of excluding such processes is to study the wavelength dependence of the desorption signal and compare it with the photo-absorption spectrum in condensed phase (which has the same shape as the photodesorption spectrum in the energy range considered, as explained in Chapter III). This was done by monitoring the signal at a fixed  $\lambda_{ion}$  and TOF (resulting in the probing of photodesorbed CO molecules in the  $v'' = 0$  and  $J'' < 7$  state, with velocity corresponding to the maximum of the signal) and by tuning the VUV wavelength. The results are presented in Figure IV.8 for  $^{13}\text{CO}$ . One can see that the experimental data obtained with the pulsed VUV source implemented during the thesis around the A-X (0,0) band are very consistent with the photodesorption spectrum of  $^{13}\text{CO}$  obtained from synchrotron runs (taken from [Berlin et al. \(2012\)](#)), the latter being due to the one-photon A-X transition of  $^{13}\text{CO}$ . This shows desorption is indeed solely induced by the A-X transition of CO in our experiments with the new VUV photon source. The results presented in the following were obtained by setting the laser wavelengths such that the VUV output is at 157 nm ( $\sim 7.9$  eV), resulting in the excitation of CO in the A-X (0,0) band. VUV photons were routed to irradiate a pure CO ice ( $\sim 60 - 100$  ML) grown (and irradiated) at 15 K and three sets of experiment were conducted :

1. the photodesorption signal was searched for in the Q branch of the REMPI(2+1)  $\text{B } ^1\Sigma^+ (v' = 0) \leftarrow \text{X } ^1\Sigma^+ (v'' = 0)$  and the REMPI(2+1)  $\text{B } ^1\Sigma^+ (v' = 1) \leftarrow \text{X } ^1\Sigma^+ (v'' = 1)$  bands near 230.10 nm and 230.23 nm for  $\lambda_{ion}$  respectively, in order to estimate the vibrational population for low  $v''$ . Photodesorbing CO molecules in higher  $v''$  states were also searched for.
2. the ionization wavelength  $\lambda_{ion}$  was set (fixed) to the Q branch of the REMPI(2+1)  $\text{B } ^1\Sigma^+ (v' = 0) \leftarrow \text{X } ^1\Sigma^+ (v'' = 0)$  or the REMPI(2+1)  $\text{B } ^1\Sigma^+ (v' = 1) \leftarrow \text{X } ^1\Sigma^+ (v'' = 1)$  band, in the low  $J''$  region, corresponding to the Q-branch head and where the REMPI signal is maximal (as explained in Chapter II.3.5, we do not resolve the individual transitions of the Q branch associated with low  $J''$ , such that we will refer to the "low  $J''$  region" as the region for which  $J'' < 7$ ). The photodesorption signal of CO was then monitored by varying the TOF delay in the 0 - 100  $\mu\text{s}$  range in order to obtain the TOF spectra  $S(t)$ . These spectra were recorded for different distances between the substrate and the ionization region in order to check the consistency of the data. TOF spectra were also obtained for higher  $J''$  states by setting  $\lambda_{ion}$  at a clearly identified REMPI transition.
3. the photodesorption signal was monitored at a fixed TOF delay and by varying the ionization wavelength  $\lambda_{ion}$  in the Q branch of the REMPI(2+1)  $\text{B } ^1\Sigma^+ (v' = 0) \leftarrow \text{X } ^1\Sigma^+ (v'' = 0)$  and the REMPI(2+1)  $\text{B } ^1\Sigma^+ (v' = 1) \leftarrow \text{X } ^1\Sigma^+ (v'' = 1)$  bands in order to try to estimate the rotational population distribution. This was done for different TOF delays.

### IV.2.1 Relative vibrational population

The first set of experiment showed that CO molecules in the  $v'' = 0, 1$  are photodesorbing with an intensity higher by a factor of  $\sim 30 \pm 10$  for  $v'' = 0$ . These measurements were made at a TOF delay and a  $\lambda_{ion}$  for which the desorption signal is maximum and no differences were observed in the shape of the TOF and the REMPI spectra between the photodesorbing CO molecules at  $v'' = 0$  and at  $v'' = 1$  (see next sections). After correction by the Franck-Condon factors of the transitions (taken from [Imhof et al. \(1972\)](#)), which are actually similar for the  $B^1\Sigma^+ (v' = 0) \leftarrow X^1\Sigma^+ (v'' = 0)$  (0.988) and the  $B^1\Sigma^+ (v' = 1) \leftarrow X^1\Sigma^+ (v'' = 1)$  (0.97211) bands, this also gives a relative vibrational population between the  $v'' = 1$  and  $v'' = 0$  states of :

$$\frac{N(v'' = 1)}{N(v'' = 0)} = 3.3 \pm 1 \times 10^{-2}$$

If the vibrational population distribution was described by a Maxwell-Boltzmann (MB) distribution, this ratio would correspond to a temperature of  $900 \pm 100$  K. For comparison, this ratio would be equal to  $3 \times 10^{-5}$  at 300 K for a MB distribution.

In order to probe photodesorbing CO molecules for  $v'' > 1$ , as discussed in [Wurm et al. \(1996\)](#) where electron stimulated desorption was used to produce highly vibrationally excited desorbing CO molecules, the REMPI (2+1) scheme of the B-X band system is not well-suited because of (i) the predissociation character of the  $B^1\Sigma^+ (v' > 1)$  states ([Eidelsberg et al., 1987](#); [Cooper and Kirby, 1987](#)) and (ii) negligible Franck-Condon factors for the  $B (v' = 0, 1) \leftarrow X (v'' > 1)$  transitions ([Imhof et al., 1972](#)). Therefore, other REMPI schemes have to be used to fully characterize the vibrational population of photodesorbing CO molecules for  $v'' > 1$ . For instance, it is suggested in [Wurm et al. \(1996\)](#) to use the REMPI (1+1)  $A^1\Pi \leftarrow X^1\Sigma^+$  or the REMPI (1+1)  $D^1\Sigma^+ \leftarrow X^1\Sigma^+$  schemes. For instance, photodesorbing  $^{12}\text{CO}$  molecules in their  $v'' = 16$  and 19 were searched for via the REMPI (1+1)  $A^1\Pi(v' = 8) \leftarrow X^1\Sigma^+(v'' = 16)$  and the REMPI (1+1)  $A^1\Pi(v' = 9) \leftarrow X^1\Sigma^+(v'' = 19)$  transitions, near 224.9 nm and 246.40 nm respectively (as seen in [Wurm \(1995\)](#)), but no desorption signal was obtained, meaning that there are no photodesorbing CO molecules in such vibrational states. Probing other higher  $v''$  states remains to be studied at the LERMA lab.

### IV.2.2 TOF, velocity and kinetic energy distributions

The TOF spectra obtained from the second set of experiment at the Q branch of the REMPI (2+1)  $B^1\Sigma^+ (v' = 0) \leftarrow X^1\Sigma^+ (v'' = 0)$  band, in the low  $J''$  region, and for different distances between the substrate and the ionization region (denoted  $r$ ) are displayed in the upper left panel of Figure [IV.9](#) for  $^{13}\text{CO}$ . When increasing  $r$ , the TOF spectrum shifts to higher delay, consistent with the fact that it globally takes more time

for the molecules to reach the ionization region. This effect is higher for slower molecules than for fast ones, which explains the broadening of the spectrum for higher  $r$ . From these spectra, the TOF, velocity and kinetic energy distributions are deduced by applying the methodology described in Section II.3.3. Results are shown in Figure IV.9. The TOF distributions depend on  $r$  but this is not the case for the velocity and kinetic energy distributions which are equivalent at all  $r$ . The mean velocity and mean kinetic energy of the photodesorbed  $^{13}\text{CO}$  molecules in the  $v'' = 0$  and for low  $J''$  states are deduced from the distributions to be  $835 \pm 100$  m/s and  $131 \pm 40$  meV respectively and by taking an uncertainty on  $r$  of 1 mm. Similar values were obtained for  $^{12}\text{CO}$ . The temperature of the MB kinetic energy distribution associated with  $E_t = 131$  meV is equal to 760 K. This distribution is displayed in the bottom right panel of Figure IV.9 in orange. One can see that the experimental distribution is not well-represented by a MB distribution because the photodesorbed molecules are not at thermal equilibrium. The shape of the previous TOF spectra and distributions is found to be similar when

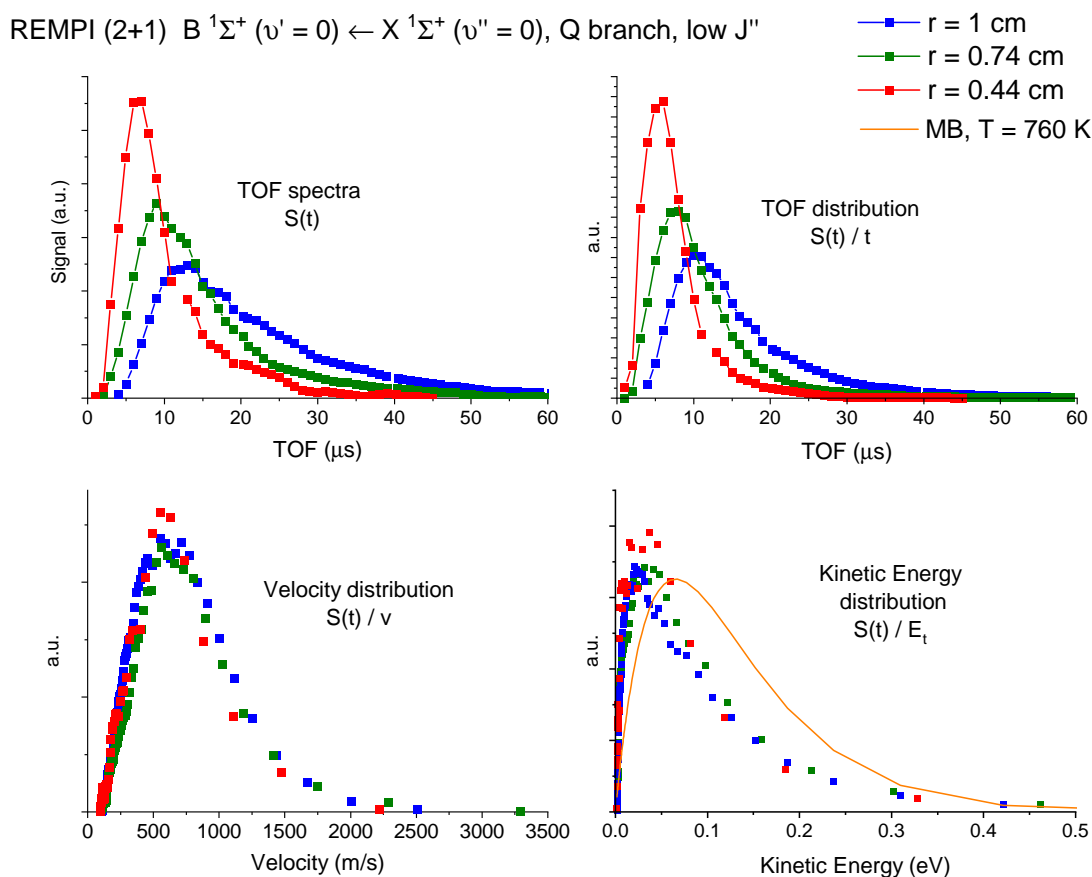


FIGURE IV.9 – From the upper left panel, clockwise : TOF spectra, TOF, velocity and kinetic energy distributions for different  $r$  obtained for photodesorbing  $^{13}\text{CO}$  molecules from a pure  $^{13}\text{CO}$  ice at 15 K. On the bottom right panel is also displayed in orange a Maxwell-Boltzmann (MB) kinetic energy distribution associated with a temperature of 760 K.

probing the photodesorbed  $^{13}\text{CO}$  molecules in the  $v'' = 1$  state via the REMPI(2+1)  $\text{B } ^1\Sigma^+ (v' = 1) \leftarrow \text{X } ^1\Sigma^+ (v'' = 1)$  band (the intensity of the raw desorption signal is however lower). This means that there is no obvious coupling between the vibrational and translational motions of the photodesorbing molecules for  $v'' = 0, 1$ . Similar results are also obtained for  $^{12}\text{CO}$  molecules.

Additionally, we obtained TOF spectra for photodesorbing  $^{12}\text{CO}$  molecules in higher  $J''$  states by setting  $\lambda_{ion}$  to the corresponding REMPI (2+1)  $\text{B}(v' = 0)\text{-X}(v'' = 0)$  transition, at  $\lambda_{ion} = 230.06$  nm for  $J'' = 27$  and at  $\lambda_{ion} = 230.04$  nm for  $J'' = 32$ . These TOF spectra are displayed in the left panel of Figure IV.10 and compared with a TOF spectrum obtained in the low  $J''$  region. The corresponding kinetic energy distributions are also shown in the right panel. One can see that there is a clear dependence of the kinetic energy distribution on  $J''$ . Namely, molecules with low  $J''$  have on average a kinetic energy lower than that of molecules with higher  $J''$ . Quantitatively speaking, we estimate, from the presented distributions, a mean kinetic energy of 131 meV, 167 meV and 207 meV for low  $J''$ ,  $J'' = 27$  and  $J'' = 32$  respectively. In other words, the CO molecules that photodesorb in a highly excited rotational state tend to have more kinetic energy than those desorbing with very little rotational energy. This coupling between the translational and the rotational motions of desorbing CO molecules can also be deduced more qualitatively by looking at REMPI spectra obtained for different TOF delays. This is discussed in the next section.

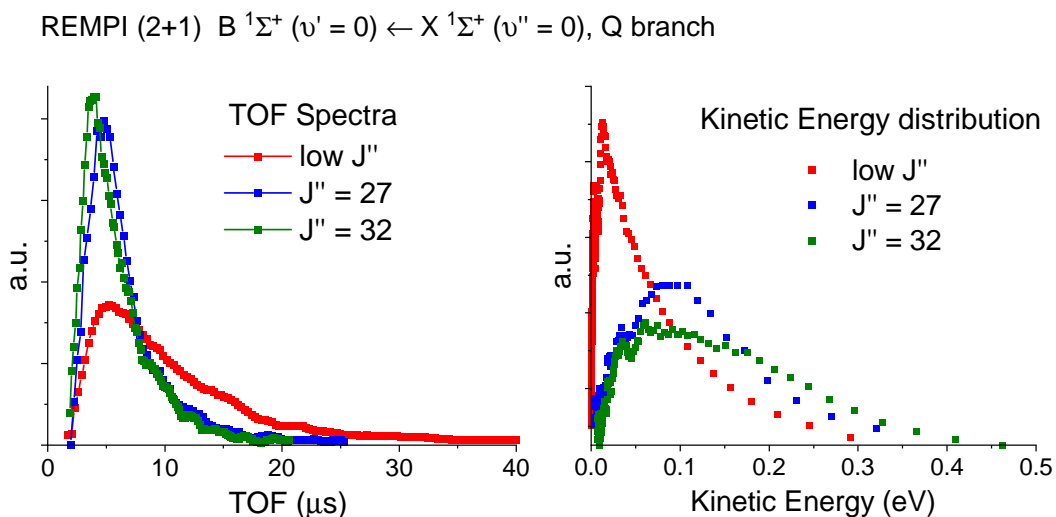


FIGURE IV.10 – Left panel : TOF spectra of photodesorbing  $^{12}\text{CO}$  molecules for different  $J''$  states at the Q branch of the REMPI (2+1)  $\text{B } ^1\Sigma^+ (v' = 0) \leftarrow \text{X } ^1\Sigma^+ (v'' = 0)$  band and at fixed  $r = 4.5$  mm. Right panel : kinetic energy distributions derived from the previous TOF spectra.

### IV.2.3 Relative rotational population

The rotational population is estimated with the third set of experiments, for the photodesorbed CO molecules in the  $v'' = 0$  state. The Q branch of an experimental REMPI(2+1) B( $v' = 0$ ) - X( $v'' = 0$ ) spectrum of such molecules is displayed in blue in Figure IV.11, for a TOF delay of 12  $\mu\text{s}$ . The global shape of the envelope of the experimental spectrum can be well-compared to a simulated one by using the PGOPHER software (Western, 2017) for a rotational temperature  $T_{rot}$  (associated with a MB distribution) of 200 K.

The REMPI spectra in the Q branch region of the REMPI (2+1) B( $v' = 0$ ) - X( $v'' = 0$ ) band were found to depend on the TOF delay, i.e. the rotational population distribution of the photodesorbing molecules depends on their velocity. This was highlighted by recording REMPI spectra for different TOF delay, as illustrated in Figure IV.12. The four experimental spectra displayed in the upper right and lower left panels were obtained by fixing the TOF delay at 6, 8, 18 and 50  $\mu\text{s}$ . This corresponds to photodesorbing molecules having a velocity of 1667, 1250, 556 and 200 m/s respectively, as displayed in the upper left panel by dashed lines. The blue REMPI spectra are then associated with "slow" molecules whereas the red ones are associated with "fast" molecules". One can

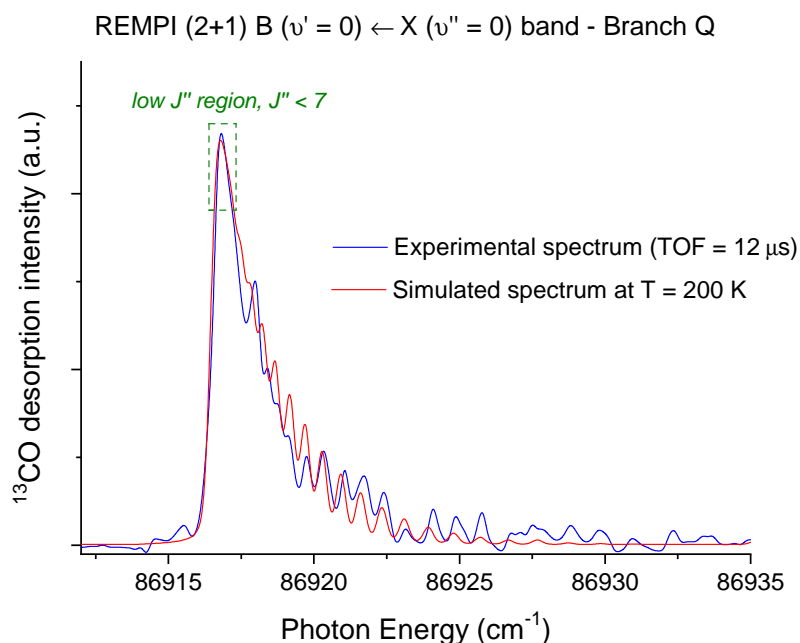


FIGURE IV.11 – In blue : REMPI (2+1) experimental spectrum of the B( $v' = 0$ ) - X( $v'' = 0$ ) band for photodesorbed  $^{13}\text{CO}$  molecules from a pure  $^{13}\text{CO}$  ice at 15 K and for a TOF delay of 12  $\mu\text{s}$ . In red : simulated spectrum of the same band for a rotational population following a MB distribution at  $T_{rot} = 200$  K. The green dashed rectangle displays the region of the spectrum where the transitions associated to a given  $J''$  cannot be resolved, which occurs for  $J'' < 7$ .

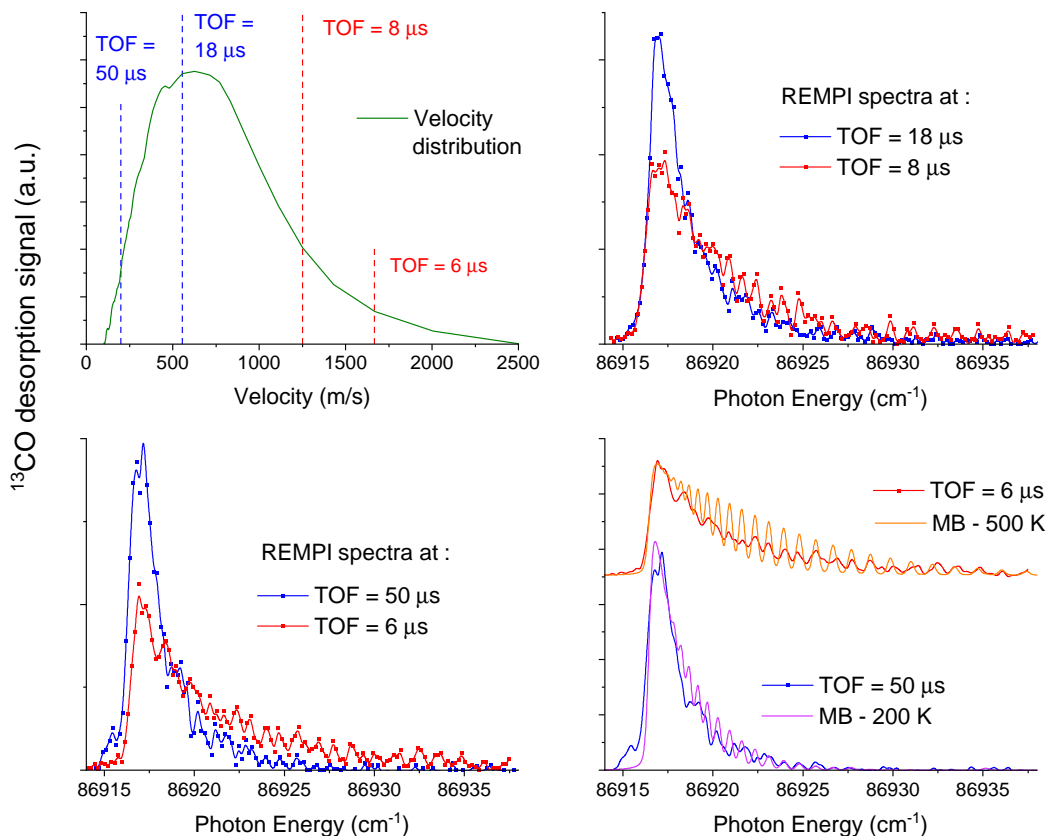


FIGURE IV.12 – Upper left panel : velocity distribution of the photodesorbed  $^{13}\text{CO}$  molecules at  $v'' = 0$  and  $J'' < 7$ . The vertical dashed lines indicate the velocity of the molecules corresponding to the TOF delay at which the REMPI (2+1)  $B(v' = 0) - X(v'' = 0)$  spectra (Q branch) of the upper right and lower left panels were done. These REMPI spectra are normalized (with respect to the curve area) in order to adequately compare them. Lower right panel : previous REMPI spectra at TOF = 6 and 50  $\mu\text{s}$  compared with their respective simulated REMPI spectra using PGOPHER (the spectra are vertically shifted for more clarity).

see that the shape of the REMPI spectra depends on the TOF delay. Namely, rotational levels with high  $J''$  are more populated for fast molecules than for slower ones. Quantitatively, we compare, in the lower right panel of Figure IV.12, the experimental REMPI spectra with simulated ones for different rotational temperatures  $T_{rot}$ . As displayed, the rotational population distribution of "slow" and "fast" molecules can be associated with a MB distribution of temperature  $T_{rot}$  at roughly 200 K and 500 K respectively although the MB distribution at 500 K follows in average only the envelope of the Q branch but does not match the individual  $J''$  lines perfectly. This is in line with what has been shown previously on TOF profiles at different  $J''$ . A similar behavior is observed for  $^{13}\text{CO}$  molecules in the  $v'' = 1$  state, probed via the Q branch of the REMPI (2+1)  $B(v' = 1) - X(v'' = 1)$  band. This means that there is no obvious coupling between the vibrational and rotational motions of the photodesorbing molecules for  $v'' = 0, 1$ .

## IV.2.4 Discussion on the photodesorption mechanisms

The theoretical study of [van Hemert et al. \(2015\)](#) can serve as a good starting point to discuss the possible photodesorption mechanisms at play in our experiment. Two different mechanisms were highlighted in this study : (1) a direct desorption mechanism for which the photo-excited molecule desorbs and (2) a kick-out mechanism by which a surface molecule is kicked-out by a neighboring photo-excited one. In these computations, the process (2) yields desorbing molecules with low vibrational, rotational and translational energy whereas the process (1) results in molecules desorbing in high vibrational states. The latter assumption is due to the fact that the de-excitation of the  $A^1\Pi$  state of CO is expected to occur via an internal conversion to the ground state, with high  $v$  ( $v \sim 48$ ). Radiative decay should be negligible because of the longer lifetime involved in this process, as argued in [van Hemert et al. \(2015\)](#). Therefore, [van Hemert et al. \(2015\)](#) mentioned that experimentalists should observe a bi-modal vibrational distribution of the desorbed molecules. Our experiment does not enable to definitively conclude on the existence of such bi-modal distribution yet as only CO molecules with high vibrational states  $v = 16$  and  $19$  were firmly found to not photodesorb. On the other hand, low vibrationally excited ( $v = 0, 1$ ) photodesorbing CO molecules were clearly observed in our experiments. As suggested in [van Hemert et al. \(2015\)](#), these molecules should desorb following an indirect process but the latter is not fully characterized in the theoretical study. According to our experimental data, the mechanism(s) associated with the photodesorption of these low vibrationally excited molecules should be consistent with the following facts :

- [1] the ratio  $N(v = 1) / N(v = 0)$  we experimentally derived is found to be  $3.3 \pm 1 \times 10^{-2}$ , which would correspond to a MB vibrational temperature of  $900 \pm 100$  K. Initially (i.e. before desorption), the CO molecules are expected to be exclusively in the  $v = 0$  state because the ice temperature is maintained at 15 K by a thermostat. Therefore, the desorption mechanism should include a non-negligible coupling with the vibrational state  $v = 1$
- [2] we did not find any significant differences in the velocity and rotational distributions between the  $v = 0$  and the  $v = 1$  states, suggesting that the desorption mechanism should be similar for these states
- [3] there is a coupling between the rotational and translational motions of the desorbing molecules. Namely, CO molecules photodesorbing in a high rotational state tend to have on average a higher kinetic energy than molecules photodesorbing in a low rotational state.

The coupling between translational and rotational degrees of freedom was also observed in an experimental study on photodesorbed NO molecules from a NiO surface (Ferm et al., 1989). Following this experimental study, the theoretical study of Hasselbrink (1990) provides a possible explanation of this coupling that can be understood in the MGR framework described in Chapter III.2.1.1. The coupling is due to the anisotropy of the substrate-adsorbate potential in the excited state, i.e. the dependence of the excited state potential with the orientation angle between the diatomic molecular axis and the surface normal. This anisotropy induces the molecule in the excited state to tend to a geometry where its molecular axis is parallel to the surface. This results in a torque effect that couples the rotation and translation motions of the molecule. The longer the molecule stays on the anisotropic excited state potential, the higher it gains translational and rotational energy due to the torque effect. The lifetime of the excited state will therefore govern the translational and rotational states of the desorbing molecules. The previous model nicely explains why the rotational energy increases with the translational energy but it describes a direct desorption process : the molecule needs to be electronically excited in order to desorb. If one considers that the photodesorbing CO molecules at  $\nu = 0, 1$  observed in our experiments are due to an indirect process, as suggested in van Hemert et al. (2015), the model of Hasselbrink (1990) cannot fully explain our results but can provide interesting insights to interpret the data.

In van Hemert et al. (2015), the indirect process is suggested to be due to a kick-out mechanism induced by the large vibrational amplitude of the initially excited  $^{13}\text{CO}$  molecule which found itself in a high  $\nu$ , after internal conversion from the excited state to the ground state. However, the exact couplings between the vibrational motion of the initially photo-excited molecule and the degrees of freedom of the desorbing one are not detailed. It is also important to mention that the authors did not find any correlation between the rotational and translational energies of the desorbed molecules, which contradicts our observation [3]. Finally, this shows that additional theoretical studies are mandatory in order to explain our experimental observations. To such end, theoretical simulations are currently being carried out at the PhLAM lab in collaboration with the LERMA lab, with promising preliminary results.

### IV.3 Conclusion and perspectives

The previous results obtained during this thesis enable to better understand and characterize the physical mechanisms responsible for photodesorption in ices made of diatomic molecules :

- in the X-ray range, it was found that XESD is the dominant process for the desorption of neutral molecules, as it was already suggested in previous X-ray photodesorption experiments. The study conducted in this thesis brings additional strong arguments showing that the desorption is governed by the Auger scattering which is a signature of the XESD process. The simple model implemented enables to estimate the desorption relevant depth as a function of the photon energy as long as the energy of the Auger electron, the photo-absorption cross section and the deposition energy profile of the Auger electrons are known. Namely, the desorption relevant depth should increase with increasing Auger energy in the X-ray range. In astrophysical environments, the XESD process implies that X-ray photodesorption should significantly depend on the ice composition due to indirect desorption. More precisely, the composition in the first tens of ML plays a role. The methodology proposed for comparing the photodesorption yields in molecules desorbed by eV deposited is also a useful tool to discuss the photodesorption mechanisms, both in the X-ray and VUV range. The previous results raise the question of the role of the Auger scattering for COMs-containing ices. In that case, it is strongly expected that the chemistry induced by the Auger scattering, dominated by the interaction of the molecules with the secondary low energy electrons, will play a role for desorption. This will be further discussed in Chapter VI. Finally, as X-ray photodesorption is mediated the Auger scattering, electron-stimulated desorption (ESD) experiments could possibly mimic the role played by the Auger electrons if the incident electrons are of the same energy. ESD studies could therefore appear as a good complementary tool to study X-ray photodesorption from interstellar ice analogues, with the advantage of being directly implementable at a lab compared to the case of X-ray experiments that necessitate having access to a synchrotron facility. However, ESD and X-ray experiments might not be directly comparable. For instance, the energy deposition profile of incident electrons in the case of ESD experiments differ from that of Auger electrons emitted from the ice bulk in the case of X-ray experiments, which might influence the desorption of molecules from the ice surface. During my thesis, I participated in ESD studies conducted at the ISMO lab on methanol ice. The objective was indeed to compare ESD results to X-ray experiments conducted at the synchrotron SOLEIL, in order to validate or not the ability of ESD to mimic X-ray photodesorption. The results of such studies will be summarized in Chapter VI.
- in the VUV range, the new set-up implemented and the methodology proposed open up a lot of possibilities to study the physical mechanisms at play in desorption from molecular ices. This was illustrated by the very first data obtained

on photodesorbed CO molecules from a pure CO ice, which revealed the couplings involved in the desorption process and the energy left to the desorbing molecules. Compared to similar set-ups implemented in other labs (for example see [Hama et al. \(2010\)](#); [DeSimone et al. \(2013\)](#)), the advantage of the technique developed during this thesis resides in the tunability of the VUV photon source, which enables to cover the whole 7 - 14 eV range, similarly to what is provided by synchrotron facilities. Experiments conducted at lower VUV wavelengths with the new VUV photon source have been already undertaken during the writing of this thesis, opening the possibility to induce the A-X ( $v' = 1$ ,  $v'' = 0$ ) transition. Comparison of the translational, vibrational and rotational population distributions with the previous results will certainly provide additional insights to understand the desorption mechanism. The lower photon flux provided by this photon source, compared to the ones used in the experiments cited above, is also more relevant to study photodesorption in the context of astrophysics. This technique will especially be useful to study the indirect desorption process of N<sub>2</sub> by photo-excitation of CO, observed in the study of [Bertin et al. \(2013\)](#). Extending the studies to COM-containing ices will also be possible. With this technique, we therefore expect to substantially progress in our understanding of VUV photodesorption from molecular ices and its role in the ISM.

## Chapter V

# VUV photodesorption of COMs

The studies presented in this chapter have been conducted at the SOLEIL synchrotron facility, on the DESIRS beamline, in 2020. They focus on the VUV photodesorption of acetonitrile  $\text{CH}_3\text{CN}$ , formic acid  $\text{HCOOH}$  and methyl formate  $\text{HCOOCH}_3$  from pure ices and from interstellar ice analogues for which the COM is embedded in a CO-rich or  $\text{H}_2\text{O}$ -rich environment. These latter experiments enable to study the influence of the ice composition on the photodesorption of COMs, with the particular aim of estimating the relevance of indirect desorption i.e. the promotion of the COM desorption induced by photo-absorption of CO or  $\text{H}_2\text{O}$ , a process known to be efficient for more simple molecules, as depicted in Chapter III. Previous results on the VUV photodesorption of  $\text{CH}_3\text{OH}$  (Öberg, K. I. et al., 2009a; Cruz-Diaz et al., 2016; Bertin et al., 2016; Bulak et al., 2020) will also be compared with the present results. I will first discuss together the data on  $\text{HCOOH}$  and  $\text{HCOOCH}_3$  as these molecules display a very similar behavior in desorption from their pure and CO/ $\text{H}_2\text{O}$ -mixed ices. Then I will present the case of  $\text{CH}_3\text{CN}$ . Interestingly, our experimental data are very consistent with astronomical observations. Average astrophysical yields will be derived and the implementation of VUV photodesorption of COMs in astrochemical models will be discussed with regards to the general behavior observed in our experimental data.

## V.1 VUV photodesorption of HCOOH and HCOOCH<sub>3</sub>

VUV photodesorption from HCOOH and HCOOCH<sub>3</sub> containing ices has never been studied before and the data presented in this section are the very first data obtained on this topic. As HCOOH and HCOOCH<sub>3</sub> behave similarly in desorption, I will present together the experimental photodesorption yields from HCOOH and HCOOCH<sub>3</sub> containing ices, first in their respective pure ice and secondly in CO and H<sub>2</sub>O-rich ices. The pure ices and the CO-containing ices were grown and irradiated at 15 K whereas the H<sub>2</sub>O-containing ices were formed at 90 K (to ensure that the resulting water ice is in its compact amorphous phase) and irradiated at 15 K after cooling down the substrate. The desorption yields were derived from "fresh" ices : the photon fluence received by the ice during the measurements from 7 to 13.5 eV by step of 0.5 eV goes from zero to  $\sim 1 \times 10^{17}$  ph/cm<sup>2</sup>, meaning that the yields are associated with ices having received a photon fluence  $< 1 \times 10^{17}$  ph/cm<sup>2</sup>.

### V.1.1 Pure ice

Experiments conducted on pure ices of HCOOH and HCOOCH<sub>3</sub> have revealed the desorption of a collection of neutral species. The associated photodesorption yields as a function of the photon energy (referred to as the photodesorption spectra in this thesis) are presented in Figure V.1 for HCOOH and Figure V.2 for HCOOCH<sub>3</sub>. In these figures, the mass channels 18 u., 28 u., 29 u., 30 u. and 44 u. were attributed to the desorption of H<sub>2</sub>O, CO, HCO radical, H<sub>2</sub>CO, and CO<sub>2</sub> respectively, which are observed in both the cases of HCOOH and HCOOCH<sub>3</sub> irradiation. In addition, signals on the

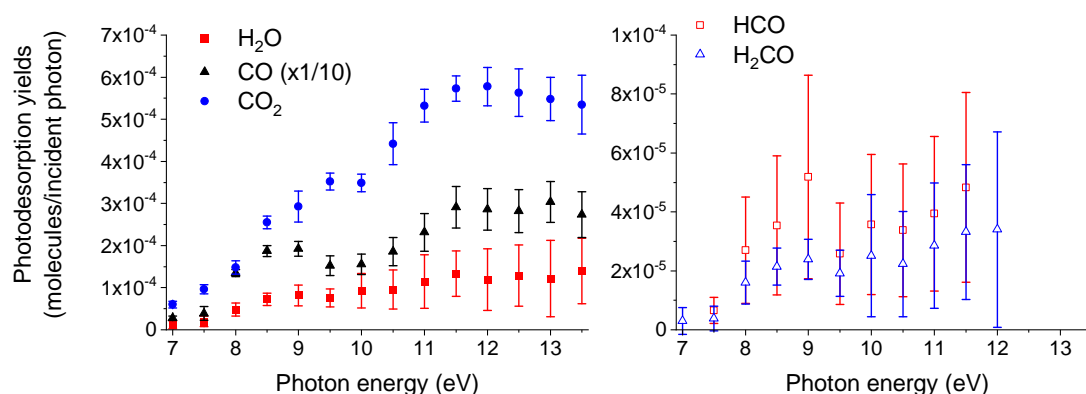


FIGURE V.1 – Photodesorption yields of neutral species from 60 ML of pure HCOOH ice at 15 K. Yields for the mass channel 29 u. and 30 u. (associated with the desorption of HCO and H<sub>2</sub>CO respectively) could not be confidently isolated from the noise for photon energies above 12 eV, and are thus not shown. For clarity, the photodesorption of CO were divided by 10.

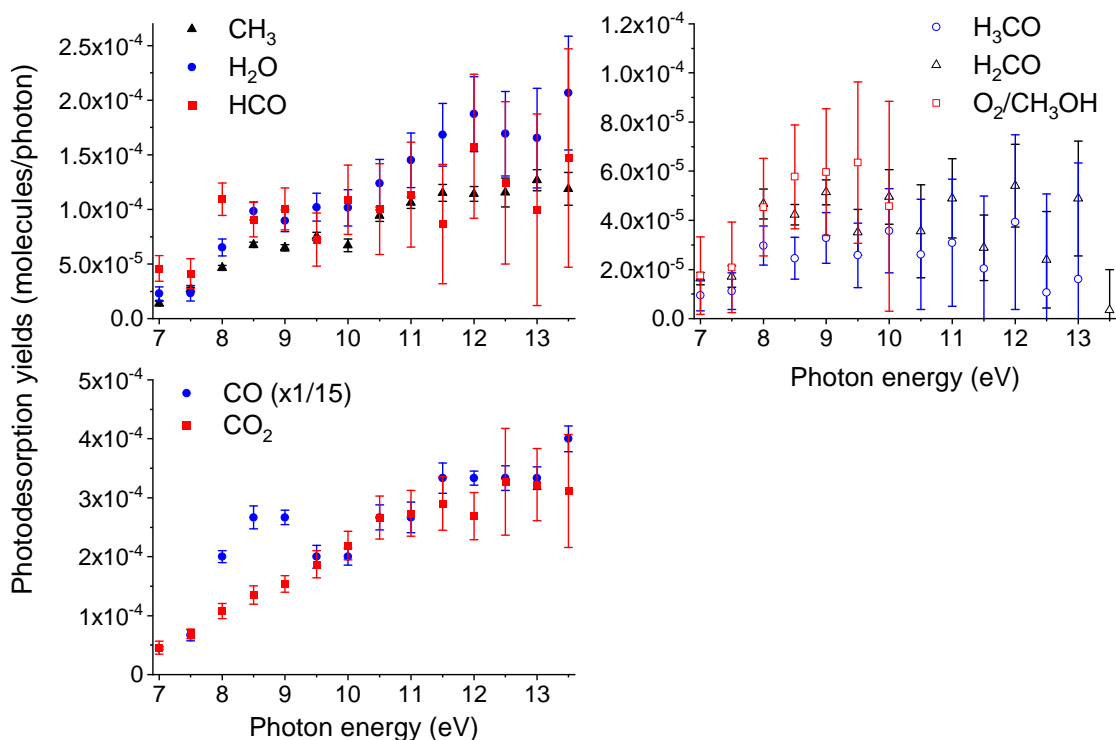


FIGURE V.2 – Photodesorption yields of neutral species from 60 ML of pure  $\text{HCOOCH}_3$  ice at 15 K. Yields for the mass channel 32  $u$  (mainly associated with the desorption of  $\text{O}_2$ , and probably some  $\text{CH}_3\text{OH}$ ) could not be isolated from the noise for photon energies above 10 eV, and are thus not shown. For clarity, the photodesorption of CO were divided by 15.

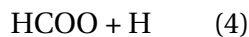
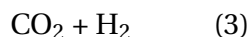
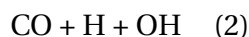
mass channels 15  $u$ ., 31  $u$ . and 32  $u$ . were observed from pure  $\text{HCOOCH}_3$  ice. The mass channel 15  $u$ . is attributed to the desorption of  $\text{CH}_3$  radical. The origin of the mass 32  $u$ . signal measured in the case of photodesorption from pure  $\text{HCOOCH}_3$  ice (Figure V.2) has been mainly attributed to  $\text{O}_2$  desorption. The mass 32  $u$ . could also correspond to the  $\text{CH}_3\text{OH}^+$  ion resulting from the ionization of some desorbing methanol  $\text{CH}_3\text{OH}$  or originating from the dissociative ionization of  $\text{HCOOCH}_3$ . The latter has been ruled out since no  $\text{HCOOCH}_3^+$  ion was detected during the experiments. Methanol dissociative ionization in the QMS is also expected to produce an important signal on the 31  $u$ . mass channel, actually higher than the 32  $u$ . signal, associated with the  $\text{CH}_3\text{O}^+$  ion (see NIST database; Wallace). In our case, we indeed detected a small signal on the mass channel 31  $u$ ., but almost three times weaker than the signal on the 32  $u$ . channel, thus ruling out the fact that 32  $u$ . solely corresponds to methanol. Moreover, if one considers that the signal at 32  $u$ . is only  $\text{O}_2$ , then the correction of its dissociative ionization into the QMS brings the level of a small signal detected on the mass 16  $u$ . channel exactly to zero (within error bars, and after correction from the water dissociative ionization). This further motivated our attribution of the mass 32  $u$ . and 31  $u$ . to respectively  $\text{O}_2$

and H<sub>3</sub>CO radical photodesorption from pure HCOOCH<sub>3</sub> ice, even if the desorption of a very small quantity of methanol, slightly participating to these two mass signals, cannot be totally ruled out.

In the case of condensed HCOOH, the desorption yields of each species follow the same energy dependence, depicting a constant increase over the whole energy range, with a small local depth at around 10 eV. We thus expect this structure to be representative of the VUV absorption spectrum of solid HCOOH, even if a direct comparison was not possible as such data are not available in the literature. The same conclusion can be drawn for solid HCOOCH<sub>3</sub>, for which most of the photodesorption spectra show the same energy-dependence (within error bars), but whose VUV absorption spectrum is not available to our knowledge. However, a notable exception is the case of CO photodesorption from pure HCOOCH<sub>3</sub> ice whose spectrum presents a clear local maximum at  $8.5 \pm 0.5$  eV. The structure can be in fact associated with the solid CO absorption feature related to the  $A(^1I) - X(^1\Sigma^+)$  transition, which presents a structured vibronic band in this energy range (Lu et al., 2005; Cruz-Diaz et al., 2014a) strongly coupled to desorption (Fayolle et al., 2011). Indeed, during irradiation, some of the formed CO can remain in the condensed phase, in return available to absorb another photon and desorb. This phenomenon, due to the accumulation of photoproducted CO in the solid, has already been observed in the case of pure CO<sub>2</sub> ices (Fillion et al., 2014), and infrared spectroscopy has confirmed the formation and accumulation of CO in the irradiated HCOOCH<sub>3</sub> ice.

Pure ices of both HCOOH and HCOOCH<sub>3</sub> behave similarly under VUV irradiation. Probably the most striking finding of these experiments is that no photodesorption of the intact molecule could be measured and only an upper limit of  $5 \times 10^{-6}$  molecule/photon and  $1 \times 10^{-5}$  molecule/photon can be derived for the photodesorption yield of HCOOH and HCOOCH<sub>3</sub> respectively. For both species, the photodesorption is dominated by the desorption of the CO molecule, followed by the desorption of CO<sub>2</sub> and H<sub>2</sub>O. The desorption of O<sub>2</sub>, CH<sub>3</sub> and H<sub>3</sub>CO could only be detected from HCOOCH<sub>3</sub>, while HCO and H<sub>2</sub>CO were detected from both HCOOH and HCOOCH<sub>3</sub> ices. Those species match the direct photo-dissociation pattern of both HCOOH and HCOOCH<sub>3</sub> as studied in the gas phase.

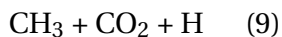
Photo-dissociation of gas phase HCOOH in the UV and VUV range results in the following fragmentations (Tabayashi et al., 1999; Su et al., 2000; Hashinokuchi et al., 2002; Schwell et al., 2006; Tso et al., 2020) :



Except for the channel (4), each of these dissociation pathways can explain the detected photodesorbed species. The photodesorption of H and H<sub>2</sub> cannot be confidently measured with our QMS, and OH may actually photodesorb, but could not be separated from the background noise after correction of H<sub>2</sub>O dissociative ionization on the 17 u. mass signal. Desorption of some H<sub>2</sub>CO is also detected, but is not explained by photo-dissociation of HCOOH as known from gas phase experiments. This could be due either to a dissociation pathway specific to the condensed phase, or to the result of subsequent chemistry in the ice, e.g. triggered by hydrogen atoms released from channel (2) or (4), leading to the H<sub>2</sub>CO formation and desorption.

The gas phase branching ratios of the previous dissociation channels for HCOOH in the studies of [Schwell et al. \(2006\)](#) and [Tso et al. \(2020\)](#) are somehow consistent with our photodesorption yields, although they are derived at 193 nm. Channels (1) and (3) are found to be the major dissociation channels in gas phase, with the channel (1) being dominant over channel (3). Interestingly, this seems to be consistent with our VUV photodesorption yields as that of CO is found to be higher than that of CO<sub>2</sub> at each photon energy. It is clear however that the previous gas phase dissociation channels and their branching ratios cannot alone explain the photodesorption yields. For instance, the desorption of H<sub>2</sub>O, expected to originate from channel (1) hence also associated with the formation of CO, displays a yield lower than that of CO and CO<sub>2</sub>. The adsorption energy of the photo-fragments, expected to be significantly higher for H<sub>2</sub>O than for CO and CO<sub>2</sub>, might participate into explaining the relative intensity of the VUV photodesorption yields derived from our experiments. Additionally, branching ratios in the solid phase are not necessarily expected to be similar than in the gas phase due to the inter-molecular interactions between molecules in the solid, especially in pure HCOOH ice where dimers are most probably formed.

Gas phase HCOOCH<sub>3</sub> photo-dissociation in the UV range has also been studied, e.g. by [Schwell et al. \(2006\)](#), [Lee \(2008\)](#) and [Nakamura et al. \(2015\)](#). The main identified dissociation channels are :



If one considers similar fragmentation patterns in the solid phase, detected photodesorbing CO, CO<sub>2</sub>, CH<sub>3</sub>, HCO and H<sub>3</sub>CO from pure solid HCOOCH<sub>3</sub> can all be attributed to direct photo-dissociation of the condensed methyl formate molecules. However, gas phase studies do not highlight H<sub>2</sub>O, O<sub>2</sub> or H<sub>2</sub>CO as results of photo-dissociation of methyl formate. Similarly to the case of H<sub>2</sub>CO from HCOOH, those species may originate from different dissociation pathways or from photochemistry in the solid HCOOCH<sub>3</sub> coupled to desorption. Contrary to the case of HCOOH, the gas phase branching ratios of the dissociation channels for HCOOCH<sub>3</sub> (at 193 nm from [Lee \(2008\)](#)) are clearly not consistent with our photodesorption yields. Indeed, the channel (7) is found to be the dominant one in the gas phase whereas the desorption of HCO and H<sub>3</sub>CO is not dominating from pure HCOOCH<sub>3</sub> ice in our experiments. This again shows that, although a qualitative agreement can be found between the photo-fragments observed in gas phase and that desorbing from the ice, gas phase studies alone cannot explain the VUV photodesorption yields.

### V.1.2 Mixed and layered ices

In order to estimate the role played by the molecular environment on the photodesorption, model ices of HCOOH and HCOOCH<sub>3</sub> embedded in a CO or H<sub>2</sub>O-rich ice were studied. For each COM, four kinds of mixed ices were investigated : icy mixture of CO:COM and H<sub>2</sub>O:COM, in which either CO or H<sub>2</sub>O were in excess, or layered ices consisting of 1 ML of the COM deposited onto a pure CO or a pure compact amorphous H<sub>2</sub>O ice. [Figure V.3](#) presents an overview of the desorbing species, together with their photodesorption yields, for an irradiation at a photon energy of 10±0.5 eV. As in the case of pure ices, no signal associated with the desorption of the intact HCOOH or HCOOCH<sub>3</sub> molecule could be detected. In these cases, only an upper limit similar to the previous ones ( $5 \times 10^{-6}$  molecule/photon and  $1 \times 10^{-5}$  molecule/photon for HCOOH and HCOOCH<sub>3</sub> respectively) can be derived from our data.

CO desorption is slightly enhanced when the COMs are codeposited with CO molecules. Indeed, CO weakly absorbs, and photodesorbs, in the 9.5 - 10.5 eV region ([Fayolle et al., 2011](#)), and thus some of the detected CO from mixed ices come from the excitation and desorption of the co-deposited CO molecules. The H<sub>2</sub>O photodesorption

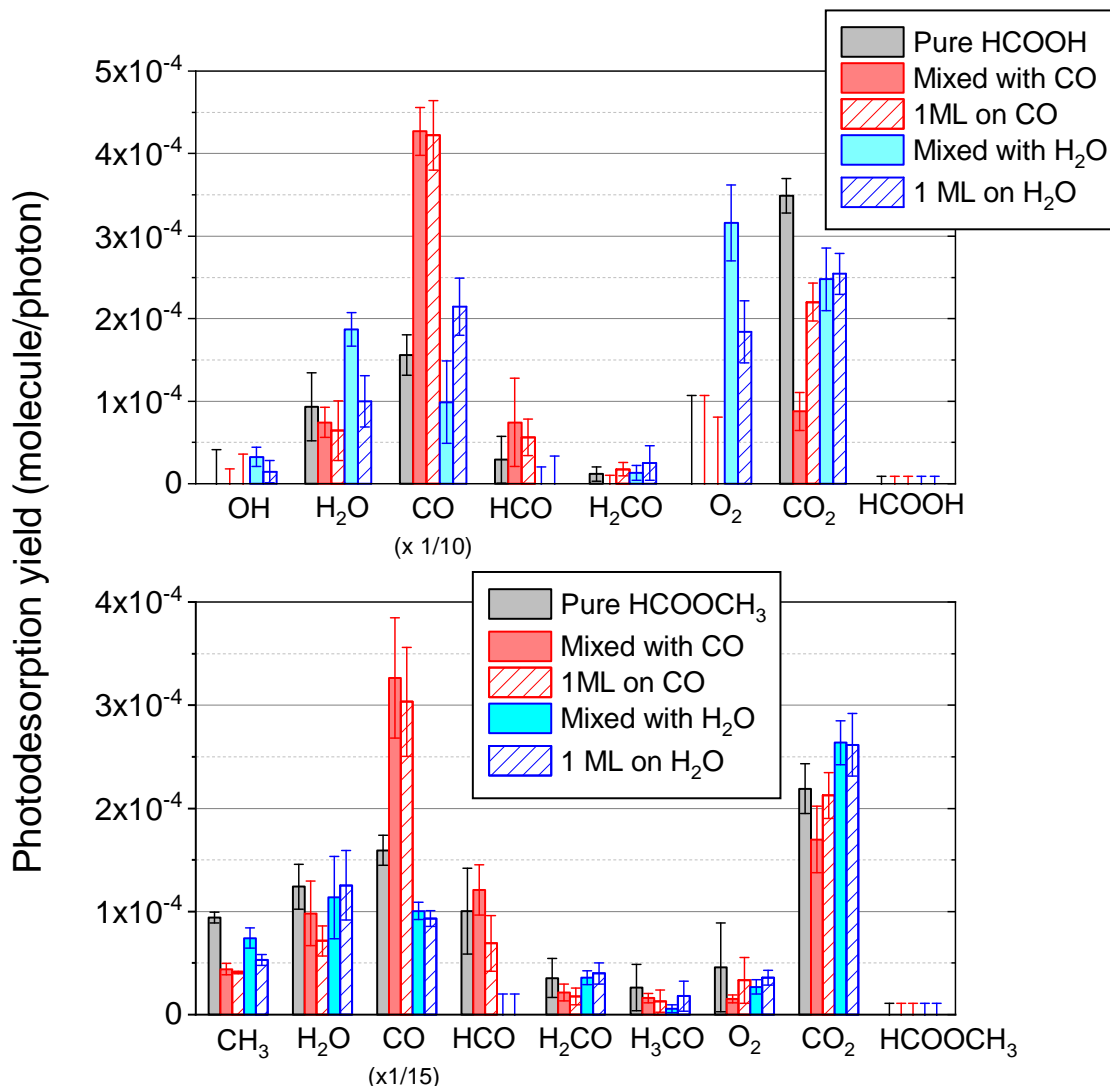


FIGURE V.3 – Photodesorption yields of neutral species from HCOOH and HCOOCH<sub>3</sub>-containing ices at 15 K, during irradiation with  $10 \pm 0.5$  eV photons and a flux of  $2.3 \times 10^{14}$  photons/s. Top : photodesorption from 60 ML of pure HCOOH, HCOOH mixed in 60 ML of CO (1:10), HCOOH mixed in 60 ML of H<sub>2</sub>O (1:10), 1 ML HCOOH on top of 30 ML of CO, and 1 ML HCOOH on top of 30 ML of H<sub>2</sub>O. Bottom : photodesorption from 60 ML of pure HCOOCH<sub>3</sub>, HCOOCH<sub>3</sub> mixed in 60 ML of CO (1:10), HCOOCH<sub>3</sub> mixed in 60 ML of H<sub>2</sub>O (1:3), 1 ML HCOOCH<sub>3</sub> on top of 30 ML of CO, and 1 ML HCOOCH<sub>3</sub> on top of 30 ML of H<sub>2</sub>O. The photodesorption yields of CO were artificially divided by 10 (top panel) and 15 (bottom panel) for clarity.

yields are also found poorly dependent on the ice composition, and almost not varying when the COMs are mixed with water. This is surprising at first since some codeposited H<sub>2</sub>O is expected to photodesorb when irradiated, and thus should, together with the dissociation of the COM, contribute to the total H<sub>2</sub>O desorption yield. VUV photodesorption of H<sub>2</sub>O from pure water ice at  $\sim 10$  eV are experimentally estimated between

$5 \times 10^{-4}$  and  $1 \times 10^{-3}$  molecules/photon, the latter value being derived from an amorphous porous ice and not a compact one (Öberg, K. I. et al., 2009b; Cruz-Diaz et al., 2017; Fillion et al., 2022). Here, H<sub>2</sub>O desorption yields are found at best more than two times lower, even from mixed ices with water. An explanation would be that coadsorption with the COM prevents the desorption of H<sub>2</sub>O from the water ice. Indeed, Fillion et al. (2022) proposed that the water photodesorption process from pure water ice, under our flux and fluence conditions, are due to a large extent to the photochemistry at the ice surface, reforming H<sub>2</sub>O molecules from H and OH radicals, which then desorb. Adjunction of the COM in the vicinity may perturbate this chemistry and hinder the water desorption by recombination, leaving mainly the COM fragmentation as a source of gas phase H<sub>2</sub>O.

OH and O<sub>2</sub> desorption are observed during irradiation of HCOOH:H<sub>2</sub>O mixed ices, but are not detected from pure HCOOH ice or in HCOOH:CO mixtures. These desorptions may originate from the desorption from the solid water itself, since the measured yields are comparable to the O<sub>2</sub> and OH photodesorption yields from pure water ice (Cruz-Diaz et al., 2017; Fillion et al., 2022). However, O<sub>2</sub> desorption is not modified in the case of HCOOCH<sub>3</sub> mixed with water, and no OH signal could be measured for these systems. The origin of O<sub>2</sub> and OH desorption from HCOOH:H<sub>2</sub>O mixed ice is thus still unclear, and could be linked either to some H<sub>2</sub>O-catalysed photochemistry or to different HCOOH dissociation branching ratio at the surface of the water ice. Finally, desorption of HCO is not detected anymore when HCOOCH<sub>3</sub> is mixed in a H<sub>2</sub>O-rich environment. HCO is believed to originate from the photo-dissociation of methyl formate also leading to some H<sub>3</sub>CO production, desorption of which is not affected by the coadsorption with water molecules. The absence of HCO desorption is still unclear, but may be associated with some chemistry between the radical HCO and H<sub>2</sub>O molecules. A similar effect is also observed in the HCOOH:H<sub>2</sub>O ices, for which the HCO desorption is also found below the detection limit. Our studies do not bring evidence, however, of this chemistry, which may lead e.g. to some CO and CO<sub>2</sub> production, as it cannot be disentangled from the much higher quantities already detected directly from the dissociation of the COM.

For each ice, all the desorbing species are identical to the case of the pure ices, except for the case of OH and O<sub>2</sub> desorption which is detected from HCOOH-containing ices only when formic acid is coadsorbed with H<sub>2</sub>O. This indicates the weak role played, in our flux and fluence conditions, by the photochemistry involving the different components of the ices, or at least that potential photochemistry is not correlated to the desorption phenomenon. This is further corroborated by the fact that the desorbing species, namely CO, CO<sub>2</sub>, H<sub>2</sub>O and H<sub>2</sub>CO for HCOOH and HCOOCH<sub>3</sub> and additionally CH<sub>3</sub>, H<sub>3</sub>CO and O<sub>2</sub> for HCOOCH<sub>3</sub>, present very similar photodesorption yields, most of

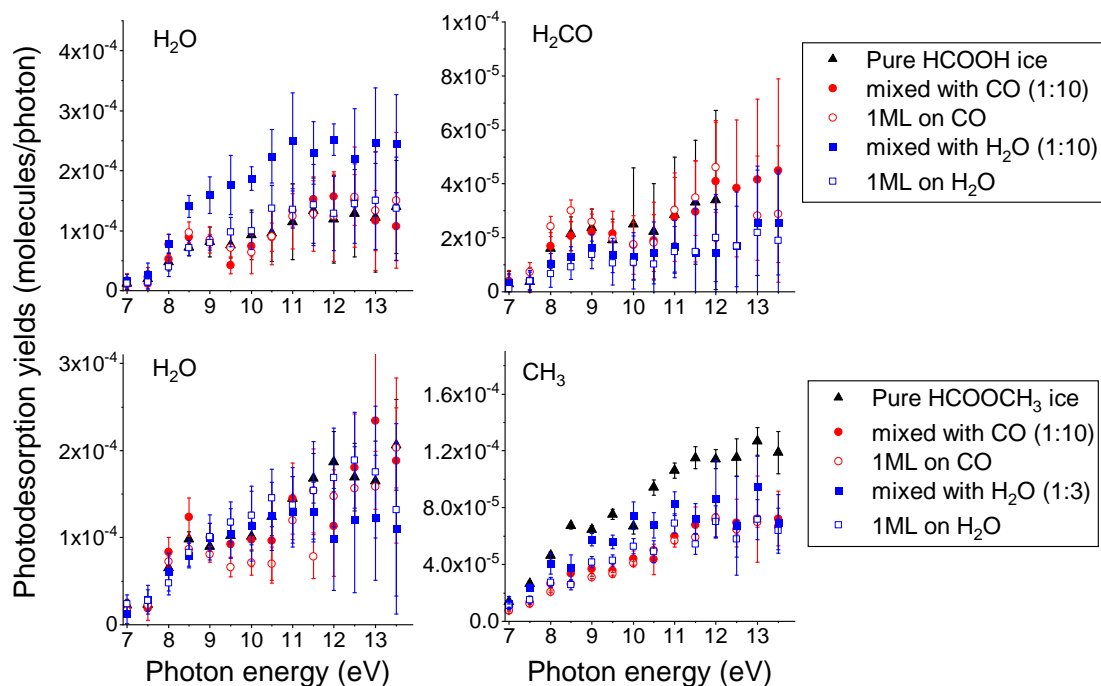


FIGURE V.4 – Photodesorption yields of some neutral species from HCOOH (top panels) and HCOOCH<sub>3</sub> (bottom panels) 60 ML containing ices at 15 K : pure ice, 1 ML of the COM onto pure ices of CO and H<sub>2</sub>O and mixed ices where the COM is embedded in a CO or H<sub>2</sub>O-rich ice

the time identical within error bar for each system, pure or mixed, with the exception of HCO whose desorption is not detected in H<sub>2</sub>O-containing ices. This stresses that the previous species most likely originate from the dissociation of the COM alone, and that their desorption does not depend on the local molecular environment.

Photon-energy dependent photodesorption yields from the mixed ices were also measured. Some example of photodesorption spectra from mixed ices are shown in Figure V.4. Except for the CO desorption from CO-containing ices, the global shape of the desorption spectra reflect the ones of the pure HCOOH or HCOOCH<sub>3</sub>. There again, the strong similarities between the pure and the mixed COM suggests that most of the observed desorption is due to the COM photo-absorption and subsequent dissociation, and that the matrix plays here a minor role. The low energy resolution employed here, the error bars and the broadness of the spectra prevent however to totally rule out any contribution of the H<sub>2</sub>O or CO photo-absorption in the photodesorption yields of water-containing ice. It is clear however that those contributions should be minimal.

## V.2 VUV photodesorption of CH<sub>3</sub>CN

Recent experimental investigations on CH<sub>3</sub>CN VUV photodesorption were conducted using an indirect method in the 7-10.2 eV range (Bulak et al., 2020). UV photodesorption of CH<sub>3</sub>CN from pure CH<sub>3</sub>CN ice was estimated to be  $< 7.4 \times 10^{-4}$  molecule desorbed by incident photon. This study is so far the only constraint on the VUV photodesorption of CH<sub>3</sub>CN from pure CH<sub>3</sub>CN ices. In the following study, we quantify the VUV photodesorption, in the 7-13.6 eV range, of CH<sub>3</sub>CN from pure CH<sub>3</sub>CN ice and from CH<sub>3</sub>CN mixed with or on top of CO and H<sub>2</sub>O ices. VUV photodesorption yields of photo-products are also derived. The yields are obtained as a function of the incident VUV photon energy. As for the case of HCOOH and HCOOCH<sub>3</sub>, the pure ices and the CO-containing ices were grown and irradiated at 15 K whereas the H<sub>2</sub>O-containing ices were formed at 90 K and irradiated at 15 K. Similarly, the desorption yields were derived from "fresh" ices i.e. having received a photon fluence  $< 1 \times 10^{17}$  ph/cm<sup>2</sup>. The results presented in this section were published in Basalgète et al. (2021c).

### V.2.1 Pure ice

In Figure V.5, we present the VUV photodesorption spectra derived from our experiments on pure CH<sub>3</sub>CN ices and we also compare these spectra with the VUV absorption spectrum (in the 7 - 11.2 eV range) of pure CH<sub>3</sub>CN ice at 10 K from Sivaraman et al. 2016. The attribution of photo-products to the mass channels is discussed in the following. The VUV photodesorption of masses 15 u. and 26 u. is attributed to CH<sub>3</sub> and CN respectively, which are expected to be direct UV photo-dissociation products of CH<sub>3</sub>CN. This is consistent with the UV photo-dissociation of gas phase acetonitrile for which C-C bond breaking is observed (Moriyama et al., 1998; Kanda et al., 1999). HCN and CH<sub>4</sub> are observed as major photo-products in VUV photolysis experiments of pure CH<sub>3</sub>CN ice at 20 K (Bulak et al., 2021) and 12 K (Hudson and Moore, 2004). Accordingly, we attributed the masses 16 u. and 27 u. to CH<sub>4</sub> and HCN photodesorption respectively. HCN was also proposed as a possible direct UV photo-dissociation product of CH<sub>3</sub>CN in gas phase by Schwell et al. 2008. We assumed that the mass 39 u. corresponds to CHCN photodesorption. Based on gas phase experiments for which H-loss reaction is assumed to occur for the UV photo-dissociation of CH<sub>3</sub>CN (Moriyama et al., 1998; Schwell et al., 2008), the detection of CHCN in our experiment could be expected to come from dehydrogenation of CH<sub>3</sub>CN induced by VUV photo-absorption. A raw photodesorption signal was detected on the mass 40 u., which could correspond to the desorption of CH<sub>2</sub>CN. However, when considering the fragmentation of the mass 41 u. (CH<sub>3</sub>CN) into the mass 40 u. (CH<sub>2</sub>CN<sup>+</sup>) in the ionization chamber of our QMS, the corrected signal on the mass 40 u. falls below our detection limit of  $\sim 1 \times 10^{-6}$  molecule/photon (this is also the case for the binary mixed ices in the next section).

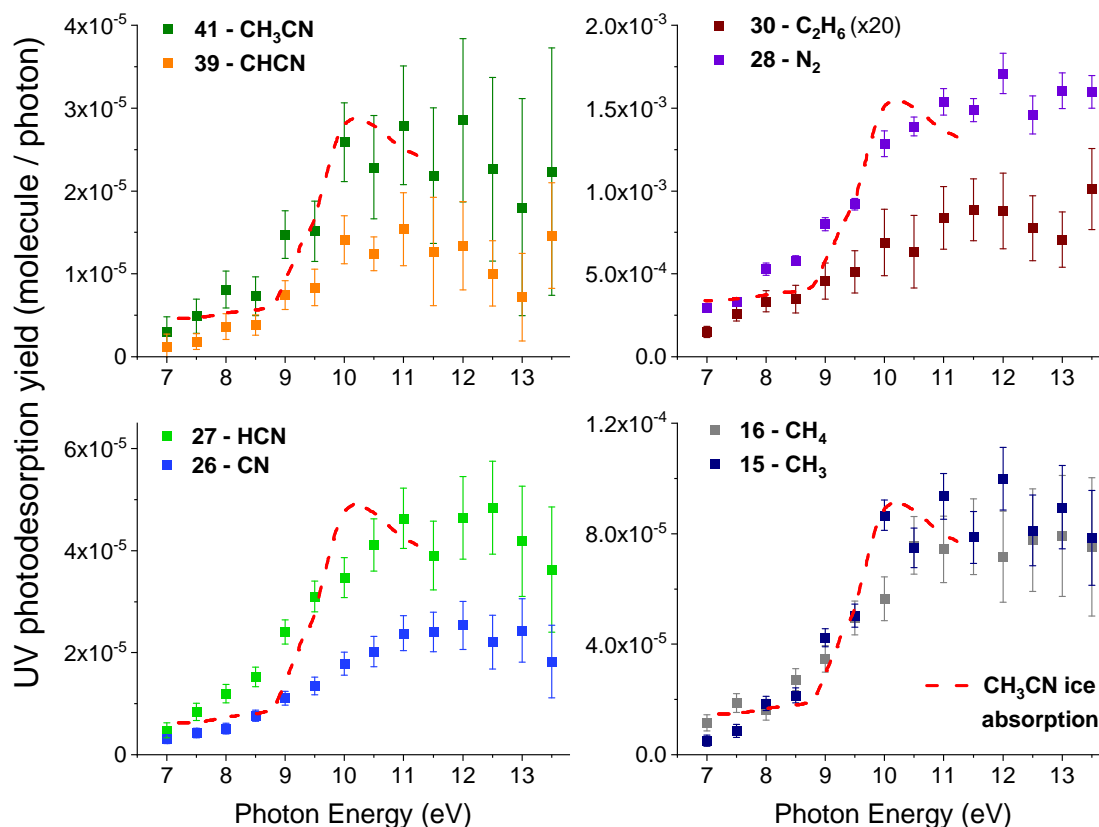


FIGURE V.5 – VUV photodesorption spectra (squares with error bars), as a function of the incident photon energy, of  $\text{CH}_3\text{CN}$  (mass 41),  $\text{CHCN}$  (mass 39),  $\text{C}_2\text{H}_6$  (mass 30),  $\text{N}_2$  (mass 28),  $\text{HCN}$  (mass 27),  $\text{CN}$  (mass 26),  $\text{CH}_4$  (mass 16) and  $\text{CH}_3$  (mass 15) from pure  $\text{CH}_3\text{CN}$  ice at 15 K. Each mass channel is corrected from the cracking of higher masses fragmentation in the mass spectrometer. The attribution of species to the mass channels is discussed in the text. In each panel, we also displayed in red dashed lines the VUV absorption spectrum of  $\text{CH}_3\text{CN}$  ice at 10 K (in arbitrary units) from [Sivaraman et al. 2016](#).

Additionally, [Hudson and Moore 2004](#) has observed the isomerization of  $\text{CH}_3\text{CN}$  into  $\text{CH}_3\text{NC}$  during VUV irradiation (with an hydrogen lamp) of pure  $\text{CH}_3\text{CN}$  ice at 12 K. This isomerization was detected by infrared via the  $-\text{N}\equiv\text{C}$  stretching mode at  $2170\text{ cm}^{-1}$ . From [Hudson and Moore 2004](#), we could expect to have only a few percent of  $\text{CH}_3\text{CN}$  isomerization during our irradiation experiments and we did not observe the  $-\text{N}\equiv\text{C}$  stretching mode by infrared on pure  $\text{CH}_3\text{CN}$  ices (this is also the case for the binary mixed ices in the next section). Therefore, we made the assumption that the VUV photodesorption of the mass 41 u. in our experiments is dominated by  $\text{CH}_3\text{CN}$  desorption rather than  $\text{CH}_3\text{NC}$ . The isomerization of  $\text{HCN}$  into  $\text{HNC}$  was not observed by [Hudson and Moore 2004](#) and accordingly, we estimated that the VUV photodesorption of the mass 27 u. in our experiments is dominated by  $\text{HCN}$  desorption and not its isomer  $\text{HNC}$ .

The mass 30 u. was attributed to  $C_2H_6$  desorption, assumed to originate from radical-radical reaction between  $CH_3$  after photo-dissociation of  $CH_3CN$ . The mass 28 u. is the most desorbing one in our experiments. It could be attributed to  $N_2$ ,  $H_2CN$  and/or  $C_2H_4$  VUV photodesorption. Post-irradiation TPD experiments have also revealed a mass 28 u. desorption features which peaks below 40 K, and intensity of which increases with the total irradiation fluence; and not observed on non-irradiated ices (see Figure V.6). This indicates that the irradiation also implies the accumulation of the associated species into the ice during irradiation. Among all the possible candidates at the origin of the mass 28 u. channel, the low desorption temperatures points toward its association with  $N_2$  (sub)monolayer desorption (Collings et al., 2004; Smith et al., 2016). Accordingly, we assumed that the photodesorption of the mass 28 u. from pure  $CH_3CN$  ice was dominated by  $N_2$ . The formation of  $N_2$  might result from photochemistry involving  $CN^*$  which is left in electronically excited states ( $A^2II$ ,  $B^2\Sigma^+$ ) after dissociation of  $CH_3CN$  according to gas phase experiments (Schwell et al., 2008). It should be noted however that TPD is not in itself sufficient to be categorical on this attribution, since, for instance,  $C_2H_4$  could also contribute to this mass 28 u. signal, even if it should be observed at slightly higher temperature in the TPD curves. Any

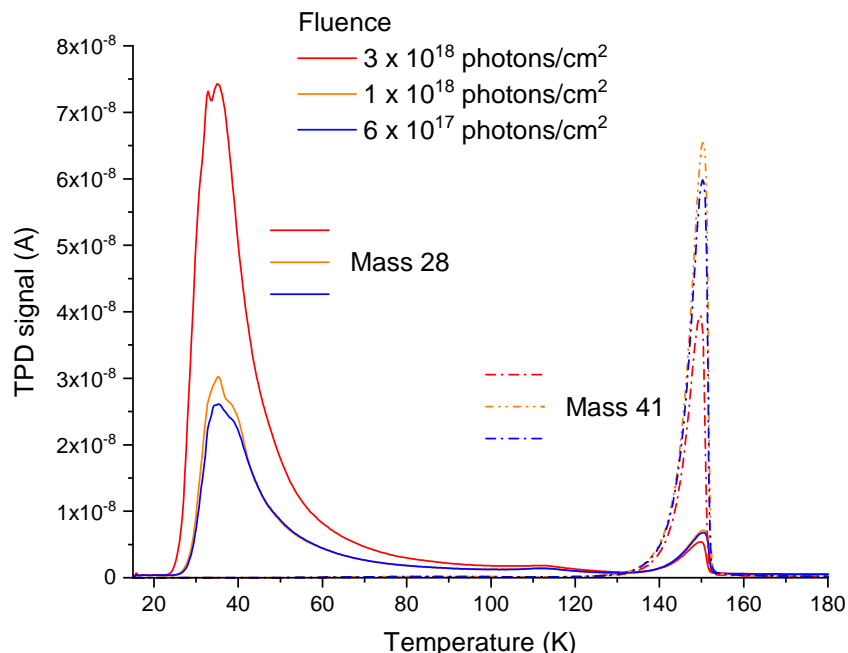


FIGURE V.6 – TPD signal on the mass 28 (solid lines) and 41 (dash dot lines) from pure  $CH_3CN$  ices as a function of the substrate temperature, conducted after the irradiation procedures. The fluence received by the ice before the TPD is also displayed. The TPD curves were recorded using a constant heating rate of 12 K/min.

possible uncontrolled pollution by another species, such as CO, has been ruled-out by (i) blank experiments, (ii) the correlation with the photon fluence, and (iii) the fact that no CO vibration could have been detected using in-situ infrared spectroscopy on the irradiated samples. The mass signal 14 u. was not monitored during the TPD experiments, which prevents us from definitively concluding on the origin of the mass 28 u. thanks to a possible fragmentation of  $N_2$  into N. A mass signal 14 u. was however detected during photodesorption experiments but it was high enough so that the possible fragmentation of  $N_2$  into N in the ionization chamber of our QMS has no significant impact on its amplitude, which also prevents us from definitively concluding. The photodesorption of this mass 14 u. is therefore due to either  $CH_2$  radical or atomic N photodesorption.

The VUV photodesorption spectra of the species presented in Figure V.5 have the same dependence in energy : the photodesorption efficiency is increasing from 7 to 10-10.5 eV and seems to be constant above 10.5 eV. The small variations above this energy are significantly lower than the error bars, and cannot be confidently considered as a "real" modification of the photodesorption yields. We can also see that there is a good correlation between the VUV absorption spectrum of  $CH_3CN$  ice and the VUV photodesorption spectra of the different molecules presented. The similarities between these spectra indicate that the photodesorption of these species originates from the same phenomena, which is the VUV absorption of  $CH_3CN$  in condensed phase. Concerning the photodesorption efficiencies, they range from  $\sim 1.2 \times 10^{-5}$  molecule/photon for CHCN to  $\sim 1.6 \times 10^{-3}$  molecule/photon for  $N_2$ , around 10.5 eV. Finally, the VUV photodesorption yield of intact  $CH_3CN$  is  $\sim 2.5 \times 10^{-5}$  molecule/photon at 10.5 eV. Our results compare very well to the recent study of [Bulak et al. 2020](#) who could not measure directly the photodesorption yield of  $CH_3CN$  from pure  $CH_3CN$  ice but provided an upper limit of  $7.4 \times 10^{-4}$  molecule/photon, compatible with our measurements.

## V.2.2 Mixed and layered ices

In Figure V.7, we summed up our results on  $CH_3CN$ , HCN and CN photodesorption from the binary ices tested : mixed  $CH_3CN:CO$  ice, mixed  $CH_3CN:H_2O$  ice and layered ices ( $\sim 1$  ML of  $CH_3CN$  on top of pure CO and on top of pure  $H_2O$  ice). For the specific case of  $CH_3CN$  photodesorption from a mixed  $CH_3CN:CO$  (1:7) ice, the yields above 10.5 eV are not shown for more visibility because of the large error bars. In addition to the presented molecules in Figure V.7, we searched for the desorption of masses 42 u., 43 u., 45 u. and 52 u. which could correspond to CNO, HCNO,  $NH_2CHO$  (formamide) and  $C_2N_2$  respectively. However, the signals on these channels were too noisy to derive a photodesorption yield and we can only provide an upper limit of  $5 \times 10^{-6}$  molecule/photon for these masses.

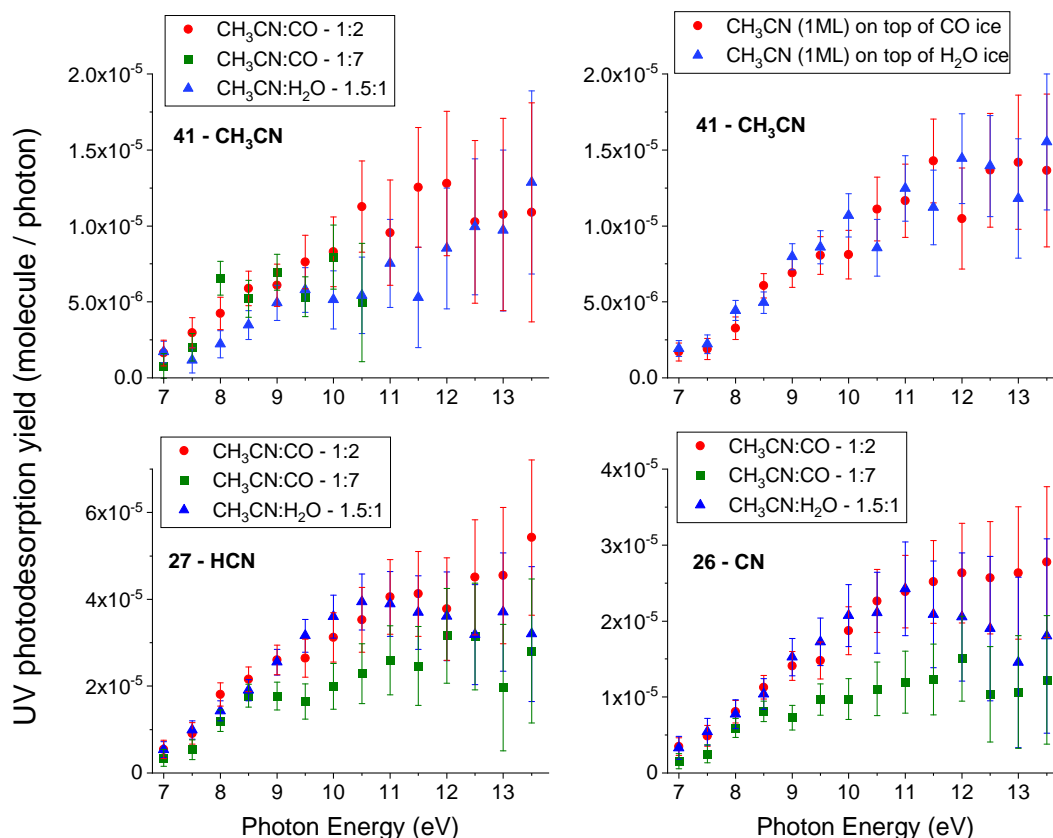


FIGURE V.7 – VUV photodesorption spectra, as a function of the incident photon energy, of  $\text{CH}_3\text{CN}$  (mass 41) from mixed  $\text{CH}_3\text{CN}:\text{CO}$  and mixed  $\text{CH}_3\text{CN}:\text{H}_2\text{O}$  ices (top left panel) and from 1 ML of  $\text{CH}_3\text{CN}$  on top of  $\text{CO}$  and on top of  $\text{H}_2\text{O}$  ice (top right panel). VUV photodesorption of  $\text{HCN}$  (mass 27) and  $\text{CN}$  (mass 26) from mixed  $\text{CH}_3\text{CN}:\text{CO}$  and  $\text{CH}_3\text{CN}:\text{H}_2\text{O}$  ices are presented in the bottom panels. These yields were derived for ices at 15 K.

The photodesorption data for the masses 39 u. ( $\text{CHCN}$ ), 30 u., 16 u. and 15 u. ( $\text{CH}_3$ ) in the case of the mixed ices are displayed in Figure V.8. The desorption signal for the mass 30 u. is significantly higher in the case of mixed  $\text{CH}_3\text{CN}:\text{CO}$  ices compared to the case of the mixed  $\text{CH}_3\text{CN}:\text{H}_2\text{O}$  ice, most probably due to the contribution of  $\text{H}_2\text{CO}$  and/or  $\text{NO}$  photodesorption in the case of mixed  $\text{CH}_3\text{CN}:\text{CO}$  ices but no definitive attribution can be made. The desorption signal on the mass 16 u. is not significantly dependent on the presence of  $\text{CO}$  or  $\text{H}_2\text{O}$  molecules in the ice but a possible contribution of atomic  $\text{O}$  photodesorption to this mass signal prevents us from precisely quantifying a possible VUV photodesorption of  $\text{CH}_4$  from the mixed ices.

We do not observe a significant influence of the presence of  $\text{H}_2\text{O}$  and  $\text{CO}$  molecules on the shape of the VUV photodesorption spectra for  $\text{CH}_3\text{CN}$ ,  $\text{CHCN}$ ,  $\text{HCN}$ ,  $\text{CN}$  and  $\text{CH}_3$ . As briefly introduced in Chapter III.2.1.2, in similar experiments, indirect desorp-

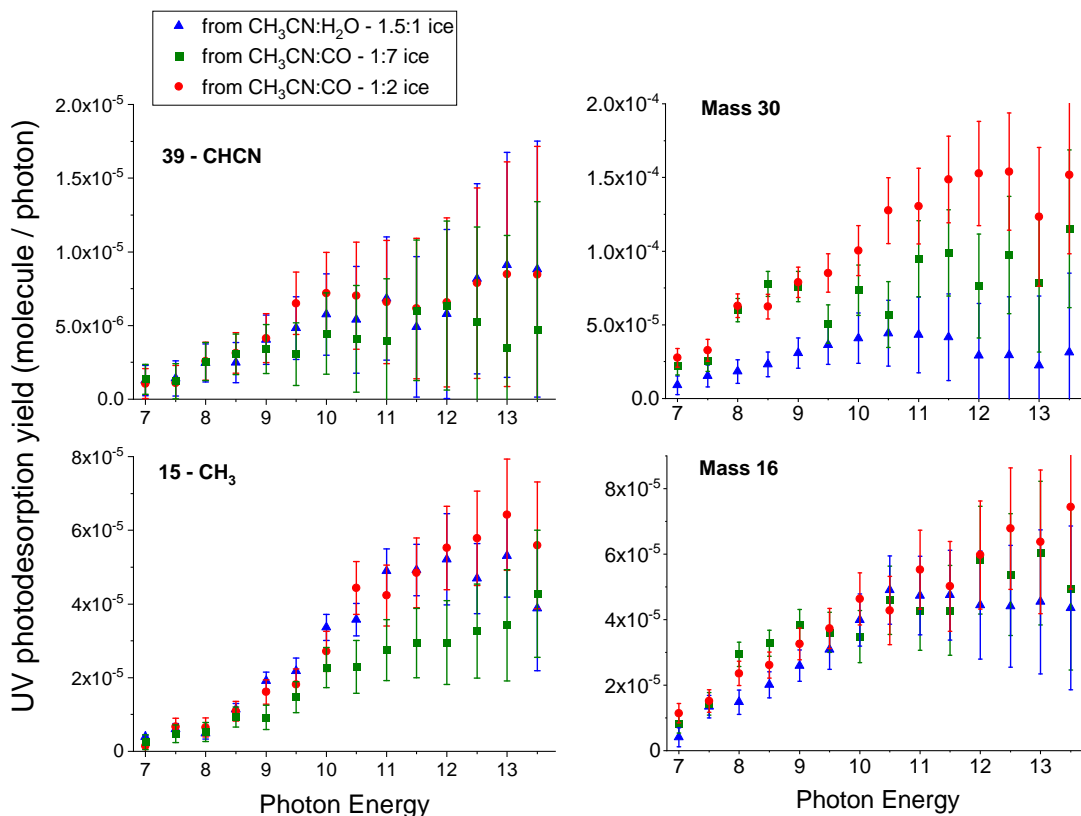


FIGURE V.8 – VUV photodesorption spectra, as a function of the incident photon energy, of masses 39 (CHCN), 30, 16 and 15 ( $\text{CH}_3$ ) from mixed  $\text{CH}_3\text{CN}:\text{CO}$  and mixed  $\text{CH}_3\text{CN}:\text{H}_2\text{O}$  ices. The attribution of species to the mass channels 30 and 16 is not possible. This is discussed in the text.

tion mechanisms have been observed in the case of simpler molecules such as  $\text{N}_2$  or  $\text{CH}_4$  deposited on top of pure CO ice (Bertin et al., 2013; Dupuy, R. et al., 2017), "pre-irradiated" pure  $\text{CO}_2$  ice (Fillion et al., 2014) or  $\text{N}_2$ , CO, Kr and Ar on top of pure water compact amorphous ice (Dupuy et al., 2021a). In these cases, the desorption of one molecule is induced by the UV photo-absorption of another one. Experimentally, this results in similarities between the VUV photodesorption spectrum of the molecule considered and the VUV absorption spectrum of CO or  $\text{H}_2\text{O}$  in condensed phase. In the case of more complex molecules, such as  $\text{CH}_3\text{OH}$ , this indirect mechanism was not observed (Bertin et al., 2016).

In our  $\text{CH}_3\text{CN}$  experiments, the VUV photodesorption spectra of  $\text{CH}_3\text{CN}$ , CHCN, HCN, CN and  $\text{CH}_3$  from the mixed and layered ices do not show any similarities with the UV absorption profile of CO or  $\text{H}_2\text{O}$  molecules in condensed phase. These data are compared for the case of  $\text{CH}_3\text{CN}$  UV photodesorption from the layered ices in Figure V.9. It is however surprising to observe that the VUV photodesorption yields of  $\text{CH}_3\text{CN}$  from CO-dominated ices are similar (when considering the error bars) between the 1:2 and

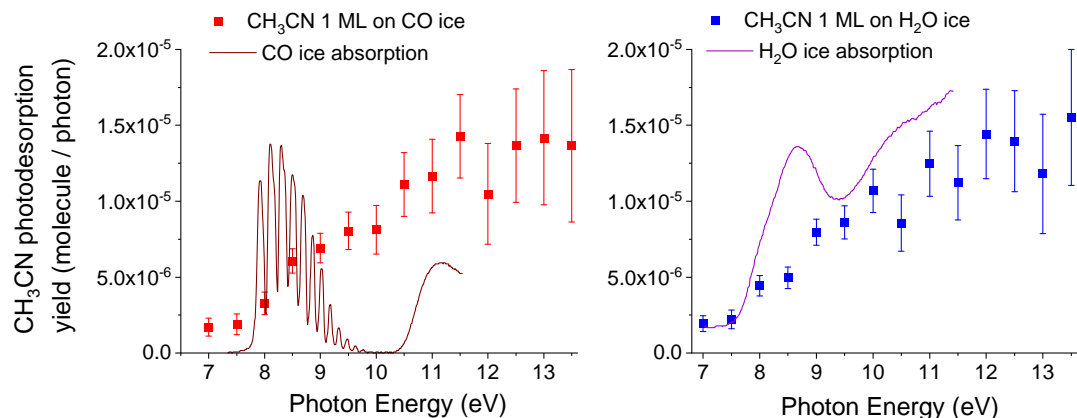


FIGURE V.9 – Left panel : comparison of CH<sub>3</sub>CN VUV photodesorption spectrum from a layered CH<sub>3</sub>CN (1 ML) on top of CO ice with the VUV absorption spectrum of CO in condensed phase (from Lu et al. 2005). Right panel : comparison of CH<sub>3</sub>CN VUV photodesorption spectrum from a layered CH<sub>3</sub>CN (1 ML) on top of H<sub>2</sub>O ice with the VUV absorption spectrum of H<sub>2</sub>O in condensed phase (from Lu et al. 2008). The VUV absorption spectrum of CO and H<sub>2</sub>O in condensed phase are shown in arbitrary units.

1:7 ratios (see Figure V.7, upper left panel). As CH<sub>3</sub>CN is more diluted in the CH<sub>3</sub>CN:CO - 1:7 ice, we would have expected to obtain a lower yield compared to the case of the CH<sub>3</sub>CN:CO - 1:2 ice. The fact that there is no clear signature of the CO UV absorption spectrum between 7.5 and 9.5 eV in the photodesorption spectrum of CH<sub>3</sub>CN from CH<sub>3</sub>CN (1 ML) on top of CO ice (see Figure V.9) seems to exclude the possibility of a significant indirect desorption mechanism induced by CO molecules when the CH<sub>3</sub>CN surface concentration is high. However, for higher dilution of CH<sub>3</sub>CN in a CO environment, a desorption of CH<sub>3</sub>CN triggered by the excitation of the CO matrix cannot be totally ruled out.

The similarities of the photodesorption yields of CH<sub>3</sub>CN from CO-dominated ices for the 1:2 and the 1:7 ratios could also be explained by less bounded CH<sub>3</sub>CN molecules in CO-dominated ices but this point would need additional experiments in lower concentration regimes to conclude. Finally, an indirect desorption mechanism induced by CO or H<sub>2</sub>O molecules does not seem to be at play or significant in our set of experiments for the desorption of the molecules cited above (CH<sub>3</sub>CN, CHCN, HCN, CN and CH<sub>3</sub>) from CH<sub>3</sub>CN-containing ices. The absolute values of the VUV photodesorption yields of CH<sub>3</sub>CN, CHCN, HCN, CN and CH<sub>3</sub> from the binary mixed ices are slightly diminished compared to the case of pure CH<sub>3</sub>CN ice but this effect is not significant when considering the error bars and could be explained by a lower number of CH<sub>3</sub>CN molecules available for desorption at the ice surface, inducing a lower desorption flux in the case of mixed ices. The deposition technique (mixed ices or layered ices) does not

have a significant influence on the VUV photodesorption of these molecules either. The photodesorption yields of CH<sub>3</sub>CN from 1 ML of CH<sub>3</sub>CN on top of CO or H<sub>2</sub>O ice are about half of that from pure CH<sub>3</sub>CN ice, which could be due to the fact that several CH<sub>3</sub>CN-containing layers are involved in the desorption of CH<sub>3</sub>CN from pure CH<sub>3</sub>CN ice. It is much likely that the VUV photodesorption of the previous molecules from the ices tested (pure, mixed and layered ices) occurs via a process for which the CH<sub>3</sub>CN molecule that absorbs the VUV photon is the one desorbing. It can be ejected as intact CH<sub>3</sub>CN or in the form of its photo-dissociation fragments. The desorption of CH<sub>3</sub>CN may involve dissociation and exothermic recombination of the photo-excited molecule (geminate recombination) but a definitive conclusion on the photodesorption mechanism for intact CH<sub>3</sub>CN cannot be drawn with regards to the data obtained. The processes involved in the desorption of these molecules seem to be independent of the presence of CO or H<sub>2</sub>O molecules surrounding the VUV absorbing CH<sub>3</sub>CN molecule.

### V.3 Astrophysical yields and discussion

The previous studies regarding the dependence of the photodesorption yields with the ice composition point out that the surrounding molecules, in our case CO and H<sub>2</sub>O, does not promote the desorption of the COMs studied, as it is the case for more "simple" coadsorbed molecules such as N<sub>2</sub> or CO (Bertin et al., 2012, 2013). Such indirect processes may have a strong influence when it comes to model the VUV photodesorption of these "simple" molecules from interstellar ices since their yields actually depend on the ice composition. Obviously, in the case of CH<sub>3</sub>CN, HCOOH and HCOOCH<sub>3</sub> (and also CH<sub>3</sub>OH as seen in the study of Bertin et al. (2016)), such indirect desorption is either not operative, or too weak to produce enough gas phase COMs for us to detect. There can be several explanations for this. One of those could be that the COMs studied present many internal degrees of freedom as compared to simple molecules such as N<sub>2</sub> or CO, and thus any external energy brought by the matrix to the molecule can be dissipated into internal energy, lowering the amount of energy left in the translation for the molecules to desorb. Alternatively, this could be due to the strength of inter-molecular interactions in the solids.

By integrating our experimental photodesorption spectra with UV spectra that are representative of the UV fields found in different regions of the ISM, as described in Chapter II.2.4, we are able to provide average photodesorption yields that are suitable for astrophysical modeling. The UV field used were : the UV emission spectra of a classical T Tauri Star representative of protoplanetary disks (France et al., 2014), the UV field produced by cosmic-ray secondary electrons representative of dense inter-

stellar clouds (Gredel et al., 1987) and the UV interstellar radiation field (ISRF) from Mathis et al. (1983). The resulting yields are presented in Table V.1. As discussed previously, we found that the VUV photodesorption of the COMs studied and that of their photo-fragments does not strongly depend on the presence of CO or H<sub>2</sub>O molecules in the ice (an exception however is the case of HCO which is not found to desorb from HCOOH:H<sub>2</sub>O and HCOOCH<sub>3</sub>:H<sub>2</sub>O mixed ices). Accordingly, we took the photodesorption spectra from the pure ices of COMs to derive the yields presented in Table V.1, which are thus assumed to be applicable to any CO or H<sub>2</sub>O dominated ices containing the COM considered. The desorption of the masses 30 u., 28 u. and 16 u. from the mixed CH<sub>3</sub>CN ices is not discussed as it is not possible to clearly attribute species to these mass channels. Moreover, the formation of the associated species (e.g., C<sub>2</sub>H<sub>6</sub>, N<sub>2</sub>, CH<sub>4</sub>) has much likely involved the absorption of at least 2 VUV photons, in a limited time and spatial interval for the resulting radicals to react. This makes their possible experimental desorption not astrophysically relevant when considering the very low UV flux observed in the discussed regions of the ISM compared to our experimental UV flux.

The yields corresponding to protoplanetary disks and dense interstellar clouds are found to be identical within the error bars and are approximately equal to the experimental yields at the Lyman  $\alpha$  around 10.2 eV, as it is the energy that dominates the UV field in these regions. The yields corresponding to the ISRF are found to be lower due to a higher contribution of the UV field at low energy (< 10 eV) where photodesorption is less efficient for all the COMs studied.

For HCOOH and HCOOCH<sub>3</sub>, the fact that the desorption yields of the intact molecules are found below our detection limits, independently of the ice (pure, mixed with H<sub>2</sub>O or CO), is an important and interesting finding. It points out that the photo-dissociation of the molecules is a more efficient decay pathway subsequent to the photo-absorption by the COM, thus competing with the desorption of the intact molecule which becomes comparatively negligible. Potential photochemistry in the ice does not participate to the reformation and desorption of the initial COM, as it is for instance the case of H<sub>2</sub>O desorption from pure water ice. To many aspects, the VUV photodesorption from HCOOH and HCOOCH<sub>3</sub>-containing ices is very similar to the one from methanol-containing ices (Bertin et al., 2016). Indeed, UV photodesorption yields of CH<sub>3</sub>OH is close to the detection limit from pure methanol ice, and it is not detected in the case of mixed ices methanol:CO (with a detection limit of  $3 \times 10^{-6}$  molecule/photon). Instead, the photodesorption from methanol is dominated by the desorption of its photo-dissociation products (Bertin et al., 2016; Cruz-Diaz et al., 2016). HCOOH and HCOOCH<sub>3</sub> seem to follow the same behavior, e.g. a weak photodesorption of the intact molecules (in these cases not even detected), not promoted by the molecular environment, and a

TABLE V.1 – Astrophysical photodesorption yield ( $\times 10^{-5}$  molecule/photon) extrapolated from our experimental results on pure  $\text{CH}_3\text{CN}$ ,  $\text{HCOOH}$  and  $\text{HCOOCH}_3$  ices at 15 K, for different astrophysical environments. More details are given in the text.

Photodesorbed species	ISRF <sup>(a)</sup>	Dense Clouds <sup>(b)</sup> and Disks <sup>(c)</sup>
from $\text{CH}_3\text{CN}$ -containing ices		
$\text{CH}_3\text{CN}$	$0.67 \pm 0.33$	$2.0 \pm 1.0$
$\text{CHCN}$	$0.34 \pm 0.17$	$1.0 \pm 0.5$
$\text{HCN}$	$1.1 \pm 0.6$	$3.3 \pm 1.7$
$\text{CN}$	$0.60 \pm 0.30$	$1.7 \pm 0.9$
$\text{CH}_3$	$2.1 \pm 1.0$	$6.5 \pm 3.3$
from $\text{HCOOH}$ -containing ices		
$\text{HCOOH}$	$< 0.5$	$< 0.5$
$\text{CO}_2$	$14 \pm 7$	$36 \pm 18$
$\text{H}_2\text{CO}$	$0.73 \pm 0.4$	$2.1 \pm 1.1$
$\text{HCO}^{(d)}$	$1.0 \pm 0.5$	$3.1 \pm 1.6$
$\text{CO}$	$73 \pm 36$	$170 \pm 90$
$\text{H}_2\text{O}$	$3.4 \pm 1.7$	$8.7 \pm 4.4$
from $\text{HCOOCH}_3$ -containing ices		
$\text{HCOOCH}_3$	$< 1$	$< 1$
$\text{CO}_2$	$7.9 \pm 4.0$	$22 \pm 11$
$\text{H}_3\text{CO}$	$1.0 \pm 0.5$	$3.0 \pm 1.5$
$\text{O}_2$	$1.0 \pm 0.7$	$1.2 \pm 0.9$
$\text{H}_2\text{CO}$	$1.6 \pm 0.8$	$4.1 \pm 2.1$
$\text{HCO}^{(d)}$	$3.8 \pm 1.9$	$10 \pm 5$
$\text{CO}$	$140 \pm 70$	$340 \pm 170$
$\text{H}_2\text{O}$	$4.3 \pm 2.2$	$11 \pm 6$
$\text{CH}_3$	$3.1 \pm 1.6$	$7.5 \pm 3.8$

<sup>(a)</sup> UV field from [Mathis et al. \(1983\)](#)

<sup>(b)</sup> UV field from [Gredel et al. \(1987\)](#)

<sup>(c)</sup> UV field from [France et al. \(2014\)](#)

<sup>(d)</sup> when mixed in  $\text{H}_2\text{O}$ -rich ices, the photodesorption of HCO is under our detection limit, which is  $2 \times 10^{-5}$  molecule/photon for this species

desorption mostly reflecting the photo-dissociation of the species. This does not, however, mean that it is a general trend for all the COMs that can be encountered in the interstellar ices. Indeed, interestingly, our results on the photodesorption of CH<sub>3</sub>CN-containing ices have shown an efficient photodesorption pathway of the intact molecule, reaching a yield of several 10<sup>-5</sup> molecule/photon, and which is in the same order of magnitude than that of its photo-fragments.

These experimental trends may be linked to the observations of gaseous COMs in protoplanetary disks : molecules which dissociate efficiently, and whose photodesorption has been experimentally found very low, such as HCOOH and HCOOCH<sub>3</sub>, are very difficult to detect, i.e. observed in only one source for HCOOH (Favre et al., 2018), or even not seen at all in the case of HCOOCH<sub>3</sub>. On the other hand, CH<sub>3</sub>CN, whose intact photodesorption has been observed and measured experimentally, is seen in many sources (Öberg, K. I. et al., 2015; Loomis et al., 2018; Bergner et al., 2018). In these cases, pure gas phase chemistry fails to explain the observed abundances of CH<sub>3</sub>CN (Öberg, K. I. et al., 2015; Loomis et al., 2018), indicating that its detection is intimately linked to processes associated with ices. In these disks, CH<sub>3</sub>CN detection extends far from the central young star, in regions where the temperature of the icy mantles is expected to be low enough ( $T < 100$  K) so that gas phase CH<sub>3</sub>CN should accrete on the surface of the icy dust grains. The presence of CH<sub>3</sub>CN in the gas phase therefore implies that a non-thermal process, including VUV photodesorption, should maintain a sufficient amount of gas phase CH<sub>3</sub>CN via desorption from the surface of icy mantles.

A quantitative comparison of CH<sub>3</sub>OH and CH<sub>3</sub>CN abundances observed in the TW Hya (Walsh et al., 2016; Loomis et al., 2018) and the HD 1632296 (Bergner et al., 2018; Carney et al., 2019) protoplanetary disks is also to be put in contrast with our experimental results. In the case of the protoplanetary disk around the T Tauri star TW Hya, gas phase abundances of CH<sub>3</sub>CN and CH<sub>3</sub>OH (and also of HCOOH; Favre et al. (2018)) are found to be similar (Walsh et al., 2016; Loomis et al., 2018) whereas in the case of the disk around the Herbig Ae star HD 163296, CH<sub>3</sub>CN is strongly detected and CH<sub>3</sub>OH emission lines are below the detection limits (Bergner et al., 2018; Carney et al., 2019). As suggested in Bergner et al. 2018, Herbig Ae stars are expected to be stronger UV emitters than T Tauri stars. Therefore, the role of VUV photodesorption of CH<sub>3</sub>CN and CH<sub>3</sub>OH from interstellar ices has been raised by Bergner et al. 2018 as a possible candidate to explain these differences in the observations. Our experimental results, that show a higher VUV photodesorption efficiency of CH<sub>3</sub>CN from interstellar ice analogs ( $\sim 10^{-5}$  molecule/photon), by at least one order of magnitude, compared to that of CH<sub>3</sub>OH ( $< 3 \times 10^{-6}$  molecule/photon when mixed in CO-rich ice), clearly support the assumption of Bergner et al. 2018. However, the VUV photodesorption yields of COMs used in disk modeling are often higher than the experimental ones (e.g., Loomis

[et al. 2018](#) considered a  $\text{CH}_3\text{CN}$  VUV photodesorption yield of  $10^{-3}$  molecule/photon in their modeling of the TW Hya disk) and other processes, such as X-ray photodesorption, may be of importance to explain the detection of gaseous COMs in these regions.

Generalizing the role of VUV photodesorption of COMs to any cold region of the ISM is however not straightforward, since the other non-thermal desorption processes described in Chapter I can be at play. Many authors tentatively attribute the origin of gas phase  $\text{HCOOH}$  or  $\text{HCOOCH}_3$  in dense cores either to VUV photodesorption (e.g. [Guzmán et al., 2014](#)), chemical desorption (e.g. [Jiménez-Serra et al. \(2016\)](#); [Taquet et al. \(2017\)](#)) or cosmic ray sputtering (e.g. [Bacmann et al., 2012](#)) from interstellar ices. Gas phase formation routes are sometimes also suggested (e.g. [Irvine et al., 1990](#); [Taquet et al., 2017](#)). In any case, the lack of quantitative data on the efficiency of each process prevents to actually conclude on the dominant mechanism. In addition, even if the desorption of the intact COM is rather weak as compared to the dissociative channels (especially for the case for  $\text{HCOOH}$ ,  $\text{HCOOCH}_3$  and  $\text{CH}_3\text{OH}$  as shown by our experimental results), the photodesorption of radicals from COM-containing ices is also a potential route to bring reactive material in the gas phase and trigger chemistry leading to COM formation. Only a proper astrochemical modeling including the gas-grain exchanges can give a good idea on the relative role played by each process, which in return implies to know the desorption yields associated with each species. Even if the previous study on  $\text{HCOOH}$  and  $\text{HCOOCH}_3$  could only provide upper limits on their VUV photodesorption yield, the yields of radicals and chemical product are derived, and it may participate to a better constrain on the role of VUV photodesorption as compared to other non-thermal desorption mechanisms in the ISM.

Finally, Photo-Dissociation Regions (PDR), where the chemical and physical processes are driven by the interaction of gas and dust with UV photons, are interesting regions of the ISM to compare our experimental results to observational data. Especially, I will focus on the case of the Horsehead nebula for which the separation between the UV-illuminated PDR and the UV-shielded dense core is easily made and where COMs have been observed by [Gratier et al. \(2013\)](#) and [Guzmán et al. \(2014\)](#). According to these astronomical observations,  $\text{CH}_3\text{OH}$  abundances are found to be similar between the PDR and the dense core region whereas  $\text{CH}_3\text{CN}$  is 30 times more abundant in the PDR than in the dense core region. In the PDR, where VUV photodesorption should play a more important role than in the dense core,  $\text{CH}_3\text{OH}$  is found to be less abundant than  $\text{CH}_3\text{CN}$  by approximatively one order of magnitude ( $\text{HCOOH}$  abundance in the PDR is found to be similar to that of  $\text{CH}_3\text{OH}$  but the author points out a large uncertainty on this estimation). Among the possible mechanisms that could explain these observations, our experiments clearly point towards a higher quantitative role of  $\text{CH}_3\text{CN}$  VUV photodesorption compared to the case of  $\text{CH}_3\text{OH}$  VUV photodesorption, as shown by

our photodesorption yields (i.e.  $\sim 10^{-5}$  molecule/photon for  $\text{CH}_3\text{CN}$  and  $< 3 \times 10^{-6}$  molecule/photon for  $\text{CH}_3\text{OH}$  from interstellar ice analogues). The higher VUV absorption cross section of  $\text{CH}_3\text{CN}$  compared to  $\text{CH}_3\text{OH}$  (based on gas phase absorption cross sections; Cheng et al. 2002, Schwell et al. 2008) along with the resilience of nitriles to UV photolysis, which has been demonstrated in the case of acetonitrile versus acetic acid in pure ices at 15 K (Bernstein et al., 2004), could be an interesting route to explain these differences in the VUV photodesorption yields.

## V.4 Conclusion and perspectives

VUV photodesorption has been studied for  $\text{HCOOH}$ ,  $\text{HCOOCH}_3$  and  $\text{CH}_3\text{CN}$  containing ices. The photodesorption yields provided should help to quantify the role of VUV photodesorption of COMs in the ISM, especially via astrochemical modeling. The main findings of these experiments are summed up in the following :

- while the photodesorption of intact  $\text{HCOOH}$  and  $\text{HCOOCH}_3$  is found below our detection limit i.e.  $< 5 \times 10^{-6}$  molecule/photon and  $10^{-5}$  molecule/photon for  $\text{HCOOH}$  and  $\text{HCOOCH}_3$  respectively, the photodesorption of  $\text{CH}_3\text{CN}$  is detected above our detection limit with a yield of several  $10^{-5}$  molecule/photon.
- for each COM, the photodesorption of their photo-fragments is observed. The species detected are globally consistent with gas phase photo-dissociation studies in the VUV range. Quantitatively, the upper limits of the desorption yield of  $\text{HCOOH}$  and  $\text{HCOOCH}_3$  are found to be below the yields of their photo-fragments. This is not the case for  $\text{CH}_3\text{CN}$ , whose desorption yield is interestingly in the same order of magnitude as that of its photo-fragments.
- the photodesorption of the COM photo-fragments is found to not strongly depend on the presence of  $\text{CO}$  or  $\text{H}_2\text{O}$  molecules in the ice hence ruling out a significant indirect desorption process induced by the photo-absorption of  $\text{CO}$  or  $\text{H}_2\text{O}$  as seen for more simple molecules (see Chapter III). This is also the case for the photodesorption of  $\text{CH}_3\text{CN}$ . Potential photo-chemistry with the surrounding molecules does not seem to influence desorption either. This suggest that the desorption of the COM's photo-fragments occur via a direct process i.e. for which the photo-absorbing COM is the molecule desorbing in its intact form (only in the case of  $\text{CH}_3\text{CN}$ ) or in the form of its photo-fragment. This finding is particularly important for astrochemical model : while the indirect desorption process, that depends on the ice composition, should be taken into account for "simple" molecules ( $\text{CO}$ ,  $\text{H}_2\text{O}$ ,  $\text{N}_2$ ,  $\text{CO}_2$  ...) during the implementation, this is not

the case for the VUV photodesorption of the COMs studied, which can be implemented by simply feeding the model with our average astrophysical photodesorption yields, independently of the ice composition.

- these experimental results are well-correlated to observational data in protoplanetary disks, PDR and dense cores i.e. the multiple detection of  $\text{CH}_3\text{CN}$  in several regions of the ISM where VUV photodesorption should play a role, compared to the more rare detection of  $\text{CH}_3\text{OH}$ ,  $\text{HCOOH}$  and  $\text{HCOOCH}_3$  could be partly explained by our experimental results.

These results showed that the VUV photodesorption of COMs from interstellar ices cannot be so far extrapolated from the specific case of one COM. The correlation between experimental findings and observations is a strong argument in favor of the key role played by VUV photodesorption to explain the observed gas phase molecular abundances of COMs in the ISM.



# Chapter VI

## X-ray photodesorption of COMs

The results presented in this chapter were obtained on the SEXTANTS beamline of the SOLEIL synchrotron facility in 2019 and 2021. The studies focus on the X-ray photodesorption of acetonitrile  $\text{CH}_3\text{CN}$ , methanol  $\text{CH}_3\text{OH}$  and formic acid  $\text{HCOOH}$  from pure ices and from ices for which the COM is embedded in a CO or  $\text{H}_2\text{O}$  environment. X-ray photodesorption of neutral molecules has been shown to occur for example from pure water ice (Dupuy et al., 2018), pure CO ice (Dupuy et al., 2021b) and interstellar ice analogues (Jiménez-Escobar et al., 2018; Ciaravella et al., 2020). In a recent modeling study (Notsu et al., 2021), X-ray photodesorption has been shown to play a role for gas phase abundances in protostellar envelopes. Except for the study of Ciaravella et al. (2020) where X-ray photodesorption was studied from a mixture of CO: $\text{CH}_3\text{OH}$  ice on top of a  $\text{H}_2\text{O}$ : $\text{CH}_4$ : $\text{NH}_3$  ice, X-ray photodesorption of COMs is poorly constrained in the literature.

In the following, I will first present the data obtained on the Total Electron Yields (TEYs), representative of the X-ray absorption of the ices studied. Their evolution with the photon fluence will also be discussed. X-ray photodesorption from the pure ices will be showed in the second section. A comparison between the X-ray, VUV and electron-induced desorption experiments will allow to discuss the possible dominant mechanisms at play for X-ray photodesorption of  $\text{CH}_3\text{OH}$ . Finally, the influence of CO and  $\text{H}_2\text{O}$  molecules on the X-ray photodesorption yields will be presented along with the astrophysical implications. As for the case of the VUV photodesorption of COMs in Chapter V, the studies presented in this Chapter are among the first few studies regarding the X-ray photodesorption of COMs. The pure ices and the mixed CO:COM ices were grown and irradiated at 15 K whereas the mixed  $\text{H}_2\text{O}$ :COM ices were formed at 90 K and then irradiated at 15 K after cooling down the substrate, to ensure that the water ice is in its compact amorphous phase. The calibration of the photon energy was done as described in Chapter IV.1.1. The results presented for the X-ray photodesorption of  $\text{CH}_3\text{OH}$  were published in Basalgète et al. (2021a) and Basalgète et al. (2021b).

## VI.1 Total Electron yields and their evolution with the irradiation

The Total Electron Yield (TEY) is measured during the X-ray irradiation of the ices as a function of the photon energy. It quantifies the number of electrons escaping the ice surface per incident photon (expressed in electrons/photon), induced by the X-ray absorption of the ice. The TEY is sensitive to the change of the molecular composition near the ice surface with the photon fluence. More precisely, the ice depth probed is estimated to be a few tens of ML based on studies of water ice (Timneanu et al., 2004) and of CO/N<sub>2</sub> ices (see Chapter IV). In the following, I will present the TEYs data measured on the pure and mixed ices containing the COMs studied. Studying the evolution of the TEYs with the photon fluence will enable to discuss the behavior of ices under X-ray irradiation.

### VI.1.1 CH<sub>3</sub>OH-containing ices

TEYs measured on CH<sub>3</sub>OH-containing ices at 15 K are displayed in Figure VI.1 near the O K-edge (~ 540 eV). In the top left panel are the TEYs obtained for a pure CH<sub>3</sub>OH ice at different photon fluence. The different features observed are numbered and can be assimilated to the X-ray absorption of the O-bearing molecules in condensed phase. The broad peak labeled 3 centered near 538 eV is attributed to a CH<sub>3</sub>OH resonance. A similar peak is observed in gas phase experiments and attributed either to a 3p Rydberg orbital or to a molecular  $\sigma^*$  orbital (see Wilson et al. (2005)). This peak is broadened when going from gas phase to condensed phase (also observed in liquid phase in Wilson et al. (2005)) due to the overlap of neighboring molecule's orbitals in condensed phase. This feature decreases with the photon fluence, showing that the photo-destruction of CH<sub>3</sub>OH occurs near the ice surface. In the semi-infinite regime, i.e. for the thick ices (~ 100 ML) grown in our experiments, X-ray photodesorption of CH<sub>3</sub>OH from the ice surface does not participate into explaining this decrease : if one molecule photodesorbs, another one from the lower layer will take its place. Instead, the decrease of the peak labeled 3 is attributed to CH<sub>3</sub>OH destruction by chemistry and dissociation induced by the incident photon and by the electrons scattering in the ice (Auger and secondary electrons). This is further confirmed by the appearance of the peak labeled 2 centered near 534.6 eV with an ongoing irradiation fluence ( $> 1 \times 10^{17}$  photon/cm<sup>2</sup>). This peak can be attributed to the accumulation of new species near the ice surface. Considering the energy at which it is observed, this feature resembles that observed on a pure CO ice at 534.4 eV (see top right panel of Figure VI.1), which corresponds to the O 1s  $\rightarrow \pi^*$  resonance of CO. A contribution of CO<sub>2</sub>, whose O 1s  $\rightarrow \pi^*$  transition is at 535.4 eV according to gas phase studies (Wight and Brion, 1974) might also be possible. The accumulation of CO and CO<sub>2</sub> in X-ray irradiated CH<sub>3</sub>OH ice has also

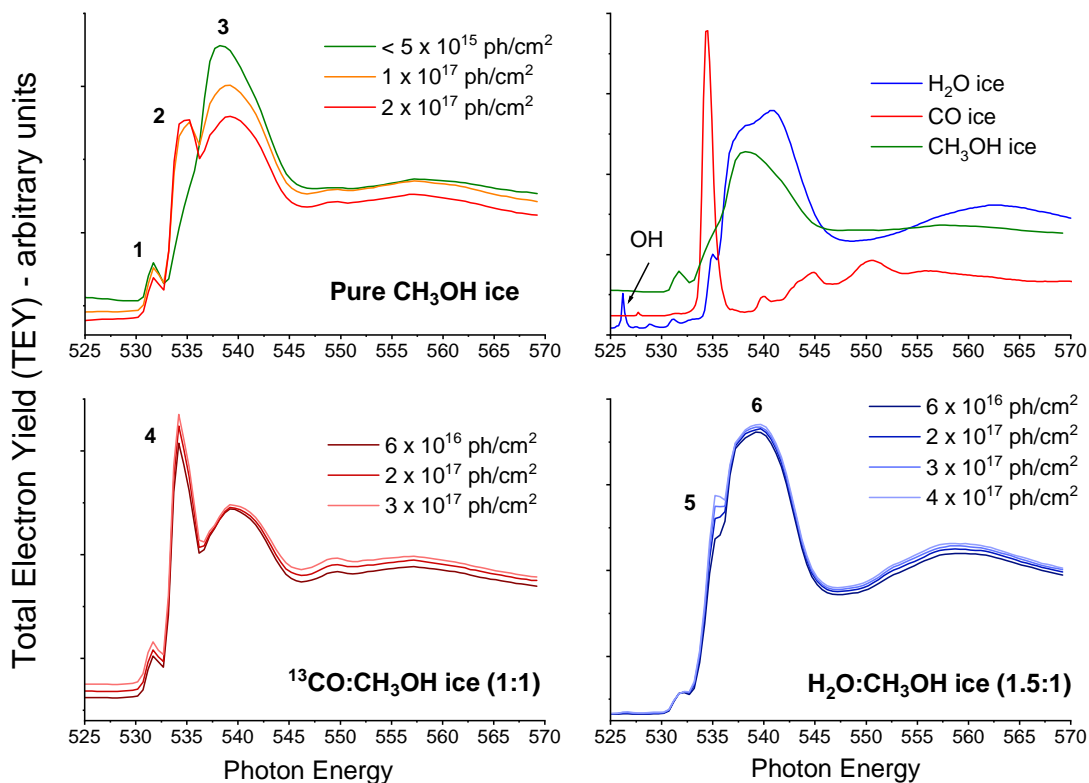


FIGURE VI.1 – TEYs near the O K-edge measured at 15 K and for different photon fluence for a pure  $\text{CH}_3\text{OH}$  ice (top left panel), a  $^{13}\text{CO}:\text{CH}_3\text{OH}$  ice - 1:1 ice (bottom left panel) and a  $\text{H}_2\text{O}:\text{CH}_3\text{OH}$  - 1.5:1 ice (bottom right panel). The photon fluence displayed correspond to the fluence received by the ice before the measurement. It is expressed in photons/ $\text{cm}^2$ . The top right panel shows the TEYs measured from pure CO (taken from Dupuy et al. (2021b)),  $\text{H}_2\text{O}$  (taken from Dupuy et al. (2020)) and  $\text{CH}_3\text{OH}$  ices at 15 K. The ices thickness is equivalent to  $\sim 100$  ML in our experiments.

been observed in similar experiments (Laffon et al., 2010; Chen et al., 2013c). Finally, the small peak labeled 1 at 531.5 eV cannot be definitively attributed as we lack published data on the X-ray absorption of solid methanol in the considered energy range. Its low dependence on the irradiation fluence indicates a structure that is associated either with intact methanol ice, that is, not to a photoproduct, or with the substrate itself.

The TEYs associated with the mixed ices are displayed in the bottom panels of Figure VI.1. The features observed in the TEYs of the binary mixed ices can be attributed to individual contributions of  $\text{CH}_3\text{OH}$ , CO, or  $\text{H}_2\text{O}$ . The sharp peak labeled 4 and observed at 534.4 eV for the  $^{13}\text{CO}:\text{CH}_3\text{OH}$  ice is attributed to the  $1s^{-1}\pi^*$  resonance of  $^{13}\text{CO}$  molecules in condensed phase. The broadened peak labeled 6 and observed for the  $\text{H}_2\text{O}:\text{CH}_3\text{OH}$  ice results from the overlap of  $\text{CH}_3\text{OH}$  and  $\text{H}_2\text{O}$  X-ray photoabsorption. For  $\text{H}_2\text{O}$  molecules, experiments on water core excitation attributed this feature to Rydberg orbitals (Tronc and Azria, 2001; Parent et al., 2002). For the  $^{13}\text{CO}:\text{CH}_3\text{OH}$

ice, the TEY is not significantly varying with the photon fluence, indicating that potential chemistry induced by the X-ray irradiation is not strongly modifying the molecular composition of the near ice surface in the regime considered (i.e. between a photon fluence of  $6 \times 10^{16}$  and  $3 \times 10^{17}$  photon/cm<sup>2</sup>). On the other hand, for the H<sub>2</sub>O:CH<sub>3</sub>OH ice, a peak, labeled 5, is appearing on the TEY above a photon fluence of  $6 \times 10^{16}$  photon/cm<sup>2</sup>, near 535.6 eV. This feature can be associated with the accumulation of CO<sub>2</sub> near the ice surface, expected to be formed via chemical reactions between CH<sub>3</sub>OH and H<sub>2</sub>O dissociation products. Indeed, the NEXAFS study of [Laffon et al. \(2010\)](#) near the C K-edge showed that the formation of CO<sub>2</sub> induced by X-ray irradiation in mixed H<sub>2</sub>O:CH<sub>3</sub>OH ices is enhanced compared to the case of pure CH<sub>3</sub>OH ice. This is due to the reaction between CO, originating from the dissociation of CH<sub>3</sub>OH, and OH radical, originating from the dissociation of H<sub>2</sub>O, resulting in the accumulation of CO<sub>2</sub> in the ice, at the expense of CO. This motivated our attribution of the peak labeled 5 to CO<sub>2</sub> accumulation. It is not possible to follow the evolution of the CH<sub>3</sub>OH feature with the photon fluence in the TEYs data of the mixed H<sub>2</sub>O:CH<sub>3</sub>OH ices as its contribution overlaps with that of H<sub>2</sub>O near 538 eV. However, based on the study of [Laffon et al. \(2010\)](#) where they showed that the survival rate of methanol is lower when it is mixed with water, we expect the destruction of CH<sub>3</sub>OH to be more efficient in H<sub>2</sub>O:CH<sub>3</sub>OH ices than in the pure or <sup>13</sup>CO:CH<sub>3</sub>OH ices. Finally, the peak observed near 526.3 eV for a X-ray irradiated pure H<sub>2</sub>O ice and attributed to OH radical accumulation (see top right panel of Figure VI.1) is not seen in the TEY of the X-ray irradiated mixed H<sub>2</sub>O:CH<sub>3</sub>OH ice. This is consistent with the consumption of OH radical (therefore not accumulating near the ice surface) by reaction with CO to form CO<sub>2</sub> in the H<sub>2</sub>O:CH<sub>3</sub>OH ice.

### VI.1.2 CH<sub>3</sub>CN-containing ices

For CH<sub>3</sub>CN-containing ices, we first discuss the spectral features of the TEYs observed near the N K-edge ( $\sim 400$  eV). The TEY of a pure CH<sub>3</sub>CN ice at 15 K (100 ML) is showed in the top left panel of Figure VI.2. The main feature observed is associated with the N 1s  $\rightarrow \pi^*$  transition of CH<sub>3</sub>CN, near 400 eV. Our TEY compares very well with that of [Parent et al. \(2000\)](#) (not shown for more clarity) except that (i) the N 1s  $\rightarrow \pi^*$  transition is blue-shifted of  $\sim 1$  eV in our TEY and (ii) a shoulder is observed before this transition for our TEY, near 399.5 eV. This latter feature might be due to the interaction of CH<sub>3</sub>CN with the substrate, lowering the energy of the N 1s  $\rightarrow \pi^*$  transition and creating a current at the substrate surface, measured in our TEY. This assumption is based on similar experiments conducted by [Parent et al. \(2000\)](#) where TEYs were compared between thick CH<sub>3</sub>CN ice and thin layers of CH<sub>3</sub>CN adsorbed on Au(111) or Pt(111). The intensity of the feature associated with the N 1s  $\rightarrow \pi^*$  transition is decreasing with the photon fluence, as seen in the top left panel of Figure VI.2. This is due to the photo-

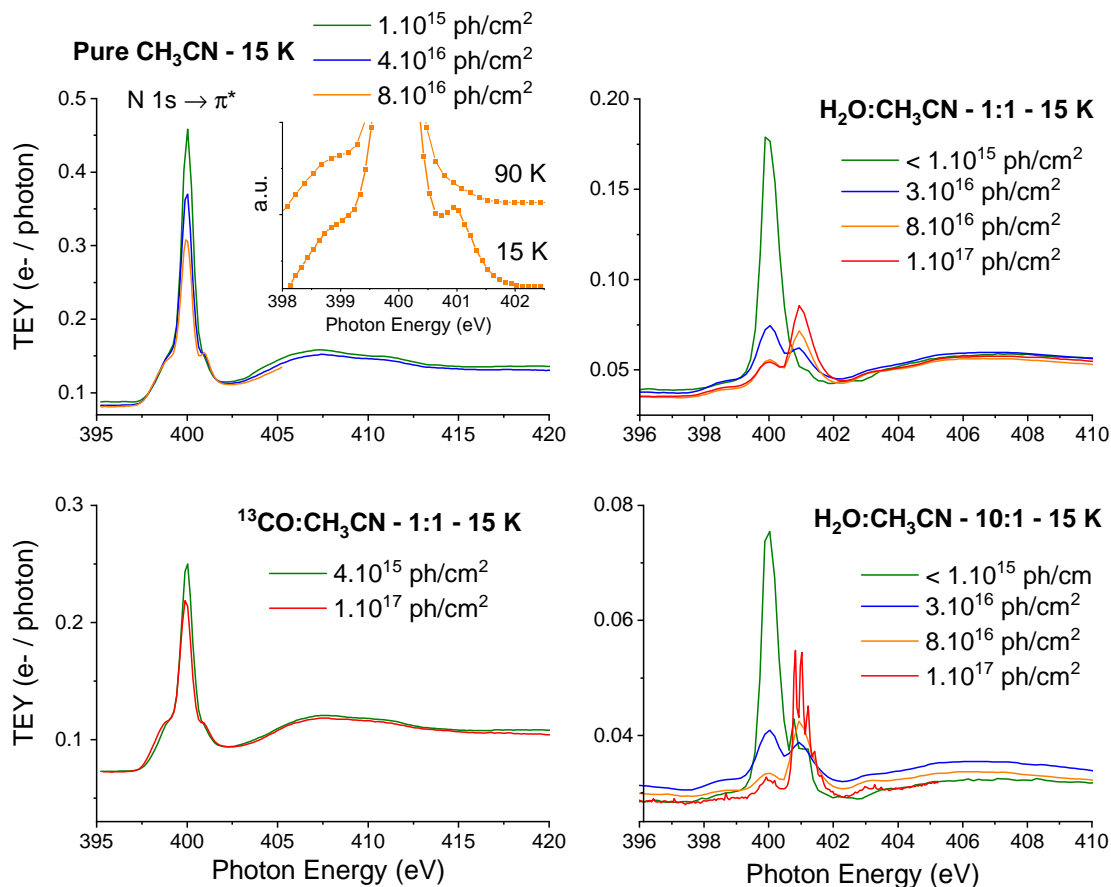


FIGURE VI.2 – TEYs near the N K-edge of a pure  $\text{CH}_3\text{CN}$  ice at 15 K (top left panel; the inset shows the region near the  $\text{N } 1s \rightarrow \pi^*$  resonance for an ice at 15 K and 90 K for the lower and upper curve respectively), a  $\text{H}_2\text{O}:\text{CH}_3\text{CN}$  ice at 15 K with dilutions ratio of 1:1 and 10:1 (top and bottom right panel respectively) and of a  $^{13}\text{CO}:\text{CH}_3\text{CN}$  ice at 15 K with a dilution ratio of 1:1 (bottom left panel). The photon fluence is also displayed. The spectral width of the beam was set to 1.2 eV for all the TEY measurements except for the one corresponding to the red curve in the bottom right panel, for a  $\text{H}_2\text{O}:\text{CH}_3\text{CN}$  ice having received a photon fluence of  $1 \times 10^{17}$  photon/ $\text{cm}^2$  and for which the spectral width was 90 meV. The ices have a total thickness of  $\sim 100$  ML.

dissociation of  $\text{CH}_3\text{CN}$  and the formation of new species near the ice surface. Among the possible species formed, a new feature appearing for a photon fluence  $\gtrsim 8 \times 10^{16}$  photon/ $\text{cm}^2$  near 401 eV indicates the accumulation of  $\text{N}_2$  near the ice surface, at 15 K (see the inset of the top left panel of Figure VI.2). Indeed, this feature is similar to the one observed from pure  $\text{N}_2$  ice irradiated with X-rays near the N K-edge, as seen in Chapter IV. Additionally, this feature is not seen in pure  $\text{CH}_3\text{CN}$  ice irradiated at 90 K, which is probably due to the thermal desorption of  $\text{N}_2$  preventing its accumulation near the ice surface at such temperature. Any photo-products other than  $\text{N}_2$  that are formed during the X-ray irradiation do not participate significantly to the photo-absorption of the ice in the 395 - 420 eV range, as no significant new features appear in the TEY.

The previous observations, i.e. (i) a slight decrease of the N  $1s \rightarrow \pi^*$  transition of  $\text{CH}_3\text{CN}$  with the photon fluence and (ii) the formation of  $\text{N}_2$ , are similar for the case of an irradiated  $^{13}\text{CO}:\text{CH}_3\text{CN}$  (1 :1) ice at 15 K, as seen in the bottom left panel of Figure VI.2. This seems to indicate that the presence of  $^{13}\text{CO}$  molecules does not significantly modify the X-ray induced chemistry network compared to the case of the pure  $\text{CH}_3\text{CN}$  ice. Note that this does not depend on the photon energy as the TEYs displayed in Figure VI.2 have been measured for ices irradiated both near the N and O K-edge. This is consistent with the fact that the chemistry is dominated by the scattering of the Auger electrons and the subsequent low energy electron cascades, and does not depend on the primary photo-excitation/ionization.

The behavior of the TEYs for the case of mixed  $\text{H}_2\text{O}:\text{CH}_3\text{CN}$  ices (1:1 and 10:1) is very different, as showed in the right panels of Figure VI.2. The decrease of the acetonitrile N  $1s^{-1}\pi^*$  feature with the photon fluence is much faster when  $\text{CH}_3\text{CN}$  is embedded in a  $\text{H}_2\text{O}$  ice and it almost totally disappears for a photon fluence  $\gtrsim 8 \times 10^{16}$  photon/cm<sup>2</sup>. This indicates that the water ice provide reactive species, e.g. OH radical, that increases the destruction kinetics of  $\text{CH}_3\text{CN}$  compared to the case of the pure  $\text{CH}_3\text{CN}$  ice and mixed  $^{13}\text{CO}:\text{CH}_3\text{CN}$  ices. This kinetic difference in the consumption of  $\text{CH}_3\text{CN}$  has also been observed when irradiating pure  $\text{CH}_3\text{CN}$  and mixed  $\text{H}_2\text{O}:\text{CH}_3\text{CN}$  ices with UV photons (with a broadband 7 - 10.2 eV hydrogen lamp), at 20 K, in the study of [Bulak et al. \(2021\)](#). The formation of  $\text{N}_2$  is also clearly seen near 401 eV in the TEYs for mixed  $\text{H}_2\text{O}:\text{CH}_3\text{CN}$  ices. In the bottom right panel of Figure VI.2, the red curve clearly and definitively confirms this attribution. Indeed, with enough spectral resolution (in that case 90 meV), the vibrational structure of the N  $(1s)^{-1}\pi^*$  state of  $\text{N}_2$  is resolved in the TEY, similarly to what has been observed for pure  $\text{N}_2$  ice in Chapter IV. Surprisingly, the formation and accumulation of  $\text{N}_2$  near the ice surface is not hindered by the presence of  $\text{H}_2\text{O}$  molecules compared to the case of pure  $\text{CH}_3\text{CN}$  and mixed  $^{13}\text{CO}:\text{CH}_3\text{CN}$  ices although the formation kinetics might be different. Once again for the case of mixed  $\text{H}_2\text{O}:\text{CH}_3\text{CN}$  ices, any photo-products other than  $\text{N}_2$  that might be formed near the ice surface do not produce any significant TEY feature in the 395 - 420 eV range. It is clear however that we do not have the full picture of this chemistry induced by the water matrix. In the literature, very few studies are available on the X-ray induced chemistry in water-acetonitrile ices. For instance, the study of [Abdoul-Carime et al. \(2022\)](#) suggested the formation of  $\text{CH}_3\text{OH}$ , detected by TPD, from mixed  $\text{H}_2\text{O}:\text{CH}_3\text{CN}$  ice irradiated by low energy electrons. As the  $\text{CH}_3\text{OH}$  absorption features overlap with that of  $\text{H}_2\text{O}$  in the TEYs near the O K-edge (see next paragraph), we cannot discuss its formation with our data set. In VUV irradiation experiments of  $\text{H}_2\text{O}:\text{CH}_3\text{CN}$  ices, although this is less comparable with the X-ray induced chemistry, the water ice has been shown to be a precursor for the formation of larger COMs ([Bulak et al., 2021](#)).

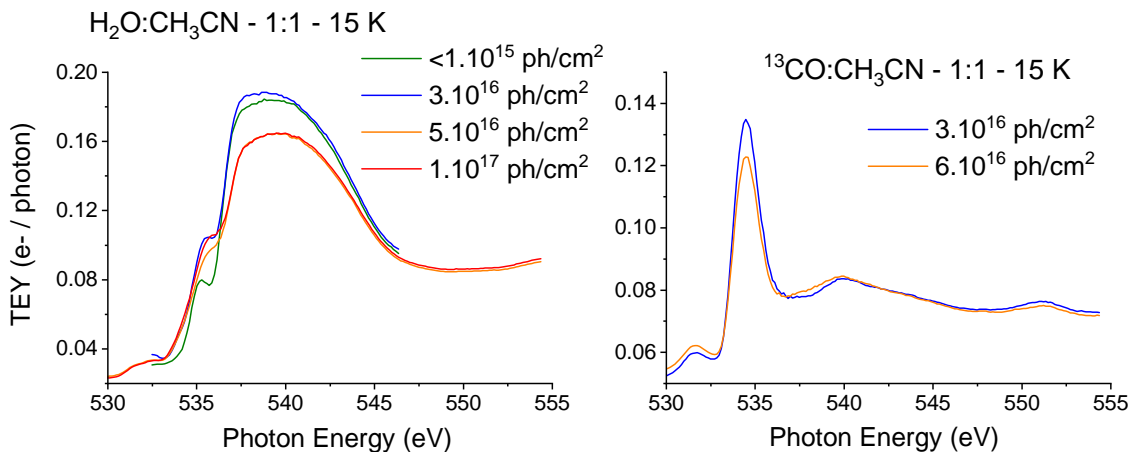


FIGURE VI.3 – TEYs near the O K-edge of a mixed  $\text{H}_2\text{O}:\text{CH}_3\text{CN}$  ice at 15 K with a dilution ratio of 1:1 (left panel) and of a mixed  $^{13}\text{CO}:\text{CH}_3\text{CN}$  ice at 15 K with a dilution ratio of 1:1 (right panel). The photon fluence received by the ice before the TEY measurement is also displayed.

The TEYs measured near the O K-edge for mixed  $^{13}\text{CO}:\text{CH}_3\text{CN}$  and  $\text{H}_2\text{O}:\text{CH}_3\text{CN}$  ices are displayed in Figure VI.3. The features observed are similar to that corresponding to pure  $\text{H}_2\text{O}$  and pure CO ice, already studied in Dupuy et al. (2020) and Dupuy et al. (2021b). The main feature for the  $^{13}\text{CO}:\text{CH}_3\text{CN}$  ice is associated with the  $\text{O } 1s \rightarrow \pi^*$  transition of  $^{13}\text{CO}$  near 534.4 eV. The features associated with  $\text{H}_2\text{O}$  are discussed in more details in Dupuy et al. (2020). Significant modifications of these TEYs with the photon fluence are not observed, meaning that potential photo-products formed during the X-ray irradiation of the mixed ices do not significantly participate to the photo-absorption of the ices in the 530 - 555 eV range. The evolution of the feature observed near 535.4 eV with the photon fluence for the mixed  $\text{H}_2\text{O}:\text{CH}_3\text{CN}$  ice is most likely due to a slight change in the structure of the water ice. As discussed in Dupuy et al. (2020), this feature can be associated with single donor, weakly coordinated,  $\text{H}_2\text{O}$  molecules in the water ice, which might increase after the formation of defects due to X-ray irradiation at 15 K.

### VI.1.3 HCOOH-containing ices

The TEYs measured from HCOOH-containing ices are displayed in Figure VI.4. In the top right panel, the main features associated with the X-ray absorption of HCOOH in condensed phase are the peaks at 532.4 and 534.4 eV and a broad bump centered near 541 eV. The first two peaks are attributed to the  $\text{O } 1s_{\text{CO}} \rightarrow \pi^*_{\text{CO}}$  and  $\text{O } 1s_{\text{OH}} \rightarrow \pi^*_{\text{CO}}$  core transitions. The broad bump, appearing above the gas phase ionization thresholds of the  $\text{O } 1s_{\text{CO}}$  and  $\text{O } 1s_{\text{OH}}$  core electrons, could be attributed to the  $\text{O } 1s_{\text{OH}} \rightarrow \sigma^*_{\text{CO}}$

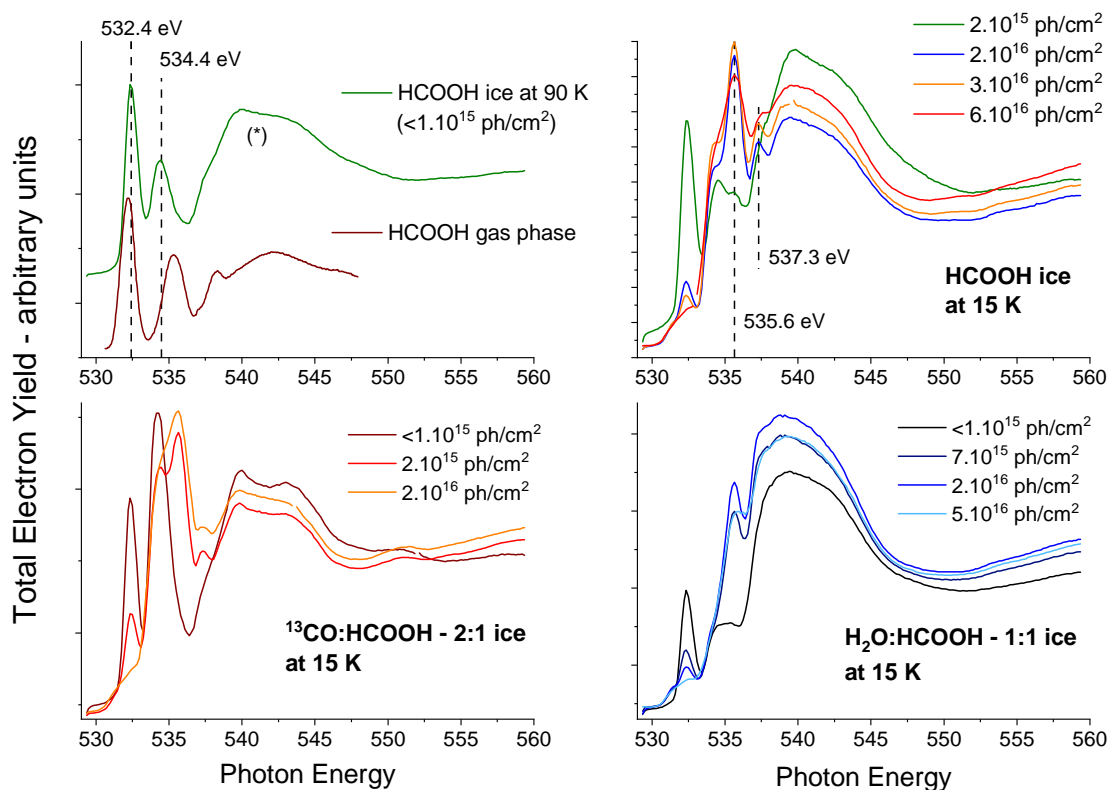


FIGURE VI.4 – TEYs near the O K-edge measured for a pure HCOOH ice at 90 K (top left panel) and 15 K (top right panel), a  $^{13}\text{CO}:\text{HCOOH}$  ice - 2:1 ice (bottom left panel) and a  $\text{H}_2\text{O}:\text{HCOOH}$  - 1:1 ice (bottom right panel). The displayed value for the photon fluence corresponds to the fluence received by the ice before the measurement. The ices thickness is equivalent to  $\sim 100$  ML. The top left panel also shows the X-ray absorption spectrum of gas phase HCOOH taken from Prince et al. (2003).

shape resonance observed in gas phase HCOOH although some states inherited from gas phase Rydberg states might also contribute to this feature just below the ionization thresholds of the condensed HCOOH. These attributions are based on X-ray spectroscopy studies of gas phase HCOOH (Prince et al., 2003; Tabayashi et al., 2006), compared with our TEY in the top left panel of Figure VI.4. The  $\text{O } 1s_{\text{CO}} \rightarrow \pi_{\text{CO}}^*$  and  $\text{O } 1s_{\text{OH}} \rightarrow \pi_{\text{CO}}^*$  transitions of the condensed HCOOH are shifted upwards by  $\sim 0.2$  eV and downwards by  $\sim 1$  eV, respectively, compared to that of gas phase HCOOH. These shifts are expected to be due to the clusterization of HCOOH in condensed phase, that can form for example dimers via hydrogen bonding. As explained in the study of Tabayashi et al. (2006), where they also observed these energy shifts in the X-ray absorption spectra of the free HCOOH molecule versus that of HCOOH clusters, the O 1s core electron binding energies are modified by a change in the electron density around the O atoms due to the formation of hydrogen bonds when HCOOH dimerizes, with a more significant effect for the hydroxyl oxygen than the carbonyl oxygen. This results in energy shifts for the core transitions when HCOOH molecules form clusters.

The evolution of the TEY of pure HCOOH ice at 15 K with the photon fluence is displayed in the top right panel of Figure VI.4. We first observe the total disappearance of the HCOOH absorption feature at 532.4 eV for a photon fluence between  $3$  and  $6 \times 10^{16}$  photon/cm<sup>2</sup>, meaning that HCOOH is only present near the ice surface in negligible amounts for such fluences. The appearance of new absorption features in the TEY also indicates the conversion of HCOOH to new species during the X-ray irradiation. The increasing features at 534.4 eV and 535.6 eV can be associated with the accumulation of CO and CO<sub>2</sub><sup>1</sup> near the ice surface. H<sub>2</sub>O accumulation might also contribute to the broad bump centered near 541 eV. In similar experiments, CO, CO<sub>2</sub> and H<sub>2</sub>O are also observed by infrared spectroscopy as main dissociation products in condensed HCOOH when irradiated with X-rays (Ryazantsev and Feldman, 2015) and heavy ions (Andrade et al., 2013; Bergantini et al., 2014). The peak observed at 537.3 eV remains to be attributed.

The TEYs of the mixed ices and their evolution with the photon fluence are displayed in the bottom panels of Figure VI.4. The new features appearing with the photon fluence in the mixed ices are similar to those in pure HCOOH ice, with the feature associated with CO<sub>2</sub> accumulation being the main one. The decrease of the HCOOH absorption feature at 532.4 eV behaves similarly with the photon fluence for the mixed and pure ices, indicating that the presence of CO or H<sub>2</sub>O molecules does not significantly modify the destruction kinetic of HCOOH in condensed phase. For instance, in each ice studied, HCOOH can be considered as nearly totally dissociated near the ice surface for a photon fluence  $\gtrsim 2\text{-}3 \times 10^{16}$  ph/cm<sup>2</sup>. A similar behavior has been observed in the study of Bergantini et al. (2014) where the authors found a similar destruction cross section of HCOOH by cosmic ray analogues in pure ice and when HCOOH is mixed with water.

Interestingly, the behavior of HCOOH ice under X-ray irradiation differs from that of CH<sub>3</sub>OH and CH<sub>3</sub>CN ices as discussed previously. Indeed, for CH<sub>3</sub>CN, we clearly observed in the TEYs data near the N K-edge that the presence of water in the mixed ices tends to accelerate the destruction of the COM with the ongoing irradiation as compared to the case of pure and CO-mixed ices. For CH<sub>3</sub>OH, such behavior is not directly observable near the O K-edge as the contribution of CH<sub>3</sub>OH overlaps with that of H<sub>2</sub>O in the TEY but it is anyway expected to be similar according to the C K-edge study of Laffon et al. (2010). On the other hand, the dissociation of HCOOH in condensed phase induced by X-rays does not seem to depend on the presence of water or CO molecules and in any case, HCOOH dissociation seems to be very efficient as compared to CH<sub>3</sub>OH or CH<sub>3</sub>CN : for instance, in pure ices and according to the X-ray absorption fea-

1. the attribution of the feature near 535.6 eV to CO<sub>2</sub> absorption is based on gas phase studies (Wight and Brion, 1974)

tures, HCOOH almost totally disappears from the near ice surface for a photon fluence  $\gtrsim 2\text{-}3 \times 10^{16}$  photon/cm<sup>2</sup> whereas CH<sub>3</sub>OH and CH<sub>3</sub>CN are still significantly present for a photon fluence  $\gtrsim 1 \times 10^{17}$  photon/cm<sup>2</sup>. This again shows that the behavior of one specific COM cannot be taken as a general rule and it has somehow important astrophysical implications : while the survival of CH<sub>3</sub>CN and CH<sub>3</sub>OH in X-ray irradiated interstellar ices, especially in protoplanetary disks, will strongly depend on the ice composition hence on the region considered, this is not the case for HCOOH whose survival rate is in any case expected to be low.

## VI.2 X-ray photodesorption from pure ices

We first discuss the X-ray photodesorption from the pure ices of COMs. Although these systems are less representative of interstellar ices, such studies allow us to discuss the physical mechanisms involved in the X-ray photodesorption of COMs. The case of CH<sub>3</sub>OH is particularly interesting because a comparison between VUV and X-ray photodesorption yields can be made, as well as a comparison with Electron-Stimulated-Desorption (ESD) yields. Such comparison for CH<sub>3</sub>CN and HCOOH is not possible since the VUV photo-absorption cross sections and the ESD yields are not available in the literature. The case of CH<sub>3</sub>OH will be presented first, followed by CH<sub>3</sub>CN and HCOOH. As discussed in the previous section, the dissociation of the COMs during the X-ray irradiation can be very efficient in some cases. Our aim is to limit this dissociation as much as possible in order to provide X-ray photodesorption yields associated with a low-processed, "intact" ice. Consequently, the yields displayed in the various tables of this section were derived for a low photon fluence (generally  $< 2 \times 10^{16}$  photon/cm<sup>2</sup>). This was done by irradiating the ices at fixed energy for a few tens of seconds. Photodesorption spectra, that is the photodesorption yields plotted as a function of the photon energy, were also obtained at higher fluence by continuously scanning the incident photon energy.

### VI.2.1 Pure CH<sub>3</sub>OH ice

#### VI.2.1.1 X-ray photodesorption yields

In Figure VI.5 we report the X-ray photodesorption yields from pure methanol ice. We do not display all available data for more clarity, as we did not observe behaviors different from the data we present. The TEY measurements are also shown in arbitrary units. The photodesorption yields derived from the irradiations at fixed energy are consistent with those measured during the scan experiments, except when the fluence received by the ice differs. The remaining relevant data we obtained are summarized in Table VI.1, where the yields are derived from our fixed energy experiments. As a lo-

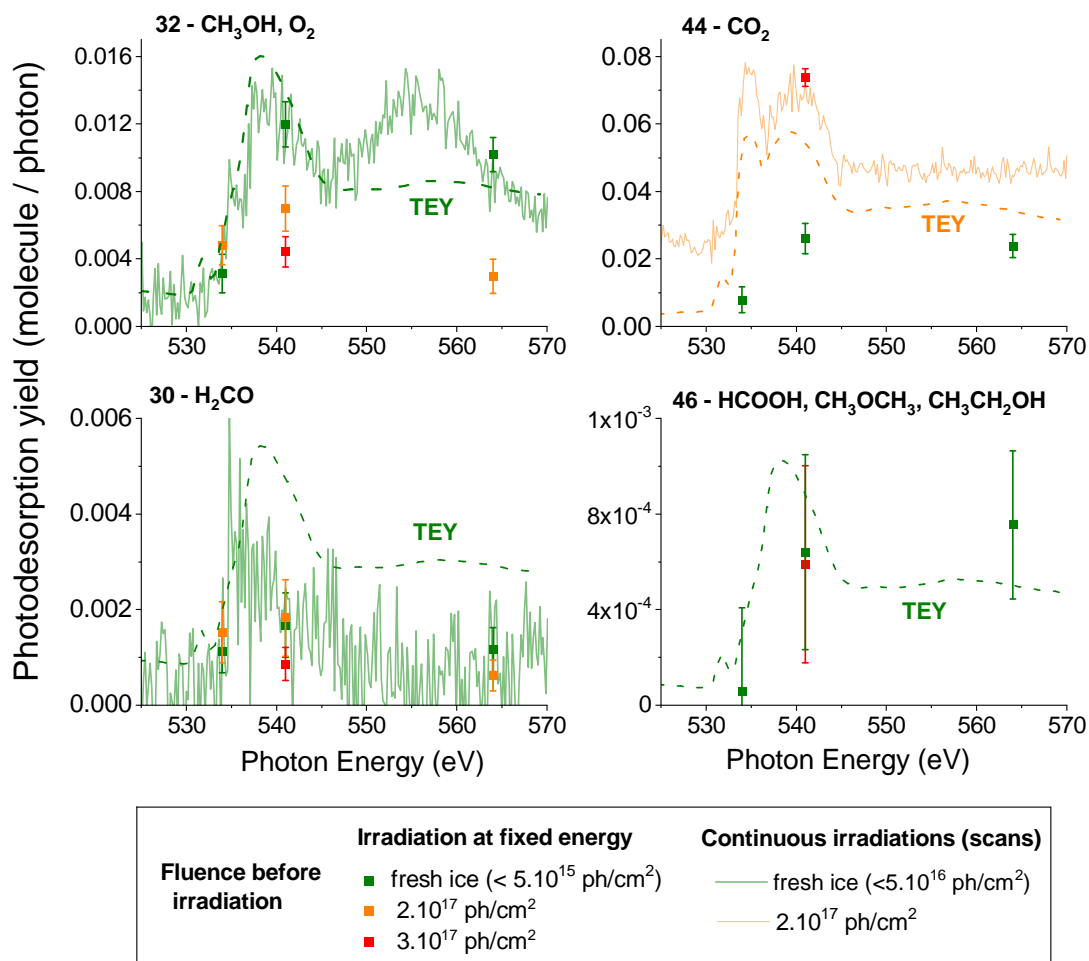


FIGURE VI.5 – Photodesorption spectra for masses 30 u., 32 u., 44 u., and 46 u. from pure methanol ice at 15 K. The attribution of the desorbing species to the mass channels is discussed in the text. The measurements at fixed energy are represented by the squares with error bars. The scan experiments are represented by solid lines. The TEYs measured simultaneously during the scan experiments are also shown as dashed lines in arbitrary units. The photon fluence received by the ice before each measurement is displayed in the bottom.

wer fluence is used compared to the scan experiments, the aging effect is limited for these yields : the fluence received by the ice before measurement ranges from  $5 \times 10^{15}$  to  $2 \times 10^{16}$  photon/cm<sup>2</sup>. These yields are derived at a fixed energy of 564 eV. CO and CO<sub>2</sub> are the most strongly desorbing species with a photodesorption yield at 564 eV of  $\sim 0.1$  molecule/photon and  $\sim 0.02$  molecule/photon, respectively. OH X-ray photodesorption is not detected during irradiations. For the desorption signal on the mass 16 u., we were not able to distinguish between the desorption of CH<sub>4</sub> or atomic O. For the mass 15 u., the displayed photodesorption yield is not corrected for any cracking pattern (especially from the mass 16 u., which could be attributed to CH<sub>4</sub> photodesorption) and it may be overestimated.

TABLE VI.1 – X-ray photodesorption yields ( $10^{-3}$  molecule/photon) at 564 eV from pure  $\text{CH}_3\text{OH}$  ice at 15 K and for a photon fluence  $< 2.10^{16}$  photon/ $\text{cm}^2$ .

	Yield		Yield
15 - $\text{CH}_3$	$1.3^{\pm 0.2}$	30 - $\text{H}_2\text{CO}$	$1.2^{\pm 0.5}$
16 - $\text{CH}_4, \text{O}$	$1.1^{\pm 0.2}$	32 - $\text{CH}_3\text{OH}$	$7.6^{\pm 0.9}$
17 - $\text{OH}$	$< 5 \times 10^{-4}$	44 - $\text{CO}_2$	$24^{\pm 1}$
18 - $\text{H}_2\text{O}$	$7.5^{\pm 1.1}$	46 - $\text{HCOOH}, \text{C}_2\text{H}_6\text{O}$	$0.8^{\pm 0.3}$
28 - $\text{CO}$	$(1.2)^{\pm 0.1} \times 10^2$		

As the QMS signal registered on the mass 32 u. could correspond to  $\text{O}_2$  or  $\text{CH}_3\text{OH}$  desorption, we used the signal on the mass 31 u. to estimate the weight of  $\text{CH}_3\text{OH}$  photodesorption on the mass channel 32 u.. We assumed that the desorption of  $\text{CH}_2\text{OH}$  or  $\text{CH}_3\text{O}$  radical (that would contribute to the mass channel 31 u.) is negligible in our experiments with pure methanol ice, so that the signal on the mass 31 u. only originates from the cracking of desorbing  $\text{CH}_3\text{OH}$  into  $\text{CH}_2\text{OH}^+$  or  $\text{CH}_3\text{O}^+$  (which are the main fragments) in the ionization chamber of the QMS. We then found that a maximum of  $\sim 75\%$  of the signal on the mass 32 u. could correspond to  $\text{CH}_3\text{OH}$  photodesorption (after correction for the cracking of  $\text{CH}_3\text{OH}$  into  $\text{CH}_2\text{OH}^+$  or  $\text{CH}_3\text{O}^+$ , this brings the signal on the mass 31 u. to below our detection threshold, which is  $5 \times 10^{-4}$  molecule/photon), at 541 and 564 eV and for a fresh ice (photon fluence  $< 5 \times 10^{15}$  photon/ $\text{cm}^2$ ). The remaining signal on the mass 32 u. ( $\sim 25\%$ ) then originates from  $\text{O}_2$  photodesorption, whose yield at 564 eV is  $\sim 2.5 \times 10^{-3}$  molecule/photon. When the fluence increases to  $3 \times 10^{17}$  photon/ $\text{cm}^2$ , we found that only  $\sim 30\%$  of the signal on the mass 32 u. could correspond to  $\text{CH}_3\text{OH}$  photodesorption at 541 eV. This decrease of the photodesorption yield of  $\text{CH}_3\text{OH}$  with the photon fluence is clearly seen in Figure VI.6 where the raw desorption signals of the masses 32 u. and 31 u. are shown as a function of the photon fluence. The estimated photodesorption yield of  $\text{CH}_3\text{OH}$  therefore decreases from  $7.6 \times 10^{-3}$  molecule/photon for a fresh ice (photon fluence  $< 5 \times 10^{15}$  photon/ $\text{cm}^2$ ) to  $1.3 \times 10^{-3}$  molecule/photon for a processed ice (photon fluence of  $2 \times 10^{17}$  photon/ $\text{cm}^2$ ) at 564 eV. The effect of the photon fluence on the experimental detection of  $\text{CH}_3\text{OH}$  X-ray photodesorption is further discussed in Section VI.3.1 with regards to similar experiments conducted by Ciaravella et al. (2020).

We also observed a photodesorption signal on the mass channel 46 u., which can be attributed to either  $\text{HCOOH}$  (formic acid) and/or  $\text{C}_2\text{H}_6\text{O}$  isomers (ethanol and dimethyl ether). These molecules have already been detected by infrared spectroscopy as accumulating in the ice when pure methanol ice is irradiated at 14 K with X-rays of 550 eV (Chen et al., 2013c).

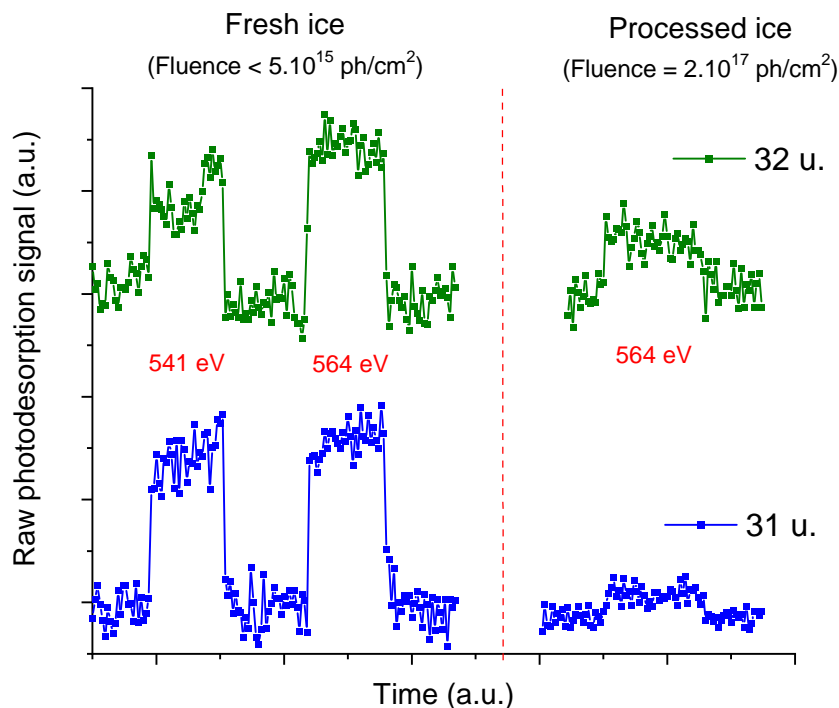


FIGURE VI.6 – Raw X-ray photodesorption signals of the masses 31 u. (lower blue data) and 32 u. (upper green data) from pure  $\text{CH}_3\text{OH}$  ice irradiated at 15 K. The left part of the data were obtained for a fresh ice (photon fluence  $< 5 \times 10^{15}$  photon/cm $^2$ ) whereas the right part of the data were obtained for a processed ice (photon fluence of  $2 \times 10^{17}$  photon/cm $^2$ ). In red is also displayed the photon energy.

The data presented in Figure VI.5 show a correlation between the photodesorption spectra and the TEYs (except for the broad peak observed on the photodesorption spectrum of the mass channel 32 u. between 545 and 565 eV, which is due to an unstable background noise and does not reflect any particular physical mechanism). The photodesorption is thus induced by the X-ray absorption of the ice, as expected. As discussed in Chapter III.2.2, the desorption can be induced by the Auger scattering and the subsequent cascade of secondary electron (X-ray induced Electron Stimulated Desorption - XESD process) or by processes decorrelated from the Auger scattering (non-XESD processes). It is however not possible at this stage to conclude on the dominant desorption mechanism only from these data because the fact that the photodesorption spectra follow the TEY is compatible with both processes.

When the fluence received by the pure methanol ice is increasing, the shape of the TEY and of the photodesorption spectra are modified in a similar way. The main modification is that a peak at 534.4 eV arises because of the accumulation of CO near the ice surface. Consequently, for a processed ice, the photodesorption can be triggered either from CO or  $\text{CH}_3\text{OH}$  absorption at different energies. For instance, the photodesorption yields on the mass channel 32 u. at 534.4 eV and at 541 eV are  $0.5 \times 10^{-2}$  mo-

lecule/photon and  $0.7 \times 10^{-2}$  molecule/photon, respectively, for a fluence of  $2 \times 10^{17}$  photon/cm<sup>2</sup>, whereas they differ by a factor of  $\sim 4$  for fresh ice. This is also observed for CO<sub>2</sub> photodesorption yields at 534 eV and 541 eV, which are  $7.6 \times 10^{-2}$  molecule/photon and  $6.8 \times 10^{-2}$  molecule/photon, respectively, for a fluence of  $2 \times 10^{17}$  photon/cm<sup>2</sup>, whereas they differ by a factor of  $\sim 4$  for a fresh ice. This highlights the importance of the ice composition and shows that the X-ray photodesorption from COMs-containing ices can be an indirect process where the photodesorption of one molecule is triggered by the X-ray absorption of another one, as it has been discussed in Chapter IV. With increasing fluence, from  $5 \times 10^{15}$  photon/cm<sup>2</sup> to  $3 \times 10^{17}$  photon/cm<sup>2</sup>, the estimated yield for the X-ray photodesorption of CH<sub>3</sub>OH is decreasing by almost one order of magnitude, from  $7.6 \times 10^{-3}$  to  $1.3 \times 10^{-3}$  molecule/photon. This photo-aging of the ice therefore quenches the desorption of the intact COM while favoring the desorption of products such as CO<sub>2</sub> or CO.

### VI.2.1.2 Comparison with VUV yields

In Table VI.2 we compare the photodesorption yields in molecules desorbed per eV deposited (displayed as molecules/eV deposited) in the X-ray (at 564 eV, from Table VI.1) and the VUV range (at 10.5 eV; from Bertin et al. (2016)) for CH<sub>3</sub>OH from pure methanol ice using the method described in Chapter II.2.3<sup>2</sup>. To compute the X-ray yields, we assumed that the X-ray absorption cross section of condensed phase methanol is equal to that of gas phase methanol, which is  $\sim 0.52$  Mbarn (Ishii and Hitchcock, 1988) at 564 eV, and we took  $\Lambda_{des} = 30$  ML, which is (i) equal to the radius of the electron cloud created by the Auger scattering in water ice (Tîmneanu et al., 2004) and (ii) consistent with our experiments on N<sub>2</sub>:CO ices presented in Chapter IV. To compute the VUV yields, we took  $\Lambda_{des} = 3$  ML according to experiments conducted on pure CO ices (Bertin et al., 2012). The VUV photo-absorption cross section of methanol in condensed phase is equal to 8.6 Mbarn at 10.5 eV (Cruz-Diaz et al., 2014a). As displayed in Table VI.2 and considering the relative uncertainty on the desorption yields derived, which is roughly 50 %, X-ray photodesorption of CH<sub>3</sub>OH from pure CH<sub>3</sub>OH ice is therefore more efficient per eV deposited than VUV photodesorption, by approximately one order of magnitude. In other words, one eV deposited through X-ray absorption is more efficiently converted to the desorption of CH<sub>3</sub>OH than one eV deposited through VUV absorption. Interestingly, it was found the opposite behavior for the photodesorption of CO from pure CO ice : in that case, the X-ray desorption yield per eV deposited was found lower, by approximately one order of magnitude than the VUV yield (see Chapter IV.1.6). This might indicate that very different photodesorption mechanisms are expected to be at play between the photodesorption of COMs and that of

2. I remind the equation here :  $\Gamma_X^{eV}(E) = \frac{\Gamma_X(E)}{E(1 - e^{-\sigma(E)\Lambda_{des} \times 10^{15}})}$

TABLE VI.2 – Photodesorption yields of CH<sub>3</sub>OH from pure CH<sub>3</sub>OH ice at 15 K in the VUV and X-ray range. The yields are expressed either in molecules desorbed per incident photon, displayed as molecule/photon, or in molecules desorbed per eV deposited in the first  $\Lambda_{des}$  ML of the ice, displayed as molecule/eV deposited.

Photon Energy	$\sigma$ (Mbarn)	$\Lambda_{des}$ (ML)	Photodesorption yield	
			molecule/photon	molecule/eV deposited
10.5 eV	8.6	3	$1.5 \times 10^{-5}$	$5.9 \times 10^{-5}$
564 eV	0.52	30	$7.6 \times 10^{-3}$	$9.8 \times 10^{-4}$

more "simple", diatomic, molecules. For instance, the desorption of CO was suggested to be due to a valence electronic excitation induced by the incident photon in the VUV range (Fayolle et al., 2011) and by the secondary low energy electrons for X-rays (Dupuy et al., 2021b). In the X-ray range, part of the incident energy is lost in channels decoupled from CO desorption because the low energy electrons induce various processes, which was suggested by Dupuy et al. (2021b) to explain why the X-ray yield per eV deposited is lower than the VUV yield for CO desorption from pure CO ice. On the other hand, the desorption of CH<sub>3</sub>OH may be due to a different mechanism. For instance, Öberg, K. I. et al. (2009a) and Bertin et al. (2016) suggested that the VUV photodesorption of CH<sub>3</sub>OH from pure methanol ice originates from the exothermic recombination of CH<sub>3</sub>O/CH<sub>2</sub>OH into CH<sub>3</sub>OH followed by its desorption.

The way the energy is deposited within the ice and its consequence on the induced chemistry could be an interesting route for explaining the differences in the X-ray and VUV yields of CH<sub>3</sub>OH per eV deposited. When an X-ray is absorbed in the ice, most of the energy ( $\sim 500$  eV in our case) goes into the Auger electron, and the deposited energy is spatially localized around the thermalization path of this Auger electron. Depositing an equivalent amount of energy with VUV photons in the ice may result in a different spatial distribution of the total deposited energy. For instance, we would expect a more homogeneous spatial distribution of the energy deposited by VUV photons. At the low temperatures considered here ( $T \sim 15$  K), where the diffusion of molecules is limited, this localization of the deposited energy would therefore favor reactions between neighboring excited molecules, radicals or ions in the case of X-ray absorption compared to VUV absorption. Moreover, X-ray induced chemistry could involve a richer reaction network as a result of ion chemistry because molecular ionizations are easily produced in the thermalization path of the Auger electron, whereas VUV photons in the range of 7-14 eV are expected to produce fewer ions because their energy is close to the ionization threshold of CH<sub>3</sub>OH. Our hypothesis is then to consider that recombination reactions leading back to the formation and subsequent desorption of

CH<sub>3</sub>OH might be favored by this richer and more spatially localized chemistry in the case of X-ray photodesorption compared to the case of VUV photodesorption, which would explain these differences observed in the yields per eV deposited.

### VI.2.1.3 Comparison with ESD yields

Previous results on CO:N<sub>2</sub> ices presented in Chapter IV have shown that desorption induced by X-rays is driven by the Auger scattering. As concluded in this chapter, Electron-Stimulated Desorption (ESD) experiments for which the incident electrons have a similar energy than the Auger electron could be a good complementary and more easily accessible tool to study X-ray photodesorption from interstellar ice analogues. During the thesis, I participated in ESD experimental studies conducted at the ISMO lab by Anne Lafosse, Lionel Amiaud and Daniela Torres-Díaz. The set-up implemented at the ISMO lab is similar to the SPICES set-up except that the ices are irradiated with electrons generated by an electron gun. More details about the set-up can be found in Houplin et al. (2013); Sala (2018); Sala et al. (2018). In the following, I will briefly present the main results of the study conducted on methanol, which are detailed in Torres-Díaz et al. (2022).

The ESD experiments consisted of irradiating a pure methanol ice with electrons of 505 eV while probing the desorption of neutral species with a QMS<sup>3</sup>. An example of the raw signals obtained from the experiments are shown in the left panel of Figure VI.7 where the sudden increase and decrease of the signal is associated with the desorption induced by the electrons. The raw signal is converted to a desorption yield (with a methodology similar than the one described in Chapter II.2) expressed in molecules desorbed by incident electron, simplified as molecules/electron in the following, and plotted as a function of the electron fluence (an example is given in the right panel of Figure VI.7). The desorption yield  $Y$  is assumed to follow a pseudo-first order kinetics in the low fluence regime (up to  $1 - 3 \times 10^{15}$  electron/cm<sup>2</sup>) described by the equation :

$$\ln Y(\phi) = \ln Y_0 - \sigma_{eff} \times \phi \quad (\text{VI.1})$$

Fitting the data with equation VI.1 gives an estimate of the desorption yield associated with the fresh ice  $Y_0$  and the effective depletion cross section  $\sigma_{eff}$ , as shown in the inset of the right panel of Figure VI.7. The ESD yields  $Y_0$  derived for the different species detected as desorbing in the ESD experiments are compared in Figure VI.8 with the X-ray photodesorption yields from the synchrotron experiments, relatively to the CH<sub>3</sub>OH yield. The chemistry induced by the incident electrons replicates well that induced by X-rays, as seen by the good match of the relative yields which are found very close to

3. similarly to the SPICES set-up, the ionization is also occurring by electron impact at 70 eV

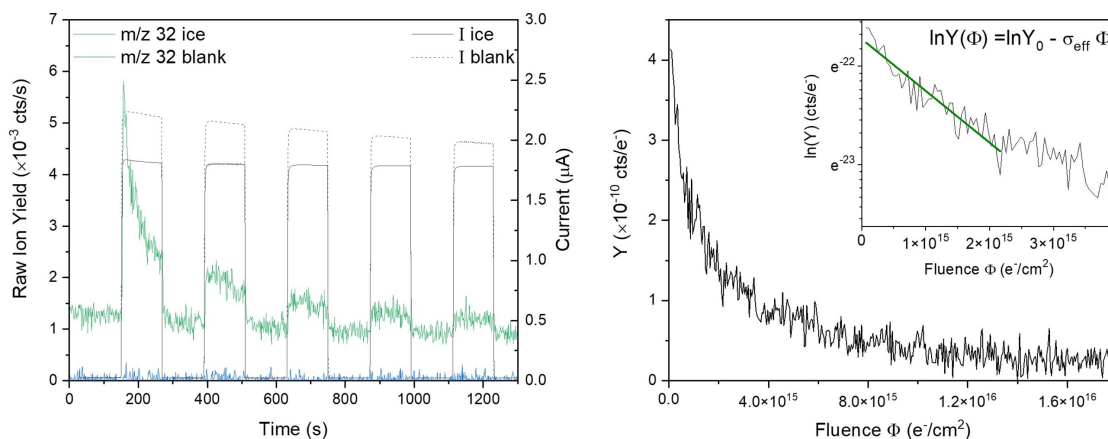


FIGURE VI.7 – Left panel : raw desorption signal and incident current  $I$  recorded as a function of time. Blank corresponds to irradiation of the clean substrate and ice corresponds to irradiation of pure  $\text{CH}_3\text{OH}$  ice. Right panel : reconstructed yield  $Y$  as a function of the electron fluence. The inset in the right panel shows the data fit with equation VI.1. Taken from [Torres-Díaz et al. \(2022\)](#).

each other for  $\text{H}_2\text{CO}$  and for the contributors of mass 46 u. ( $\text{HCOOH}$ ,  $\text{C}_2\text{H}_6\text{O}$  isomers) and slightly differ for the other products but are found in any case in the same order of magnitude.

More importantly, the absolute ESD yield derived for intact  $\text{CH}_3\text{OH}$  was found to be  $0.15 \pm 0.01$  molecules/electron. To compare this yield with the X-ray yield, we should consider that, in the case of the X-ray experiments, all the incident photons will not necessarily participate in the desorption of molecules from the ice surface. In that case, we assume that the photons that actually induce desorption are the photons absorbed in the first 30 ML of the ice. We should also consider that one photon absorbed generates one Auger electron in the ice, as the Auger decay occurs with a probability close to 1, which makes the X-ray yield expressed in molecules per absorbed photon directly comparable with the ESD yield expressed in molecules per incident electron. After computation, we found a X-ray yield at 564 eV of 0.49 molecules/absorbed photons, to compare to the ESD yield of 0.15 molecules/electron. Considering the experimental uncertainties, there is an excellent agreement between the ESD yield and the X-ray yield. This quantitative comparison along with the yields shown in Figure VI.8 show clear evidences that ESD experiments replicate well the X-ray experiments and can indeed be a complementary tool to study X-ray photodesorption from interstellar ice analogues. This is also a strong argument to justify that the desorption induced by X-rays is governed by the Auger scattering.

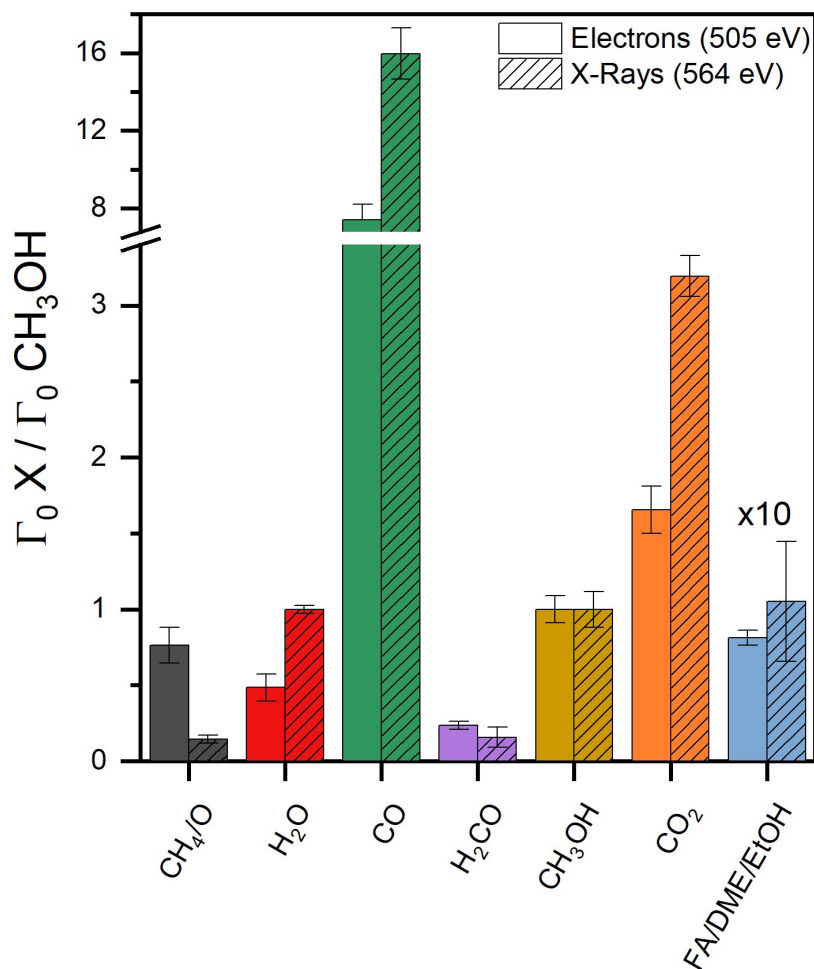


FIGURE VI.8 – Comparison of relative desorption yields between ESD and X-Ray photodesorption. Each data set is normalized to the CH<sub>3</sub>OH yield. The data corresponding to the blue color are associated with the mass 46 u. desorption (FA = formic acid, DME = dimethyl ether, EtOH = ethanol). Taken from [Torres-Díaz et al. \(2022\)](#).

## VI.2.2 Pure CH<sub>3</sub>CN ice

The irradiation experiments on pure CH<sub>3</sub>CN ice at 15 K have shown the X-ray induced desorption of several species. The photodesorption spectra are shown for some mass channels in Figure VI.9 near the N K-edge. Similarly to the case of CH<sub>3</sub>OH, the spectra display the same energy dependence as the TEYs, where the desorption signal is maximum near 400 eV, at the N 1s → π\* transition of CH<sub>3</sub>CN. This confirms that the photodesorption is well-correlated to the X-ray photo-absorption of the ice. The attribution of the desorbing species to the mass signals are done by monitoring the change in the signals with two isotopes of acetonitrile, namely, CH<sub>3</sub><sup>12</sup>C<sup>14</sup>N and CH<sub>3</sub><sup>13</sup>C<sup>15</sup>N. In Figure VI.10, we compare the raw photodesorption intensities (QMS signal in A) of the different mass channels monitored as a function of the isotopes in order to discuss the attribution of the desorbing species to the mass channels. The comparison is made at

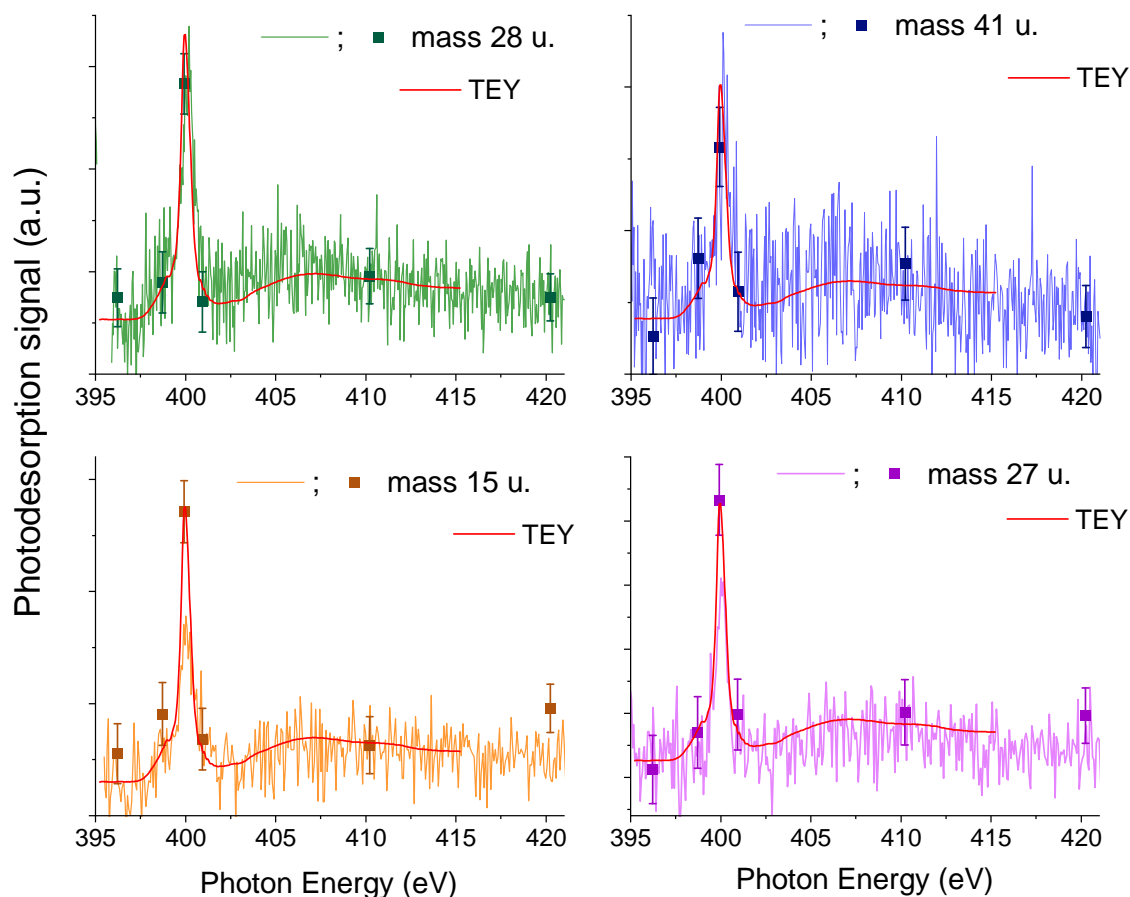


FIGURE VI.9 – Photodesorption spectra of masses 15 u., 27 u., 28 u. and 41 u. (in arbitrary units) from a pure  $\text{CH}_3\text{CN}$  ice at 15 K. The solid noisy lines are associated with the desorption signal monitored during a continuous irradiation from 395 to 420 eV whereas the squares with error bars result from the desorption measurement corresponding to irradiations at fixed energies for a few seconds. The TEY measured simultaneously during the continuous irradiation is shown in solid red line. The attribution of the desorbing species to the mass channels is done in the text.

420 eV, in the ionization region of the core N 1s electron. The intensities are not corrected from any possible cracking of the desorbing species in the ionization chamber of the QMS. The masses 26 u., 29 u. and 30 u. were not monitored during the X-ray irradiation of the pure natural isotope  $\text{CH}_3^{12}\text{C}^{14}\text{N}$  ice and the mass 16 u. was not detected. The desorption intensities of the masses 41 u. and 43 u. from pure  $\text{CH}_3^{12}\text{C}^{14}\text{N}$  and  $\text{CH}_3^{13}\text{C}^{15}\text{N}$  ices respectively are similar. This confirms the X-ray photodesorption of the intact acetonitrile molecule from the ices studied. The desorption intensity of the mass 15 u. is not significantly changing from one isotope to the other, hinting towards the X-ray photodesorption of  $\text{CH}_3$ . For the  $\text{CH}_3^{13}\text{C}^{15}\text{N}$  ice, the desorption intensity of the mass 29 u. is  $\sim 3.3 \times 10^{-12}$  A. For the mass 27 u., the same level of signal is observed for the  $\text{CH}_3^{12}\text{C}^{14}\text{N}$  ice whereas it is divided by  $\sim 4$  for the  $\text{CH}_3^{13}\text{C}^{15}\text{N}$  ice. This indicates that the desorption of  $\text{H}^{13}\text{C}^{15}\text{N}$  and  $\text{H}^{12}\text{C}^{14}\text{N}$  contributes to the mass channels 29 u. and 27 u.

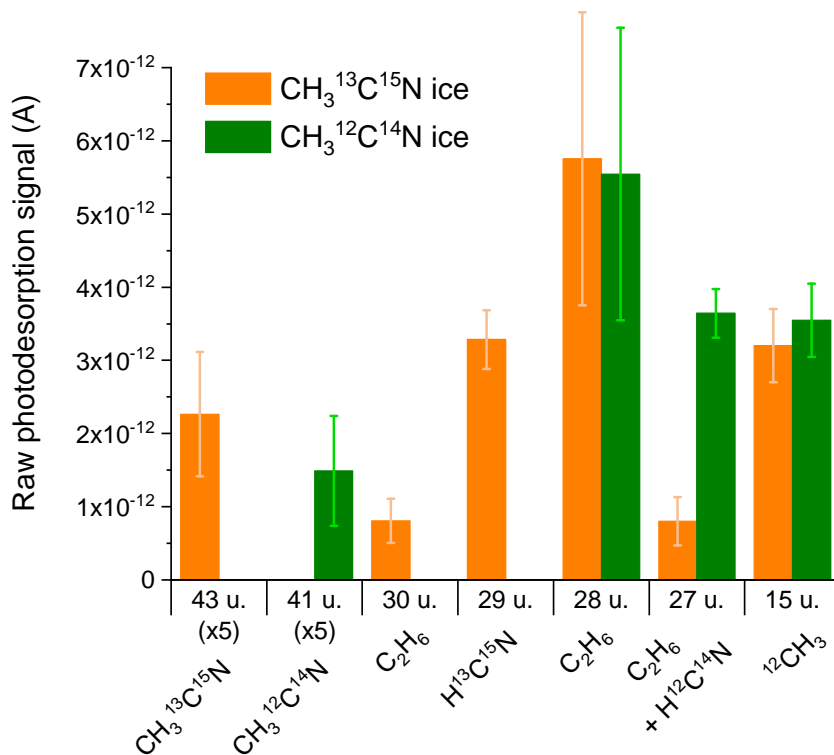


FIGURE VI.10 – Raw photodesorption signals (in A) at 420 eV of desorbing masses from pure acetonitrile ices. The different colors are associated with a natural CH<sub>3</sub><sup>12</sup>C<sup>14</sup>N or an isotopic CH<sub>3</sub><sup>13</sup>C<sup>15</sup>N ice, irradiated at 15 K. The attribution of the desorbing species to the mass channels is done in the text. The signals were obtained for a fluence < 2 × 10<sup>16</sup> ph/cm<sup>2</sup> and are not corrected from any possible cracking of desorbing species in the ionization chamber of our QMS.

from the CH<sub>3</sub><sup>13</sup>C<sup>15</sup>N and CH<sub>3</sub><sup>12</sup>C<sup>14</sup>N ice respectively. The X-ray photodesorption of HCN from acetonitrile ices is supported by its accumulation in the ice as seen in the study of [Ipolyi et al. \(2007\)](#). In this study, the irradiation (at 35 K) of a pure acetonitrile ice by low energy electrons (5 - 16 eV) displayed in post-TPD experiments the appearance of a (thermal) desorption peak attributed by the authors to the formation of HCN. Additionally, low energy electron-stimulated desorption of CH<sub>2</sub><sup>-</sup> from pure CH<sub>3</sub>CN ice at 30 K observed in the study of [Bass et al. \(2012\)](#) led the authors to suggest the formation of HCN after H migration from CH<sub>3</sub><sup>-</sup> to CN (due to a cage effect of the surrounding molecules) that both originate from Dissociative Electron Attachment (DEA) of CH<sub>3</sub>CN. In our experiments, the X-ray induced chemistry is dominated by the Auger thermalization and the subsequent cascade of low energy secondary electrons. It is therefore expected that HCN formation and subsequent photodesorption could occur according to the studies of [Ipolyi et al. \(2007\)](#) and [Bass et al. \(2012\)](#). The signal observed on the mass channel 27 u. from the CH<sub>3</sub><sup>13</sup>C<sup>15</sup>N ice can be related to the mass 30 u., as discussed in the following.

TABLE VI.3 – Photodesorption yields in molecule/photon, of intact CH<sub>3</sub>CN and fragments, from pure CH<sub>3</sub>CN ices irradiated at 15 K and at a photon energy of 420 eV. The fluence received by the ice before the measurements is  $< 2 \times 10^{16}$  ph/cm<sup>2</sup>.

Species	Yield	Species	Yield
CH <sub>3</sub> CN	$5.2 \pm 1.5 \times 10^{-4}$	HCN	$1.6 \pm 0.3 \times 10^{-3}$
C <sub>2</sub> H <sub>6</sub>	$2.4 \pm 0.9 \times 10^{-3}$	CH <sub>3</sub>	$1.3 \pm 0.7 \times 10^{-3}$

The desorption of the mass 30 u. is attributed to C<sub>2</sub>H<sub>6</sub> desorption, also supported by the studies of [Ipolyi et al. \(2007\)](#) and [Bass et al. \(2012\)](#) where the formation of C<sub>2</sub>H<sub>6</sub> is proposed to occur via reactions between CH<sub>3</sub> radicals after DEA of CH<sub>3</sub>CN into CN<sup>-</sup> and CH<sub>3</sub>. A possible significant contribution of <sup>15</sup>N<sub>2</sub> desorption to the mass 30 u. for the CH<sub>3</sub><sup>13</sup>C<sup>15</sup>N ice can be excluded by the fact that N<sub>2</sub> desorption should contribute to an increase of the mass 28 u. signal for the CH<sub>3</sub><sup>12</sup>C<sup>14</sup>N ice compared to the CH<sub>3</sub><sup>13</sup>C<sup>15</sup>N ice. Considering the level of signals on the masses 30 u. and 28 u., such an increase is not observed. Excluding N<sub>2</sub> desorption first seems to be contradictory with the TEYs data that showed an accumulation of N<sub>2</sub> near the ice surface with the photon fluence. However, the intensities displayed in [Figure VI.10](#) for the mass 28 u. were derived for a photon fluence  $< 2 \times 10^{16}$  photon/cm<sup>2</sup> whereas the N<sub>2</sub> feature is only clearly observed in the TEY for a photon fluence  $> 8 \times 10^{16}$  photon/cm<sup>2</sup>. This would mean that N<sub>2</sub> is not sufficiently produced at the ice surface to desorb in the low fluence regime in which the intensities of [Figure VI.10](#) are derived. However, we did not monitor the evolution of the intensity of the mass 28 u. from a pure CH<sub>3</sub><sup>12</sup>C<sup>14</sup>N ice with the photon fluence to check if any N<sub>2</sub> desorption might increase the signal on this mass channel for high fluence ( $> 8 \times 10^{16}$  photon/cm<sup>2</sup>). By taking into account the cracking of the mass 30 u., considered to be C<sub>2</sub>H<sub>6</sub>, in the ionization chamber of the QMS, the signal on the mass channel 28 u. is under our detection limit. Similarly, after this correction, the signal on the mass 27 u. is very close to zero for the pure CH<sub>3</sub><sup>13</sup>C<sup>15</sup>N ice. Finally, after conversion of the raw intensities, we display in [Table VI.3](#) the X-ray photodesorption yields derived at 420 eV from our experiments on pure acetonitrile ices.

### VI.2.3 Pure HCOOH ice

X-ray photodesorption from pure HCOOH ice irradiated at 15 K results in the desorption of neutral molecules detected on the QMS mass channels 18 u., 28 u., 30 u., 32 u., 44 u. and 46 u., attributed respectively to H<sub>2</sub>O, CO, H<sub>2</sub>CO, O<sub>2</sub>, CO<sub>2</sub> and HCOOH desorption. No signal was detected on the mass channel 31 u. such that the possible photodesorption of CH<sub>3</sub>OH, that would produce a signal on the mass 31 u. due to its dissociative ionization at the QMS entrance, is not occurring. Photodesorption spec-

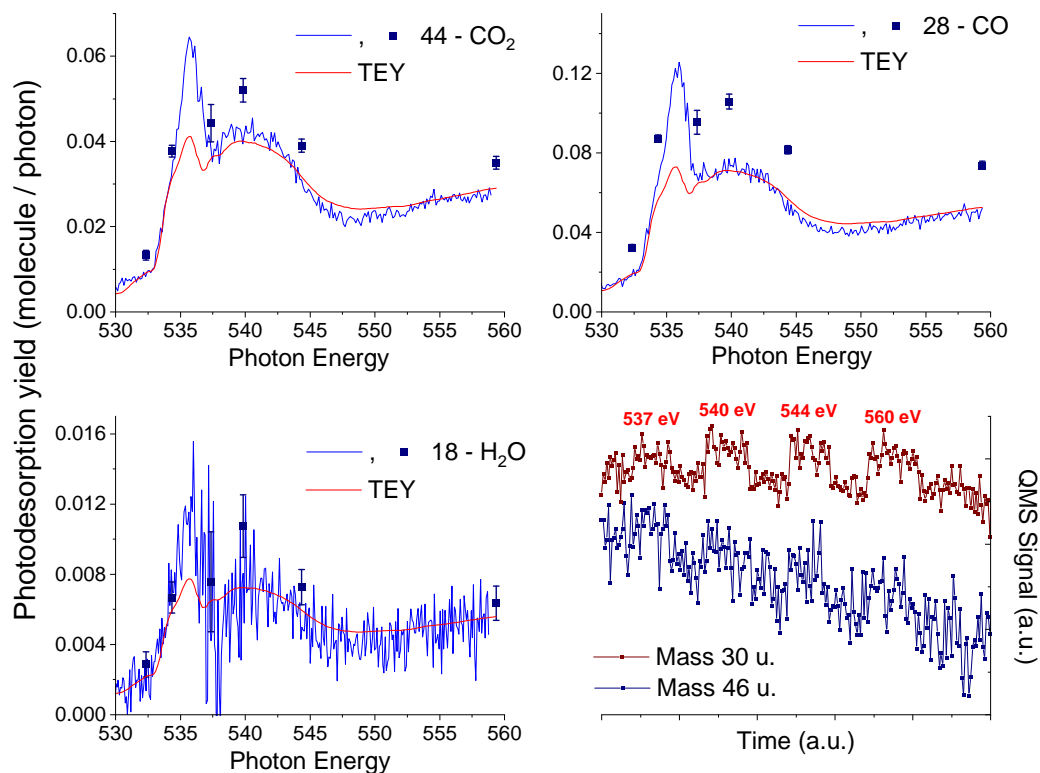


FIGURE VI.11 – X-ray photodesorption spectra of  $\text{CO}_2$  (top left panel),  $\text{CO}$  (top right panel) and  $\text{H}_2\text{O}$  (bottom left panel) from pure  $\text{HCOOH}$  ice at 15 K. The solid blue lines correspond to the desorption yields derived from continuous irradiation experiments and the blue squares with error bars are derived from the irradiations at fixed energy. In red line is also displayed the TEY measured simultaneously with the desorption signal during the continuous irradiation experiments. In the bottom right panel are displayed the raw QMS signal obtained during the irradiations at fixed energy for the mass channels 30 u. and 46 u., associated with the desorption of  $\text{H}_2\text{CO}$  and  $\text{HCOOH}$  respectively.

tra of  $\text{CO}_2$ ,  $\text{CO}$  and  $\text{H}_2\text{O}$  are displayed in Figure VI.11. The continuous spectra were derived for an ice already well-processed i.e. associated with a photon fluence  $> 3 \times 10^{16}$  ph/cm<sup>2</sup> hence for which no  $\text{HCOOH}$  absorption features are visible in the TEY, meaning that  $\text{HCOOH}$  molecules were barely present near the ice surface during these measurements. No photodesorption spectrum of  $\text{HCOOH}$  could be obtained from our experiments as its desorption signal is very close to our detection limit. Indeed, in the bottom right panel of Figure VI.11, we show the raw QMS signals of masses 30 u. ( $\text{H}_2\text{CO}$ ) and 46 u. ( $\text{HCOOH}$ ) monitored during step-like irradiation at fixed energy. The sudden increase and decrease of the mass 30 u. signal is associated with the irradiation of the ice and the corresponding photon energy is displayed in red. The desorption of  $\text{H}_2\text{CO}$  is clearly seen from this signal whereas that of  $\text{HCOOH}$  (measured simultaneously, hence for which the signal increase and decrease should match that of  $\text{H}_2\text{CO}$ ) is still detectable but with a signal-to-noise ratio very close to 1.

TABLE VI.4 – Photodesorption yields in molecule/photon, of intact HCOOH and fragments, from pure HCOOH irradiated at 15 K and at a photon energy of 560 eV. The fluence received by the ice before the measurements is  $< 1 \times 10^{16}$  ph/cm<sup>2</sup>.

Species	Yield	Species	Yield
HCOOH	$1.5 \pm 1.1 \times 10^{-3}$	CO	$7.4 \pm 0.2 \times 10^{-2}$
CO <sub>2</sub>	$3.5 \pm 0.2 \times 10^{-2}$	H <sub>2</sub> CO	$6.6 \pm 2.2 \times 10^{-4}$
O <sub>2</sub>	$1.1 \pm 0.5 \times 10^{-3}$	H <sub>2</sub> O	$6.4 \pm 1.0 \times 10^{-3}$

Interestingly, unlike the case of pure CH<sub>3</sub>OH and pure CH<sub>3</sub>CN ices, the photodesorption spectra from pure HCOOH ice are not exactly following the TEY variations, measured simultaneously. The relative intensities of the different features are indeed not matching for each photon energy. The most significant difference is that the desorption yield near 535.6 eV is above that near 540 eV whereas the TEY values at these energies are similar. This is more easily observable for the photodesorption of CO and CO<sub>2</sub> whereas less clear in the H<sub>2</sub>O photodesorption spectrum which is more noisy. This is typical of non-XESD processes, as discussed in Chapter III.2.2, i.e. desorption processes decorrelated from the Auger scattering. The most probable explanation would be that non-XESD processes are contributing to the desorption of CO<sub>2</sub>, CO and H<sub>2</sub>O near 535.6 eV, in addition to the desorption induced by the Auger scattering (XESD). At this energy, the X-ray absorption is due to a CO<sub>2</sub> core transition (Wight and Brion, 1974). This would mean that the desorption of CO<sub>2</sub>, CO and H<sub>2</sub>O near 535.6 eV is partly due to non-XESD processes induced by the photo-absorption of CO<sub>2</sub>. While the desorption of CO could originate from the dissociation of CO<sub>2</sub> after Auger decay (in that case into CO and O<sup>+</sup>), that of CO<sub>2</sub> and H<sub>2</sub>O necessarily imply other kind of processes. In Table VI.4, we display the photodesorption yields of the different species desorbing from pure HCOOH ice at 15 K and at 560 eV. The yields were derived for a photon fluence  $< 1 \times 10^{16}$  ph/cm<sup>2</sup>, meaning that the yields should be representative of a low-processed ice. However, as HCOOH has been shown to quickly dissociate with the irradiation in our experiments (according to the TEY measurements discussed in Section VI.1.3), the molecular composition of the ice surface during the measurements might significantly differs from a surface only composed of HCOOH molecules. Namely, the yields provided in Table VI.4 might actually originate from an ice surface consisting of a mix of HCOOH and its dissociation products (such as CO, CO<sub>2</sub> and H<sub>2</sub>O). This illustrates the experimental difficulty of measuring photodesorption yields for COMs that easily dissociate under irradiation.

## VI.3 X-ray photodesorption from analogues of interstellar ices

### VI.3.1 CH<sub>3</sub>OH-containing ices

In Figure VI.12 we display the photodesorption spectra from <sup>13</sup>CO:CH<sub>3</sub>OH ice (top panels) and H<sub>2</sub>O:CH<sub>3</sub>OH ice (bottom panels) for some desorbing species detected in our experiments. The TEY measurements are also shown in arbitrary units in dashed lines. The photodesorption spectra shown are following the TEY variations, meaning that photodesorption is indeed triggered by the ice photo-absorption. We do not display all the data available for more clarity and we did not observe a different behavior in the photodesorption spectra for each mass channel monitored in the sense that the photodesorption spectra are systematically following the TEYs. We first discuss the photodesorption of molecules from the mixed <sup>13</sup>CO:CH<sub>3</sub>OH ices. The desorption signals

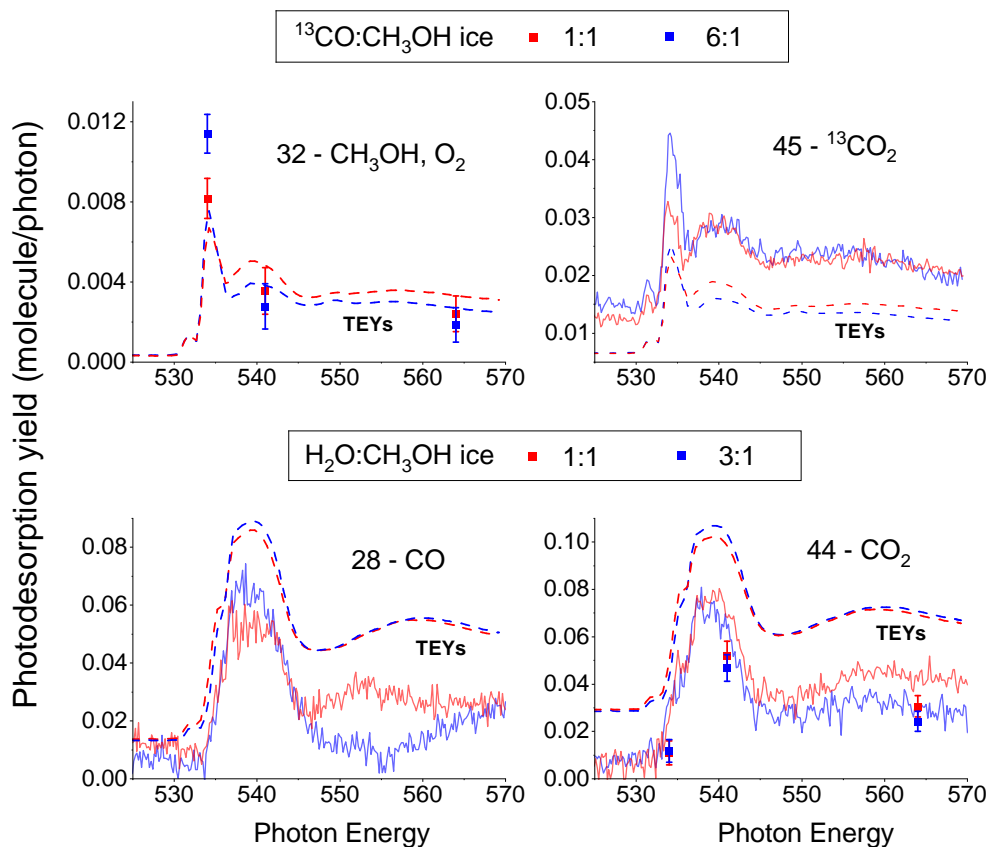


FIGURE VI.12 – Photodesorption spectra (in solid lines for the continuous irradiation and in squares with error bars for the irradiations at fixed energy) for masses 32 u. and 45 u. from <sup>13</sup>CO:CH<sub>3</sub>OH ice (top panels) and of masses 28 u. and 44 u. from H<sub>2</sub>O:CH<sub>3</sub>OH ice (bottom panels) irradiated at 15 K. Red and blue are associated with different mixing ratios displayed in the legend. The TEYs measured during the continuous irradiation experiments are also shown in arbitrary units by the dashed lines.

observed on the mass channels 45 u., 44 u., 33 u., 29 u. and 28 u. were attributed to photodesorbing  $^{13}\text{CO}_2$ ,  $^{12}\text{CO}_2$ ,  $^{13}\text{CH}_3\text{OH}$ ,  $^{13}\text{CO}$  and  $^{12}\text{CO}$  respectively. A desorption signal was observed on the masses 47 u. and 46 u. for the mixed  $^{13}\text{CO}:\text{CH}_3\text{OH}$  ices. Similarly to the case of pure  $\text{CH}_3\text{OH}$  ice, we cannot definitively attribute this signal to a desorbing species as it could be due to either  $\text{H}^{12/13}\text{COOH}$ ,  $^{12/13}\text{C}_2\text{H}_6\text{O}$  isomers or to the fragmentation of desorbing species of higher mass in the ionization chamber of the QMS.

In order to estimate the X-ray photodesorption yield of  $\text{CH}_3\text{OH}$ , we used the same methodology as for pure methanol ice i.e. we considered the relative intensity of the signals on the mass channels 31 u. and 32 u. by first assuming that the mass 31 u. originates solely from the cracking of desorbing  $\text{CH}_3\text{OH}$  into  $\text{CH}_2\text{OH}^+$  or  $\text{CH}_3\text{O}^+$  in the ionization chamber of the QMS. This methodology is however less robust for the mixed  $^{13}\text{CO}:\text{CH}_3\text{OH}$  ices as the signal on the mass channel 31 u. could also correspond to  $\text{H}_2^{13}\text{CO}$  desorption. This molecule might for instance originate from the hydrogenation of  $^{13}\text{CO}$ , due to the de-hydrogenation of  $\text{CH}_3\text{OH}$  by low energy electrons, which has been shown to be the main dissociation channel in irradiated methanol ice with 5 keV electrons (Bennett et al., 2007). At 564 eV, for a mixing ratio of 1:1, we found that a maximum of  $\sim 80\%$  of the mass signal 32 u. could correspond to  $\text{CH}_3\text{OH}$  photodesorption from  $^{13}\text{CO}:\text{CH}_3\text{OH}$  ice. Assuming this maximum yield, this brings the mass signal 31 u. to below our detection limit after correction for the cracking of  $\text{CH}_3\text{OH}$  into  $\text{CH}_2\text{OH}^+$  or  $\text{CH}_3\text{O}^+$ . For a mixing ratio of 6:1, the signal on the mass 32 u. is not high enough to consider that the mass 31 u. signal originates solely from the cracking of desorbing  $\text{CH}_3\text{OH}$  into  $\text{CH}_2\text{OH}^+$  or  $\text{CH}_3\text{O}^+$ . Indeed, by assuming the whole signal on the mass 32 u. to be due to photodesorbing  $\text{CH}_3\text{OH}$ , some signal remained on the mass 31 u., which can be attributed to either  $\text{H}_2^{13}\text{CO}$  or  $\text{CH}_3\text{O}/\text{CH}_2\text{OH}$  desorption. As the signal on the mass 31 u. increases when more  $^{13}\text{CO}$  molecules are present in the mixed ice, we can however assume that  $\text{H}_2^{13}\text{CO}$  should dominantly contribute to the remaining 31 u. signal.

In Figure VI.13, we compare the photodesorption yields at 564 eV between the pure  $\text{CH}_3\text{OH}$  ice and the mixed  $^{13}\text{CO}:\text{CH}_3\text{OH}$  ice for different species. At such energy, the photo-absorption of the ice is dominated by the core ionization of O-bearing molecules, whose cross section is similar between  $\text{CH}_3\text{OH}$  and  $^{13}\text{CO}$  (Berkowitz, 2002). Therefore, the possible variations observed in the yields at 564 eV can solely be attributed to an effect of the ice composition. The variations of the photodesorption yields presented in Figure VI.13 might reflect the differences in the X-ray induced chemistry between pure  $\text{CH}_3\text{OH}$  ice and mixed  $^{13}\text{CO}:\text{CH}_3\text{OH}$  ices. This chemistry is expected to be driven by low energy secondary electrons originating from the Auger scattering after X-ray absorption. In similar experiments where pure methanol ice was irradiated

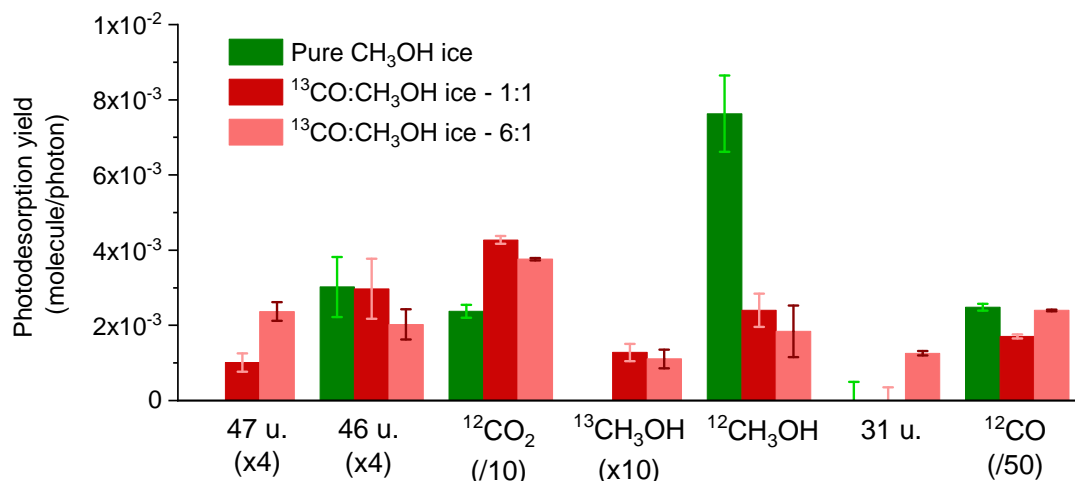


FIGURE VI.13 – X-ray photodesorption yields of desorbing species from pure CH<sub>3</sub>OH and mixed <sup>13</sup>CO:CH<sub>3</sub>OH ices irradiated at 15 K. The attribution of the desorbing species to the mass channels is discussed in the text.

ted by 5 keV electrons (Bennett et al., 2007), the induced-chemistry, also expected to be dominated by low energy secondary electrons, was shown to result mainly in the de-hydrogenation of CH<sub>3</sub>OH. In mixed <sup>13</sup>CO:CH<sub>3</sub>OH ices, the de-hydrogenation of CH<sub>3</sub>OH might lead to the hydrogenation of <sup>13</sup>CO molecules, which may explain the detected desorption signals on the masses 33 u. and 31 u. associated with the desorption of <sup>13</sup>CH<sub>3</sub>OH and most probably H<sup>13</sup>CO respectively. Consequently, less H atoms should be available for recombination reactions leading back to CH<sub>3</sub>OH formation in the mixed ices compared to the pure CH<sub>3</sub>OH ice. This might participate into explaining why we estimate that the X-ray photodesorption yield of CH<sub>3</sub>OH, although estimated with a rough approximation, is lower for the mixed <sup>13</sup>CO:CH<sub>3</sub>OH ices. Surprisingly, the desorption yield of <sup>12</sup>CO is not significantly varying with the dilution of CH<sub>3</sub>OH and that of <sup>12</sup>CO<sub>2</sub> increases when less CH<sub>3</sub>OH molecules are deposited. Although the reason is still not clear, the formation and subsequent desorption of <sup>12</sup>CO might be favored in the mixed <sup>13</sup>CO:CH<sub>3</sub>OH ices, due to less H atoms available for re-hydrogenation of <sup>12</sup>CO as discussed previously. <sup>12</sup>CO might be responsible for the formation and subsequent desorption of <sup>12</sup>CO<sub>2</sub>. It was suggested in Jamieson et al. (2006) that formation of CO<sub>2</sub> in pure CO ice irradiated by 5 keV electrons could be due to the reaction between electronically excited CO and CO in its fundamental state. This reaction might explain the increase in the photodesorption yields of <sup>12</sup>CO<sub>2</sub> whose formation might be favored in mixed <sup>13</sup>CO:CH<sub>3</sub>OH ices because of more available <sup>12/13</sup>CO molecules that can be excited and react. Finally, the photodesorption yields of the masses 47 u. and 46 u., associated with the desorption of either H<sup>12/13</sup>COOH, <sup>12/13</sup>C<sub>2</sub>H<sub>6</sub>O isomers or desorbing species of higher mass do not significantly vary with the dilution of CH<sub>3</sub>OH in the <sup>13</sup>CO matrix.

In similar experiments, when irradiating a thick CO:CH<sub>3</sub>OH (3:1) ice (~ 700 ML) with 250-1250 eV X-rays and with a flux of  $7.6 \times 10^{14}$  photon/s, almost two orders of magnitude higher than that in our experiments, [Ciaravella et al. \(2020\)](#) did not detect a desorption signal on the mass channel 31 u. (attributed to methanol desorption) and estimated that only ~ 20% of methanol molecules remained intact in the first minutes of the irradiation. This is at first not consistent with our data as we clearly detected desorption signals on both mass channels 31 u. and 32 u. from our <sup>13</sup>CO:CH<sub>3</sub>OH ices such that CH<sub>3</sub>OH desorption most probably occurs. However, as CH<sub>3</sub>OH is expected to be efficiently dissociated, a possible explanation would be that the flux and fluence conditions of [Ciaravella et al. \(2020\)](#) differ too much from ours to detect methanol desorption. This would indicate that the irradiation flux and the photon fluence are critical parameters for detecting methanol desorption in X-ray irradiation experiments.

The photodesorption yields derived at 564 eV from the mixed <sup>13</sup>CO:CH<sub>3</sub>OH ices are summed up in Table VI.5 along with that from mixed H<sub>2</sub>O:CH<sub>3</sub>OH ices which are discussed in the following. In the case of the mixed H<sub>2</sub>O:CH<sub>3</sub>OH ices, we detected the photodesorption of the masses 28 u., 30 u., 31 u. and 44 u. Surprisingly, no desorption signal was detected on the mass channel 32 u., meaning that the X-ray photodesorption of CH<sub>3</sub>OH is no longer occurring when methanol is mixed with water (at least not efficient enough compared to our detection limit of  $5 \times 10^{-4}$  molecule/photon). Additionally, we do not detect any desorption signal on the mass 46 u., associated with the formation and desorption of more complex molecules than CH<sub>3</sub>OH. The desorption

TABLE VI.5 – Photodesorption yields (in  $10^{-3}$  molecule/photon) of detected desorbing species from pure CH<sub>3</sub>OH, <sup>13</sup>CO:CH<sub>3</sub>OH and H<sub>2</sub>O:CH<sub>3</sub>OH ices irradiated at 15 K and at a photon energy of 564 eV. The fluence received by the ice before the measurements is  $< 2 \times 10^{16}$  ph/cm<sup>2</sup>.

Species	Pure CH <sub>3</sub> OH	<sup>13</sup> CO:CH <sub>3</sub> OH - 6:1	H <sub>2</sub> O:CH <sub>3</sub> OH - 3:1
<sup>12</sup> CO	124 ± 6	119 ± 1	22 ± 2
<sup>13</sup> CO		376 ± 10	
<sup>12</sup> CO <sub>2</sub>	24 ± 1	38 ± 3	24 ± 2
<sup>13</sup> CO <sub>2</sub>		70 ± 7	
H <sub>2</sub> <sup>12</sup> CO	1.2 ± 0.5		0.6 ± 0.1
H <sub>2</sub> <sup>13</sup> CO		1.3 ± 0.5	
<sup>12</sup> CH <sub>3</sub> O or <sup>12</sup> CH <sub>2</sub> OH	< 0.5	< 0.5	1.3 ± 0.2
<sup>12</sup> CH <sub>3</sub> OH	7.6 ± 0.9	1.8 ± 0.7	< 0.5
<sup>13</sup> CH <sub>3</sub> OH		0.13 ± 0.02	
Mass 46 u. <sup>(*)</sup>	0.8 ± 0.3	0.6 ± 0.1	< 0.5

<sup>(\*)</sup> to quantify the yields of the mass 46 u., we took the conversion factor associated with formic acid

signals on the masses 28 u., 30 u. and 44 u. are associated with the photodesorption of CO, H<sub>2</sub>CO and CO<sub>2</sub> respectively. The signal observed on the mass 31 u. is associated with the desorption of CH<sub>3</sub>O or CH<sub>2</sub>OH radical, according to the following discussion.

For H<sub>2</sub>O:CH<sub>3</sub>OH mixtures, the X-ray induced chemistry may play a major role in the photodesorption process. In the study of Laffon et al. (2010), it was estimated, based on NEXAFS spectroscopy, that the X-ray irradiation at 150 eV of H<sub>2</sub>O:CH<sub>3</sub>OH ice at 20 K leads to a methanol survival rate of ~45% and ~25% for 1:1 and 84:16~5:1 mixture ratios respectively and after a sufficiently high photon dose. This was found to be lower than the case of pure CH<sub>3</sub>OH ice for which a survival rate of ~ 50% was derived. Laffon et al. 2010 assumed that this decrease in the survival rate of methanol when the H<sub>2</sub>O concentration is increasing was mainly explained by destruction of methanol reacting with the OH radical (this is condensed in reaction (VI.3)), where OH radical comes from the dissociation of H<sub>2</sub>O by photolysis and/or radiolysis via reaction (VI.2) which is the main dissociation channel of H<sub>2</sub>O (Laffon et al., 2006, 2010). Laffon et al. 2010 also observed that CO formation (originating from the dissociation of CH<sub>3</sub>OH) and subsequent reaction with OH radical via (VI.4) enhances CO<sub>2</sub> formation in H<sub>2</sub>O:CH<sub>3</sub>OH ices compared to pure methanol ice.

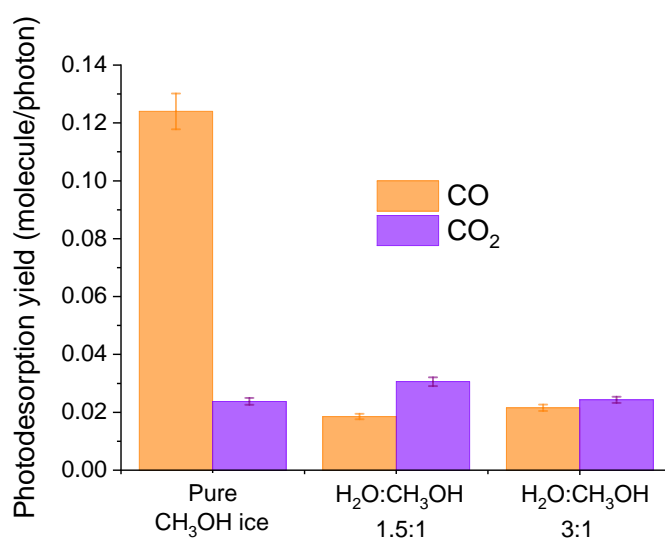
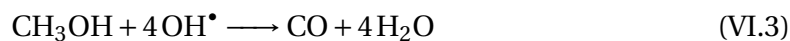


FIGURE VI.14 – X-ray photodesorption yields of CO and CO<sub>2</sub> from pure CH<sub>3</sub>OH and mixed H<sub>2</sub>O:CH<sub>3</sub>OH ices irradiated at 15 K.

The X-ray photodesorption yields derived from our experiment are somehow consistent with the previous chemistry network. First, in Figure VI.14, we see that the CO yield is higher than the CO<sub>2</sub> yield for pure methanol ice by almost one order of magnitude at 564 eV, whereas in H<sub>2</sub>O:CH<sub>3</sub>OH ices the CO yield is lower than the CO<sub>2</sub> yield for both mixing ratios. This is consistent with reaction (VI.4). Consumption of OH radical by reaction (VI.3) and (VI.4) may also explain why we do not detect an OH radical contribution to the TEY in H<sub>2</sub>O:CH<sub>3</sub>OH ices compared to pure H<sub>2</sub>O ice (see Figure VI.1) for which fewer consumption channels of the OH radical are available. Additionally, OH reactivity with CH<sub>3</sub>OH at low temperature (T < 100 K) in gas phase has been proven to be efficient due to possible quantum tunneling effect (Gómez Martín et al., 2014; Ocaña et al., 2019), with the main reaction product suggested to be CH<sub>3</sub>O (Shannon et al., 2013). Similar reactions occurring in the solid phase may explain why we do not observe any photodesorption of CH<sub>3</sub>OH (mass 32 u.) from H<sub>2</sub>O:CH<sub>3</sub>OH ices, but instead a clear photodesorption on the mass 31 u., thereby most probably associated with the desorption of CH<sub>3</sub>O radical. Finally, the non-detection of a photodesorption signal on the mass 46 u. seems to indicate that mixing water with methanol molecules may close reaction channels that lead to the formation of more complex molecules.

### VI.3.2 CH<sub>3</sub>CN-containing ices

X-ray irradiation experiments near the N K-edge and near the O K-edge were conducted when CH<sub>3</sub>CN is mixed in <sup>13</sup>CO or H<sub>2</sub>O ices with different dilution factors. This enables to selectively photo-excite either CH<sub>3</sub>CN, <sup>13</sup>CO or H<sub>2</sub>O at their respective reso-

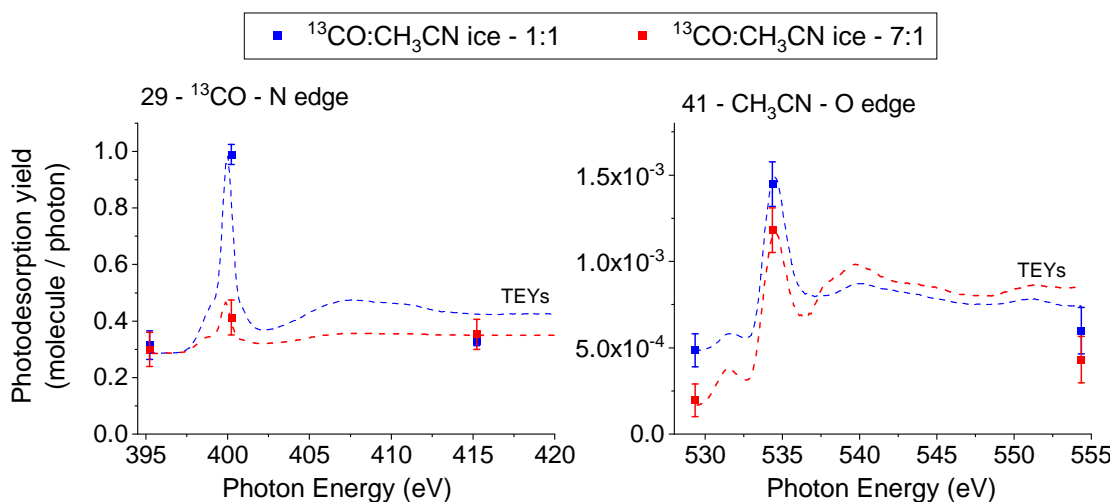


FIGURE VI.15 – X-ray photodesorption yields of <sup>13</sup>CO near the N K-edge and CH<sub>3</sub>CN near the O K-edge (squares with error bars) from a mixed <sup>13</sup>CO:CH<sub>3</sub>CN ice at 15 K, with dilution ratios of 1:1 (blue color) and 7:1 (red color). The yields were measured for a "fresh" ice at 15 K having received a photon fluence < 1 × 10<sup>16</sup> photon/cm<sup>2</sup>. The TEYs, measured at higher fluences, are displayed in dashed lines.

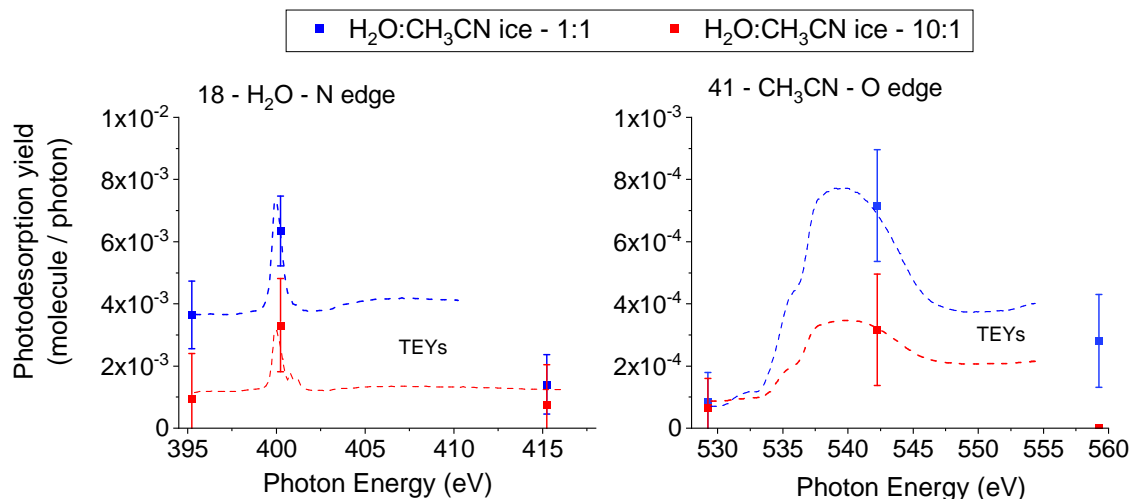


FIGURE VI.16 – X-ray photodesorption yields of H<sub>2</sub>O near the N K-edge and CH<sub>3</sub>CN near the O K-edge (squares with error bars) from a mixed H<sub>2</sub>O:CH<sub>3</sub>CN ice at 15 K, with dilution ratios of 1:1 (blue color) and 10 :1 (red color). The yields were measured for a "fresh" ice at 15 K having received a photon fluence  $< 1 \times 10^{16}$  photon/cm<sup>2</sup>. The TEYs, measured at higher fluences, are displayed in dashed lines.

nance in order to trigger photodesorption from the ices. For example, the X-ray photodesorption yields of <sup>13</sup>CO near the N K-edge and that of CH<sub>3</sub>CN near the O K-edge, measured at fixed energy and for a low fluence, from mixed <sup>13</sup>CO:CH<sub>3</sub>CN ices, are presented in Figure VI.15. The photodesorption yields of H<sub>2</sub>O near the N K-edge and that of CH<sub>3</sub>CN near the O K-edge, also measured at fixed energy and for a low fluence, from mixed CH<sub>3</sub>CN:H<sub>2</sub>O ices are presented in Figure VI.16. As shown in these figures, photo-exciting CH<sub>3</sub>CN, <sup>13</sup>CO and H<sub>2</sub>O at their molecular resonance (respectively near 400 eV, 534.4 eV and around 540 eV) is inducing the desorption of other molecules from the ice surface. In these figures, the photodesorption yields are well-correlated to the TEYs measured at higher fluence except for the case of mixed CH<sub>3</sub>CN:H<sub>2</sub>O ices where the relative intensity of the yields at different energy do not necessarily matches the variations of the TEYs. This is expected to be due to the fact that the desorption yields and the TEYs were not measured at the same fluence. As discussed in Section VI.1.2, in mixed CH<sub>3</sub>CN:H<sub>2</sub>O ices, the presence of intact CH<sub>3</sub>CN molecules near the ice surface is rapidly decreasing with the fluence, meaning that both the desorption yields of CH<sub>3</sub>CN and the photo-absorption spectra near the N K-edge are expected to change dramatically with the fluence when CH<sub>3</sub>CN is mixed with water ice. This would explain the discrepancy between the photodesorption yields measured at low fluence and the TEYs measured at higher fluence.

More globally, when a photodesorption signal was clearly detected during the experiments, the corresponding photodesorption spectrum of the mass channel monitored

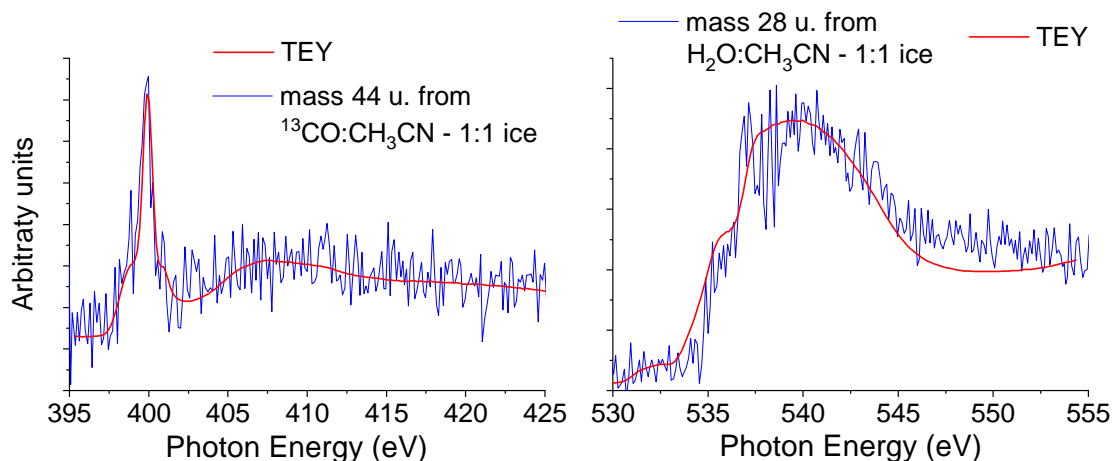


FIGURE VI.17 – Photodesorption spectra (in blue) of the mass channel 44 u. from a  $^{13}\text{CO}:\text{CH}_3\text{CN}$  (1:1) ice near the N K-edge (left panel) and of the mass channel 28 u. from a  $\text{H}_2\text{O}:\text{CH}_3\text{CN}$  (1:1) ice near the O K-edge (right panel). In red is also displayed the TEYs. The photodesorption signal and the TEYs were measured simultaneously, at 15 K. The Y-scale is in arbitrary units.

is following the photo-absorption spectrum (TEY) of the ice measured. An example is given in Figure VI.17 for the mass channel 44 u. from a  $^{13}\text{CO}:\text{CH}_3\text{CN}$  (1:1) ice near the N K-edge and for the mass channel 28 u. from a  $\text{H}_2\text{O}:\text{CH}_3\text{CN}$  (1:1) ice near the O K-edge, where the TEYs and the photodesorption signals have been measured simultaneously. Similarly to the case of  $\text{CH}_3\text{OH}$ -containing ices, this indicates that the X-ray photodesorption of the molecules from the ices studied is due to an indirect process where the photo-absorption of one molecule is inducing the desorption of another one, most probably mediated by the Auger scattering.

In Figure VI.18, we display the raw photodesorption signals associated with the mass channels monitored during the experiments at low fluence ( $< 2 \times 10^{16}$  ph/cm $^2$ ) in order to discuss the attribution of the desorbing species to these mass channels. The comparison is made at 560 eV, energy at which the photo-absorption cross section is not expected to significantly differ between the mixed ices hence for which the possible differences observed in the desorption signals can be solely attributed to differences in the ice composition. The fact that the TEY values are similar at 560 eV for the mixed ices supports the idea that their X-ray photo-absorption cross sections are similar.

The mass 15 u. displays a desorption signal in the same order of magnitude for any ice studied. We attribute this mass to  $\text{CH}_3$  photodesorption, whose yields slightly decrease with the dilution of  $\text{CH}_3\text{CN}$ . The X-ray photodesorption of the masses 30 u., 28 u., 27 u. and 26 u. significantly depends on the ice composition. For the  $^{13}\text{CO}:\text{CH}_3\text{CN}$  ices, the masses 30 u. and 28 u. are increasing when more  $^{13}\text{CO}$  molecules are present

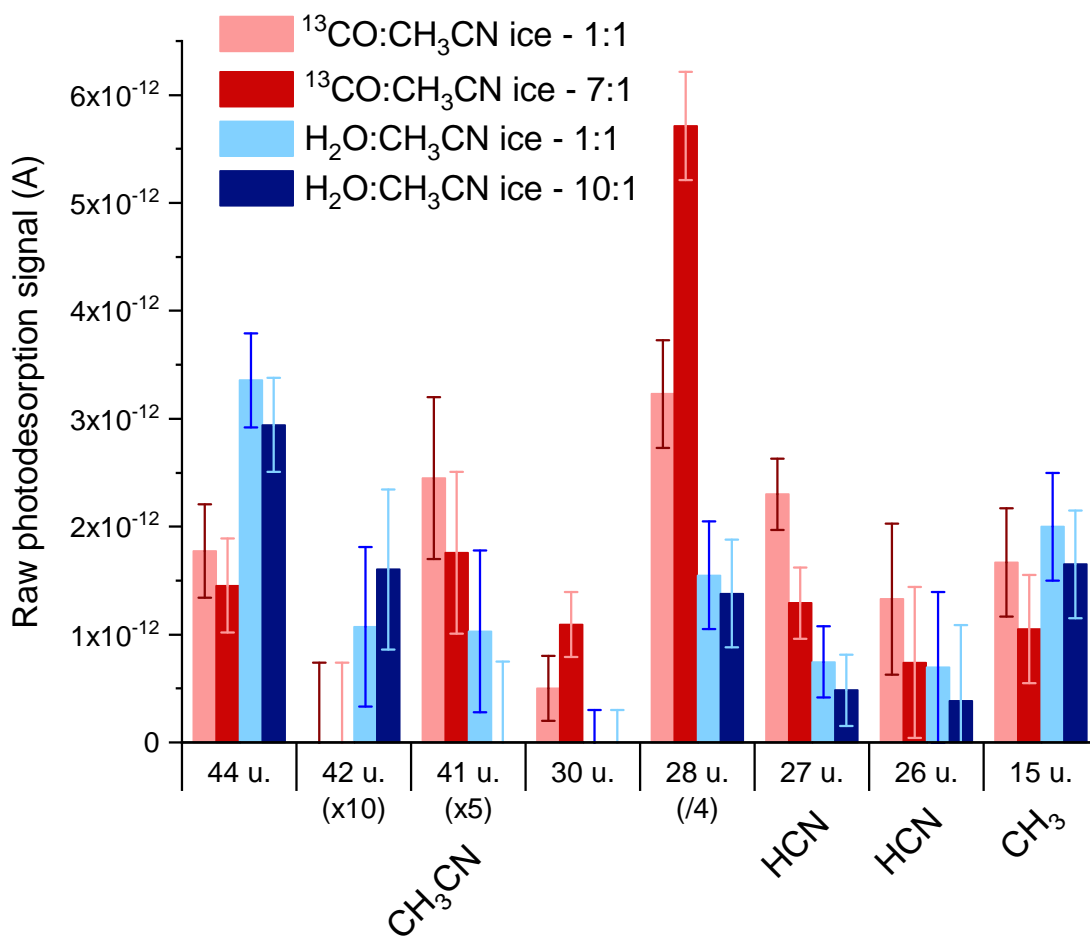


FIGURE VI.18 – Raw photodesorption signals (in A) at 560 eV of desorbing masses from mixed  $^{13}\text{CO}:\text{CH}_3\text{CN}$  and  $\text{H}_2\text{O}:\text{CH}_3\text{CN}$  ices, irradiated at 15 K. The attribution of the desorbing species to the mass channels is done in the text. The signals were obtained for a fluence  $< 2 \times 10^{16}$  ph/cm<sup>2</sup> and are not corrected from any possible cracking of desorbing species in the ionization chamber of our QMS.

in the ice. This indicates that the desorption of these masses most certainly originate from the  $^{13}\text{CO}$  matrix. No signal remained on the mass channel 30 u. after correction from the cracking of  $^{13}\text{CO}$  in the ionization chamber of our QMS, according to the fragmentation pattern of the NIST (Wallace) (which was counter-checked by gas phase experiments in our set-up). The desorption of the mass 30 u. is not observed for the case of mixed  $\text{H}_2\text{O}:\text{CH}_3\text{CN}$  ices. This is consistent with our attribution of the mass 30 u. for pure  $\text{CH}_3\text{CN}$  ice to  $\text{C}_2\text{H}_6$  desorption, whose formation is hindered when  $\text{CH}_3\text{CN}$  is surrounded by  $\text{H}_2\text{O}$  molecules in the ice.

We attribute the desorption of the mass 28 u. from the mixed  $^{13}\text{CO}:\text{CH}_3\text{CN}$  ices dominantly to  $^{12}\text{CO}$  photodesorption originating from the natural isotope present in our  $^{13}\text{CO}$  gas sample (isotopic purity of  $\sim 99\%$ ). According to Dupuy et al. (2021b), CO X-

ray photodesorption yield from pure CO ice is  $\sim 0.15$  molecule/photon at 560 eV. This yield is very high, for example compared to the yields derived previously for the case of pure CH<sub>3</sub>CN ices in Table VI.3, which supports our attribution. However, we cannot totally exclude the possible contribution of N<sub>2</sub> desorption as it is seen as accumulating near the ice surface in the TEY measurements. The desorption signal of the mass 28 u. from the mixed H<sub>2</sub>O:CH<sub>3</sub>CN ices is not varying with the dilution ratios. The high signal compared to the other mass channels also points towards molecules with high desorption efficiency such as CO or N<sub>2</sub> (the X-ray photodesorption yield of N<sub>2</sub> from pure N<sub>2</sub> ice is also found to be high, i.e.  $\sim 0.13$  molecule/photon at 440 eV, as showed in Chapter IV). Accumulation of CO near the ice surface, which should be visible in our TEYs near 534.4 eV, is not observed in the mixed H<sub>2</sub>O:CH<sub>3</sub>CN ices (see left panel of Figure VI.3) whereas N<sub>2</sub> accumulation is clearly seen in the TEYs near 401 eV, even in the low fluence regime at which the yields were derived (see right panels of Figure VI.2). This might indicate that the desorption of the mass 28 u. from mixed H<sub>2</sub>O:CH<sub>3</sub>CN ices is dominated by the X-ray photodesorption of N<sub>2</sub>, although a contribution of CO desorption cannot be totally ruled out.

The masses 27 u. and 26 u. observed for mixed <sup>13</sup>CO:CH<sub>3</sub>CN ices are decreasing when CH<sub>3</sub>CN is more diluted, pointing towards the X-ray photodesorption of respectively HCN and CN. However, when correcting the mass 26 u. by the fragmentation of HCN in the ionization chamber of the QMS, the remaining signal is under our detection limit, which indicates that CN X-ray photodesorption is actually not occurring or at least not significant enough compared to our detection limit. Similarly, we attribute the signal on the mass channels 27 u. and 26 u. from mixed H<sub>2</sub>O:CH<sub>3</sub>CN ices to HCN desorption, whose intensity slightly decreases when CH<sub>3</sub>CN is more diluted. The decrease of the X-ray photodesorption signal of HCN from the mixed ices is somehow consistent with the fact that this molecule might desorb following the dissociation of CH<sub>3</sub>CN at the ice surface, for example via DEA due to low energy electrons as suggested in Bass et al. (2012). This process might therefore not be hindered by the surrounding <sup>13</sup>CO or H<sub>2</sub>O molecules but the associated desorption signal should be less detectable when less CH<sub>3</sub>CN molecules are present at the ice surface. A lower desorption signal of HCN for the case of H<sub>2</sub>O:CH<sub>3</sub>CN ices compared to the <sup>13</sup>CO:CH<sub>3</sub>CN ices with similar dilution ratios might be due to (i) a higher desorption barrier to overcome in the case of mixed H<sub>2</sub>O:CH<sub>3</sub>CN ices or (ii) the fact that CH<sub>3</sub>CN is more rapidly consumed hence present in lesser amount at the ice surface for the case of mixed H<sub>2</sub>O:CH<sub>3</sub>CN ices, even for the low fluence regime in which the signals were measured.

The desorption signal of the mass 41 u. is attributed to CH<sub>3</sub>CN X-ray photodesorption. In mixed <sup>13</sup>CO:CH<sub>3</sub>CN ices, it is decreasing when CH<sub>3</sub>CN is more diluted. The signals in the H<sub>2</sub>O:CH<sub>3</sub>CN ices are lower than in the <sup>13</sup>CO:CH<sub>3</sub>CN ices for similar di-

TABLE VI.6 – X-ray photodesorption yields (in  $10^{-4}$  molecule/photon) of  $\text{CH}_3\text{CN}$  and photo-products at 560 eV from mixed  $^{13}\text{CO}:\text{CH}_3\text{CN}$  and  $\text{H}_2\text{O}:\text{CH}_3\text{CN}$  ices irradiated at 15 K. The fluence received by the ice before the measurements is  $< 2 \times 10^{16}$  ph/cm<sup>2</sup>.

Species	$\text{CO}:\text{CH}_3\text{CN}$ - 7:1	$\text{H}_2\text{O}:\text{CH}_3\text{CN}$ - 10:1
$\text{CH}_3\text{CN}$	$4.3 \pm 1.2$	$< 1$
$\text{HCN}$	$8.3 \pm 2.1$	$3.1 \pm 2.1$
$\text{CH}_3$	$3.9 \pm 2.3$	$6.1 \pm 2.3$

lution ratios, indicating that mixing  $\text{CH}_3\text{CN}$  with water tends to defavor its X-ray photodesorption. As for the case of  $\text{HCN}$ , this could be due to either a difference in adsorption energies between  $\text{CH}_3\text{CN}$  and the water or the  $^{13}\text{CO}$  matrix or it could be due to a rapid consumption of  $\text{CH}_3\text{CN}$  by X-ray induced chemistry when it is mixed with water. Desorption signals on higher masses than 41 u., namely 42 u. and 44 u., were observed from the mixed ices. The attribution of the desorbing species to these mass channels cannot be definitively made as these mass channels can correspond either to  $^{12}\text{CNO}$  and  $^{12}\text{CO}_2$  for the mass 42 u. and 44 u. respectively or they can originate from the fragmentation of molecules of higher mass at the QMS entrance. The relative intensity of these signals indicates a different X-ray induced chemistry in  $^{13}\text{CO}:\text{CH}_3\text{CN}$  and  $\text{H}_2\text{O}:\text{CH}_3\text{CN}$  ices. For instance, more desorption signal is found on the mass 44 u. for  $\text{H}_2\text{O}:\text{CH}_3\text{CN}$  ices and the mass 42 u. is not detected for  $^{13}\text{CO}:\text{CH}_3\text{CN}$  ices, which is consistent with the water matrix acting as a catalyst for chemical reactions compared to the  $^{13}\text{CO}$  matrix. We do not however have the full picture of this X-ray induced chemistry in the mixed ices. Finally, after conversion of the raw desorption signals, we display in Table VI.6 the X-ray photodesorption yields at 560 eV of the previous mass channels from the mixed ices with dilution ratios that are the most representative of interstellar ices.

### VI.3.3 HCOOH-containing ices

X-ray photodesorption spectra from mixed  $^{13}\text{CO}:\text{HCOOH}$  and  $\text{H}_2\text{O}:\text{HCOOH}$  ices are globally following the TEYs variations, similarly to the case of  $\text{CH}_3\text{OH}$  and  $\text{CH}_3\text{CN}$ . An example is given in Figure VI.19 for the desorption of  $^{12}\text{CO}_2$  from a  $\text{H}_2\text{O}:\text{HCOOH}$  (1:1) and a  $^{13}\text{CO}:\text{HCOOH}$  (2:1) ice. The relative intensities of the different features observed in the photodesorption spectra are however not necessarily matching that of the TEYs, as also observed in pure  $\text{HCOOH}$  ice (see Section VI.2.3). For example, the photodesorption yields of  $^{12}\text{CO}_2$  from a  $^{13}\text{CO}:\text{HCOOH}$  (2:1) ice at 534.4 eV and 535.6 eV do not exactly match the relative intensity of the TEY values at these energies, as seen in the right panel of Figure VI.19. As discussed previously, this could be due to non-XESD

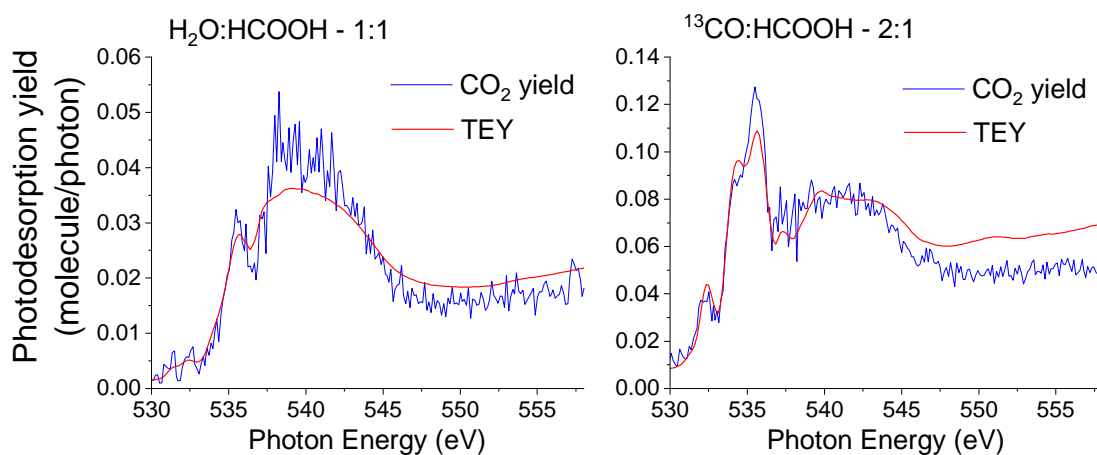


FIGURE VI.19 – X-ray photodesorption spectra of  $^{12}\text{CO}_2$  from a  $\text{H}_2\text{O}:\text{HCOOH}$  - 1:1 (left panel) and a  $^{13}\text{CO}:\text{HCOOH}$  (2:1) (right panel) ice (blue lines). The ices were irradiated at 15 K. The TEYs measured simultaneously are displayed in red.

processes contributing to the desorption of  $^{12}\text{CO}_2$  at specific energies. In order to discuss the possible X-ray photodesorption of the intact HCOOH from the mixed ices, we display in Figure VI.20 the raw QMS signals monitored on the mass channels 18 u. and 46 u. during the irradiation at fixed energies. The photodesorption associated with the mass 18 u. ( $\text{H}_2\text{O}$ ) is clearly seen through the sudden increase and decrease of the signals. As the masses 18 u. and 46 u. were monitored simultaneously, the mass signal 18 u. serves as a reference to know at which time the increase and decrease should appear on the mass 46 u. if HCOOH desorption occurs. As seen in top panels of Figure VI.20, we detect the desorption of intact HCOOH from the mixed  $^{13}\text{CO}:\text{HCOOH}$  ices at several energies although the desorption intensity is often very close to the background level. The X-ray photodesorption of HCOOH from the mixed  $\text{H}_2\text{O}:\text{HCOOH}$  ices is less clear, as seen in the bottom panels. From the  $\text{H}_2\text{O}:\text{HCOOH}$  (1:1) ice, a possible desorption occurs at 560 eV. On the other hand, no clear desorption signal is observed from the  $\text{H}_2\text{O}:\text{HCOOH}$  (10:1) ice at all tested energies. We then conclude that the X-ray photodesorption of intact HCOOH from interstellar ice analogues, that is ices where HCOOH is very diluted in a CO or  $\text{H}_2\text{O}$  matrix hence for which a dilution ratio of 10:1 is more representative among the studied systems, is not occurring near the O K-edge when HCOOH is mixed with water, with a detection limit of  $10^{-3}$  molecule/photon at 560 eV. On the other hand, HCOOH desorption occurs when it is mixed with CO although the desorption yield at 560 eV is very close to our detection limit.

The X-ray photodesorption yields of  $\text{H}_2\text{O}$ ,  $^{12}\text{CO}$  and  $^{12}\text{CO}_2$  from the pure HCOOH ice and the mixed ices are shown in Figure VI.21 for a photon energy of 560 eV, energy at which the photo-absorption of the different ices is expected to be similar and dominated by the core O 1s ionization of O-bearing molecules. Surprisingly, the desorption

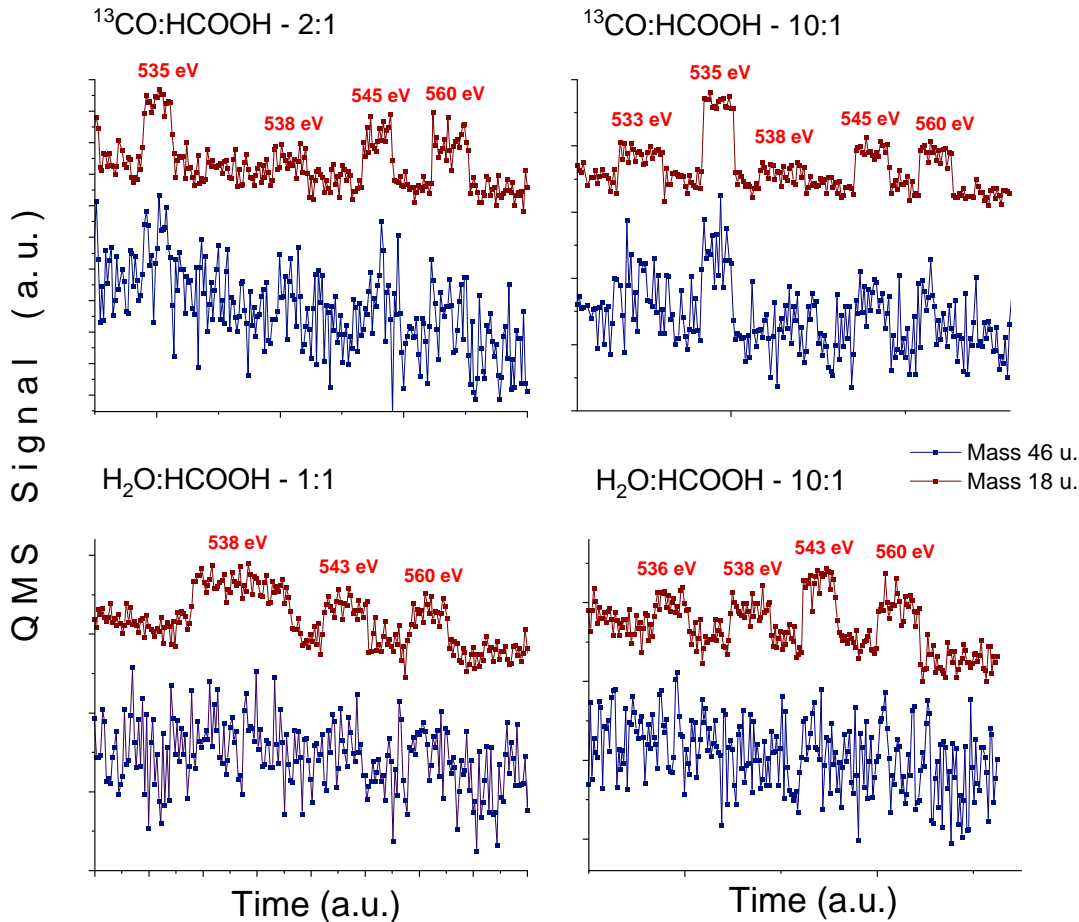


FIGURE VI.20 – QMS signal monitored during the irradiation of the mixed ices at fixed energy for the mass channels 18 u. (associated with  $\text{H}_2\text{O}$  desorption, in dark red) and 46 u. (associated with the desorption of  $\text{HCOOH}$ , in dark blue). The top panels display the signals from the  $^{13}\text{CO}:\text{HCOOH}$  (2:1 and 10:1) ices and the bottom panels display the signals from  $\text{H}_2\text{O}:\text{HCOOH}$  (1:1 and 10:1).

yield of  $\text{H}_2\text{O}$  is similar between the ices, even when  $\text{H}_2\text{O}$  molecules are dominantly deposited. For comparison, the X-ray photodesorption yield at 560 eV derived from a pure  $\text{H}_2\text{O}$  ice is  $\sim 5 \times 10^{-3}$  molecule/photon at 15 K (Dupuy et al., 2018), therefore found very similar than the ones derived from  $\text{HCOOH}$ -containing ices. This is not well understood yet. The behavior of the  $^{12}\text{CO}$  and  $^{12}\text{CO}_2$  yields for  $\text{HCOOH}$ -containing ice resembles that from  $\text{CH}_3\text{OH}$ -containing ice : the  $^{12}\text{CO}$  and  $^{12}\text{CO}_2$  yields do not vary significantly between the pure and mixed CO-ices, with the  $^{12}\text{CO}$  yield being higher than the  $^{12}\text{CO}_2$  yield, whereas, when the COM is diluted in a  $\text{H}_2\text{O}$  ice, the  $^{12}\text{CO}$  yields are found similar than the  $^{12}\text{CO}_2$  yields, which is a signature of the chemistry occurring between  $^{12}\text{CO}$ , originating from the dissociation of the COM, and OH radical, originating from the dissociation of water. We do not know, however, if the chemistry induced by the OH radical defavor the desorption of the intact  $\text{HCOOH}$  in  $\text{H}_2\text{O}:\text{HCOOH}$  ices compared to  $^{13}\text{CO}:\text{HCOOH}$  ices, a behavior that was suggested for  $\text{CH}_3\text{OH}$ . Indeed,

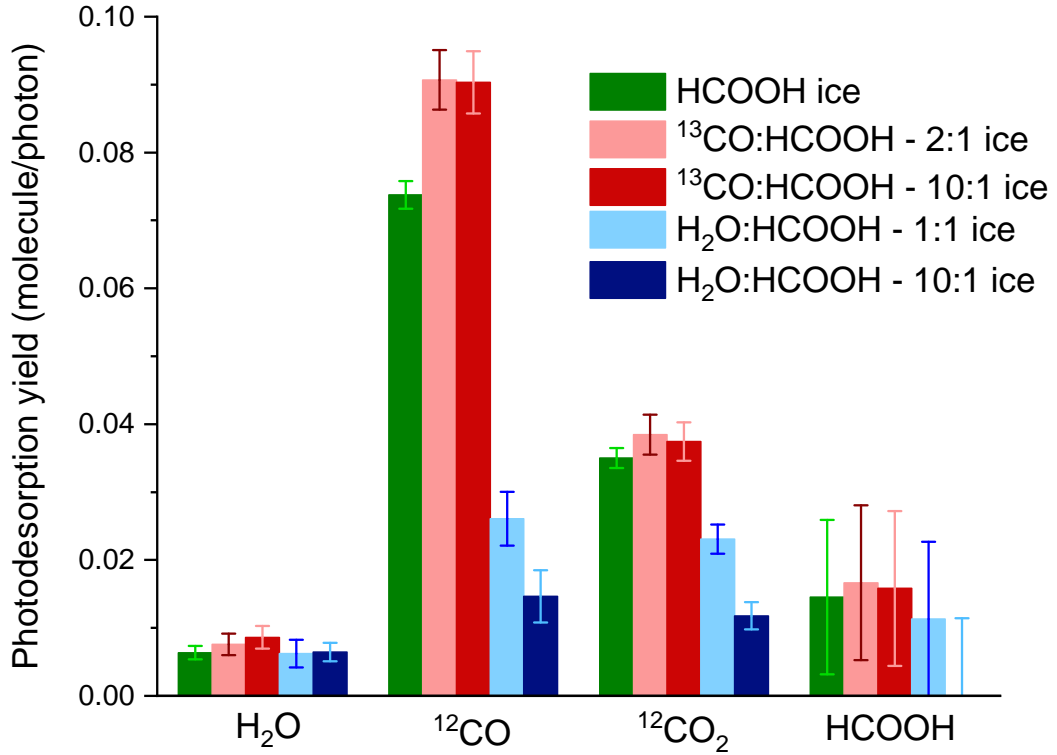


FIGURE VI.21 – X-ray photodesorption yields of intact HCOOH and other species derived at 560 eV from pure HCOOH ice and mixed CO/H<sub>2</sub>O ices, irradiated at 15 K.

as discussed in Section VI.1.3, we did not observe in the TEY data a significant difference in the destruction kinetic of HCOOH in H<sub>2</sub>O:HCOOH and <sup>13</sup>CO:HCOOH ices. The fact that HCOOH is not detected in the H<sub>2</sub>O:HCOOH - 10:1 ice compared to the <sup>13</sup>CO:HCOOH with a similar dilution may be solely due to a higher adsorption energy of HCOOH at the water ice surface due to possible hydrogen bonds. We display in Table VI.7 the X-ray photodesorption yields at 560 eV of the previous mass channels from the mixed ices with the highest dilution ratios, more relevant to interstellar ices.

TABLE VI.7 – X-ray photodesorption yields (in 10<sup>-3</sup> molecule/photon) of CH<sub>3</sub>CN and photo-products at 560 eV from mixed <sup>13</sup>CO:HCOOH and H<sub>2</sub>O:HCOOH ices irradiated at 15 K. The fluence received by the ice before the measurements is < 2 × 10<sup>16</sup> ph/cm<sup>2</sup>.

Species	<sup>13</sup> CO:HCOOH - 10:1	H <sub>2</sub> O:HCOOH - 10:1
HCOOH	1.6 ± 1.1	< 1
<sup>12</sup> CO	90 ± 5	15 ± 4
<sup>12</sup> CO <sub>2</sub>	37 ± 3	12 ± 2
H <sub>2</sub> O	8.6 ± 1.7	6.5 ± 1.4

## VI.4 Astrophysical yields and implications

The previous experimental X-ray photodesorption yields were derived at energies in the  $\sim 400 - 560$  eV range. As explained in Chapter I, the local energy spectrum of the X-rays expected to irradiate interstellar ices depend on the region considered. In protoplanetary disks, X-rays emitted from the central young star, referred to as stellar X-rays in the following, irradiate the disk. Stellar soft X-rays (0.1 - 5 keV) tend to be attenuated by absorption by gas and dust when going deeper into the disk whereas stellar hard X-rays (5 - 10 keV) can be scattered via Compton scattering hence they dominate the energy spectrum for deep regions of the disk. On the other hand, background X-rays, for example originating from a cluster of young star, can irradiate the disk out of its plane. As the gas and dust densities are lower in the outer regions of the disk compared to the inner regions, the energy spectrum of the background X-ray field might not be significantly attenuated when penetrating the outer regions of the disk such that soft X-rays might also contribute to the local spectrum in that case. To take these differences into account, we will consider several X-ray emission spectra that we will attenuate using the photoelectric cross section of [Bethell and Bergin \(2011\)](#).

We extrapolate our experimental desorption yields to higher energy, as described in Section II, by considering that the yields are following the X-ray absorption of the ices, which is dominated, above 560 eV, by the core O 1s ionization of O-bearing molecules and which follows the measured TEYs below 560 eV. Finally, we compute an astrophysical photodesorption yield averaged on the  $\sim 0.4 - 10$  keV energy range using formula II.9. In Figure VI.22 are shown extrapolated photodesorption spectra for CH<sub>3</sub>CN from CO and H<sub>2</sub>O-mixed ices (left panel) and the local X-ray spectrum attenuated as a func-

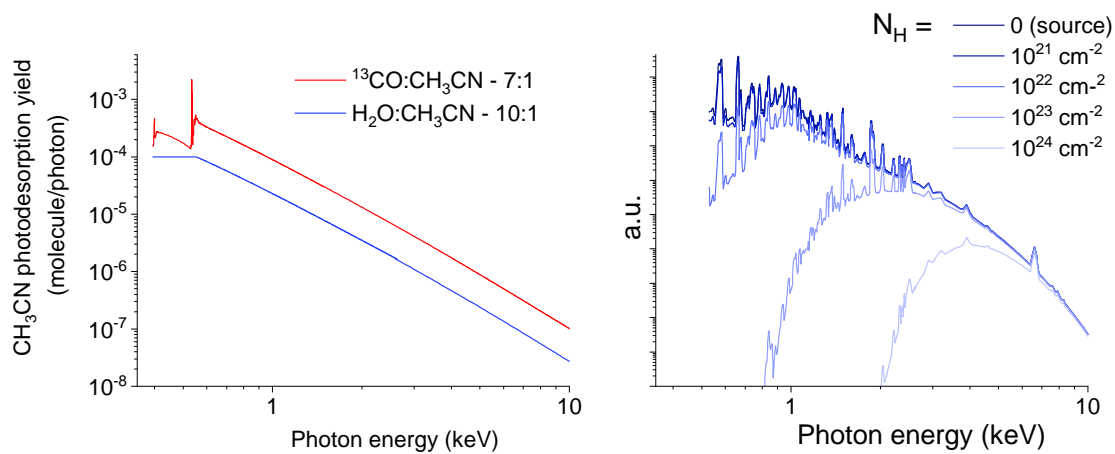


FIGURE VI.22 – Left panel : X-ray photodesorption yield of CH<sub>3</sub>CN from CO and H<sub>2</sub>O-mixed ices extrapolated to higher energy. Right panel : estimation of the local X-ray spectrum irradiating interstellar ices as a function of attenuation by gas and dust.

tion of  $N_H$  (right panel). Note that when the desorption of the molecule is under our detection limit, we took a constant yield equal to this limit for the  $\sim 400 - 560$  eV range, which is the case for  $\text{CH}_3\text{CN}$  yield from  $\text{H}_2\text{O}:\text{CH}_3\text{CN} - 10:1$  ice in the left panel of Figure VI.22.

We provide in Table VI.8 the corresponding yields of the intact  $\text{HCOOH}$ ,  $\text{CH}_3\text{OH}$  and  $\text{CH}_3\text{CN}$  from interstellar ice analogues and for different attenuation factors represented by the column density  $N_H$ . Note that using the different X-ray emission spectra displayed in Figure I.8, namely the X-ray spectrum of a T Tauri star (Nomura et al., 2007), that of a Herbig Ae/Be star (Skinner et al., 2004) or the X-ray background field from Rab et al. (2018), gives similar astrophysical yields. According to our computation, X-ray photodesorption yields vary on 2 orders of magnitude depending on the local X-ray spectrum. For regions where hard X-rays dominate the spectrum, the photodesorption yields are the lowest. This is due to our extrapolation that results in yields that are several orders of magnitude lower for hard X-rays than for soft X-rays. Although we have shown by a few measurements near 1 keV that CO X-ray photodesorption yield from pure CO ice seems to follow the X-ray absorption cross section of CO (see Figure II.12), measurements at higher energy remain to be made to validate this approximation for

TABLE VI.8 – X-ray astrophysical photodesorption yields (in molecule/photon) of the COMs studied in this thesis from CO and  $\text{H}_2\text{O}$  mixed ices. The dilution ratios are 7:1, 10:1 and 6:1 from mixed CO:COM ice and 10:1, 10:1 and 3:1 from mixed  $\text{H}_2\text{O}:\text{COM}$  ice for  $\text{CH}_3\text{CN}$ ,  $\text{HCOOH}$  and  $\text{CH}_3\text{OH}$ , respectively. These yields were derived by extrapolation of the experimental yields and they are averaged on the estimated local X-ray spectrum which is attenuated as a function of the column density  $N_H$ .

	$\text{CH}_3\text{CN}$	$\text{HCOOH}$	$\text{CH}_3\text{OH}$
Mixed with CO			
Source Spectrum	$2.0 \pm 1.0 \times 10^{-4}$	$7.5 \pm 3.8 \times 10^{-4}$	$9.6 \pm 4.8 \times 10^{-4}$
$N_H = 10^{21} \text{ cm}^{-2}$	$1.8 \pm 0.9 \times 10^{-4}$	$6.8 \pm 3.4 \times 10^{-4}$	$8.7 \pm 4.4 \times 10^{-4}$
$N_H = 10^{22} \text{ cm}^{-2}$	$9.1 \pm 4.5 \times 10^{-5}$	$3.4 \pm 1.7 \times 10^{-4}$	$4.4 \pm 2.2 \times 10^{-4}$
$N_H = 10^{23} \text{ cm}^{-2}$	$1.2 \pm 0.6 \times 10^{-5}$	$4.5 \pm 2.6 \times 10^{-5}$	$5.7 \pm 2.9 \times 10^{-5}$
$N_H = 10^{24} \text{ cm}^{-2}$	$1.6 \pm 0.8 \times 10^{-6}$	$6.0 \pm 3.0 \times 10^{-6}$	$7.4 \pm 3.7 \times 10^{-6}$
Mixed with $\text{H}_2\text{O}$			
Source Spectrum	$< 5.6 \pm 2.8 \times 10^{-5}$	$< 5.0 \pm 2.5 \times 10^{-4}$	$< 2.3 \pm 1.4 \times 10^{-4}$
$N_H = 10^{21} \text{ cm}^{-2}$	$< 5.1 \pm 2.5 \times 10^{-5}$	$< 4.7 \pm 2.4 \times 10^{-4}$	$< 2.2 \pm 1.3 \times 10^{-4}$
$N_H = 10^{22} \text{ cm}^{-2}$	$< 2.4 \pm 1.2 \times 10^{-5}$	$< 2.3 \pm 1.1 \times 10^{-4}$	$< 1.2 \pm 0.6 \times 10^{-4}$
$N_H = 10^{23} \text{ cm}^{-2}$	$< 3.2 \pm 1.6 \times 10^{-6}$	$< 3.2 \pm 1.6 \times 10^{-5}$	$< 1.6 \pm 0.8 \times 10^{-5}$
$N_H = 10^{24} \text{ cm}^{-2}$	$< 4.3 \pm 2.6 \times 10^{-7}$	$< 4.3 \pm 2.6 \times 10^{-6}$	$< 2.1 \pm 1.0 \times 10^{-6}$

COMs. The most important finding is that the yields are found to significantly depend on the ice composition. Namely, for similar dilution ratios, the X-ray photodesorption of the COMs studied is less efficient when the COM is mixed with water ice than the case where it is mixed in a CO ice. For CH<sub>3</sub>OH, this has been assumed to be due to reaction involving OH radical and leading to the destruction of the COM, hence competing with its desorption. A similar behavior might also occur for CH<sub>3</sub>CN although less experimental studies are available to support this idea compared to CH<sub>3</sub>OH. For HCOOH, the reason is less clear. These findings have important astrophysical implications : when considering a similar local X-ray spectrum, the X-ray photodesorption of the COMs should be more efficient in cold regions ( $T_{dust} < 20$  K), when CO freeze-out occurs, than in warmer regions where interstellar ices are mainly composed of water. Interestingly, the X-ray photodesorption of the COMs studied shows a very different behavior compare to the case of VUV photodesorption. Indeed, the desorption of the intact CH<sub>3</sub>CN was found to be similar in CO-dominated and H<sub>2</sub>O-dominated ices and that of HCOOH and HCOOCH<sub>3</sub> were in any case under our detection limit. This stresses that different desorption mechanisms are involved in the X-ray and VUV photodesorption of COMs, which implies a different role played by these processes in the interstellar medium.

Finally, trying to quantitatively compare our astrophysical yields in the X-ray range with astronomical observations seems difficult. For example, astronomical observations in the TW Hya disk shows disk-averaged column density of CH<sub>3</sub>CN, HCOOH and CH<sub>3</sub>OH in the same order of magnitude (Walsh et al., 2016; Loomis et al., 2018; Favre et al., 2018). At first, the fact that we found similar X-ray photodesorption yields for CH<sub>3</sub>OH and HCOOH from CO-mixed ices is somehow consistent with similar abundances of HCOOH and CH<sub>3</sub>OH in the TW Hya disk. On the other hand, the yield for CH<sub>3</sub>CN is found lower by almost one order of magnitude. This is globally not consistent with the observational survey of Bergner et al. (2018) where CH<sub>3</sub>CN was detected in several protoplanetary disks whereas no CH<sub>3</sub>OH transitions were detected. We stress however that our yields depend both on the ice composition and on the local X-ray energy spectrum. It is therefore not straightforward to predict the role of X-ray photodesorption as the region considered determines both the ice composition and the local X-ray spectrum. All that we can deduce from our experimental results is that X-ray photodesorption should participate into explaining the presence of gas phase COMs in protoplanetary disks, with a more important contribution when the COMs are mixed in CO ice instead of water ice. The yields provided in Table VI.8 should anyway help to understand the quantitative role of X-ray photodesorption in protoplanetary disks, especially via astrochemical modeling.

## VI.5 Conclusion and perspectives

X-ray photodesorption of  $\text{CH}_3\text{OH}$ ,  $\text{CH}_3\text{CN}$  and  $\text{HCOOH}$  has been studied from pure, CO-mixed and  $\text{H}_2\text{O}$ -mixed ices. The TEY measurements first enabled to discuss the general dissociation behavior of the COMs under X-ray irradiation. For instance, it was found that mixing  $\text{CH}_3\text{OH}$  and  $\text{CH}_3\text{CN}$  in water ice accelerates the destruction kinetic of the intact COM compared to the case of the pure and CO-mixed ices. This is consistent with the general behavior observed in similar experiments (for example in [Laffon et al. \(2010\)](#); [Bulak et al. \(2021\)](#); [Abdoul-Carime et al. \(2022\)](#)) where the water matrix is thought to act as a chemical catalyst by providing reactive species, dominantly OH radical, that react with the intact COM. For  $\text{HCOOH}$ , on the other hand, we did not observe a significant difference in the destruction of  $\text{HCOOH}$  under X-ray irradiation when it is mixed in CO or  $\text{H}_2\text{O}$  ices, probably due to the fact that its dissociation induced by the photons and the electrons largely dominates compared to its destruction via chemical reactions.

Interestingly, the behavior observed in the TEYs data can be put in contrast with the experimental X-ray photodesorption yields derived for the intact COMs. Indeed, it was found that the X-ray photodesorption yields of  $\text{CH}_3\text{OH}$  and  $\text{CH}_3\text{CN}$  from  $\text{H}_2\text{O}$  dominated ices were under our detection limit whereas for similar dilution ratios, the intact COMs were found to desorb when mixed in CO-dominated ices. This can be assumed to be due to chemical reactions, mediated by the Auger scattering, preventing the desorption of the intact COM when it is mixed with water, somehow consistent with the behavior observed in the TEYs data. For the case of  $\text{HCOOH}$  however, we did not have evidence of such behavior and the X-ray photodesorption yields of the intact  $\text{HCOOH}$  were found very close to our detection limit for the CO-dominated ices and under our detection limit for  $\text{H}_2\text{O}$ -dominated ices, for similar dilution ratios.

The previous findings have important astrophysical implications. First, we clearly demonstrated that the X-ray photodesorption of COMs is possible hence it should participate in the gas-to-ice exchanges in the cold and X-ray irradiated regions of the ISM. Secondly, the quantitative role of X-ray photodesorption should depend on the ice composition hence on the region considered. Namely, the X-ray photodesorption of the intact COMs studied should be less efficient in regions where COMs are mixed in water ice than in regions where they are mixed with CO ice. We should however remind that the experimental yields and the previous behaviors were observed in the soft X-ray range whereas the X-ray emission spectrum of young stars covers the whole energy range from 0.1 to 10 keV. Although we have made the assumption that the X-ray photodesorption yields should follow the X-ray core O 1s ionization cross section for energies higher than 560 eV, additional experiments should be conducted in the

hard X-ray range to conclude on this assumption. Finally, the recent modeling study of [Notsu et al. \(2021\)](#) showed that taking into account the X-ray photodesorption of H<sub>2</sub>O from interstellar ices affects its gas-phase molecular abundance outside the water snowline. This further encourages to conduct additional experimental studies on X-ray photodesorption from interstellar ices and somehow justifies the studies carried out during the thesis.

# Conclusion

Photodesorption of diatomic ( $\text{CO}$ ,  $\text{N}_2$ ) and Complex Organic Molecules (COMs) was experimentally studied at the LERMA lab in a ultra-high vacuum set-up. Photodesorption was probed by a mass spectrometry technique, in the VUV (7 - 13.6 eV) and soft X-ray (400 - 560 eV) range and an extrapolation to higher X-ray energies is proposed. Results were obtained from synchrotron experiments at the SOLEIL facility in Paris-Saclay and experiments were also conducted directly at the LERMA lab thanks to the implementation of a new VUV photon source that opens very promising scientific opportunities. The studies focused on the photodesorption of neutral molecules and provided (i) quantitative photodesorption yields and (ii) a better understanding of the fundamental mechanisms involved in the desorption process.

In the VUV range, photodesorption has already been extensively studied by several groups for "simple" molecules such as  $\text{CO}$ ,  $\text{CO}_2$ ,  $\text{H}_2\text{O}$ ,  $\text{CH}_4$ ,  $\text{H}_2\text{CO}$  and  $\text{NH}_3$ . Beside their importance in astrochemistry, the only COM studied so far regarding photodesorption is methanol  $\text{CH}_3\text{OH}$ . The present thesis extends the study of VUV photodesorption for other COMs that have been detected in the cold regions of the interstellar medium (ISM), namely acetonitrile  $\text{CH}_3\text{CN}$ , formic acid  $\text{HCOOH}$  and methyl formate  $\text{HCOOCH}_3$ . VUV photodesorption yields were derived for ices of the pure COM and for ices where the COM is mixed in a  $\text{CO}$ -rich or  $\text{H}_2\text{O}$ -rich ice. Those two kinds of mixed ices can serve as models of the realistic icy mantles that could be found in the ISM, mainly composed of water, but which can also present a  $\text{CO}$ -rich phase in denser regions beyond the  $\text{CO}$  snowlines.

The VUV photodesorption of the intact  $\text{HCOOH}$  and  $\text{HCOOCH}_3$  was found below our detection limit of  $5 \times 10^{-6}$  molecule/photon and  $1 \times 10^{-5}$  molecule/photon respectively, for each ice studied. The neutral species desorbing from  $\text{HCOOH}$  and  $\text{HCOOCH}_3$ -containing ices match the UV photo-dissociation fragments observed in gas phase studies ( $\text{CO}$ ,  $\text{CO}_2$ ,  $\text{H}_2\text{CO}$ ,  $\text{H}_2\text{O}$  ...) but the branching ratios differ. By contrast, VUV photodesorption of  $\text{CH}_3\text{CN}$  was clearly detected from each ice studied, with a yield of  $\sim 10^{-5}$  molecule/photon at 10.5 eV in mixed ices.  $\text{CH}_3\text{CN}$  photo-fragments ( $\text{HCN}$ ,  $\text{CN}$ ,  $\text{CHCN}$ ,  $\text{CH}_3$ ), also similar to that observed in gas phase dissociation studies, were found to de-

sorb with a yield in the same order of magnitude than that of  $\text{CH}_3\text{CN}$ . The fact that the VUV photodesorption yields of the  $\text{CH}_3\text{CN}$  photo-fragments and of the intact  $\text{CH}_3\text{CN}$  are found to not significantly depend on the ice composition points toward a direct desorption process for which the molecule that absorbs the photon desorbs in its intact form or in the form of its dissociation products. The same mechanism can be deduced from the data for the desorption of the  $\text{HCOOH}$  and  $\text{HCOOCH}_3$  photo-fragments. Indirect desorption processes, i.e. the desorption of surface molecules induced by the photo-absorption of sub-surface  $\text{H}_2\text{O}$  or  $\text{CO}$  molecules, previously observed for simple species such as  $\text{N}_2$ , do not seem to occur for the COMs studied in mixed ices. Interestingly, the experimental results are quantitatively consistent with astronomical observations showing that  $\text{CH}_3\text{CN}$  is more easily detected than  $\text{HCOOH}$  and  $\text{HCOOCH}_3$  (and also  $\text{CH}_3\text{OH}$ ) in regions where VUV photodesorption could play a role (photo-dominated regions, protoplanetary disks). Finally, this shows that the VUV photodesorption of COMs cannot be extrapolated from the behavior of a single COM. The photodesorption of some COMs might be favored compared to other ones, which implies that photodesorption is expected to play an important role in the evolution of the molecular complexity of both the gas and solid phases in regions where it occurs.

Still in the VUV range, fundamental desorption mechanisms remain to be understood. To reveal such mechanisms, one can try to have access to the internal and kinetic states of photodesorbed molecules. To such end, an important part of my work was to develop a VUV photon source directly at the LERMA lab by using a well-known third order non-linear optic effect in a rare gas medium. The successful implementation resulted in a nanosecond-pulsed, monochromatic and tunable VUV photon source now available at the lab. The use of such source, combined with a Time-Of-Flight delay and a Resonance Enhanced Multi-Photon Ionization (REMPI) technique, enabled to obtain the first quantitative data on the internal and kinetic states of photodesorbed  $\text{CO}$  molecules from a pure  $\text{CO}$  ice, the desorption being induced by the A-X electronic transition of  $\text{CO}$ . The mean kinetic energy and the vibrational and rotational population distributions of the desorbed molecules were estimated.  $\text{CO}$  was found to photodesorb with little vibrational energy and with a rotational energy coupled to its kinetic energy, the latter having a mean value of the order of 100 meV. Theoretical simulations are currently being performed at the PhLAM lab in order to be compared to our experimental results which are somehow depicting a scenario not predicted by previous theoretical studies. Thanks to this collaboration, we will hopefully answer fundamental questions that have been unresolved for several years.

Finally, X-ray irradiation of ices has experimentally been proven in the past years to induce the desorption of simple neutral molecules such as  $\text{CO}$  and  $\text{H}_2\text{O}$ . By focusing on a simple system, namely mixed  $\text{CO}:\text{N}_2$  ices, the thesis brings new interesting in-

sights on the desorption mechanisms involved in the X-ray range. The selective photo-excitation of the  $N_2$  molecules near the N K-edge ( $\sim 401$  eV) or the CO molecules near the O K-edge ( $\sim 534.4$  eV) enabled to trigger indirect photodesorption from the mixed ices. Indeed, the desorption of CO from  $N_2$  excitation, and inversely, was observed, which provides a clear evidence of an indirect mechanism at play. Additionally, a layered ice experiment enabled us to estimate the relevant depth of the indirect desorption process observed, which was further related, thanks to a nice simple model, to the scattering of Auger electrons. These experiments provided strong proofs on the dominant mechanism involved in the desorption process induced by X-rays, which was found to be a X-ray Electron Stimulated Desorption (XESD) process. The study of X-ray photodesorption was extended to COMs detected in protoplanetary disks :  $CH_3OH$ ,  $CH_3CN$  and  $HCOOH$ . The desorption yields of the intact COM and of the photo-fragments were derived for the pure COM ice and when the COM is mixed in CO-rich or  $H_2O$ -rich ices, similarly to the case of VUV. Globally, the X-ray photodesorption of the COMs depends on the ice composition. The water matrix was found to reduce the desorption yields of the intact COM compared to the case where the COM is mixed with a CO ice. In the case of  $CH_3OH$ , this was strongly suggested to be due to its reaction with OH radical competing with the desorption channel. The TEYs data for  $CH_3CN$ -containing ices also pointed towards a catalytic role of the water matrix leading to a fast destruction kinetic of  $CH_3CN$  in  $H_2O:CH_3CN$  ices compared to the case of  $CO:CH_3CN$  ices, eventually explaining the decrease of the  $CH_3CN$  desorption yields from  $H_2O:CH_3CN$  ices. The X-ray photodesorption yields of  $HCOOH$  were in any case found very close to our detection limit but less easily detectable when  $HCOOH$  is significantly diluted in a water ice (with a dilution ratio of 10 :1). The yields were derived in the soft X-ray range (400-560 eV) and an extrapolation to higher energies was proposed in order to provide photodesorption yields averaged on local X-ray spectra representative of the different regions of the ISM, especially relevant for different regions of protoplanetary disks. These results showed that X-ray photodesorption of COMs should play a role in their gas-to-ice exchanges in the cold regions of disks. As the yields derived were found to significantly depend on the ice composition and on the local X-ray spectrum, astrochemical model might provide a better understanding of the influence of X-ray photodesorption in protoplanetary disks compared to the other non-thermal desorption processes at play (VUV photodesorption, CR sputtering ...).

Quantitative photodesorption yields of COMs from interstellar ice analogues, that were previously lacking, are now available for the astrophysics community. Yields associated with the desorption of the photo-fragments of COMs and branching ratios are also provided. These data should enrich the discussions on the role of the photodesorption of COMs in the gas-to-ice exchanges occurring in the cold and dense ISM. A quantitative comparison with the other non-thermal desorption processes such as CR sputte-

ring or chemical desorption should be possible, especially for  $\text{CH}_3\text{OH}$  which has been extensively studied. The studies presented in this thesis can be additionally extended to cometary and planetary science for icy bodies that share common properties and composition with interstellar ices. By providing photodesorption yields averaged in energy, we facilitate the implementation of photodesorption in astrochemical models. The systematic study of the photodesorption as a function of the ice composition remains to be extended to more complex mixtures than binary ones. This is especially relevant for X-ray photodesorption since we have shown that the X-ray induced chemistry, that depends on the ice composition, can have a significant influence on desorption. The influence of other important parameters, such as the ice temperature, is still an open question. This is to be contrasted with the recent launch of the James Webb Space Telescope (JWST) that promises new observational data. Especially, the spatial resolution provided by the JWST should allow astrophysicists to isolate specific regions of the ISM corresponding to particular physical conditions. This might reveal some key physical parameters involved in the gas-to-ice abundances in the cold ISM, including that relevant for photodesorption. In the future, studying the dependence of the photodesorption yields with the experimental photon flux is also critical to validate the extrapolation of our experimental data to astrophysical environments.

A major result of this thesis is the finding that X-ray photodesorption of COMs can occur in protoplanetary disks depending on the region considered. This is globally consistent with previous observational data showing gas phase COMs in disks but with abundances often averaged on the entire disk. With JWST, we expect to go further on the analysis. Namely, if JWST is able to isolate sub-regions of the disk, this would allow us to compare more directly and more quantitatively our experimental results to observational data. In particular, we have found the X-ray photodesorption yields to be lower when the COM is embedded in water ice compared to the case where it is embedded in a CO ice. This would mean that gas phase abundances of COMs should significantly depend on the region of the disk, especially with respect to the water and CO snowlines. Observational data showing such dependence would definitively correlate with our results. X-ray induced processes in ices have gained an increasing interest in the laboratory astrophysics community in the recent years. With the current experimental setup, the combination of the X-ray synchrotron source, the mass spectrometry technique to probe photodesorption and the infrared spectroscopy technique to probe chemical changes in the ice bulk, would provide an excellent tool to obtain a full picture on the surface and bulk X-ray induced chemistry. This would ultimately lead to better quantitative constraints on the molecular evolution of ice analogues under X-ray radiation, by for example providing desorption branching ratios or by characterizing the chemical kinetics. In addition, we have shown Electron-Stimulated-Desorption (ESD) experiments to be an interesting candidate for complementary studies in the X-ray range. An

excellent agreement between ESD and X-ray experiments was found for pure CH<sub>3</sub>OH ice. It is still needed to compare these methods on other systems (e.g. for mixed ices) but ESD experiments clearly appear as a good solution if one cannot have access to a synchrotron facility. The desorption induced by hard X-rays remains a crucial topic to study as stellar hard X-rays should dominate the energy spectrum for deep regions of protoplanetary disks. For photon energies of a few keV, it is expected that both the Auger electron and the primary ionized core electron thermalize in the ice. Whether this enhances desorption yields is a major question. Ultimately, hard X-ray studies will lead to a complete picture of the photodesorption behavior in the full 0.1 - 10 keV range.

While providing quantitative photodesorption yields helps to constrain the molecular composition of the cold ISM, the fundamental mechanisms of photodesorption are still not well understood. How an electronic excitation leads in fine to the desorption of a surface molecule is still an open question. The direct or indirect nature of the desorption mechanism is sometimes difficult to discuss, especially in the VUV range. For COMs, photo-dissociation and recombination processes play a major role but are poorly constrained. Finally, for ice mixtures relevant to astrophysics, many processes are expected to compete. Ideally, the identification of dominant desorption mechanisms will enable to predict desorption from ices of any molecular composition, temperature ... To answer such challenge, the new VUV photon source implemented during my thesis coupled with the REMPI + TOF technique offers a great opportunity. Indeed, the signature of the desorption mechanism should be encrypted in the internal and kinetic energy states of photo-desorbed molecules. The current set-up implemented enables to have access to such information. Starting from a simple system to more complex ones, we might be able to isolate each desorption mechanism and to quantify their efficiency independently. The energy balance associated with each mechanism will provide a full picture of the various processes at play. For instance, while we have already obtained quantitative data from a pure CO ice for which both direct and indirect processes can occur, extending the studies to mixed ices should enable to isolate the direct from the indirect processes. Concretely, photo-exciting CO in mixed CO:N<sub>2</sub> ices while probing photodesorption should allow us to study indirect processes (by looking at the desorption of N<sub>2</sub>) and direct processes (by looking at the desorption of CO) separately. Furthermore, photo-dissociation and photo-chemistry processes coupled with desorption might be highlighted when studying systems like water ice or COMs-containing ices. Quantifying the energy states of desorbing fragments or products should provide key information especially relevant for COMs. The recent collaboration with the theoretical team of the PhLAM lab will bring important theoretical inputs to interpret the experimental data. This is already demonstrated by the recent and promising results obtained from pure CO ice.



# **Appendix A : Partial ionization cross sections by electron impact at 70 eV**

TABLE VI.9 – Partial ionization cross sections by electron impact at 70 eV.

Mass (a.m.u.)	Species $X^+ / X$	$\sigma(X^+ / X)$ ( $10^{-16} \text{ cm}^2$ )	Reference and assumption
60	$\text{CH}_3\text{OCHO}^+ / \text{CH}_3\text{OCHO}$	1.13	<a href="#">Mozejko (2007)</a> ; assumed to be equal to the total cross section of acetic acid (isomer) corrected from the cracking pattern of $\text{CH}_3\text{OCHO}$
46	$\text{HCOOH}^+ / \text{HCOOH}$	0.8	<a href="#">Zawadzki (2018)</a>
44	$\text{CO}_2^+ / \text{CO}_2$	2.74	<a href="#">Orient and Strivastava (1987)</a>
41	$\text{CH}_3\text{CN}^+ / \text{CH}_3\text{CN}$	3.11	<a href="#">Zhou et al. (2019)</a> ; deduce from the total cross section corrected from the cracking pattern of $\text{CH}_3\text{CN}$
39	$\text{CHCN}^+ / \text{CHCN}$	3.11	assumed to be equal that of $\text{CH}_3\text{CN}$
32	$\text{O}_2^+ / \text{O}_2$	1.57	<a href="#">Straub et al. (1996)</a>
32	$\text{CH}_3\text{OH}^+ / \text{CH}_3\text{OH}$	1.17	<a href="#">Srivastava et al. (1996)</a>
30	$\text{C}_2\text{H}_6^+ / \text{C}_2\text{H}_6$	0.78	<a href="#">Chatham et al. (1984)</a>
30	$\text{H}_2\text{CO}^+ / \text{H}_2\text{CO}$	1.3	<a href="#">Vacher et al. (2009)</a>
30	$\text{NO}^+ / \text{NO}$	2.42	<a href="#">Lopez et al. (2003)</a>
29	$\text{HCO}^+ / \text{HCO}$	1.3	assumed to be equal to that of $\text{H}_2\text{CO}$
28	$\text{CO}^+ / \text{CO}$	1.78	<a href="#">Tian and Vidal (1998)</a>
28	$\text{N}_2^+ / \text{N}_2$	1.88	<a href="#">Straub et al. (1996)</a>
28	$\text{C}_2\text{H}_4^+ / \text{C}_2\text{H}_4$	2.38	<a href="#">Kumar and Sharma (2020)</a>
27	$\text{HCN}^+ / \text{HCN}$	2.83	<a href="#">Pandya et al. (2012)</a> ; deduce from the total cross section corrected from the cracking pattern of $\text{HCN}$
26	$\text{CN}^+ / \text{CN}$	2.8	<a href="#">Pandya et al. (2012)</a> ; assumed to be equal to the total cross section
18	$\text{H}_2\text{O}^+ / \text{H}_2\text{O}$	1.62	<a href="#">Orient and Strivastava (1987)</a>
17	$\text{OH}^+ / \text{OH}$	1.85	<a href="#">Tarnovsky et al. (1998)</a> ; assumed to be equal to that of $\text{OD}^+ / \text{OD}$
16	$\text{CH}_4^+ / \text{CH}_4$	1.71	<a href="#">Tian and Vidal (1998)</a>
16	$\text{O}^+ / \text{O}$	1.28	<a href="#">Laher and Gilmore (1990)</a>
15	$\text{CH}_3^+ / \text{CH}_3$	1.73	<a href="#">Tarnovsky et al. (1996)</a> ; assumed to be equal to that of $\text{CD}_3^+ / \text{CD}_3$
14	$\text{N}^+ / \text{N}$	1.5	<a href="#">Ciccarino and Savin (2019)</a>

# Bibliographie

- Abdoul-Carime, H., Thiam, G., Rabilloud, F., Charlieux, F., and Kopyra, J. Chemistry in acetonitrile–water films induced by slow (<15 eV) electrons : Application to the earth and space chemistry. *ACS Earth and Space Chemistry*, **6(4):1126–1132**, 2022.
- Adams, F. C., Fatuzzo, M., and Holden, L. Background X-ray Radiation Fields Produced by Young Embedded Star Clusters. *Publications of the Astronomical Society of the Pacific*, **124(919):913–921**, September 2012.
- Allamandola, L. J., Tielens, A. G. G. M., and Barker, J. R. Polycyclic aromatic hydrocarbons and the unidentified infrared emission bands : auto exhaust along the milky way. *ApJ*, **290:L25–L28**, March 1985.
- Andersson, S., Arasa, C., Yabushita, A., Yokoyama, M., Hama, T., Kawasaki, M., Western, C. M., and Ashfold, M. N. R. A theoretical and experimental study on translational and internal energies of H<sub>2</sub>O and OH from the 157 nm irradiation of amorphous solid water at 90 K. *Phys. Chem. Chem. Phys.*, **13:15810–15820**, 2011.
- Andrade, D. P. P., Rocco, M. L. M., and Boechat-Roberty, H. M. X-ray photodesorption from methanol ice : Ion desorption by soft X-ray. *Monthly Notices of the Royal Astronomical Society*, **409(3):1289–1296**, December 2010.
- Andrade, D. P. P., de Barros, A. L. F., Pilling, S., Domaracka, A., Rothard, H., Boduch, P., and da Silveira, E. F. Chemical reactions induced in frozen formic acid by heavy ion cosmic rays. *Monthly Notices of the Royal Astronomical Society*, **430(2):787–796**, April 2013.
- Antoniewicz, P. R. Model for electron- and photon-stimulated desorption. *Physical Review B*, **21(9):3811–3815**, May 1980.
- Arumainayagam, C. R., Garrod, R. T., Boyer, M. C., Hay, A. K., Bao, S. T., Campbell, J. S., Wang, J., Nowak, C. M., Arumainayagam, M. R., and Hodge, P. J. Extraterrestrial prebiotic molecules : photochemistry vs. radiation chemistry of interstellar ices. *Chemical Society Reviews*, **48(8):2293–2314**, 2019.
- Baber, A. E., Mudiyansele, K., Senanayake, S. D., Beatriz-Vidal, A., Luck, K. A., Sykes, E. C. H., Liu, P., Rodriguez, J. A., and Stacchiola, D. J. Assisted deprotonation of formic acid on Cu(111) and self-assembly of 1D chains. *Phys. Chem. Chem. Phys.*, **15:12291–12298**, 2013.
- Bacmann, A., Taquet, V., Faure, A., Kahane, C., and Ceccarelli, C. Detection of complex organic molecules in a prestellar core : a new challenge for astrochemical models. *Astronomy & Astrophysics*, **541:L12**, May 2012.
- Bahr, D. A. and Baragiola, R. A. Photodesorption of solid CO<sub>2</sub> LY $\alpha$ . *The Astrophysical Journal*, **761(1):36**, nov 2012.

- Barrus, D. M., Blake, R. L., Burek, A. J., Chambers, K. C., and Pregoner, A. L. K-shell photoabsorption coefficients of O<sub>2</sub>, CO<sub>2</sub>, CO, and N<sub>2</sub>O. *Physical Review A*, **20(3):1045–1061**, September 1979.
- Basalgète, R., Dupuy, R., Féraud, G., Romanzin, C., Philippe, L., Michaut, X., Michoud, J., Amiaud, L., Lafosse, A., Fillion, J.-H., and Bertin, M. Complex organic molecules in protoplanetary disks : X-ray photodesorption from methanol-containing ices : I. Pure methanol ices. *Astronomy & Astrophysics*, **647:A35**, March 2021a.
- Basalgète, R., Dupuy, R., Féraud, G., Romanzin, C., Philippe, L., Michaut, X., Michoud, J., Amiaud, L., Lafosse, A., Fillion, J.-H., and Bertin, M. Complex organic molecules in protoplanetary disks : X-ray photodesorption from methanol-containing ices : II. Mixed methanol-CO and methanol-H<sub>2</sub>O ices. *Astronomy & Astrophysics*, **647:A36**, March 2021b.
- Basalgète, R., Torres-Díaz, D., Lafosse, A., Amiaud, L., Féraud, G., Jeseck, P., Philippe, L., Michaut, X., Fillion, J.-H., and Bertin, M. Indirect x-ray photodesorption of <sup>15</sup>N<sub>2</sub> and <sup>13</sup>CO from mixed and layered ices. *The Journal of Chemical Physics*, **157(8):084308**, 2022.
- Basalgète, R., Ocaña, A. J., Féraud, G., Romanzin, C., Philippe, L., Michaut, X., Fillion, J.-H., and Bertin, M. Photodesorption of Acetonitrile CH<sub>3</sub>CN in UV-irradiated Regions of the Interstellar Medium : Experimental Evidence. *The Astrophysical Journal*, **922(2):213**, December 2021c.
- Bass, A. D., Bredehöft, J. H., Böhler, E., Sanche, L., and Swiderek, P. Reactions and anion desorption induced by low-energy electron exposure of condensed acetonitrile. *The European Physical Journal D*, **66(2):53**, February 2012.
- Bennett, C. J. and Kaiser, R. I. On the formation of glycolaldehyde (HCOCH<sub>2</sub>OH) and methyl formate (HCOOCH<sub>3</sub>) in interstellar ice analogs. *The Astrophysical Journal*, **661(2):899–909**, jun 2007.
- Bennett, C. J., Chen, S., Sun, B., Chang, A. H. H., and Kaiser, R. I. Mechanistical Studies on the Irradiation of Methanol in Extraterrestrial Ices. *The Astrophysical Journal*, **660(2):1588–1608**, May 2007.
- Bennett, C. J., Hama, T., Kim, Y. S., Kawasaki, M., and Kaiser, R. I. Laboratory studies on the formation of formic acid (HCOOH) in interstellar and cometary ices. *The Astrophysical Journal*, **727(1):27**, January 2011.
- Bennett, C. J., Pirim, C., and Orlando, T. M. Space-weathering of solar system bodies : A laboratory perspective. *Chemical Reviews*, **113(12):9086–9150**, 2013.
- Bergantini, A., Pilling, S., Rothard, H., Boduch, P., and Andrade, D. P. P. Processing of formic acid-containing ice by heavy and energetic cosmic ray analogues. *Monthly Notices of the Royal Astronomical Society*, **437(3):2720–2727**, January 2014.
- Bergner, J. B., Öberg, K. I., and Rajappan, M. Methanol Formation via Oxygen Insertion Chemistry in Ices. *The Astrophysical Journal*, **845(1):29**, August 2017.
- Bergner, J. B., Guzmán, V. G., Öberg, K. I., Loomis, R. A., and Pegues, J. A Survey of CH<sub>3</sub>CN and HC<sub>3</sub>N in Protoplanetary Disks. *The Astrophysical Journal*, **857(1):69**, April 2018.
- Bergner, J. B., Martin-Domenech, R., Öberg, K. I., Jorgensen, J. K., de la Villarmois, E. A., and Brinch, C. Organic complexity in protostellar disk candidates. *ACS Earth and Space Chemistry*, **3(8):1564–1575**, August 2019.

- Berkowitz, J. *Atomic and molecular photoabsorption : absolute total cross sections*. Academic Press, San Diego, CA, 2002. URL <http://cds.cern.ch/record/1087021>.
- Bernstein, M. P., Sandford, S. A., Allamandola, L. J., Chang, S., and Scharberg, M. A. Organic Compounds Produced by Photolysis of Realistic Interstellar and Cometary Ice Analogs Containing Methanol. *Apj*, **454**:327, November 1995.
- Bernstein, M. P., Ashbourn, S. F. M., Sandford, S. A., and Allamandola, L. J. The Lifetimes of Nitriles (CN) and Acids (COOH) during Ultraviolet Photolysis and Their Survival in Space. *The Astrophysical Journal*, **601**(1):365–370, January 2004.
- Bertin, M., Romanzin, C., Michaut, X., Jeseck, P., and Fillion, J.-H. Adsorption of Organic Isomers on Water Ice Surfaces : A Study of Acetic Acid and Methyl Formate. *The Journal of Physical Chemistry C*, **115**(26):12920–12928, July 2011.
- Bertin, M., Doronin, M., Fillion, J.-H., Michaut, X., Philippe, L., Lattelais, M., Markovits, A., Pauzat, F., Ellinger, Y., and Guillemin, J.-C. Nitrile versus isonitrile adsorption at interstellar grains surfaces : I. Hydroxylated surfaces. *Astronomy & Astrophysics*, **598**:A18, February 2017.
- Bertin, M., Fayolle, E. C., Romanzin, C., Öberg, K. I., Michaut, X., Moudens, A., Philippe, L., Jeseck, P., Linnartz, H., and Fillion, J.-H. UV photodesorption of interstellar CO ice analogues : from subsurface excitation to surface desorption. *Physical Chemistry Chemical Physics*, **14**(28):9929, 2012.
- Bertin, M., Fayolle, E. C., Romanzin, C., Poderoso, H. A. M., Michaut, X., Philippe, L., Jeseck, P., Öberg, K. I., Linnartz, H., and Fillion, J.-H. Indirect ultraviolet photodesorption from CO:N<sub>2</sub> binary ices - an efficient grain-gas process. *The Astrophysical Journal*, **779**(2):120, December 2013.
- Bertin, M., Romanzin, C., Doronin, M., Philippe, L., Jeseck, P., Ligterink, N., Linnartz, H., Michaut, X., and Fillion, J.-H. UV photodesorption of methanol in pure and CO-rich ices : desorption rates of the intact molecule and of the photofragments. *The Astrophysical Journal*, **817**(2):L12, January 2016.
- Bethell, T. J. and Bergin, E. A. Photoelectric cross-section of gas and dust in protoplanetary disk. *The Astrophysical Journal*, **740**(1):7, October 2011.
- Bhuin, R. G., Methikkalam, R. R. J., Sivaraman, B., and Pradeep, T. Interaction of Acetonitrile with Water-Ice : An Infrared Spectroscopic Study. *The Journal of Physical Chemistry C*, **119**(21):11524–11532, May 2015.
- Bisschop, S. E., Fraser, H. J., Öberg, K. I., van Dishoeck, E. F., and Schlemmer, S. Desorption rates and sticking coefficients for CO and N<sub>2</sub> interstellar ices. *Astronomy & Astrophysics*, **449**(3):1297–1309, April 2006.
- Bisschop, S. E., Fuchs, G. W., Boogert, A. C. A., van Dishoeck, E. F., and Linnartz, H. Infrared spectroscopy of HCOOH in interstellar ice analogues. *Astronomy & Astrophysics*, **470**(2):749–759, August 2007.
- Bonin, K. D. and McIlrath, T. J. Two-photon electric-dipole selection rules. *J. Opt. Soc. Am. B*, **1**(1):52–55, Mar 1984.
- Boogert, A. A., Gerakines, P. A., and Whittet, D. C. Observations of the Icy Universe. *Annual Review of Astronomy and Astrophysics*, **53**(1):541–581, August 2015.

- Bulak, M., Paardekooper, D. M., Fedoseev, G., and Linnartz, H. Novel approach to distinguish between vacuum UV-induced ice photodesorption and photoconversion : Investigation of CH<sub>4</sub>, CH<sub>3</sub>OH, and CH<sub>3</sub>CN. *Astronomy & Astrophysics*, [636:A32](#), April 2020.
- Bulak, M., Paardekooper, D., Fedoseev, G., and Linnartz, H. Photolysis of acetonitrile in a water-rich ice as a source of complex organic molecules : CH<sub>3</sub>CN and H<sub>2</sub>O :CH<sub>3</sub>CN ices. *Astronomy & Astrophysics*, [A82:647](#), January 2021.
- Calcutt, H., Fiechter, M. R., Willis, E. R., Müller, H. S. P., Garrod, R. T., Jørgensen, J. K., Wampfler, S. F., Bourke, T. L., Coutens, A., Drozdovskaya, M. N., Ligterink, N. F. W., and Kristensen, L. E. The ALMA-PILS survey : first detection of methyl isocyanide (CH<sub>3</sub>NC) in a solar-type protostar. *Astronomy & Astrophysics*, [617:A95](#), September 2018.
- Campbell, E. K., Holz, M., Gerlich, D., and Maier, J. P. Laboratory confirmation of C<sub>60</sub><sup>+</sup> as the carrier of two diffuse interstellar bands. *Nature*, [523\(7560\):322–323](#), July 2015.
- Carney, M. T., Hogerheijde, M. R., Guzmán, V. V., Walsh, C., Öberg, K. I., Fayolle, E. C., Cleeves, L. I., Carpenter, J. M., and Qi, C. Upper limits on CH<sub>3</sub>OH in the HD 163296 protoplanetary disk : Evidence for a low gas-phase CH<sub>3</sub>OH-to-H<sub>2</sub>CO ratio. *Astronomy & Astrophysics*, [623:A124](#), March 2019.
- Carrascosa, H., Cruz-Díaz, G. A., Muñoz Caro, G. M., Dartois, E., and Chen, Y.-J. Photon-induced desorption of larger species in UV-irradiated methane ice. *Monthly Notices of the Royal Astronomical Society*, [493:821–829](#), February 2020.
- Caselli, P. and Ceccarelli, C. Our astrochemical heritage. *The Astronomy and Astrophysics Review*, [20\(1\):56](#), October 2012.
- Cecchi-Pestellini, C. and Aiello, S. Cosmic ray induced photons in dense interstellar clouds. *Monthly Notices of the Royal Astronomical Society*, [258\(1\):125–133](#), September 1992.
- Chan, W., Cooper, G., and Brion, C. Absolute optical oscillator strengths for discrete and continuum photoabsorption of carbon monoxide (7–200 eV) and transition moments for the X<sup>1</sup>σ<sup>+</sup> - A<sup>1</sup>π system. *Chemical Physics*, [170\(1\):123–138](#), 1993.
- Chatham, H., Hils, D., Robertson, R., and Gallagher, A. Total and partial electron collisional ionization cross sections for CH<sub>4</sub>, C<sub>2</sub>H<sub>6</sub>, SiH<sub>4</sub>, and Si<sub>2</sub>H<sub>6</sub>. *The Journal of Chemical Physics*, [81\(4\):1770–1777](#), August 1984.
- Chen, C. T., Ma, Y., and Sette, F. K-shell photoabsorption of the N<sub>2</sub> molecule. *Physical Review A*, [40\(11\):6737–6740](#), December 1989.
- Chen, Y.-J., Chuang, K.-J., Caro, G. M. M., Nuevo, M., Chu, C.-C., Yih, T.-S., Ip, W.-H., and Wu, C.-Y. R. Vacuum ultraviolet emission spectrum measurement of a microwave-discharge hydrogen-flow lamp in several configurations : application to photodesorption of CO ice. *The Astrophysical Journal*, [781\(1\):15](#), dec 2013a.
- Chen, Y.-J., Ciaravella, A., Caro, G. M. M., Cecchi-Pestellini, C., Jiménez-Escobar, A., Juang, K.-J., and Yih, T.-S. Soft x-ray irradiation of methanol ice : formation of products as a function of photon energy. *The Astrophysical Journal*, [778\(2\):162](#), nov 2013b.
- Chen, Y.-J., Ciaravella, A., Muñoz Caro, G. M., Cecchi-Pestellini, C., Jiménez-Escobar, A., Juang, K.-J., and Yih, T.-S. SOFT X-RAY IRRADIATION OF METHANOL ICE : FORMATION OF PRODUCTS AS A FUNCTION OF PHOTON ENERGY. *The Astrophysical Journal*, [778\(2\):162](#), November 2013c.

- Chen, Y.-J., Muñoz Caro, G. M., Aparicio, S., Jiménez-Escobar, A., Lasne, J., Rosu-Finsen, A., McCoustra, M. R. S., Cassidy, A. M., and Field, D. Wannier-mott excitons in nanoscale molecular ices. *Phys. Rev. Lett.*, **119**:157703, Oct 2017.
- Cheng, B.-M., Liu, C.-P., Lo, W.-J., and Lee, Y.-P. Photodissociation thresholds of OH produced from CH<sub>3</sub>OH in solid neon and argon. *Nuclear Instruments and Methods in Physics Research Section A : Accelerators, Spectrometers, Detectors and Associated Equipment*, **467-468**:1461–1464, July 2001.
- Cheng, B.-M., Bahou, M., Chen, W.-C., Yui, C.-h., Lee, Y.-P., and Lee, L. C. Experimental and theoretical studies on vacuum ultraviolet absorption cross sections and photodissociation of CH<sub>3</sub>OH, CH<sub>3</sub>OD, CD<sub>3</sub>OH, and CD<sub>3</sub>OD. *The Journal of Chemical Physics*, **117**(4):1633–1640, July 2002.
- Christiaens, W. and Phariseau, P. On the exciton theory of amorphous solids. *Physica*, **38**(1):155–172, 1968.
- Ciaravella, A., Jiménez-Escobar, A., Muñoz Caro, G. M., Cecchi-Pestellini, C., Candia, R., Giarrusso, S., Barbera, M., and Collura, A. Soft x-ray irradiation of pure carbon monoxide interstellar ice analogues. *The Astrophysical Journal*, **746**(1):L1, February 2012.
- Ciaravella, A., Chen, Y.-J., Cecchi-Pestellini, C., Jiménez-Escobar, A., Caro, G. M. M., Chuang, K.-J., and Huang, C.-H. Chemical evolution of a co ice induced by soft x-rays. *The Astrophysical Journal*, **819**(1): 38, feb 2016.
- Ciaravella, A., Muñoz Caro, G. M., Jiménez-Escobar, A., Cecchi-Pestellini, C., Hsiao, L.-C., Huang, C.-H., and Chen, Y.-J. X-ray processing of a realistic ice mantle can explain the gas abundances in protoplanetary disks. *Proceedings of the National Academy of Sciences*, page 202005225, June 2020.
- Ciccarino, C. J. and Savin, D. W. Electron-Impact Ionization of Atomic Nitrogen. *Journal of Thermophysics and Heat Transfer*, **33**(1):154–162, January 2019.
- Cleeves, L. I., Adams, F. C., and Bergin, E. A. Exclusion of cosmic rays in protoplanetary disks : stellar and magnetic effects. *The Astrophysical Journal*, **772**(1):5, June 2013.
- Collings, M. P., Anderson, M. A., Chen, R., Dever, J. W., Viti, S., Williams, D. A., and McCoustra, M. R. S. A laboratory survey of the thermal desorption of astrophysically relevant molecules. *Monthly Notices of the Royal Astronomical Society*, **354**(4):1133–1140, November 2004.
- Compiègne, M., Verstraete, L., Jones, A., Bernard, J. P., Boulanger, F., Flagey, N., Le Boulot, J., Paradis, D., and Ysard, N. The global dust SED : tracing the nature and evolution of dust with DustEM. *A&A*, **525** :A103, January 2011.
- Cooper, D. L. and Kirby, K. Theoretical study of low-lying  $^1\Sigma^+$  and  $^1\Pi$  states of CO. I. potential energy curves and dipole moments. *The Journal of Chemical Physics*, **87**(1):424–432, 1987.
- Corazzi, M. A., Brucato, J. R., Poggiali, G., Podio, L., Fedele, D., and Codella, C. Thermal desorption of astrophysically relevant ice mixtures of acetaldehyde and acetonitrile from olivine dust. *The Astrophysical Journal*, **913**(2):128, jun 2021.
- Cronin, J. W., Gaisser, T. K., and Swordy, S. P. Cosmic Rays at the Energy Frontier. *Scientific American*, **276**:44–49, January 1997.
- Cruikshank, D. P., Roush, T. L., Owen, T. C., Geballe, T. R., de Bergh, C., Schmitt, B., Brown, R. H., and Bartholomew, M. J. Ices on the surface of triton. *Science*, **261**(5122):742–745, 1993.

- Cruz-Diaz, G. A. Ph.d. thesis. *Universidad Autonoma de Madrid, Spain*, 2015.
- Cruz-Diaz, G. A., Muñoz Caro, G. M., Chen, Y.-J., and Yih, T.-S. Vacuum-UV spectroscopy of interstellar ice analogs : I. Absorption cross-sections of polar-ice molecules. *Astronomy & Astrophysics*, **562:A119**, February 2014a.
- Cruz-Diaz, G. A., Muñoz Caro, G. M., Chen, Y.-J., and Yih, T.-S. Vacuum-UV spectroscopy of interstellar ice analogs : II. Absorption cross-sections of nonpolar ice molecules. *Astronomy & Astrophysics*, **562:A120**, February 2014b.
- Cruz-Diaz, G. A., Martín-Doménech, R., Muñoz Caro, G. M., and Chen, Y.-J. Negligible photodesorption of methanol ice and active photon-induced desorption of its irradiation products. *Astronomy & Astrophysics*, **592:A68**, August 2016.
- Cruz-Diaz, G. A., Martín-Doménech, R., Moreno, E., Muñoz Caro, G. M., and Chen, Y.-J. New measurements on water ice photodesorption and product formation under ultraviolet irradiation. *Monthly Notices of the Royal Astronomical Society*, **474(3):3080–3089**, November 2017.
- Cuppen, H. M., Ioppolo, S., Romanzin, C., and Linnartz, H. Water formation at low temperatures by surface O<sub>2</sub> hydrogenation II : the reaction network. *Phys. Chem. Chem. Phys.*, **12:12077–12088**, 2010.
- Danger, G., Orthous-Daunay, F.-R., de Marcellus, P., Modica, P., Vuitton, V., Duvernay, F., Flandinet, L., Le Sergeant d'Hendecourt, L., Thissen, R., and Chiavassa, T. Characterization of laboratory analogs of interstellar/cometary organic residues using very high resolution mass spectrometry. *Geochimica et Cosmochimica Acta*, **118:184–201**, 2013.
- Danger, G., Bossa, J.-B., de Marcellus, P., Borget, F., Duvernay, F., Theulé, P., Chiavassa, T., and d'Hendecourt, L. Experimental investigation of nitrile formation from VUV photochemistry of interstellar ices analogs : acetonitrile and amino acetonitrile. *A&A*, **525:A30**, 2011.
- Dartois, E., Chabot, M., Id Barkach, T., Rothard, H., Augé, B., Agnihotri, A. N., Domaracka, A., and Boduch, P. Cosmic ray sputtering yield of interstellar H<sub>2</sub>O ice mantles : Ice mantle thickness dependence. *Astronomy & Astrophysics*, **618:A173**, October 2018.
- Dartois, E., Chabot, M., Id Barkach, T., Rothard, H., Augé, B., Agnihotri, A. N., Domaracka, A., and Boduch, P. Non-thermal desorption of complex organic molecules : Efficient CH<sub>3</sub>OH and CH<sub>3</sub>COOCH<sub>3</sub> sputtering by cosmic rays. *Astronomy & Astrophysics*, **627:A55**, July 2019.
- Dartois, E., Chabot, M., Bacmann, A., Boduch, P., Domaracka, A., and Rothard, H. Non-thermal desorption of complex organic molecules : Cosmic-ray sputtering of CH<sub>3</sub>OH embedded in CO<sub>2</sub> ice. *Astronomy & Astrophysics*, **634:A103**, February 2020a.
- Dartois, E., Chabot, M., Id Barkach, T., Rothard, H., Boduch, P., Augé, B., Duprat, J., and Rojas, J. Electronic sputtering of solid N<sub>2</sub> by swift ions. *Nuclear Instruments and Methods in Physics Research Section B : Beam Interactions with Materials and Atoms*, **485:13–19**, December 2020b.
- Dartois, E., Chabot, M., Id Barkach, T., Rothard, H., Boduch, P., Augé, B., and Agnihotri, A. N. Cosmic ray sputtering yield of interstellar ice mantles - CO and CO<sub>2</sub> ice thickness dependence. *A&A*, **647:A177**, 2021.
- de Barros, A. L. F., Mejía, C., Seperuelo Duarte, E., Domaracka, A., Boduch, P., Rothard, H., and da Silveira, E. F. Chemical reactions in H<sub>2</sub>O:CO interstellar ice analogues promoted by energetic heavy-ion irradiation. *Monthly Notices of the Royal Astronomical Society*, **511(2):2491–2504**, April 2022.

- Demtröder, W. *Atoms, Molecules and Photons*. Springer Berlin, Heidelberg, San Diego, CA, 2002. doi: <https://doi.org/10.1007/978-3-642-10298-1>.
- DeSimone, A. J., Crowell, V. D., Sherrill, C. D., and Orlando, T. M. Mechanisms of H<sub>2</sub>O desorption from amorphous solid water by 157-nm irradiation : An experimental and theoretical study. *The Journal of Chemical Physics*, **139(16):164702**, 2013.
- Doronin, M., Bertin, M., Michaut, X., Philippe, L., and Fillion, J.-H. Adsorption energies and prefactor determination for CH<sub>3</sub>OH adsorption on graphite. *The Journal of Chemical Physics*, **143(8):084703**, August 2015.
- Draine, B. T. *Physics of the Interstellar and Intergalactic Medium*. 2011.
- Draine, B. Interstellar dust grains. *Annual Review of Astronomy and Astrophysics*, **41(1):241–289**, sep 2003.
- Dulieu, F., Congiu, E., Noble, J., Baouche, S., Chaabouni, H., Moudens, A., Minissale, M., and Cazaux, S. How micron-sized dust particles determine the chemistry of our Universe. *Scientific Reports*, **3(1):1338**, December 2013.
- Dupuy, R. Ph.d. thesis. *Sorbonne Université, Observatoire de Paris, LERMA, France*, 2019.
- Dupuy, R., Féraud, G., Bertin, M., Michaut, X., Putaud, T., Jeseck, P., Philippe, L., Romanzin, C., Baglin, V., Cimino, R., and Fillion, J.-H. The efficient photodesorption of nitric oxide (NO) ices : A laboratory astrophysics study. *Astronomy & Astrophysics*, **606:L9**, October 2017.
- Dupuy, R., Bertin, M., Féraud, G., Hassenfratz, M., Michaut, X., Putaud, T., Philippe, L., Jeseck, P., Angelucci, M., Cimino, R., Baglin, V., Romanzin, C., and Fillion, J.-H. X-ray photodesorption from water ice in protoplanetary disks and X-ray-dominated regions. *Nature Astronomy*, **2(10):796–801**, October 2018.
- Dupuy, R., Féraud, G., Bertin, M., Romanzin, C., Philippe, L., Putaud, T., Michaut, X., Cimino, R., Baglin, V., and Fillion, J.-H. Desorption of neutrals, cations, and anions from core-excited amorphous solid water. *The Journal of Chemical Physics*, **152(5):054711**, February 2020.
- Dupuy, R., Bertin, M., Féraud, G., Michaut, X., Marie-Jeanne, P., Jeseck, P., Philippe, L., Baglin, V., Cimino, R., Romanzin, C., and Fillion, J.-H. Mechanism of indirect photon-induced desorption at the water ice surface. *Phys. Rev. Lett.*, **126:156001**, Apr 2021a.
- Dupuy, R., Bertin, M., Féraud, G., Romanzin, C., Putaud, T., Philippe, L., Michaut, X., Jeseck, P., Cimino, R., Baglin, V., and Fillion, J.-H. X-Ray induced desorption and photochemistry in CO ice. *Physical Chemistry Chemical Physics*, **23(30):15965–15979**, 2021b.
- Dupuy, R., Bertin, M., Féraud, G., Michaut, X., Jeseck, P., Doronin, M., Philippe, L., Romanzin, C., and Fillion, J.-H. Spectrally-resolved UV photodesorption of CH<sub>4</sub> in pure and layered ices. *A&A*, **603:A61**, 2017.
- Eidelsberg, M., Roncin, J. Y., Le Floch, A., Launay, F., Letzelter, C., and Rostas, J. Reinvestigation of the vacuum ultraviolet spectrum of CO and isotopicspecies : the B<sup>1</sup>Σ<sup>+</sup> downarrow X<sup>1</sup>Σ<sup>+</sup> transition. *Journal of Molecular Spectroscopy*, **121(2):309–336**, January 1987.

- Faris, G. W., Meyer, S. A., Dyer, M. J., and Banks, M. J. Two-photon-resonant difference-frequency mixing with an ArF excimer laser : vacuum-ultraviolet generation and multiphoton spectroscopy. *Journal of the Optical Society of America B*, **17(11):1856**, November 2000.
- Favre, C., Fedele, D., Semenov, D., Parfenov, S., Codella, C., Ceccarelli, C., Bergin, E. A., Chapillon, E., Testi, L., Hersant, F., Lefloch, B., Fontani, E., Blake, G. A., Cleeves, L. I., Qi, C., Schwarz, K. R., and Taquet, V. First Detection of the Simplest Organic Acid in a Protoplanetary Disk. *The Astrophysical Journal*, **862(1):L2**, July 2018.
- Fayolle, E. C., Bertin, M., Romanzin, C., M Poderoso, H. A., Philippe, L., Michaut, X., Jeseck, P., Linnartz, H., Öberg, K. I., and Fillion, J.-H. Wavelength-dependent UV photodesorption of pure N<sub>2</sub> and O<sub>2</sub> ices. *Astronomy & Astrophysics*, **556:A122**, August 2013.
- Fayolle, E. C., Bertin, M., Romanzin, C., Michaut, X., Öberg, K. I., Linnartz, H., and Fillion, J.-H. CO ice photodesorption : a wavelength-dependent study. *The Astrophysical Journal*, **739(2):L36**, October 2011.
- Feifel, R., Andersson, M., Öhrwall, G., Sorensen, S., Piancastelli, M., Tchapyguine, M., Björneholm, O., Karlsson, L., and Svensson, S. A quantitative analysis of the N 1s →  $\pi^*$  photoabsorption profile in N<sub>2</sub> : new spectroscopical constants for the core-excited state. *Chemical Physics Letters*, **383(3-4):222–229**, January 2004.
- Feigelson, E. D. X-ray insights into star and planet formation. *Proceedings of the National Academy of Sciences*, **107(16):7153–7157**, April 2010.
- Ferm, P., Budde, E., Hamza, A., Jakubith, S., Ertl, G., Weide, D., Andresen, P., and Freund, H. UV-laser-induced photodesorption of NO from NiO. *Surface Science*, **218(2):467–493**, 1989.
- Feulner, P., Scheuerer, R., Scheuer, M., Remmers, G., Wurth, W., and Menzel, D. High resolution photon stimulated desorption spectroscopy of solid nitrogen by resonant N 1s core level excitation. *Applied Physics A*, **55(5):478–481**, November 1992.
- Feulner, P., Romberg, R., Frigo, S., Weimar, R., Gsell, M., Ogurtsov, A., and Menzel, D. Recent progress in the investigation of core hole-induced photon stimulated desorption from adsorbates : excitation site-dependent bond breaking, and charge rearrangement. *Surface Science*, **451(1-3):41–52**, April 2000.
- Feulner, P., Ecker, M., Romberg, R., Weimar, R., and Föhlisch, A. Core-excitation-induced bond breaking of chemisorbed molecules probed by emission of ions, neutrals and electrons. *Surface Review and Letters*, **09(02):759–768**, April 2002.
- Fiermans, L. and Phariseau, P. On the exciton problem in disordered structures. *Physica*, **32(7):1345–1349**, 1966.
- Fillion, J.-H., Fayolle, E. C., Michaut, X., Doronin, M., Philippe, L., Rakovsky, J., Romanzin, C., Champion, N., Öberg, K. I., Linnartz, H., and Bertin, M. Wavelength resolved UV photodesorption and photochemistry of CO<sub>2</sub> ice. *Faraday Discussions*, **168:533**, January 2014.
- Fillion, J.-H., Dupuy, R., Féraud, G., Romanzin, C., Philippe, L., Putaud, T., Baglin, V., Cimino, R., Marie-Jeanne, P., Jeseck, P., Michaut, X., and Bertin, M. Vacuum-uv photodesorption from compact amorphous solid water : Photon energy dependence, isotopic and temperature effects. *ACS Earth and Space Chemistry*, **6(1):100–115**, 2022.

- France, K., Schindhelm, E., Bergin, E. A., Roueff, E., and Abgrall, H. High-resolution ultraviolet radiation fields of classical t tauri stars. *The Astrophysical Journal*, [784\(2\):127](#), March 2014.
- Fraser, H. J., Collings, M. P., McCoustra, M. R. S., and Williams, D. A. Thermal desorption of water ice in the interstellar medium. *Monthly Notices of the Royal Astronomical Society*, [327\(4\):1165–1172](#), November 2001.
- Fredon, A., Radchenko, A. K., and Cuppen, H. M. Quantification of the role of chemical desorption in molecular clouds. *Accounts of Chemical Research*, [54\(4\):745–753](#), 2021.
- Frenkel, J. On the transformation of light into heat in solids. i. *Phys. Rev.*, [37:17–44](#), Jan 1931.
- Frigo, S. P., Feulner, P., Kassühlke, B., Keller, C., and Menzel, D. Observation of Neutral Atomic Fragments for Specific 1 s Core Excitations of an Adsorbed Molecule. *Physical Review Letters*, [80\(13\):2813–2816](#), March 1998.
- Fuchs, G. W., Cuppen, H. M., Ioppolo, S., Romanzin, C., Bisschop, S. E., Andersson, S., van Dishoeck, E. F., and Linnartz, H. Hydrogenation reactions in interstellar CO ice analogues : A combined experimental/theoretical approach. *Astronomy & Astrophysics*, [505\(2\):629–639](#), October 2009.
- Garg, A., Marhas, K. K., and Goyal, V. Sputtering of presolar grains via galactic cosmic rays in the interstellar medium. *The Astrophysical Journal*, [905\(1\):80](#), dec 2020.
- Güdel, M. and Nazé, Y. X-ray spectroscopy of stars. *The Astronomy and Astrophysics Review*, [17\(3\):309–408](#), September 2009.
- Gerakines, P. A., Schutte, W., and Ehrenfreund, P. Ultraviolet processing of interstellar ice analogs I. pure ices. *Astronomy & Astrophysics*, 1996.
- Gómez Martín, J. C., Caravan, R. L., Blitz, M. A., Heard, D. E., and Plane, J. M. C. Low Temperature Kinetics of the CH<sub>3</sub>OH + OH Reaction. *The Journal of Physical Chemistry A*, [118\(15\):2693–2701](#), April 2014.
- González Delgado, D., Olofsson, H., Kerschbaum, F., Schöier, F. L., Lindqvist, M., and Groenewegen, M. A. T. "thermal" sio radio line emission towards m-type agb stars : A probe of circumstellar dust formation and dynamics\*. *A&A*, [411\(2\):123–147](#), 2003.
- Grady, M. M., Wright, I. P., Engrand, C., and Siljeström, S. The Rosetta Mission and the Chemistry of Organic Species in Comet 67P/Churyumov–Gerasimenko. *Elements*, [14\(2\):95–100](#), April 2018.
- Gratier, P., Pety, J., Guzmán, V., Gerin, M., Goicoechea, J. R., Roueff, E., and Faure, A. The IRAM-30 m line survey of the Horsehead PDR : III. High abundance of complex (iso-)nitrile molecules in UV-illuminated gas. *Astronomy & Astrophysics*, [557:A101](#), September 2013.
- Gredel, R., Lepp, S., and Dalgarno, A. The C/CO Ratio in Dense Interstellar Clouds. *Apjl*, [323:L137](#), December 1987.
- Gredel, R., Lepp, S., Dalgarno, A., and Herbst, E. Cosmic-ray–induced photodissociation and photoionization rates of interstellar molecules. *Apj*, [347:289](#), dec 1989.
- Guelachvili, G., de Villeneuve, D., Farrenq, R., Urban, W., and Verges, J. Dunham coefficients for seven isotopic species of co. *Journal of Molecular Spectroscopy*, [98\(1\):64–79](#), 1983.

- Guzmán, V. V., Pety, J., Gratier, P., Goicoechea, J. R., Gerin, M., Roueff, E., Le Petit, F., and Le Bourlot, J. Chemical complexity in the horsehead photodissociation region. *Faraday Discuss.*, [168:103–127](#), 2014.
- Hama, T., Yokoyama, M., Yabushita, A., Kawasaki, M., Andersson, S., Western, C. M., Ashfold, M. N. R., Dixon, R. N., and Watanabe, N. A desorption mechanism of water following vacuum-ultraviolet irradiation on amorphous solid water at 90 K. *The Journal of Chemical Physics*, [132\(16\):164508](#), 2010.
- Hashinokuchi, M., Koumura, R., Che, D.-C., Ohoyama, H., and Kasai, T. A new channel of hydrogen elimination in the 121.6-nm photodissociation of formic acid detected by a doppler-selected tof mass spectrometry. *Journal of the Mass Spectrometry Society of Japan*, [50\(1\):7–10](#), 2002.
- Hasselbrink, E. Coupling of the rotational and translational degrees of freedom in molecular diet : A classical trajectory study. *Chemical Physics Letters*, [170\(4\):329–334](#), 1990.
- Herbst, E. The synthesis of large interstellar molecules. *International Reviews in Physical Chemistry*, [36\(2\):287–331](#), April 2017.
- Herbst, E. and van Dishoeck, E. F. Complex Organic Interstellar Molecules. *Annual Review of Astronomy and Astrophysics*, [47\(1\):427–480](#), September 2009.
- Hilbig, R. and Wallenstein, R. Narrowband tunable VUV radiation generated by nonresonant sum- and difference-frequency mixing in xenon and krypton. *Applied Optics*, [21\(5\):913](#), March 1982.
- Hilbig, R. and Wallenstein, R. Tunable VUV radiation generated by two-photon resonant frequency mixing in xenon. *IEEE Journal of Quantum Electronics*, [19\(2\):194–201](#), February 1983.
- Hirashita, H. and Nozawa, T. Synthesized grain size distribution in the interstellar medium. *Earth, Planets and Space*, [65\(3\):7](#), March 2013.
- Hitchcock, A. and Brion, C. K-shell excitation spectra of CO, N<sub>2</sub> and O<sub>2</sub>. *Journal of Electron Spectroscopy and Related Phenomena*, [18\(1\):1–21](#), 1980.
- Houplin, J., Amiaud, L., Humblot, V., Martin, I., Matar, E., Azria, R., Pradier, C.-M., and Lafosse, A. Selective terminal function modification of sams driven by low-energy electrons (0–15 ev). *Phys. Chem. Chem. Phys.*, [15:7220–7227](#), 2013.
- Howells, M. R. Beam line design for synchrotron spectroscopy in thevuv. *Appl. Opt.*, [19\(23\):4027–4034](#), Dec 1980.
- Hudson, R. and Moore, M. Laboratory studies of the formation of methanol and other organic molecules by water+carbon monoxide radiolysis : Relevance to comets, icy satellites, and interstellar ices. *Icarus*, [140\(2\):451–461](#), 1999.
- Hudson, R. and Moore, M. Reactions of nitriles in ices relevant to Titan, comets, and the interstellar medium : formation of cyanate ion, ketenimines, and isonitriles. *Icarus*, [172\(2\):466–478](#), December 2004.
- Imhof, R. E., Read, F. H., and Beckett, S. T. Determination of the transition moment of the B-X transition in co. *Journal of Physics B : Atomic and Molecular Physics*, [5\(4\):896–902](#), apr 1972.
- Ioppolo, S., Cuppen, H. M., Romanzin, C., van Dishoeck, E. F., and Linnartz, H. Laboratory evidence for efficient water formation in interstellar ices. *The Astrophysical Journal*, [686\(2\):1474–1479](#), oct 2008.

- Ioppolo, S., Cuppen, H. M., Romanzin, C., van Dishoeck, E. F., and Linnartz, H. Water formation at low temperatures by surface O<sub>2</sub> hydrogenation I : characterization of ice penetration. *Phys. Chem. Chem. Phys.*, [12:12065–12076](#), 2010.
- Ioppolo, S., Cuppen, H. M., and Linnartz, H. Surface formation routes of interstellar molecules : hydrogenation reactions in simple ices. *Rendiconti Lincei*, [22\(3\):211](#), September 2011.
- Ipolyi, I., Michaelis, W., and Swiderek, P. Electron-induced reactions in condensed films of acetonitrile and ethane. *Phys. Chem. Chem. Phys.*, [9:180–191](#), 2007.
- Irvine, W., Friberg, P., Kaifu, N., Matthews, H., Minh, Y., Ohishi, M., and Ishikawa, S. Detection of formic acid in the cold, dark cloud L134N. *Astron Astrophys.*, [229:L9–12:11538681](#), 1990.
- Ishibashi, A., Hidaka, H., Oba, Y., Kouchi, A., and Watanabe, N. Efficient formation pathway of methyl formate : The role of OH radicals on ice dust. *The Astrophysical Journal Letters*, [921\(1\):L13](#), oct 2021.
- Ishii, I. and Hitchcock, A. The oscillator strengths for C1s and O1s excitation of some saturated and unsaturated organic alcohols, acids and esters. *Journal of Electron Spectroscopy and Related Phenomena*, [46\(1\):55–84](#), 1988.
- Jamieson, C. S., Mebel, A. M., and Kaiser, R. I. Understanding the Kinetics and Dynamics of Radiation-induced Reaction Pathways in Carbon Monoxide Ice at 10 K. *The Astrophysical Journal Supplement Series*, [163\(1\):184–206](#), March 2006.
- Jedlovszky, P., Hantal, G., Neuróhr, K., Picaud, S., Hoang, P. N. M., von Hessberg, P., and Crowley, J. N. Adsorption Isotherm of Formic Acid on the Surface of Ice, as Seen from Experiments and Grand Canonical Monte Carlo Simulation. *The Journal of Physical Chemistry C*, [112\(24\):8976–8987](#), June 2008.
- Jiménez-Escobar, A., Ciaravella, A., Cecchi-Pestellini, C., Huang, C.-H., Sie, N.-E., Chen, Y.-J., and Muñoz Caro, G. M. X-Ray Photo-desorption of H<sub>2</sub>O:CO:NH<sub>3</sub> Circumstellar Ice Analogs : Gas-phase Enrichment. *The Astrophysical Journal*, [868\(1\):73](#), November 2018.
- Jiménez-Serra, I., Vasyunin, A. I., Caselli, P., Marcelino, N., Billot, N., Viti, S., Testi, L., Vastel, C., Lefloch, B., and Bachiller, R. The spatial distribution of complex organic molecules in the L1544 pre-stellar core. *The Astrophysical Journal*, [830\(1\):L6](#), October 2016.
- Jones, A. P. Variations on a theme - the evolution of hydrocarbon solids - i. compositional and spectral modelling - the ercn and dg models. *A&A*, [540:A1](#), 2012a.
- Jones, A. P. Variations on a theme - the evolution of hydrocarbon solids - ii. optical property modelling - the optec(s) model. *A&A*, [540:A2](#), 2012b.
- Jones, A. P. Variations on a theme - the evolution of hydrocarbon solids - iii. size-dependent properties - the optec(s)(a) model. *A&A*, [542:A98](#), 2012c.
- Jugnet, Y., Himpsel, F. J., Avouris, P., and Koch, E. E. High-Resolution C 1 s and O 1 s Core-Excitation Spectroscopy of Chemisorbed, Physisorbed, and Free CO. *Physical Review Letters*, [53\(2\):198–201](#), July 1984.
- Kaiser, R. I., Maity, S., and Jones, B. M. Synthesis of prebiotic glycerol in interstellar ices. *Angewandte Chemie International Edition*, [54\(1\):195–200](#), 2014.

- Kanda, K., Nagata, T., and Ibuki, T. Photodissociation of some simple nitriles in the extreme vacuum ultraviolet region. *Chemical Physics*, **243(1-2):89–96**, May 1999.
- Kato, M., Morishita, Y., Oura, M., Yamaoka, H., Tamenori, Y., Okada, K., Matsudo, T., Gejo, T., Suzuki, I., and Saito, N. Absolute photoionization cross sections with ultra-high energy resolution for Ar, Kr, Xe and N<sub>2</sub> in inner-shell ionization regions. *Journal of Electron Spectroscopy and Related Phenomena*, **160(1-3):39–48**, August 2007.
- Kempgens, B., Kivimäki, A., Neeb, M., Köppe, H. M., Bradshaw, A. M., and Feldhaus, J. A high-resolution N 1s photoionization study of the molecule in the near-threshold region. *Journal of Physics B: Atomic, Molecular and Optical Physics*, **29(22):5389–5402**, nov 1996.
- Kimmel, G. A., Stevenson, K. P., Dohnálek, Z., Smith, R. S., and Kay, B. D. Control of amorphous solid water morphology using molecular beams. I. experimental results. *The Journal of Chemical Physics*, **114(12):5284–5294**, 2001.
- King, G. C., Read, F. H., and Tronc, M. Investigation of the energy and vibrational structure of the inner shell  $(1s)^{-1}(\pi 2p)^1 II$  state of the nitrogen molecule by electron impact with high resolution. *Chemical Physics Letters*, **52(1):50–54**, 1977.
- Knauth, D. C., Andersson, B.-G., McCandliss, S. R., and Warren Moos, H. The interstellar N<sub>2</sub> abundance towards HD 124314 from far-ultraviolet observations. *Nature*, **429(6992):636–638**, June 2004.
- Kobayashi, K. Optical spectra and electronic structure of ice. *The Journal of Physical Chemistry*, **87(21):4317–4321**, 1983.
- Krause, M. O. Atomic radiative and radiationless yields for K and L shells. *Journal of Physical and Chemical Reference Data*, **8(2):307–327**, 1979.
- Kumar, R. and Sharma, P. K. Electron impact ionization cross sections of C<sub>2</sub>H<sub>4</sub> molecule. *Chemical Physics Impact*, **1:100004**, December 2020.
- Kuo, Y.-P., Lu, H.-C., Wu, Y.-J., Cheng, B.-M., and Ogilvie, J. Absorption spectra in the vacuum ultraviolet region of methanol in condensed phases. *Chemical Physics Letters*, **447(1-3):168–174**, October 2007.
- Laffon, C., Lacombe, S., Bournel, F., and Parent, P. Radiation effects in water ice : A near-edge x-ray absorption fine structure study. *The Journal of Chemical Physics*, **125(20):204714**, November 2006.
- Laffon, C., Lasne, J., Bournel, F., Schulte, K., Lacombe, S., and Parent, P. Photochemistry of carbon monoxide and methanol in water and nitric acid hydrate ices : A NEXAFS study. *Physical Chemistry Chemical Physics*, **12(36):10865**, 2010.
- Laher, R. R. and Gilmore, F. R. Updated Excitation and Ionization Cross Sections for Electron Impact on Atomic Oxygen. *Journal of Physical and Chemical Reference Data*, **19(1):277–305**, January 1990.
- Leach, S., Schwell, M., Un, S., Jochims, H.-W., and Baumgärtel, H. VUV absorption spectroscopy of acetonitrile between 7 and 20eV : A revisionist study. *Chemical Physics*, **344(1-2):147–163**, February 2008.
- Lee, L. and Suto, M. Quantitative photoabsorption and fluorescence study of H<sub>2</sub>O and D<sub>2</sub>O at 50-190 nm. *Chemical Physics*, **110(1):161–169**, 1986.

- Lee, S.-H. Photodissociation dynamics of methyl formate at 193.3 nm : Branching ratios, kinetic-energy distributions, and angular anisotropies of products. *The Journal of Chemical Physics*, [129\(19\):194304](#), 2008.
- Leger, A. and Puget, J. L. Identification of the unidentified infrared emission features of interstellar dust. *A&A*, [137 :L5–L8](#), August 1984.
- Liu, S., Mehringer, D. M., and Snyder, L. E. Observations of Formic Acid in Hot Molecular Cores. *The Astrophysical Journal*, [552\(2\):654–663](#), May 2001.
- Loeffler, M. J. and Baragiola, R. A. Photolysis of solid NH<sub>3</sub> and NH<sub>3</sub>–H<sub>2</sub>O mixtures at 193 nm. *The Journal of Chemical Physics*, [133\(21\):214506](#), 2010.
- Loeffler, M. J., Baratta, G. A., Palumbo, M. E., Strazzulla, G., and Baragiola, R. A. CO<sub>2</sub> synthesis in solid CO by lyman-tons and 200 keV protons. *A&A*, [435\(2\):587–594](#), 2005.
- Loomis, R. A., Cleaves, L. I., Öberg, K. I., Aikawa, Y., Bergner, J., Furuya, K., Guzman, V. V., and Walsh, C. The Distribution and Excitation of CH<sub>3</sub>CN in a Solar Nebula Analog. *The Astrophysical Journal*, [859\(2\):131](#), June 2018.
- Lopez, J., Tarnovsky, V., Gutkin, M., and Becker, K. Electron-impact ionization of NO, NO<sub>2</sub>, and N<sub>2</sub>O. *International Journal of Mass Spectrometry*, [225\(1\):25–37](#), February 2003.
- Lu, H.-C., Chen, H.-K., Cheng, B.-M., Kuo, Y.-P., and Ogilvie, J. F. Spectra in the vacuum ultraviolet region of CO in gaseous and solid phases and dispersed in solid argon at 10 K. *Journal of Physics B : Atomic, Molecular and Optical Physics*, [38\(20\):3693–3704](#), sep 2005.
- Lu, H.-C., Chen, H.-K., Cheng, B.-M., and Ogilvie, J. Absorption spectra in the vacuum ultraviolet region of small molecules in condensed phases. *Spectrochimica Acta Part A : Molecular and Biomolecular Spectroscopy*, [71\(4\):1485–1491](#), December 2008.
- Manigand, S., Calcutt, H., Jørgensen, J. K., Taquet, V., Müller, H. S. P., Coutens, A., Wampfler, S. F., Ligtnerink, N. F. W., Drozdovskaya, M. N., Kristensen, L. E., van der Wiel, M. H. D., and Bourke, T. L. The ALMA-PILS survey : the first detection of doubly deuterated methyl formate (CHD<sub>2</sub>OCHO) in the ISM. *Astronomy & Astrophysics*, [623:A69](#), March 2019.
- Marangos, J. P., Shen, N., Ma, H., Hutchinson, M. H. R., and Connerade, J. P. Broadly tunable vacuum-ultraviolet radiation source employing resonant enhanced sum–difference frequency mixing in krypton. *Journal of the Optical Society of America B*, [7\(7\):1254](#), July 1990.
- Marchione, D., Thrower, J. D., and McCoustra, M. R. S. Efficient electron-promoted desorption of benzene from water ice surfaces. *Physical Chemistry Chemical Physics*, [18\(5\):4026–4034](#), 2016.
- Martín-Doménech, R., Muñoz Caro, G. M., Bueno, J., and Goesmann, F. Thermal desorption of circumstellar and cometary ice analogs. *A&A*, [564:A8](#), 2014.
- Martín-Doménech, R., Manzano-Santamaría, J., Muñoz Caro, G. M., Cruz-Díaz, G. A., Chen, Y.-J., Herero, V. J., and Tanarro, I. Uv photoprocessing of CO<sub>2</sub> ice : a complete quantification of photochemistry and photon-induced desorption processes. *A&A*, [584:A14](#), 2015a.
- Martín-Doménech, R., Manzano-Santamaría, J., Muñoz Caro, G. M., Cruz-Díaz, G. A., Chen, Y.-J., Herero, V. J., and Tanarro, I. UV photoprocessing of CO<sub>2</sub> ice : a complete quantification of photochemistry and photon-induced desorption processes. *A&A*, [584:A14](#), 2015b.

- Martín-Doménech, R., Muñoz Caro, G. M., and Cruz-Díaz, G. A. Study of the photon-induced formation and subsequent desorption of CH<sub>3</sub>OH and H<sub>2</sub>CO in interstellar ice analogs. *A&A*, **589**:A107, 2016.
- Martín-Doménech, R., Cruz-Díaz, G. A., and Muñoz Caro, G. M. UV photoprocessing of NH<sub>3</sub> ice : photon-induced desorption mechanisms. *Monthly Notices of the Royal Astronomical Society*, **473**(2): 2575–2582, January 2018.
- Mathis, J. S., Mezger, P. G., and Panagia, N. Interstellar radiation field and dust temperatures in the diffuse interstellar medium and in giant molecular clouds. *A&A*, **128** :212–229, November 1983.
- Mehring, D. M. and Snyder, L. E. The Location of Complex Molecules in G34.3 + 0.2 : Further Evidence for Grain-Surface Chemistry. *The Astrophysical Journal*, **471**(2):897–902, November 1996.
- Mennella, V., Baratta, G. A., Palumbo, M. E., and Bergin, E. A. Synthesis of CO and CO<sub>2</sub> molecules by UV irradiation of water ice-covered hydrogenated carbon grains. *The Astrophysical Journal*, **643**(2): 923–931, jun 2006.
- Menzel, D. and Feulner, P. Selective bond breaking in adsorbates by core excitations. *Journal of Physics : Condensed Matter*, **13**(49):11249–11266, December 2001.
- Menzel, D. and Gomer, R. Desorption from metal surfaces by low-energy electrons. *The Journal of Chemical Physics*, **41**(11):3311–3328, 1964a.
- Menzel, D. and Gomer, R. Desorption from surfaces by slow-electron impact. *The Journal of Chemical Physics*, **40**(4):1164–1165, 1964b.
- Minissale, M., Dulieu, F., Cazaux, S., and Hocuk, S. Dust as interstellar catalyst : I. Quantifying the chemical desorption process. *Astronomy & Astrophysics*, **585**:A24, January 2016a.
- Minissale, M., Moudens, A., Baouche, S., Chaabouni, H., and Dulieu, F. Hydrogenation of CO-bearing species on grains : unexpected chemical desorption of CO. *Monthly Notices of the Royal Astronomical Society*, **458**(3):2953–2961, May 2016b.
- Miyauchi, N., Hidaka, H., Chigai, T., Nagaoka, A., Watanabe, N., and Kouchi, A. Formation of hydrogen peroxide and water from the reaction of cold hydrogen atoms with solid oxygen at 10 K. *Chemical Physics Letters*, **456**(1):27–30, 2008.
- Moddeman, W. E., Carlson, T. A., Krause, M. O., Pullen, B. P., Bull, W. E., and Schweitzer, G. K. Determination of the *K*–*LL* Auger Spectra of N<sub>2</sub>, O<sub>2</sub>, CO, NO, H<sub>2</sub>O, and CO<sub>2</sub>. *The Journal of Chemical Physics*, **55**(5):2317–2336, September 1971.
- Modica, P. and Palumbo, M. E. Formation of methyl formate after cosmic ion irradiation of icy grain mantles. *A&A*, **519**:A22, 2010.
- Mozejko, P. Calculations of electron impact ionization cross section for simple biomolecules : Formic and acetic acids. *The European Physical Journal Special Topics*, **144**(1):233–237, May 2007.
- Moore, M., Hudson, R., and Gerakines, P. Mid- and far-infrared spectroscopic studies of the influence of temperature, ultraviolet photolysis and ion irradiation on cosmic-type ices. *Spectrochimica Acta Part A : Molecular and Biomolecular Spectroscopy*, **57**(4):843–858, 2001.
- Moriyama, M., Tsutsui, Y., and Honma, K. Vacuum ultraviolet photodissociation dynamics of acetonitrile. *The Journal of Chemical Physics*, **108**(15):6215–6221, April 1998.

- Muñoz Caro, G. M., Jiménez-Escobar, A., Martín-Gago, J. Á., Rogero, C., Atienza, C., Puertas, S., Sobrado, J. M., and Torres-Redondo, J. New results on thermal and photodesorption of CO ice using the novel interstellar astrochemistry chamber (ISAC). *A&A*, [522:A108](#), 2010.
- Muñoz Caro, G. M., Chen, Y.-J., Aparicio, S., Jiménez-Escobar, A., Rosu-Finsen, A., Lasne, J., and McCoustra, M. R. S. Photodesorption and physical properties of CO ice as a function of temperature. *A&A*, [589:A19](#), 2016.
- Mumma, M. J. and Charnley, S. B. The chemical composition of comets—emerging taxonomies and natal heritage. *Annual Review of Astronomy and Astrophysics*, [49\(1\):471–524](#), 2011a.
- Mumma, M. J. and Charnley, S. B. The Chemical Composition of Comets—Emerging Taxonomies and Natal Heritage. *Annual Review of Astronomy and Astrophysics*, [49\(1\):471–524](#), September 2011b.
- Muñoz Caro, G. M., Meierhenrich, U. J., Schutte, W. A., Barbier, B., Arcones Segovia, A., Rosenbauer, H., Thiemann, W. H.-P., Brack, A., and Greenberg, J. M. Amino acids from ultraviolet irradiation of interstellar ice analogues. *Nature*, [416\(6879\):403–406](#), March 2002.
- Muñoz Caro, G. M. and Dartois, E. Prebiotic chemistry in icy grain mantles in space. An experimental and observational approach. *Chemical Society Reviews*, [42\(5\):2173](#), 2013.
- Muñoz Caro, G. M., Ciaravella, A., Jiménez-Escobar, A., Cecchi-Pestellini, C., González-Díaz, C., and Chen, Y.-J. X-ray versus ultraviolet irradiation of astrophysical ice analogs leading to formation of complex organic molecules. *ACS Earth and Space Chemistry*, [3\(10\):2138–2157](#), 2019.
- Nahon, L., de Oliveira, N., Garcia, G. A., Gil, J.-F., Pilette, B., Marcouillé, O., Lagarde, B., and Polack, F. DESIRS : a state-of-the-art VUV beamline featuring high resolution and variable polarization for spectroscopy and dichroism at SOLEIL. *Journal of Synchrotron Radiation*, [19\(4\):508–520](#), Jul 2012.
- Nakamura, M., Tsai, P.-Y., Kasai, T., Lin, K.-C., Palazzetti, F., Lombardi, A., and Aquilanti, V. Dynamical, spectroscopic and computational imaging of bond breaking in photodissociation : roaming and role of conical intersections. *Faraday Discuss.*, [177:77–98](#), 2015.
- Nguyen, T., Baouche, S., Congiu, E., Diana, S., Pagani, L., and Dulieu, F. Segregation effect and N<sub>2</sub> binding energy reduction in CO-N<sub>2</sub> systems adsorbed on water ice substrates. *Astronomy & Astrophysics*, [619:A111](#), November 2018.
- Nguyen, T., Oba, Y., Shimonishi, T., Kouchi, A., and Watanabe, N. An experimental study of chemical desorption for phosphine in interstellar ice. *The Astrophysical Journal Letters*, [898\(2\):L52](#), aug 2020.
- Nishi, N., Shinohara, H., and Okuyama, T. Photodetachment, photodissociation, and photochemistry of surface molecules of icy solids containing NH<sub>3</sub> and pure H<sub>2</sub>O ices. *The Journal of Chemical Physics*, [80\(8\):3898–3910](#), 1984.
- Noble, J. A., Congiu, E., Dulieu, F., and Fraser, H. J. Thermal desorption characteristics of CO, O<sub>2</sub> and CO<sub>2</sub> on non-porous water, crystalline water and silicate surfaces at submonolayer and multilayer coverages : Desorption from H<sub>2</sub>O(np), H<sub>2</sub>O(c) and SiOx. *Monthly Notices of the Royal Astronomical Society*, January 2012.
- Nomura, H., Aikawa, Y., Tsujimoto, M., Nakagawa, Y., and Millar, T. J. Molecular Hydrogen Emission from Protoplanetary Disks. II. Effects of X-Ray Irradiation and Dust Evolution. *The Astrophysical Journal*, [661\(1\):334–353](#), May 2007.

- Notsu, S., van Dishoeck, E. F., Walsh, C., Bosman, A. D., and Nomura, H. X-ray-induced chemistry of water and related molecules in low-mass protostellar envelopes. *Astronomy & Astrophysics*, [650:A180](#), June 2021.
- Oba, Y., Tomaru, T., Lamberts, T., Kouchi, A., and Watanabe, N. An infrared measurement of chemical desorption from interstellar ice analogues. *Nature Astronomy*, [2\(3\):228–232](#), March 2018.
- Öberg, K. I. Photochemistry and astrochemistry : photochemical pathways to interstellar complex organic molecules. *Chemical Reviews*, [116\(17\):9631–9663](#), September 2016.
- Öberg, K. I., van Broekhuizen, F., Fraser, H. J., Bisschop, S. E., van Dishoeck, E. F., and Schlemmer, S. Competition between CO and N<sub>2</sub> Desorption from Interstellar Ices. *The Astrophysical Journal*, [621\(1\):L33–L36](#), March 2005.
- Öberg, K. I., Fuchs, G. W., Awad, Z., Fraser, H. J., Schlemmer, S., van Dishoeck, E. F., and Linnartz, H. Photodesorption of CO ice. *The Astrophysical Journal*, [662\(1\):L23–L26](#), may 2007.
- Öberg, K. I., Garrod, R. T., van Dishoeck, E. F., and Linnartz, H. Formation rates of complex organics in UV irradiated CH<sub>3</sub>OH-rich ices I : Experiments. *Astronomy & Astrophysics*, [504\(3\):891–913](#), September 2009a.
- Öberg, K. I., Linnartz, H., Visser, R., and van Dishoeck, E. F. Photodesorption of ices. II. H<sub>2</sub>O and D<sub>2</sub>O. *The Astrophysical Journal*, [693\(2\):1209–1218](#), mar 2009b.
- Öberg, K. I., van Dishoeck, E. F., and Linnartz, H. Photodesorption of ices I : CO, N<sub>2</sub>, and CO<sub>2</sub>. *Astronomy & Astrophysics*, [496\(1\):281–293](#), March 2009c.
- Öberg, K. I., Bottinelli, S., Jørgensen, J. K., and van Dishoeck, E. F. A cold complex chemistry toward the low-mass protostar B1-b : evidence for complex molecule production in ices. *The Astrophysical Journal*, [716\(1\):825–834](#), June 2010.
- Öberg, K. I., Guzmán, V. V., Furuya, K., Qi, C., Aikawa, Y., Andrews, S. M., Loomis, R., and Wilner, D. J. The comet-like composition of a protoplanetary disk as revealed by complex cyanides. *Nature*, [520\(7546\):198–201](#), April 2015.
- Ocaña, A. J., Blázquez, S., Potapov, A., Ballesteros, B., Canosa, A., Antiñolo, M., Vereecken, L., Albaladejo, J., and Jiménez, E. Gas-phase reactivity of CH<sub>3</sub>OH toward OH at interstellar temperatures (11.7–177.5 K) : experimental and theoretical study. *Physical Chemistry Chemical Physics*, [21\(13\):6942–6957](#), 2019.
- Olbert-Majkut, A., Ahokas, J., Lundell, J., and Pettersson, M. Photolysis of HCOOH monomer and dimer in solid argon : Raman characterization of in situ formed molecular complexes. *Physical Chemistry Chemical Physics*, [12\(26\):7138](#), 2010.
- Orient, O. J. and Strivastava, S. K. Electron impact ionisation of H<sub>2</sub>O, CO, CO<sub>2</sub> and CH<sub>4</sub>. *Journal of Physics B : Atomic and Molecular Physics*, [20\(15\):3923–3936](#), August 1987.
- Orlando, T. and Kimmel, G. The role of excitons and substrate temperature in low-energy (5–50 eV) electron-stimulated dissociation of amorphous d<sub>2</sub>o ice. *Surface Science*, [390\(1\):79–85](#), 1997. Desorption Induced by Electronic Transitions.
- Owen, T. C., Roush, T. L., Cruikshank, D. P., Elliot, J. L., Young, L. A., de Bergh, C., Schmitt, B., Geballe, T. R., Brown, R. H., and Bartholomew, M. J. Surface ices and the atmospheric composition of Pluto. *Science*, [261\(5122\):745–748](#), 1993.

- Pandya, S. H., Shelat, F. A., Joshipura, K., and Vaishnav, B. G. Electron ionization of exotic molecular targets CN, C<sub>2</sub>N<sub>2</sub>, HCN, HNC and BF—Theoretical cross sections. *International Journal of Mass Spectrometry*, [323-324:28–33](#), June 2012.
- Parent, P., Laffon, C., and Bournel, F. Core-induced photofragmentation of acetonitrile adsorbed on Au(111) and Pt(111). *The Journal of Chemical Physics*, [112\(2\):986–991](#), January 2000.
- Parent, P., Laffon, C., Mangeney, C., Bournel, F., and Tronc, M. Structure of the water ice surface studied by x-ray absorption spectroscopy at the O K-edge. *The Journal of Chemical Physics*, [117\(23\):10842–10851](#), 2002.
- Petrik, N. G. and Kimmel, G. A. Electron-Stimulated Reactions at the Interfaces of Amorphous Solid Water Films Driven by Long-Range Energy Transfer from the Bulk. *Physical Review Letters*, [90\(16\):166102](#), April 2003.
- Pontoppidan, K. M., Fraser, H. J., Dartois, E., Thi, W.-F., van Dishoeck, E. F., Boogert, A. C. A., d’Hendecourt, L., Tielens, A. G. G. M., and Bisschop, S. E. A 3-5  $\mu\text{m}$  VLT spectroscopic survey of embedded young low mass stars I - structure of the CO ice. *A&A*, [408\(3\):981–1007](#), 2003.
- Potapov, A., Jäger, C., and Henning, T. Ice Coverage of Dust Grains in Cold Astrophysical Environments. *Physical Review Letters*, [124\(22\):221103](#), June 2020.
- Potapov, A., Bouwman, J., Jäger, C., and Henning, T. Dust/ice mixing in cold regions and solid-state water in the diffuse interstellar medium. *Nature Astronomy*, [5\(1\):78–85](#), January 2021.
- Poteet, C. A., Whittet, D. C. B., and Draine, B. T. The composition of interstellar grains toward  $\zeta$  Ophiuchi : constraining the elemental budget near the diffuse-dense cloud transition. *The Astrophysical Journal*, [801\(2\):110](#), mar 2015.
- Prince, K. C., Richter, R., de Simone, M., Alagia, M., and Coreno, M. Near Edge X-ray Absorption Spectra of Some Small Polyatomic Molecules. *The Journal of Physical Chemistry A*, [107\(12\):1955–1963](#), March 2003.
- Purcell, C. R., Balasubramanyam, R., Burton, M. G., Walsh, A. J., Minier, V., Hunt-Cunningham, M. R., Kedziora-Chudczer, L. L., Longmore, S. N., Hill, T., Bains, I., Barnes, P. J., Busfield, A. L., Calisse, P., Crighton, N. H. M., Curran, S. J., Davis, T. M., Dempsey, J. T., Derragopian, G., Fulton, B., Hidas, M. G., Hoare, M. G., Lee, J.-K., Ladd, E. F., Lumsden, S. L., Moore, T. J. T., Murphy, M. T., Oudmaijer, R. D., Pracy, M. B., Rathborne, J., Robertson, S., Schultz, A. S. B., Shobbrook, J., Sparks, P. A., Storey, J., and Travouillon, T. A CH<sub>3</sub>CN and HCO<sup>+</sup> survey towards southern methanol masers associated with star formation. *Monthly Notices of the Royal Astronomical Society*, [367\(2\):553–576](#), April 2006.
- Qasim, D., Chuang, K.-J., Fedoseev, G., Ioppolo, S., Boogert, A. C. A., and Linnartz, H. Formation of interstellar methanol ice prior to the heavy CO freeze-out stage. *Astronomy & Astrophysics*, [612:A83](#), April 2018.
- Qasim, D., Lamberts, T., He, J., Chuang, K.-J., Fedoseev, G., Ioppolo, S., Boogert, A. C. A., and Linnartz, H. Extension of the HCOOH and CO<sub>2</sub> solid-state reaction network during the CO freeze-out stage : inclusion of H<sub>2</sub>CO. *Astronomy & Astrophysics*, [626:A118](#), June 2019.
- Rab, C., Güdel, M., Woitke, P., Kamp, I., Thi, W.-F., Min, M., Aresu, G., and Meijerink, R. X-ray radiative transfer in protoplanetary disks : The role of dust and X-ray background fields. *Astronomy & Astrophysics*, [609:A91](#), January 2018.

- Rakhovskaia, O., Wiethoff, P., and Feulner, P. Thresholds for electron stimulated desorption of neutral molecules from solid N<sub>2</sub>, CO, O<sub>2</sub> and NO. *Nuclear Instruments and Methods in Physics Research Section B: Beam Interactions with Materials and Atoms*, **101(1):169–173**, 1995.
- Redhead, P. A. Desorption of CO and O<sup>+</sup> from polycrystalline mo surfaces by slow electron impact. *Applied Physics Letters*, **4(9):166–167**, 1964a.
- Redhead, P. A. Interaction of slow electrons with chemisorbed oxygen. *Canadian Journal of Physics*, **42(5):886–905**, 1964b.
- Redhead, P. Thermal desorption of gases. *Vacuum*, **12(4):203–211**, 1962.
- Remijan, A., Shiao, Y., Friedel, D. N., Meier, D. S., and Snyder, L. E. A Survey of Large Molecules of Biological Interest toward Selected High-Mass Star-forming Regions. *The Astrophysical Journal*, **617(1):384–398**, December 2004.
- Romberg, R., Heckmair, N., Frigo, S. P., Ogurtsov, A., Menzel, D., and Feulner, P. Atom-Selective Bond Breaking in a Chemisorbed Homonuclear Molecule Induced by Core Excitation: N<sub>2</sub>/Ru(001). *Physical Review Letters*, **84(2):374–377**, January 2000.
- Rubin, M., Altwegg, K., Balsiger, H., Bar-Nun, A., Berthelier, J.-J., Bieler, A., Bochslers, P., Briois, C., Calmonte, U., Combi, M., Keyser, J. D., Dhooaghe, F., Eberhardt, P., Fiethe, B., Fuselier, S. A., Gasc, S., Gombosi, T. I., Hansen, K. C., Hässig, M., Jäckel, A., Kopp, E., Korth, A., Roy, L. L., Mall, U., Marty, B., Mousis, O., Owen, T., Rème, H., Sémon, T., Tzou, C.-Y., Waite, J. H., and Wurz, P. Molecular nitrogen in comet 67p/churyumov-gerasimenko indicates a low formation temperature. *Science*, **348(6231):232–235**, 2015.
- Ruffle, D. P. and Herbst, E. New models of interstellar gas-grain chemistry — III. Solid CO<sub>2</sub>. *Monthly Notices of the Royal Astronomical Society*, **324(4):1054–1062**, July 2001.
- Ryazantsev, S. V. and Feldman, V. I. Radiation-induced transformations of matrix-isolated formic acid: evidence for the HCOOH → HOCO + H channel. *Physical Chemistry Chemical Physics*, **17(45):30648–30658**, 2015.
- Ryden, B. and Pogge, R. *Interstellar and Intergalactic Medium*. 2021. doi: [10.1017/9781108781596](https://doi.org/10.1017/9781108781596).
- Sacchi, M., Jaouen, N., Popescu, H., Gaudemer, R., Tonnerre, J. M., Chiuzbaian, S. G., Hague, C. F., Delmotte, A., Dubuisson, J. M., Cauchon, G., Lagarde, B., and Polack, F. The SEXTANTS beamline at SOLEIL: a new facility for elastic, inelastic and coherent scattering of soft x-rays. *Journal of Physics: Conference Series*, **425(7):072018**, mar 2013.
- Sala, L., Szymańska, I. B., Dablemont, C., Lafosse, A., and Amiaud, L. Response under low-energy electron irradiation of a thin film of a potential copper precursor for focused electron beam induced deposition (febid). *Beilstein Journal of Nanotechnology*, **9:57–65**, 2018.
- Sala, L. A. *Low-energy Electron Induced Chemistry in Supported Molecular Films*. Theses, Université Paris-Saclay, November 2018. URL <https://tel.archives-ouvertes.fr/tel-02073621>.
- Sandford, S. A. and Allamandola, L. J. The volume- and surface-binding energies of ice systems containing CO, CO<sub>2</sub> and H<sub>2</sub>O. *Icarus*, **87(1):188–192**, 1990.

- Schwaner, A. L., Fieberg, J. E., and White, J. M. Methyl formate on ag(111). 1.thermal adsorption-desorption characteristics and alignment in monolayers. *The Journal of Physical Chemistry B*, [101\(51\):11112–11118](#), December 1997.
- Schwell, M., Jochims, H.-W., Baumgärtel, H., Dulieu, F., and Leach, S. Vuv photochemistry of small biomolecules. *Planetary and Space Science*, [54\(11\):1073–1085](#), 2006. Simulations in Laboratory.
- Schwell, M., Jochims, H.-W., Baumgärtel, H., and Leach, S. VUV photophysics of acetonitrile : Fragmentation, fluorescence and ionization in the 7–22eV region. *Chemical Physics*, [344\(1-2\):164–175](#), February 2008.
- Shannon, R. J., Blitz, M. A., Goddard, A., and Heard, D. E. Accelerated chemistry in the reaction between the hydroxyl radical and methanol at interstellar temperatures facilitated by tunnelling. *Nature Chemistry*, [5\(9\):745–749](#), September 2013.
- Shen, C. J., Greenberg, J. M., Schutte, W. A., and van Dishoeck, E. F. Cosmic ray induced explosive chemical desorption in dense clouds. *A&A*, [415\(1\):203–215](#), 2004.
- Shiozawa, Y., Koitaya, T., Mukai, K., Yoshimoto, S., and Yoshinobu, J. Quantitative analysis of desorption and decomposition kinetics of formic acid on Cu(111) : The importance of hydrogen bonding between adsorbed species. *The Journal of Chemical Physics*, [143\(23\):234707](#), 2015.
- Sipilä, O., Silsbee, K., and Caselli, P. A revised description of the cosmic ray induced desorption of interstellar ices. *The Astrophysical Journal*, [922\(2\):126](#), nov 2021.
- Sivaraman, B., Pavithraa, S., Lo, J.-I., Sekhar, B. N. R., Hill, H., Cheng, B.-M., and Mason, N. J. Vacuum ultraviolet photoabsorption spectra of nitrile ices for their identification on Pluto. *The Astrophysical Journal*, [825\(2\):141](#), July 2016.
- Skinner, S. L., Gudel, M., Audard, M., and Smith, K. New Perspectives on the X-Ray Emission of HD 104237 and Other Nearby Herbig Ae/Be Stars from *XMM-Newton* and *Chandra*. *The Astrophysical Journal*, [614\(1\):221–234](#), October 2004.
- Smith, R. S., Huang, C., Wong, E., and Kay, B. D. Desorption and crystallization kinetics in nanoscale thin films of amorphous water ice. *Surface Science*, [367\(1\):L13–L18](#), 1996.
- Smith, R. S., Huang, C., and Kay, B. D. Evidence for molecular translational diffusion during the crystallization of amorphous solid water. *The Journal of Physical Chemistry B*, [101\(32\):6123–6126](#), 1997.
- Smith, R. S., May, R. A., and Kay, B. D. Desorption Kinetics of Ar, Kr, Xe, N<sub>2</sub>, O<sub>2</sub>, CO, Methane, Ethane, and Propane from Graphene and Amorphous Solid Water Surfaces. *The Journal of Physical Chemistry B*, [120\(8\):1979–1987](#), March 2016.
- Sodhi, R. N. and Brion, C. Reference energies for inner shell electron energy-loss spectroscopy. *Journal of Electron Spectroscopy and Related Phenomena*, [34\(4\):363–372](#), 1984.
- Speedy, R. J., Debenedetti, P. G., Smith, R. S., Huang, C., and Kay, B. D. The evaporation rate, free energy, and entropy of amorphous water at 150 K. *The Journal of Chemical Physics*, [105\(1\):240–244](#), July 1996.
- Srivastava, S. K., Krishnakumar, E., Fucaloro, A. F., and van Note, T. Cross sections for the production of cations by electron impact on methanol. *Journal of Geophysical Research : Planets*, [101\(E11\):26155–26160](#), November 1996.

- Straub, H. C., Renault, P., Lindsay, B. G., Smith, K. A., and Stebbings, R. F. Absolute partial cross sections for electron-impact ionization of H<sub>2</sub>, N<sub>2</sub>, and O<sub>2</sub> from threshold to 1000 eV. *Physical Review A*, **54(3)**: 2146–2153, September 1996.
- Su, H., He, Y., Kong, F., Fang, W., and Liu, R. Photodissociation of formic acid. *The Journal of Chemical Physics*, **113(5)**:1891–1897, 2000.
- Tabayashi, K., Aoyama, J.-i., Matsui, M., Hino, T., and Saito, K. Dissociative excitation of HCOOH by single-vacuum ultraviolet and two-ultraviolet photon. *The Journal of Chemical Physics*, **110(19)**:9547–9554, 1999.
- Tabayashi, K., Yamamoto, K., Takahashi, O., Tamenori, Y., Harries, J. R., Gejo, T., Iseda, M., Tamura, T., Honma, K., Suzuki, I. H., Nagaoka, S.-i., and Ibuki, T. Inner-shell excitation spectroscopy and fragmentation of small hydrogen-bonded clusters of formic acid after core excitations at the oxygen K edge. *The Journal of Chemical Physics*, **125(19)**:194307, November 2006.
- Takigawa, A., Kamizuka, T., Tachibana, S., and Yamamura, I. Dust formation and wind acceleration around the aluminum oxide-rich agb star w hydrae. *Science Advances*, **3(11)**:eaao2149, 2017.
- Taquet, V., Wirström, E. S., Charnley, S. B., Faure, A., López-Sepulcre, A., and Persson, C. M. Chemical complexity induced by efficient ice evaporation in the Barnard 5 molecular cloud. *Astronomy & Astrophysics*, **607**:A20, November 2017.
- Tarnovsky, V., Levin, A., Deutsch, H., and Becker, K. Electron impact ionization of CD<sub>x</sub> (x = 1-4). *Journal of Physics B : Atomic, Molecular and Optical Physics*, **29(1)**:139–152, jan 1996.
- Tarnovsky, V., Deutsch, H., and Becker, K. Electron impact ionization of the hydroxyl radical. *The Journal of Chemical Physics*, **109(3)**:932–936, July 1998.
- Testa, P. X-ray emission processes in stars and their immediate environment. *Proceedings of the National Academy of Sciences*, **107(16)**:7158–7163, April 2010.
- Tian, C. and Vidal, C. R. Cross sections of the electron impact dissociative ionization of CO, and. *Journal of Physics B : Atomic, Molecular and Optical Physics*, **31(4)**:895–909, February 1998.
- Tielens, A. G. G. M. The Molecular Universe. *Proceedings of the International Astronomical Union*, **7 (S280)**:3–18, June 2011.
- Timneanu, N., Caleman, C., Hajdu, J., and van der Spoel, D. Auger electron cascades in water and ice. *Chemical Physics*, **299(2)**:277–283, 2004.
- Torres-Díaz, D., Basalgète, R., Bertin, M., Fillion, J.-H., Michaut, X., Amiaud, L., and Lafosse, A. Quantifying the role of high energy electrons in non-thermal desorption : Pure methanol ices. *To be submitted*, 2022.
- Tronc, M. and Azria, R. Role of morphology of D<sub>2</sub>O ice (20-160 k) in low energy electron stimulated desorption and x-ray photon stimulated desorption. *International Journal of Mass Spectrometry*, **205 (1)**:325 – 331, 2001.
- Tso, C.-J., Kasai, T., and Lin, K.-C. Roaming Dynamics and Conformational Memory in Photolysis of Formic Acid at 193nm Using Time resolved Fourier transform Infrared Emission Spectroscopy. *Scientific Reports*, **10(1)**:4769, March 2020.

- Vacher, J., Jorand, F., Blin-Simiand, N., and Pasquiers, S. Electron impact ionization of formaldehyde. *Chemical Physics Letters*, **476(4-6):178–181**, July 2009.
- Valkealahti, S., Schou, J., and Nieminen, R. M. Energy deposition of keV electrons in light elements. *Journal of Applied Physics*, **65(6):2258–2266**, March 1989.
- van der Marel, N., Booth, A. S., Leemker, M., van Dishoeck, E. F., and Ohashi, S. A major asymmetric ice trap in a planet-forming disk : I. Formaldehyde and methanol. *Astronomy & Astrophysics*, **651:L5**, July 2021.
- van Dishoeck, E. F. Astrochemistry of dust, ice and gas : introduction and overview. *Faraday Discuss.*, **168:9–47**, 2014.
- van Dishoeck, E. F. Astrochemistry : overview and challenges. *Proceedings of the International Astronomical Union*, **13(S332):3–22**, March 2017.
- van Dishoeck, E. F., Herbst, E., and Neufeld, D. A. Interstellar Water Chemistry : From Laboratory to Observations. *Chemical Reviews*, **113(12):9043–9085**, December 2013.
- van Hemert, M. C., Takahashi, J., and van Dishoeck, E. F. Molecular Dynamics Study of the Photodesorption of CO Ice. *The Journal of Physical Chemistry A*, **119(24):6354–6369**, June 2015.
- van 't Hoff, M. L. R., Tobin, J. J., Trapman, L., Harsono, D., Sheehan, P. D., Fischer, W. J., Megeath, S. T., and van Dishoeck, E. F. Methanol and its Relation to the Water Snowline in the Disk around the Young Outbursting Star V883 Ori. *The Astrophysical Journal*, **864(1):L23**, August 2018.
- Vasconcelos, F., Pilling, S., Agnihotri, A., Rothard, H., and Boduch, P. Methyleneimine and cyanomethanimine synthesis from ion irradiation of N<sub>2</sub>-CH<sub>4</sub> ice : Implication on the formation of prebiotic molecules in outer solar system bodies. *Icarus*, **351:113944**, 2020.
- Vastel, C., Ceccarelli, C., Lefloch, B., and Bachiller, R. The origin of complex organic molecules in prestellar cores. *The Astrophysical Journal*, **795(1):L2**, oct 2014.
- Vasyunin, A. I. and Herbst, E. Reactive desorption and radiative associations as possible drivers of complex molecule formation in the cold interstellar medium. *The Astrophysical Journal*, **769(1):34**, May 2013.
- Vasyunin, A. I., Caselli, P., Dulieu, F., and Jiménez-Serra, I. Formation of Complex Molecules in Prestellar Cores : A Multilayer Approach. *The Astrophysical Journal*, **842(1):33**, June 2017.
- Vasyunina, T., Vasyunin, A. I., Herbst, E., Linz, H., Voronkov, M., Britton, T., Zinchenko, I., and Schuller, F. Organic species in infrared dark clouds. *The Astrophysical Journal*, **780(1):85**, December 2013.
- Volosatova, A. D., Lukianova, M. A., Zasimov, P. V., and Feldman, V. I. Direct evidence for a radiation-induced synthesis of acetonitrile and isoacetonitrile from a 1:1 CH<sub>4</sub>-HCN complex at cryogenic temperatures : is it a missing link between inorganic and prebiotic astrochemistry? *Phys. Chem. Chem. Phys.*, **23:18449–18460**, 2021.
- Walker, G. A. H., Bohlender, D. A., Maier, J. P., and Campbell, E. K. Identification of more interstellar C<sub>60</sub><sup>+</sup> bands. *The Astrophysical Journal*, **812(1):L8**, oct 2015.
- Wallace, W. E. Mass spectra. *NIST Mass Spectrometry Data Center*.

- Walsh, C., Nomura, H., Millar, T. J., and Aikawa, Y. Chemical processes in protoplanetary disks. II. on the importance of photochemistry and x-ray ionization. *The Astrophysical Journal*, [747\(2\):114](#), March 2012.
- Walsh, C., Loomis, R. A., Öberg, K. I., Kama, M., van 't Hoff, M. L. R., Millar, T. J., Aikawa, Y., Herbst, E., Widicus Weaver, S. L., and Nomura, H. First detection of gas-phase methanol in a protoplanetary disk. *The Astrophysical Journal*, [823\(1\):L10](#), May 2016.
- Walters, D. L. and Bhalla, C. P. Nonrelativistic auger rates, x-ray rates, and fluorescence yields for the K shell. *Phys. Rev. A*, [3:1919–1927](#), Jun 1971.
- Wannier, G. H. The structure of electronic excitation levels in insulating crystals. *Phys. Rev.*, [52:191–197](#), Aug 1937.
- Watanabe, N. and Kouchi, A. Efficient formation of formaldehyde and methanol by the addition of hydrogen atoms to CO in H<sub>2</sub>O-CO ice at 10 K. *The Astrophysical Journal*, [571\(2\):L173–L176](#), jun 2002.
- Weingartner, J. C. and Draine, B. T. Dust grain–size distributions and extinction in the milky way, large magellanic cloud, and small magellanic cloud. *The Astrophysical Journal*, [548\(1\):296–309](#), feb 2001.
- Western, C. M. Pgopher : A program for simulating rotational, vibrational and electronic spectra. *Journal of Quantitative Spectroscopy and Radiative Transfer*, [186:221–242](#), 2017.
- Wight, G. and Brion, C. K-shell energy loss spectra of 2.5 keV electrons in CO<sub>2</sub> and N<sub>2</sub>O. *Journal of Electron Spectroscopy and Related Phenomena*, [3\(3\):191–205](#), 1974.
- Williams, D. A. Gas and dust in the interstellar medium. *Journal of Physics : Conference Series*, [6:1–17](#), jan 2005.
- Wilson, K. R., Cavalleri, M., Rude, B. S., Schaller, R. D., Catalano, T., Nilsson, A., Saykally, R. J., and Pettersson, L. G. M. X-ray Absorption Spectroscopy of Liquid Methanol Microjets : Bulk Electronic Structure and Hydrogen Bonding Network. *The Journal of Physical Chemistry B*, [109\(20\):10194–10203](#), May 2005.
- Winkler, A. K., Holmes, N. S., and Crowley, J. N. Interaction of methanol, acetone and formaldehyde with ice surfaces between 198 and 223 K. *Physical Chemistry Chemical Physics*, [4\(21\):5270–5275](#), October 2002.
- Wurm, S. Ph.d. thesis. *Universität München Fakultät für Physik, Institut für Festkörperphysik und Technische Physik, Munich, Germany*, 1995.
- Wurm, S., Feulner, P., and Menzel, D. *The Journal of Chemical Physics*, [105\(16\):6673–6687](#), 1996.
- Yabushita, A., Hama, T., Iida, D., Kawanaka, N., Kawasaki, M., Watanabe, N., Ashfold, M. N. R., and Loock, H.-P. Measurements of energy partitioning in H<sub>2</sub> formation by photolysis of amorphous water ice. *The Astrophysical Journal*, [682\(1\):L69–L72](#), jun 2008.
- Yuan, C. and Yates, J. T. Radiation damage and associated phase change effect on photodesorption rates from ices—LY $\alpha$  studies of the surface behavior of CO<sub>2</sub> ice. *The Astrophysical Journal*, [780\(1\):8](#), dec 2013.
- Zawadzki, M. Electron-impact ionization cross section of formic acid. *The European Physical Journal D*, [72\(1\):12](#), January 2018.

Zhou, W., Wilkinson, L., Lee, J. W. L., Heathcote, D., and Vallance, C. Total electron ionization cross-sections for molecules of astrochemical interest. *Molecular Physics*, [117\(21\):3066–3075](#), November 2019.

Zimmermann, F. M. and Ho, W. State resolved studies of photochemical dynamics at surfaces. *Surface Science Reports*, [22\(4-6\):127–247](#), December 1995.